

UNIVERSITY OF BELGRADE
FACULTY OF MECHANICAL ENGINEERING



Hasan Mehdi Nagiar

**STRESS ANALYSIS OF CORNER WELDED
JOINTS STRUCTURE BY MODERN
NUMERICAL-EXPERIMENTAL APPROACH**

Doctoral Dissertation

Belgrade, 2013

UNIVERZITET U BEOGRADU

MAŠINSKI FAKULTET

Hasan Mehdi Nagiar

**NAPONSKA ANALIZA UGAONIH
ZAVARENIH SPOJEVA NOSAČA
KONSTRUKCIJA SAVREMENIM
NUMERIČKO-EKSPERIMENTALNIM
PRISTUPOM**

doktorska disertacija

Beograd, 2013

Dedicated to all my family

Supervisor of doctoral dissertation

Dr. Tasko Maneski, full professor

University of Belgrade, Faculty of Mechanical Engineering

Committee members for the doctoral dissertation

Dr. Aleksandar Sedmak, full professor

University of Belgrade, Faculty of Mechanical Engineering

Dr. Vesna Milosevic-Mitic, full professor

University of Belgrade, Faculty of Mechanical Engineering

Dr. Dragan Ignjatovic, full professor

University of Belgrade, Faculty of Mining and Geology

Dr. Nenad Gubeljak, full professor

University of Maribor, Faculty of Mechanical Engineering

Date of defense:

Acknowledgment

I wish to record my deep gratitude. Thanks and sincere appreciation to my supervisor Prof. Tasko Maneski for his supervision, guidance, advice, continuous help, interest and encouragement throughout the different stages of my Ph.D. study.

I would like to thank all the staff members of the Mechanical Engineering Faculty for their help and guidance during my Ph.D. study.

A special thank is given to my family for their continuous support and help during my Ph.D. study.

In the last, I would like to record my thanks to all who contributed in any way to this work.

Author

Belgrade, November 2013

STRESS ANALYSIS OF CORNER WELDED JOINTS STRUCTURE BY MODERN NUMERICAL-EXPERIMENTAL APPROACH

Abstract:

Hollow and non hollow section members are widely used in industrial applications for the design of many machine and structural components. These components are often fabricated by welding rather than by casting or forging. For example, in agricultural machinery, the hollow tubes are typically connected together through welding to form a corner welded joints. Such joint connections are also employed in other engineering applications such as construction machinery, offshore structures, bridges, and vehicle frames. In this dissertation, the behavior of tubular (box and circle profile) and non tubular (L, Z, C and X profiles) joint connections profiles, subjected to static loads were studied both experimentally and numerically.

From a structural analysis point of view, despite of the wide use of corner welded joints as efficient load carrying members, there is no available practical, simple and accurate approach for their design and analysis. For this purpose, engineers must often prepare relatively complicated and time consuming Finite Element models made up of shell or solid elements. This is because unlike solid-section members, when hollow section members are subjected to general loadings, they may experience severe deformations of their cross-sections that results in stress concentrations in the connection's vicinity. One of the objectives/contributions of this research work is the better understanding of the behavior of the corner welded joint connections under out-of- plane bending and torsion loading conditions. Through a detailed Finite Element Analysis (FEA) using shell and solid elements, the stress distribution at the connection of the tubular and non tubular corner welded joints were obtained for different loading conditions. It is observed that at a short distance away from the connection of the corner welded joints, the structure behaves similar to beams when subjected to loadings.

Finite element models with different modeling techniques and meshing with various size and types of elements were created and analyzed. The full displacement field results were obtained experimentally by using the digital image correlation (DIC) technique. Experimental tests were performed to validate numerical simulations in order to investigate the mechanical performance of a series of fillet-welded connections under combined loading. The full displacement field results show good agreement comparing with the experimental results.

In the numerical study, the connections were modeled using beam, shell and solid elements using software for Finite Element Analysis - Abaqus. The performance of the connections under combined loading was further studied by a simple analytical method aiming for rapid information on the influence of the weld modeling on prediction of the structural performance. Experiments of many beam joints subjected to bending were used for further assessment of the FE models developed in the present study. The study was performed with focus on the prediction of the structural strength of fillet welded joints.

The finite element results of the solid element model show that a generally linear stress distribution across the thickness of the beams is observed. Therefore, the use of shell elements for the analysis of the beam-joint connection is appropriate. Also, at a relatively short distance from the connection, the effects of the local stresses and deformations disappear.

The results show that the normal stresses in the 1 or 2-direction are the highest at the weld path (top of the path) on the top surface, and at horizontal weld path of the beam. It can be observed that the 1 or 2-direction component of normal stress causes the most damage. The values of the Von-Mises equivalent stresses are very close to the values of the stresses in the 1 or 2-direction (absolute value). This is expected as the stresses in the 1 or 2-direction are much larger than the other components of stress. This means that the strains and stresses normal to the weld (i.e., 1 or 2 -direction in this study) are mainly responsible for plasticity/crack initiation and propagation.

Keywords:

Corner welded joints, Finite element method, 3D optical analysis, stress, strain

Scientific field:

Doctor science, Mechanical engineering

Narrow scientific field: Strength of structures

UDC number: 621.791.052:624.014(043.3)

NAPONSKA ANALIZA UGAONIH ZAVARENIH SPOJEVA NOSAČA KONSTRUKCIJA SAVREMENIM NUMERIČKO-EKSPERIMENTALNIM PRISTUPOM

Rezime:

Otvoreni i zatvoreni tankozidi preseki imaju široku primenu u industrijskim aplikacijama za dizajn mnogih mašina i strukturnih komponenti. Ove komponente su često fabrikovane zavarivanjem, a ne livenjem ili kovanjem. Tankozidi profili su obično povezani pomoću ugaonih zavarenih spojeva. Takvi spojevi su takođe korišćeni u drugim inženjerskim aplikacijama kao što su građevinske mašine, mostovi, ramovi, šasije vozila i dr.. U ovoj disertaciji ponašanje zatvorenih profila (kutija, okrugla cev) i otvorenih profila (L, Z, C i K profili) šavnih profila, proučavani su tako što su izlagani statičkim opterećenjima i numeričko-eksperimentalnim pristupom.

Sa tačke gledišta strukturne analize, uprkos široko rasprostranjenim ugaono zavarenim spojevima koji efikasno nose opterećenja na elementima, ne postoji praktičan, jednostavan i precizan pristup za njihov dizajn i analizu. U tu svrhu, inženjeri često moraju pripremiti relativno komplikovan model konačnih elemenata ploče ili zapremine. To je zato što navedeni elementi izloženi opštim opterećenjima proizvode koncentracije napona u blizini spojeva. Jedan od doprinosa ovog istraživanja je bolje razumevanje ponašanja ugaono zavarenih spojeva izloženi naprezanju savijanja i naprezanja savijanja sa uvijanjem. Primena metode konačnih elemenata predstavlja osnovni numerički pristup. Posmatrani profili su medelilirani različitim konačnim elementima (greda, ploča i zapremina) i sa različitim slučajevima opterećenja. Primećuje se da na kratkom rastojanju od spoja putem ugaono zavarenih spojeva struktura nosećeg elementa pod izloženim opterećenjem ponaša se kao greda.

Zavareni spojevi su generisani različitim tehnikama modeliranja sa primenom različitih tipova i veličina konačnih elemenata. Kompletni rezultati deformacija su, takođe, eksperimentalno dobijeni pomoću tehnike primene korelacije digitalne slike (DIC). Eksperimentalni testovi se izvode za proveru numeričkih simulacija u cilju ispitivanja mehaničkih performansi zavarenih spojeva izloženi kombinovanim opterećenjima. Rezultati numeričkog proračuna pokazuju dobro slaganje sa eksperimentalnim rezultatom.

U numeričkom modeliranju primenom metode konačnih elelemenata zavareni spojevi se modeluju pomoću greda, ploča i zapremina korišćenjem softvera - Abakus. Performanse zavarenih spojeva dalje su proučavani korišćenjem jednostavnih analitičkih metoda sa ciljem dobijanja brzih informacija o uticaju zavarenog spoja na predviđanju strukturalnih performansi. Eksperimenti na mnogim spojevima na gredi koji su podvrgnuti savijanju se koriste za dalju procenu FE modela razvijenih u ovoj studiji. Studija se obavlja sa fokusom na predviđanje nosivosti strukture zavarenih spojeva.

Rezultati proračun na grednom modelu pokazuju prostiranje linearnog napona posmatranog preko debljine grede. Zato je, upotrebna ploča za analizu spojeva odgovarajuća. Takođe, na relativno maloj udaljenosti od spoja, efekti lokalnih napona i deformacija nestaju.

Rezultati pokazuju da normalan napon u jednom ili dva pravca su najviši na ivici zavarenog spoja na gornjoj površini i na horizontalnoj liniji zavarenog spoja poprečnog preseka profila. Primetno je da komponenta normalnog napona u jednom ili dva pravca ima najveću vrednost. Normalni naponi u jednom ili dva pravca mnogo veći od ostalih komponenti napona. To znači da su naponi istezanja u zavarenom spoju uglavnom odgovorni za pojavu plastičnosti i naprslina, kao i njihovo širenje.

Ključne reči :

Ugaoni zavareni spoj, Metoda konačnih elemenata, 3D optička analiza, napon, deformacija

Naučna oblast :

Doktor nauka, Mašinsko inženjerstvo

Uža naučna oblast :

Otpornost konstrukcija

UDK broj : 621.791.052:624.014 (043.3)

Contents

Acknowledgment	ii
Abstract:	iii
Nomenclature	xv
Chapter 1	1
General Introduction	1
1.2. Background	1
1.2 Review of the Literature	1
1.3 Objective and scope	5
1.4 literature review of experimental research	6
1.5 Fundamental Theory of Digital Image Correlation Techniques	8
1.5.1 Two-dimensional digital image correlation method	8
1.5.2 Two-Dimensional Image Correlation: Mathematical Formulation	12
1.5.3 Three-Dimensional Video Image Correlation	13
Chapter 2	16
Analytical Analysis of Welding	16
2.1 Introduction	16
2.2 Assumption	17
2.3 Fillet Weld case(a)	18
2.3.1 Rectangular section	22
2.3.1.1 The effect of F_1	22
2.3.1.2 The effect of F_2	23
2.3.2 I section	24
2.3.2.1 The effect of the force F_1	24
2.3.2.2 The effect of the force F_2	25
2.3.3 X section	27
2.3.3.1 The effect of the force F_1	27
2.3.3.2 The effect of the force F_2	27
2.3.4 Z Section	28
2.3.4.1 The effect of the force F_1	28
2.3.4.2 The effect of the force F_2	29

2.3.5 C section.....	30
2.3.5.1 The effect of the force F_1	30
2.3.5.2 The effect of the force F_2	31
2.3.6 circular section.....	32
2.3.6.1 The effect of the force F_1	32
2.3.6.2 The effect of the force F_2	33
2.4. V Weld Case (b).....	34
2.4.1. Rectangular section.....	35
2.4.1.1. The effect of F_1	35
2.4.1.2. The effect of F_2	36
2.4.2 I section.....	37
2.4.2.1 The effect of the force F_1	37
2.4.2.2. The effect of the force F_2	37
2.4.3. X section	38
2.4.3.1. The effect of the force F_1	38
2.4.3.2. The effect of the force F_2	39
2.4.4. Z Section	40
2.4.4.1. The effect of the force F_1	40
2.4.4.2. The effect of the force F_2	41
2.4.5. C section.....	42
2.4.5.1. The effect of the force F_1	42
2.4.5.2 The effect of the force F_2	42
2.4.6 circular section.....	43
2.4.6.1 The effect of the force F_1	43
2.4.6.2 The effect of the force F_2	44
Chapter 3.....	46
Three dimensional optical strain measurements	46
3.1 Brief introduction to the Aaramis system	47
3.2 Main hardware and software components	48
3.3 Principle of deviation measurements	48
3.4 Facet computation.....	50
3.5 Steps to carry out a typical measuring procedure	51
3.6 Calibration.....	52

3.6.1 Calibration objects	52
3.6.2 When is calibration required?	53
3.6.3 Background information about calibration theory	54
3.7 Measuring	54
3.7.1 Selecting the correct measuring volume	54
3.7.2 Preparing a specimen	54
3.7.3 Spraying a stochastic pattern	55
3.7.4 Computations	57
3.8 Facets	57
3.8.1 Facet shapes	57
3.8.2 Rectangular facets	57
3.8.3 Quadrangular facets	58
3.9 Computation masks.....	58
3.10 Start point.....	60
3.11 Strain computation.....	61
3.11.1 Linear strain	61
3.11.2 Spline strain	61
Chapter 4.....	62
Finite element method.....	62
4.1 Physical problems, mathematical models and the finite element solution	63
4.2 General steps of the finite element method.....	64
4.2.1 Step 1 Discretize and select the element types	64
4.2.2 Step 2 Selection of a proper interpolation or displacement model	66
4.2.3. Step 3 Define the strain displacement and stress strain relationships.....	66
4.2.4. Step 4 Derive the element stiffness matrix and equations	66
4.2.4. 1 Direct equilibrium method.....	67
4.2.4.2 Work or energy methods.....	67
4.2.4.3 Methods of weighted residuals	67
4.2.5. Step 5 Assemble the element equations to obtain the global or total equations	68
4.2.6 Step 6 Solve for the unknown degrees of freedom (or generalized displacements)	68
4.2.7 Step7 Computation of element strains and stresses	69
4.2.8 Step 8 Interpret the results	69

4.3 Advantages of the finite element method	69
4.4 Guidelines on element layout.....	70
4.4.1 Mesh refinement	70
4.4.2 Element aspect ratios	71
4.4.3. Physical interfaces	71
4.4.4. Preferred shapes	71
4.5 Plane stress and plane strain stiffness equations.....	72
4.5.1 Basic concepts of plane stress and plane strain	73
4.5.1.1 Plane stress.....	73
4.5.1.2 Plane strain.....	73
4.5.2 Two-dimensional state of stress and strain	74
4.5.3 Stress/strain relationships.....	75
4.6. Finite element theory	76
4.6.1. Constant strain triangle	76
4.6.2 Plate bending element	82
4.6.2.1 Finite elements for plates	82
4.7 Shells.....	86
4.7.1 Shell element.....	86
4.7.2 Finite elements for shells	87
Chapter 5.....	90
Finite element modeling of the welded joints using beam elements	90
5.1 Fillet weld	91
5.1.1 Finite element results of beam shell coupling of fillet weld in case of bending.....	91
5.1.1.1 Rectangular Section	91
5.1.1.2 I section.....	92
5.1.1.3. C- section	93
5.1.1.4 Circular- section.....	95
5.1.1.5 Z- section	96
5.1.1.6 X- section	97
5.1.2 Finite element results of beam shell coupling of fillet weld in case of twisting.....	98
5.2. V welded joint.....	100
5. 2.1 Finite element results of beam shell coupling of V-welded joint in case of bending.....	100

5. 2.2 Finite element results of beam shell coupling of V-welded joint in case of twisting.....	101
5.4 Comparison.....	102
5.4.1 Comparison between V and fillet welded joints in case of bending.....	102
5.4.2 Comparison between V and fillet welded joints in case of twisting.....	104
5.5 Discussion.....	105
Chapter 6.....	106
V-weld modeling using solid and shell elements	106
6.1 V-weld modelling using solid elements.....	106
6.1.1 Finite element results of solid element model of V- weld in case of bending.....	108
6.1.1.1 Rectangular cross-section	108
6.1.1.2 I section.....	109
6.1.1.3 C section.....	110
6.1.1.4 Circular section	110
6.1.1.5 Z – section.....	111
6.1.1.6 X – section	111
6.1.2 Finite element results of solid element model of V- weld in case of twisting.....	112
6.1.2.1 Rectangular cross-section	112
6.1.2.2 I-section.....	112
6.1.2.3 C-section	113
6.1.2.4 Circular-section.....	113
6.1.2.5 Z-section	114
6.1.2.6 X-section.....	115
6.2 V-Weld modelling using shell elements.....	115
6.2.1 Finite Element Results of Shell element model of V- weld in case of bending. ...	116
6.2.1.1 Rectangular cross-section	116
6.2.1.2 I cross-section	116
6.2.1.3 C cross-section.....	117
6.2.1.4 Circular cross-section.....	118
6.2.1.5 Z cross-section	119
6.2.1.6 X cross-section.....	120
6.2.2 Finite element results of shell element model of V- weld in case of twisting.....	120
6.2.2.1 Rectangular section.....	120

6.2.2.2 I section.....	121
6.2.2.3 C section.....	122
6.2.2.4 Circular section.....	123
6.2.2.5 Z section.....	123
6.2.2.6 X section.....	124
6.3 Comparison between shell and solid elements.....	125
6.3.1 Case (a) Bending.....	125
6.3.1.1 Rectangular cross-section.....	125
6.3.1.2 I- section.....	125
6.3.1.3 C- section.....	126
6.3.1.4 Circular- section.....	126
6.3.1.5 Z- section.....	127
6.3.1.6 X - section.....	128
6.3.2 Case (b) Twisting.....	128
6.3.2.1 Box- section.....	128
6.3.2.2 I - section.....	129
6.3.2.3 C - section.....	129
6.3.2.4 Circular - section.....	130
6.3.2.5 Z - section.....	130
6.3.2.6 X - section.....	131
6.4 Discussion.....	131
Chapter 7.....	133
Fillet weld modeling using solid and shell elements.....	133
7.1 Fillet weld modelling using solid elements.....	133
7.1.1 Finite element results of solid element model of fillet- weld in case of bending. 134	
7.1.1.1 Rectangular cross-section.....	134
7.1.1.2 I-section.....	134
7.1.1.3 C-section.....	135
7.1.1.4 Circular-section.....	135
7.1.1.5 Z-section.....	136
7.1.1.6 X-section.....	136
7.1.2 Finite element results of solid element model of fillet- weld in case of twisting. 137	
7.1.2.1 Rectangular cross-section.....	137

7.1.2.2 I-section.....	138
7.1.2.3 C-section	138
7.1.2.4 Circular -section.....	139
7.1.2.5 Z –section.....	139
7.1.2.6 X –section	140
7.1.3 Discusion.....	140
7.2 Fillet weld modeling using oblique shell elements.....	140
7.2.1 Finite element results of shell element model of fillet- weld in case of bending. 142	
7.2.1.1 Rectangular -section.....	142
7.2.1.2 I-section.....	142
7.2.1.3 C-section	143
7.2.1.4 Circular –section	143
7.2.1.5 Z -section	144
7.2.1.6 X –section	144
7.2.2 Finite element results of shell element model of fillet- weld in case of twisting. 145	
7.2.2.1 Rectangular cross-section	145
7.2.2.2 I-section.....	146
7.2.2.3 C-section	146
7.2.2.4 circular section	147
7.2.2.5 Z- section	148
7.2.2.6 X- section.....	148
7.3 Comparison between solid and shell elements of fillet welds.....	149
7.3.1 Case(a) Bending.....	149
7.3.1.1 Rectangular cross-section	149
7.3.1.2 I-section.....	149
7.3.1.3 C-section	150
7.3.1.4 Circular-section.....	150
7.3.1.5 Z-section	151
7.3.1.6 X-section.....	152
7.3.2 Case (b) Twisting.....	152
7.3.2.1 Rectangular cross-section	152
7.3.2.2 I-section.....	153
7.3.2.2 C-section	153

7.3.2.2 Circular-section.....	154
7.3.2.5 Z-section	154
7.3.2.6 X-section.....	155
7.4 Comparison between V and fillet welds	155
7.4.1 Box section.....	155
7.4.2 I section.....	156
7.4.3 C section.....	156
7.4.4 Circular section	157
7.4.5 Z section.....	157
7.4.6 X section	158
7.5 Discusion.....	158
Chapter 8.....	160
Experimental results using digital image correlation (DIC).....	160
8.1 Rectangular section.....	161
8.2 I-section.....	164
8.3 C-section	167
8.4 Z-Section.....	171
8.5 X-Section	175
Chapter 9.....	180
Conclusion	180
References.....	183

Nomenclature

σ_{\perp}	the normal stress perpendicular to the critical plane of the throat
σ_{\parallel}	the normal stress parallel to the axis of the weld
τ_{\perp}	the shear stress perpendicular to the weld axis,
τ_{\parallel}	the shear stress parallel to the weld axis.
F_1	The force that makes bending
F_2	The force that makes bending and twisting
τ_{\parallel, F_1}	direct shear stress due to load F_1
M_{x, F_1}	bending moment due to load F_1
τ_{\parallel, F_2}	direct shear stress due to load F_2
σ_{M_x, F_2}	bending stress due to bending moment due to load F_2
M_t	twisting moment
τ_{M_t}	shear stress due to the turning moment M_t
I_x	the moment of inertia about neutral bending x-axis
I_v	the moment of inertia about neutral bending x-axis for vertical weld
I_h	the moment of inertia about neutral bending x-axis for horizontal weld
Z_x	the section modulus of rectangular weld section
j_G	the polar moment of inertia about the centroid of the weld group G
l	weld length
a	throat thickness
R_m	mean radius
σ_{F_1}	the resultant stress due to the force F_1
σ_{F_2}	the resultant stress due to the force F_2
CST	the constant-strain triangular element
DIC	digital image correlation
σ_z	the normal stress
τ_{xz}, τ_{yz}	the shear stress
A^e	the element area
$\varepsilon_x, \varepsilon_y$	the normal strain

γ_{xy}	the shear strain
$[k^e]$	element stiffness matrix
t	thickness
$[k_n^e]$	element stiffness matrix due to normal stress
$[k_s^e]$	element stiffness matrix due to shear stress
E	Young modulus
ν	Poisson ratio

Chapter 1

General Introduction

1.2. Background

Welded structures made from steel are used in several applications. Some applications are buildings, bridges, and other structures. Among these structures, Structural hollow sections, circular (CHS) and rectangular (RHS) are widely used in all kinds of structures under different types of loading. Many examples in nature show the excellent properties of the tubular shape with regard to loading in compression, torsion and bending in all directions. These excellent properties are combined with an attractive shape for architectural applications. Furthermore, the closed shape without sharp corners reduces the area to be protected and extends the corrosion protection life. Another aspect which is especially favorable for circular hollow sections is the lower drag coefficients if exposed to wind or water forces [1].

1.2 Review of the Literature

The aim of this literature review is to outline the progress of research and development work in welded joints over the years.

In the recent years, various aspects and interests in the numerical modeling of welding stresses and distortions have been done by using finite element method.

Butler and Kulak [2] showed that the strength and ductility of fillet welds in shear are markedly dependent upon the orientation of the weld with respect to the line of action of the load. Welds placed parallel to the direction of the load have the lowest strength. Also his results showed that the increase in strength of the fillet welds tested in this program was approximately 44% as the angle of load changed from zero degrees (longitudinal weld) to 90 deg (transverse weld) strength and highest ductility. Also, they presented that fillet welds loaded in shear do not exhibit any well defined yield point. The load-deformation response of fillet welds cannot be generally represented as elastic or elastic-perfectly plastic. Dawe, J. L., and Kulak, G. L.[3] investigated the behavior of weld groups subjected to shear and out-of-plane bending. The test results were used to

validate an analysis procedure presented by Butler, L. J., and Kulak [2]. Lesik, D. F., and D. J. L. Kennedy [4] established a simplified expression for predicting the ultimate strength of fillet welds loaded in shear at any angle of loading. Vanam B. C. L., Rajyalakshmi M., Inala R.[5] in their research work, they analyzed the static analysis of an isotropic rectangular plate with various boundary conditions and various types of load applications. Finite element analysis has been carried out for an isotropic rectangular plate by considering the master element as a four node quadrilateral element. Finite element analysis (FEA) has been carried out by developing programming in mathematical software MATLAB and the results obtained from MATLAB are giving good agreement with the results obtained by classical method - exact solutions. Later, for the same structure, analysis has been carried out using finite element analysis software ANSYS. The results were obtained not only at node points but also the entire surface of the rectangular plate. Comparison has been done between the results obtained from FEA numerical analysis, and ANSYS results with classical method - exact solutions. Their numerical results showed that, the results obtained by finite element analysis and ANSYS simulation results are in close agreement with the results obtained from exact solutions from classical method. During their analysis, the optimal thickness of the plate has been obtained when the plate is subjected to different loading and boundary conditions. M. F. Ghanameh, D. Thevenet [6] analyzed tubular elements that used to design offshore platforms which are subjected to combined loading conditions. These loading conditions generate, in the vicinity of joints, zones of strong stress concentration. Determination of stresses at hot-spot points by finite element analysis gives results in good agreement with literature of simple loading, which validates the modeling approach employed. Pawel Bilous, Tadeusz Lagoda [7] discussed stress concentrators occurring in welded joints. Methods of fatigue life evaluation for welded joints have been presented. Moreover, their work contains a description and methods of determination of the fatigue notch coefficient. Histories of the fatigue notch coefficient (K_f) were plotted for a double-Vee butt weld. N. S. Raghavendrantg, M. E. Fournery [8] illustrated the use of the two dimensional finite element method (FEM) in finding the stress distribution across a butt-welded joint for two types of loading conditions, tension and bending. In their work, they used two dimensional photo-elastic analysis (PEA) of a butt weld under plane stress conditions.

S. Krscanski, G. Turkalj [9] presented the concentrations factors for fillet welded CHS-Plate T-Joint. They modeled the problem with finite element method. The modeling of the mesh was according to IIW (International Institute of Welding) recommendations and their results were compared to experimental data from other authors and to a simple analytical solution. They found stress concentration factors calculated by finite element model analysis to be higher than those interpolated from experimental data. P.M.Gedkar, D.V. Bhope [10] presented stress analysis of two pressurized cylindrical intersection using finite element method. Their results showed that the lower value of branch pipe thickness are preferable for lower stress values at intersecting junction provided the stresses in branch pipe are within the safe limits. This reduction of stresses at the intersection with lesser branch pipe thickness may be due to the less constraining effect of branch pipe on the run pipe. X.W. Ye, Y.Q. Ni, J.M. Ko [11] described an experimental study on determining the stress concentration factor (SCF) and its stochastic characteristics for a typical welded steel bridge T-joint. A full-scale segment model was fabricated and tested. With the measurement data obtained from strain gauges deployed on the web and flanges, the hot spot strain at the weld toe is determined by a linear regression method. The SCF can be calculated as the ratio between the hot spot strain and the nominal strain which is obtained directly by measurement. To fully account for the effect of predominant factors on the scatter of SCF, the experiments are carried out under different moving load conditions.

Shao YB.[12] presented general remarks of the effect of the geometrical parameters on the stress distribution in the hot spot stress region for tubular T- and K-joints subjected to brace axial loading. His parametric study has also been carried out to investigate the effect of three popularly used joint geometrical parameters on the stress distribution. From parametric study, he found that chord thickness has remarkable effect on the stress distribution for both T- and K-joints, while brace thickness has no effect on such stress distribution. Hellier AK, Connolly MP, Dover WD [13] presented parametric study using finite elements of the stress concentration factors in tubular K joints commonly found in offshore platforms. Their study covers a comprehensive range of geometric joint parameters for unbalanced out-of-plane moment loading. They proposed new equations for the maximum SCFs on the chord and the brace, and they have been found to provide a good fit to the large finite element database and to meet the proposed

assessment criteria. Chang E, Dover WD [15] conducted systematic thin shell finite element (FE) analyses for 330 different tubular X and DT-joints (Double T joint), typical of those used in offshore structures, subjected to six different modes of loading. They derived a set of parametric equations to predict the stress distributions along both chord and brace toes in tubular X and DT-joints under each mode of loading. Karamanos SA, Romeijn A, Wardenier J [16] showed the prediction of stress concentration factors (SCFs) of multi-planar welded tubular (CHS) XX-joints in steel structures. They proposed a set of parametric equations to determine the SCFs for multi-planar welded CHS XX-connections. In their study, weld profile was modeled using 20-node solid elements while eight-node shell elements were used to model the chord and brace. Their research covered the various loading modes.

Karamanos SA, Romeijn A, Wardenier J. [17] repeated the previous study for tubular gap K joints. Chiew SP, Soh CK, Wu NW. [18] presented parametric stress analysis of steel multi-planar tubular XX-joints using the finite element method (FEM). Five different load cases of basic brace and chord axial load, in-plane-bending (IPB) and out-of-plane-bending (OPB) moments were considered. Through the parametric study, they established a set of SCF design equations for general end loading. Karamanos SA, Romeijn A, Wardenier J.[19] developed a methodology for the calculation of the maximum local stress, referred to as “hot-spot stress”, in a multi-planar DT-joint(Double T joint), with particular emphasis on the effects of bending moments on the braces and the chord. Gho WM, Gao F. [20] conducted finite element models to predict the stress concentration factors (SCF) of completely overlapped tubular K-joints under lap brace axial compression. In their analysis, they found suitable both 8-node thick shell and 20-node solid elements for modelling the joint. Gao F. [21] investigated experimentally the stress and strain concentrations of a completely overlapped tubular joint specimen under lap brace out-of-plane bending (OPB) load. The experimental results showed that the strain distribution near the weld toe is fairly linear. The comparison of SCF showed that the existing T/Y-joint parametric equations for predicting the SCF of completely overlapped tubular joints are inappropriate under OPB load. Gao F, Shao YB, Gho WM.[22] repeated the previous study for completely overlapped tubular K(N)-joints under lap in-plane bending loading. Woghiren CO, Brennan FP [23] proposed a set of parametric equations to predict the values of stress

concentration factor in multi-planar stiffened tubular KK-joints. The equations describe the SCF at the different locations as a function of the non-dimensional ratios. The equations not only allow the rapid optimization of multi-planar joints but also can be used to quickly identify the location of maximum stress concentration. Lie ST, Lee CK, Wong SM [24] described a systematic method of modelling the weld thickness of a tubular Y joint. N Diaye A, Hariri S, Pluvinage G, Azari Z [25] conducted the finite element method (FEM) on a welded tubular T-joint, in order to analyze stress distribution in the vicinity of the weld fillet. The finite element method analysis shows that stresses are very high on the brace member, in the vicinity of the weld, and decrease gradually, in the direction of the brace extremity. N Diaye A, Hariri S, Pluvinage G, Azari Z [26] conducted the finite element analysis to predict the location of hot-spot stresses in a welded tubular T-joint. T. Wanga, O.S. Hopperstada , O.-G. Lademoa, P.K. Larsena [27] performed finite element analyses to predict the structural behaviour of welded and un-welded I-section aluminum members subjected to four-point bending. Their modelling procedure was using shell elements. Their numerical results were compared with existing experimental data, and, in general, good agreement with the experimental results was obtained. Seng-Keat Yeoh, Ai-Kah Soh , Chee-Kiong Soh [28] describes the behaviour of tubular T-Joints subjected to combined loadings. The stress concentration factor (SCF) obtained for these load cases were compared with those obtained by other authors. His results showed that the peak SCF under axial load was slightly higher than those other authors.

1.3 Objective and scope

This thesis focuses on the development of a predictive methodology for fillet welded structures using beam, shell and solid elements. However, three-dimensional finite element analysis of complete structural hollow sections can be complex and time-consuming. Due to the complex nature of the finite element analysis codes, this method has limited application. It can be used in research area but cannot be widely used by structural engineers in their real-world projects. Therefore, there is a need to develop a simplified modeling method that can be implemented by using commonly available commercial software and easily employed.

The objective is to eventually provide a validated finite element method -based procedure for large-scale analyses of such structures. Also to establish an appropriate

level of finite element modeling and in order to determine the optimal quality of meshing for stress analysis of welded steel structures. Finite element models with different modeling techniques and meshing with various size and types of elements were created and analyzed. Experimental tests are performed to validate numerical simulations in order to investigate the mechanical performance of a series of fillet-welded connections under combined loading. Figure 1.1 shows pictures of the investigated specimens. In the numerical study, the connections are modelled using beam, shell and solid elements in Abaqus [59]. The performance of the connections under combined loading is further studied by a simple analytical method aiming for rapid information on the influence of the weld modeling on prediction of the structural performance. Experiments of many beam joints subjected to combined loading are used for further assessment of the FE models developed in the present study. The study is performed with focus on the prediction of the structural strength of the fillet welded joints.



Figure 1.1 Pictures of the Investigated Specimens

1.4 literature review of experimental research

Strain measurements are very important in mechanical sciences. A strain in any material can be defined as the coefficient of the change in length and the initial length. Strains are involved in many important material properties and parameters. Recently, new and

more complex investigations are requiring strain measurements at any point inside an area of interest to improve the study of the behavior of materials and structural components. For this reason, researchers are interested on a strain map over an entire specimen surface. Some conventional instruments which measure strains (i.e. strain gage) are not accessible to create strain maps, because it would be very expensive and not practical [29].

In the past, there are two methods for surveying strains developed in an object which in subject to external forces. One method is to measure the relative displacement between two specific points on the surface of an object, and then estimate the strain between these two points. The disadvantage of this method is that the global strain distribution of the object cannot be determined directly. The other method is to map meshes on the surface of an object before deformation occurs, and then survey the displacement of nodes surrounding these meshes after deformation. Further, the strain distribution of an object is derived from the displacement field. Contrarily, this technique is a complex and time-consuming process [30].

Due to the fact that strain maps are needed to perform new investigations, a new technology was developed to obtain these desired results. This technology is the digital image correlation, which provides a contour map of strains of an entire specimen surface subject to mechanical tests.

The digital image correlation (DIC) method is probably one of the most commonly used methods, and many applications can be found in the literature [31–40].

When it is used with a single camera (classical DIC) , the DIC method can only give in-plane displacement/strain fields on planar objects. By using two cameras (stereovision), the 3-D displacement fields and the surface strain field of any 3-D object can be measured. Using stereovision in conjunction with DIC leads to so called digital image stereo-correlation technique (DISC), also called 3-D DIC [41].

The Developed Digital Image Correlation (DIC) technique is an image identification method for measuring object deformation. The digital images of an object before and after deformation that are captured using an optic instrument are subject to correlation analysis. The corresponding positions recorded on the image are obtained by calculating

the correlation coefficient of images so that the displacement function and strain distribution of an object can be inferred. This technique is non-destructive for inspecting the whole displacement and strain field [29].

Thus, developing a monitor system to inspect the mechanics behaviour of a welded joints member is an essential and important study. The feasibility of applying DIC technique to monitor welded joints is tested in this research.

1.5 Fundamental Theory of Digital Image Correlation Techniques

The fundamental theory of the digital-image-correlation technique is to compare the digital images before and after deformation. The analysis procedure of the DIC method is shown in figure 1.2. The analysis region is divided into several sub-images. The grayscale distribution of image is used to identify the relative positions of the same point on the specimen surface in two images. Correlation analyses of images are carried out to search the point that has the highest grayscale correlating with the initial position displacement vector so that the displacement field of specimen can be derived. After that the strain field can be calculated [29].

1.5.1 Two-dimensional digital image correlation method

The basis of two-dimensional video image correlation for the measurement of surface displacements is the matching of one point from an image of an object's surface before loading (the undeformed image) to a point in an image of the object's surface taken at a later time/loading (the deformed image). Assuming a one-to-one correspondence between the deformations in the image recorded by the camera and the deformations of the surface of the object, an accurate, point-to-point mapping from the undeformed image to the deformed image will allow the displacement of the object's surface to be measured. Two main requirements must be met for the successful use of DIC-2D. First, in order to provide features for the matching process, the surface of the object must have a pattern that produces varying intensities of diffusely reflected light from its surface. This pattern may be applied to the object or it may occur naturally. Secondly, the imaging camera must be positioned so that its sensor plane is parallel to the surface of the planar object, as shown in Figure 1.2 [42].

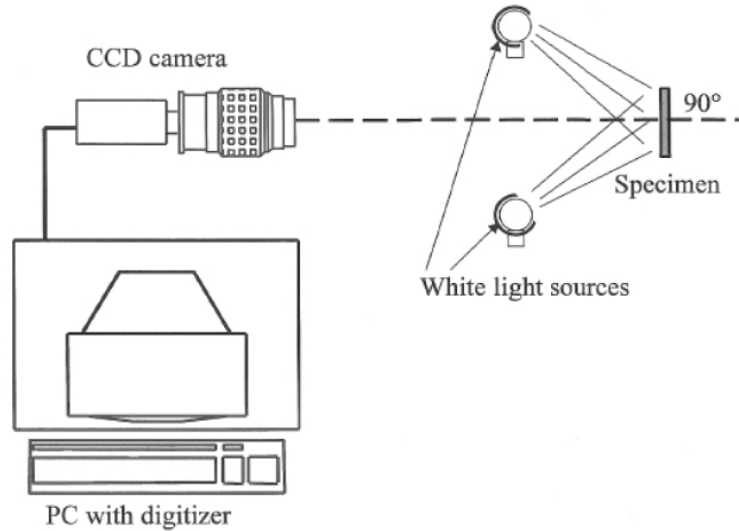


Figure 1.2 two-dimensional video image correlations[42].

The imaging process of the camera converts the continuous intensity field reflected from the surface $O(X, Y)$ into a discrete field $I(X, Y)$ of integer intensity levels. In a CCD camera (a charge-coupled-device which converts light into a digital signal), this transformation occurs when the light incident on a sensor (commonly known as a pixel) is integrated over a fixed time period. The rectangular array of sensors in a charge coupled device (CCD) array converts the continuous intensity pattern into a discrete array of integer intensity values, $I(i, j)$, where i denotes the row number and j denotes the column number in the sensor plane. The displacement field for an object is obtained at a discrete number of locations by choosing subsets from the initial image and searching throughout the second image to obtain the optimal match. Details of this process are outlined in the following paragraphs.

The process of deformation in two dimensions is shown schematically in Figure 1.3. The functions are defined as follows; (a) $O(X, Y)$ denotes the continuous intensity pattern for the undeformed object, (b) $\bar{O}(X, Y)$ is the continuous intensity pattern for the deformed object, (c) $I(X, Y)$ is the discretely sampled intensity pattern for the undeformed object and (d) $\bar{I}(X, Y)$ is the discretely sampled intensity pattern for the deformed object. It is important to note that a basic tenet of the DIC-2D method is that points in $I(X, Y)$ and $\bar{I}(X, Y)$ are assumed to be in one-to-one correspondence with points in $O(X, Y)$ and $\bar{O}(X, Y)$, respectively. Thus, one can use $I(X, Y)$ and $\bar{I}(X, Y)$ to determine the displacement field for the object $O(X, Y)$. We should note that obtaining

accurate estimates for surface deformations using $I(X,Y)$ and $\bar{I}(X,Y)$ requires an interpolation scheme to reconstruct a continuous intensity function.

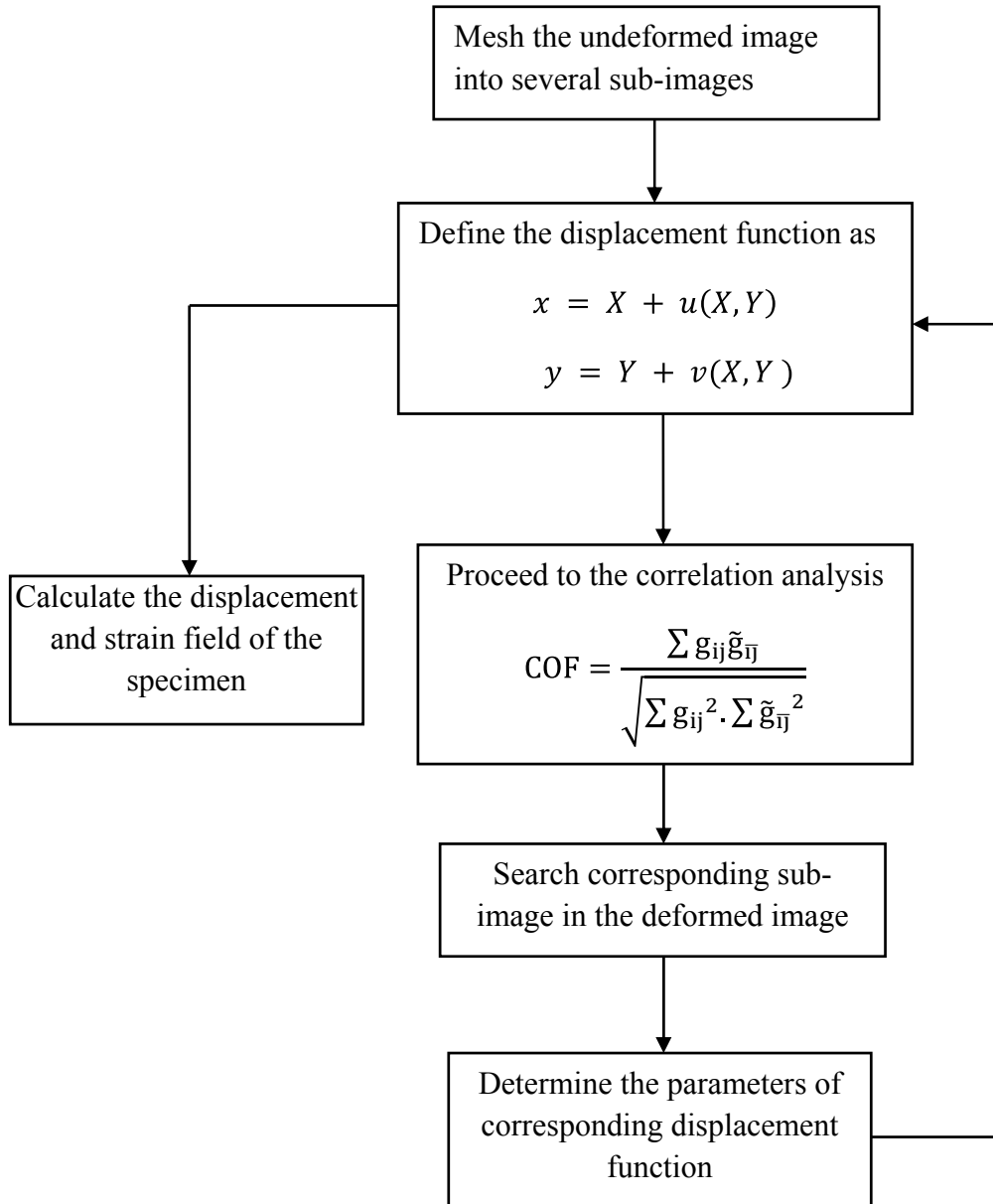


Figure 1.3 Analysis Procedure of Digital Image Correlation Method [29].

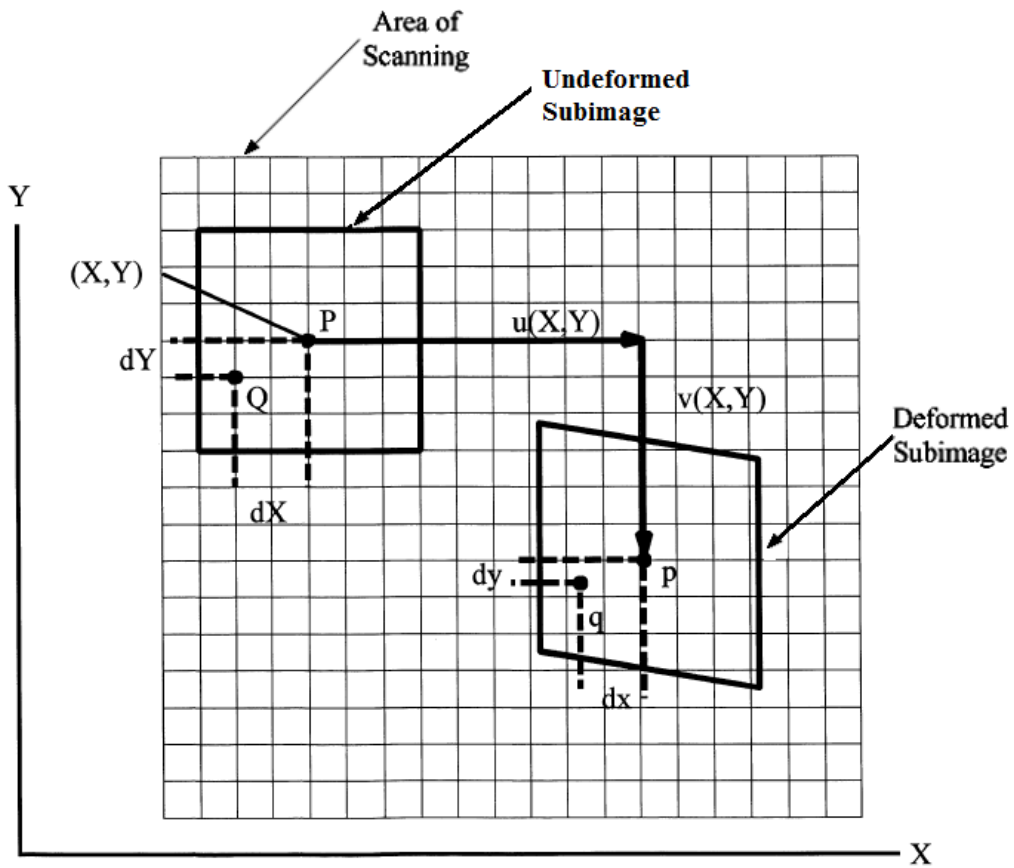


Figure 1.4 The relative position of the sub images before and after deformation.

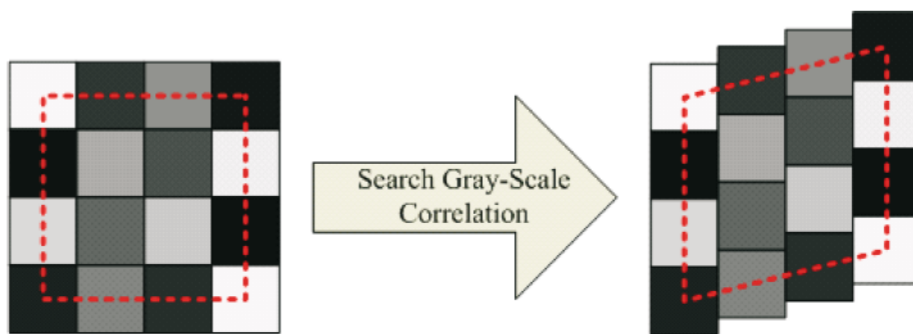


Figure 1.5. Gray-scale correlation between deformed and undeformed sub-image.

1.5.2 Two-Dimensional Image Correlation: Mathematical Formulation

For the small subset centered at (X, Y) on the undeformed object in Figure 1.4, the discretely sampled and continuously interpolated intensity pattern at points P and Q, located at positions (X, Y) and $(X + dX, Y + dY)$ respectively, can be written as

$$\begin{aligned} I(P) &= I(X, Y), \\ I(Q) &= I(X + dX, Y + dY), \end{aligned} \quad (1.1)$$

Where (dX, dY) represent small distances in the (X, Y) coordinate system. Note that, if the values for dX and dY are integer pixel values, then no interpolation is required for the undeformed image. As shown in Figure 1.4, after deformation of an object, points P and Q are deformed into positions p and q, respectively. Assuming that the intensity pattern recorded after deformation is related to the undeformed pattern by the object deformations, and defining $\{u(X, Y), v(X, Y)\}$ the displacement vector field, we can write

$$x = X + u(X, Y), \quad y = Y + v(X, Y)$$

so that

$$\bar{I}(x, y) = I(X + u(X, Y), Y + v(X, Y))$$

$$\begin{aligned} \bar{I}(x + dx, y + dy) &= I[X + dX + u(X + dX, Y + dY), Y + dY + v(X + dX, Y + dY)], \\ &= I\left[X + u(X, Y) + \left(1 + \frac{\partial u}{\partial X}\right) dX + \frac{\partial u}{\partial Y} dY, Y + u(X, Y) + Y + \frac{\partial v}{\partial Y} dY\right] \end{aligned} \quad (1.2)$$

Assuming that the subset is sufficiently small so that the displacement gradients are nearly constant throughout the region of interest, each subset undergoes uniform strain resulting in the parallelogram shape for the deformed subset shown in Figure 1.5. Conceptually, determining for each subset is simply a matter of determining all six parameters so that the intensity values at each point in the undeformed and deformed regions match. To obtain these values, there are several measures of intensity pattern correspondence that could be used, including the following summations for a series of selected points Q_i [42].

a- magnitude of intensity value difference

$$\sum_i |\bar{I}(q_i) - I(Q_i)| \quad (1.3)$$

b- sum of squares of intensity value differences

$$\sum_i (\bar{I}(q_i) - I(Q_i))^2 \quad (1.4)$$

c- normalized cross-correlation

$$\frac{\sum_i (\bar{I}(q_i) - I(Q_i))}{\sqrt{(\sum_i \bar{I}(q_i)^2) (\sum_i I(Q_i)^2)}} \quad (1.5)$$

d- cross-correlation

$$\sum_i (\bar{I}(q_i) - I(Q_i)) \quad (1.6)$$

In order to get optimal estimates for all six parameters (u , v , $\partial u/\partial X$, $\partial u/\partial Y$, $\partial v/\partial X$, $\partial v/\partial Y$), minimization of (a,b) and maximization of (c,d) for each subset should be done.

1.5.3 Three-Dimensional Video Image Correlation

Basic Concepts

Single camera DIC systems are limited to planar specimens that experience little or no out-of-plane motion. This limitation can be overcome by the use of a second camera observing the surface from a different direction. Three-dimensional Digital Image Correlation (DIC-3D) is based on a simple binocular vision model. In principle, the binocular vision model is similar to human depth perception. By comparing the locations of corresponding subsets in images of an object's surface taken by the two cameras, information about the shape of the object can be obtained. In addition, by comparing the changes between an initial set of images and a set taken after load is applied, full-field, three-dimensional displacement can be measured. Both the initial shape measurement and the displacement measurement require accurate information about the placement and operating characteristics of the cameras being used. To obtain this information, a camera calibration process must be developed and used to accurately determine the model parameters. In the following paragraphs, key aspects of the DIC-3D method are outlined [42].

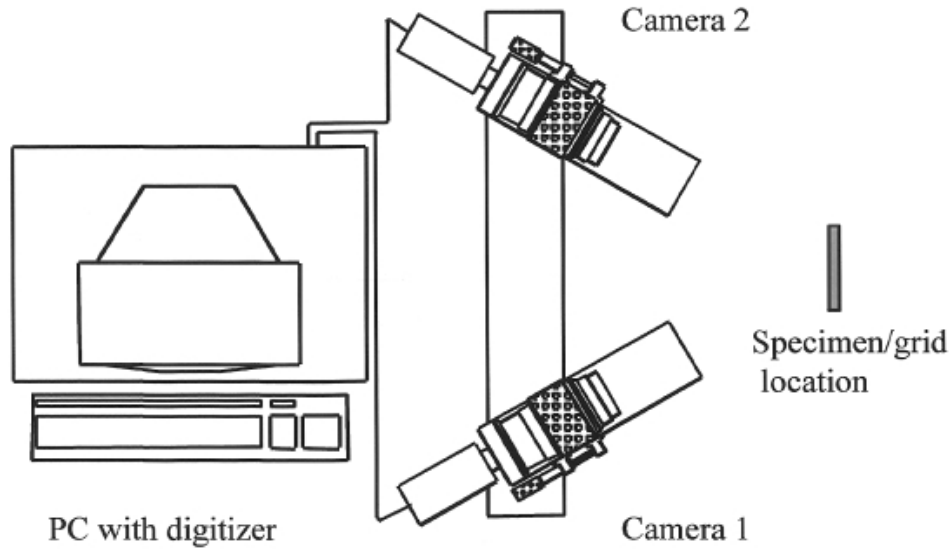


Figure 1-6 A complete three-dimensional measurement system [42].

Figure 1.6 shows a typical DIC-3D system. As already indicated in previous paragraphs, based on the discretization operation of finite element method (FEM), the undeformed image is meshed into several sub-images for image analyses. As shown in figure 1.4, the central point prior to deformation is point P; it is shifted to point q after deformation.

The functional relationship is expressed as:

$$x_q = x_Q + u(x, y), \quad y_q = y_Q + v(x, y) \quad (1.7)$$

Where, (x_Q, y_Q) and (x_q, y_q) are the coordinates of point P before and after deformation. $u(x, y)$ and $v(x, y)$ are the displacement functions in x- and y-direction separately. Calculating the grayscale correlation coefficient will lead to find the corresponding relationship between deformed and undeformed sub-images for establishing the deformation of sub-image as shown in figure 1.5. The correlation coefficient is defined as:

$$\text{COF} = \frac{\sum g_{ij} \tilde{g}_{\bar{i}\bar{j}}}{\sqrt{\sum g_{ij}^2 \cdot \sum \tilde{g}_{\bar{i}\bar{j}}^2}} \quad (1.8)$$

Where, g_{ij} and $\tilde{g}_{\bar{i}\bar{j}}$ are the grayscale of the undeformed sub-image on coordinate (i, j) and deformed sub-image on coordinate (\bar{i}, \bar{j}) respectively. When the deformed sub-image corresponds exactly to the undeformed sub-image, the correlation coefficient

between both sub-images equals 1. Accordingly, the optimal parameters of equation (1.7) are determined based on the results of correlation analyses. Thus, the displacement and strain field can be computed individually.

Chapter 2

Analytical Analysis of Welding

2.1 Introduction

Fillet welded joints are widely used in civil engineering construction due to their relatively high strength and the ease of surface preparation required for such welds. In many joint configurations used in practice in-plane or out-of-plane eccentricity are unavoidable, creating more complex stress conditions in the joint than concentrically loaded joints where the welds are generally subjected to shear in only one direction [43]. A welded joint is a permanent joint which is obtained by the fusion of the edges of the two parts to be joined together, with or without the application of pressure and a filler material. The heat required for the fusion of the material may be obtained by burning of gas (in case of gas welding) or by an electric arc (in case of electric arc welding). The latter method is extensively used because of greater speed of welding [44]. Figure 2.1 shows the effective length of a fillet weld with a throat thickness a , V and fillet joints.

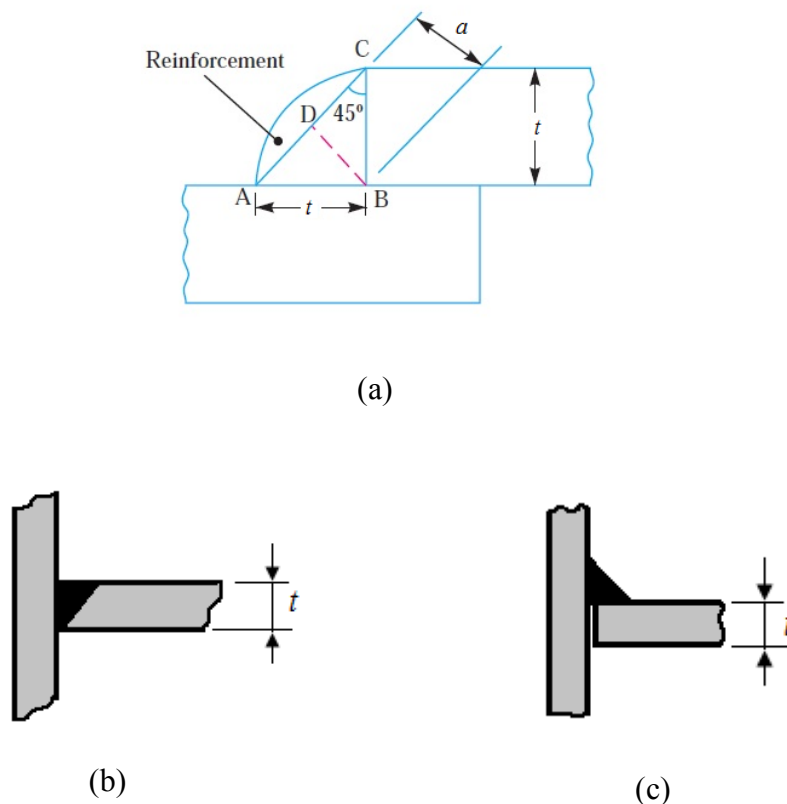


Figure 2.1 a) Definition of throat thickness a , b) V joint , c) fillet joint

In the analysis procedure, the internal force on the fillet weld is resolved into components parallel and transverse to the critical plane of the weld throat, see Figure 2.2. A uniform stress distribution is assumed on the critical throat section of the weld, leading to the following normal stresses and shear stresses:

σ_{\perp} the normal stress perpendicular to the critical plane of the throat,

σ_{\parallel} the normal stress parallel to the axis of the weld, it should be neglected when calculating the design resistance of a fillet weld,

τ_{\perp} the shear stress (in the critical plane of the throat) perpendicular to the weld axis,

τ_{\parallel} the shear stress (in the critical plane of the throat) parallel to the weld axis.

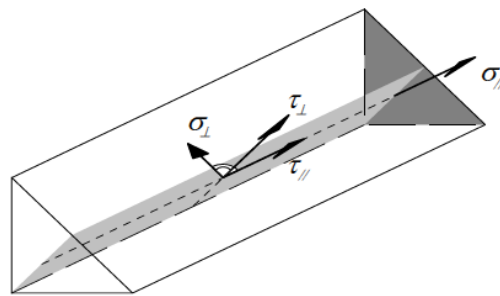


Figure 2.2 Stress in critical plane of fillet weld

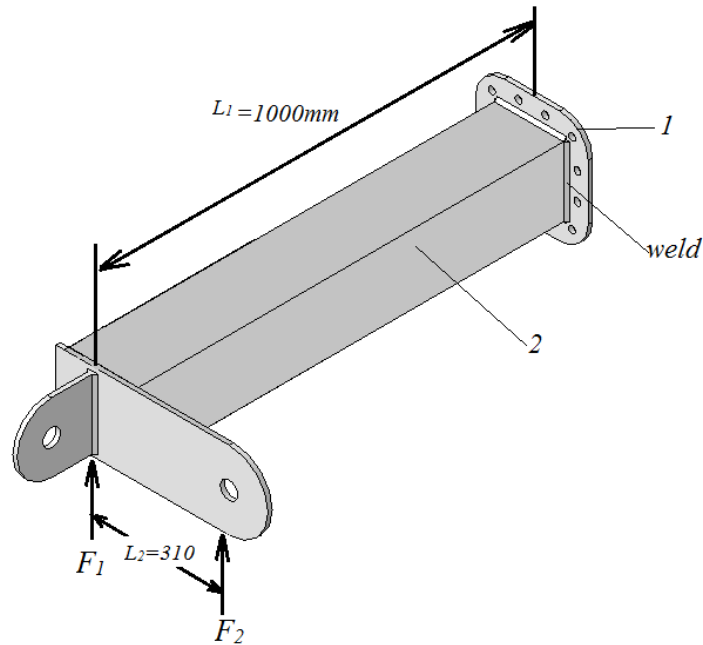
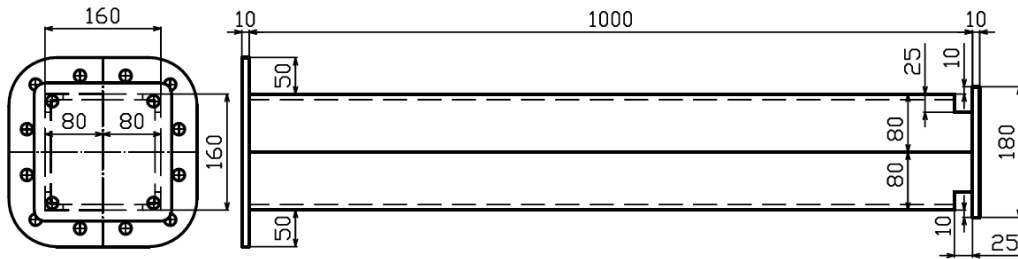
In this chapter, the analytical analysis of fillet welded beam of different cross-sections is discussed.

2.2 Assumption

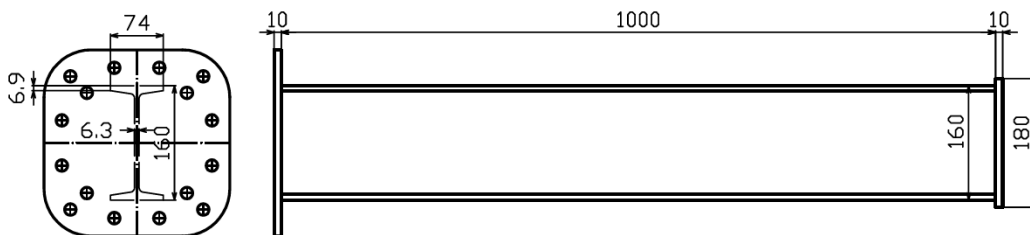
1. For calculating moments of inertia of the weld linear segments, the effective weld width in the weld plane is the same as the throat length a .
2. The transverse shear stress is given by V/A where V is the shear force and A is the weld throat area.
3. The shear force is carried by the vertical weld [45].
4. The resultant shear stress acting in the plane of the weld throat is the resultant of the bending and transverse shear stresses [46].

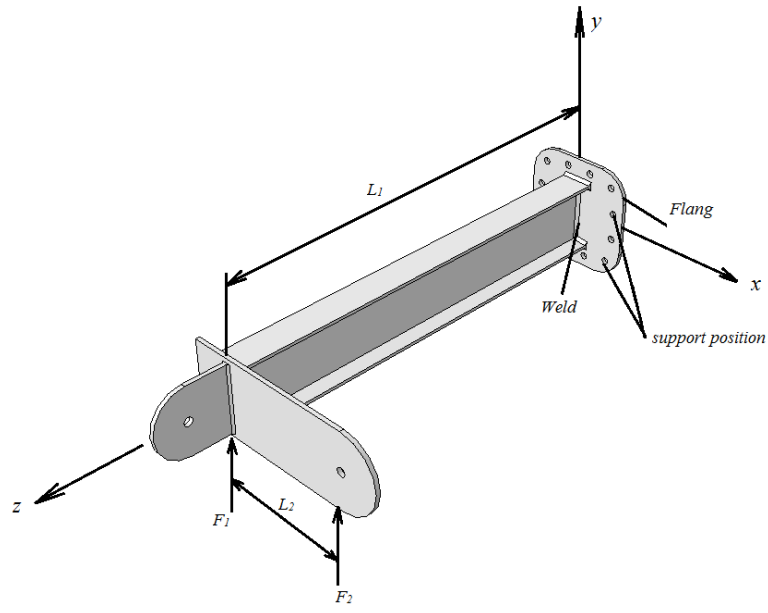
2.3 Fillet Weld case(a)

Figure 2.3 a-f shows specimens; Rectangular, I, X, Z, C and circular cross sections are welded to a support plate by means of fillet weld on their one end. The other ends are loaded by $F_1 = F_2 = 10\text{KN}$. The throat size of weld is 5mm and the dimensions L_1 and L_2 are 1000mm and 310mm, respectively.

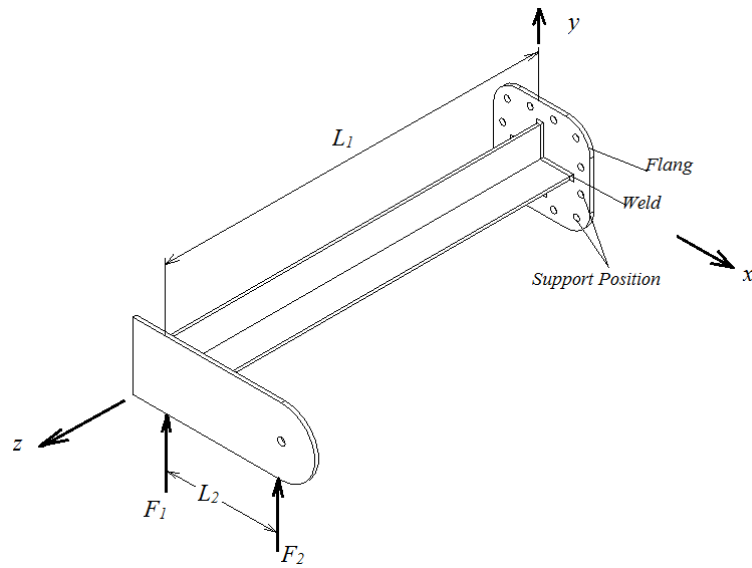
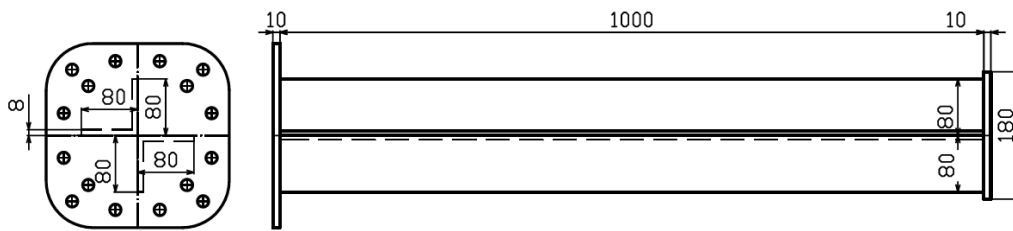


a- Box beam profile

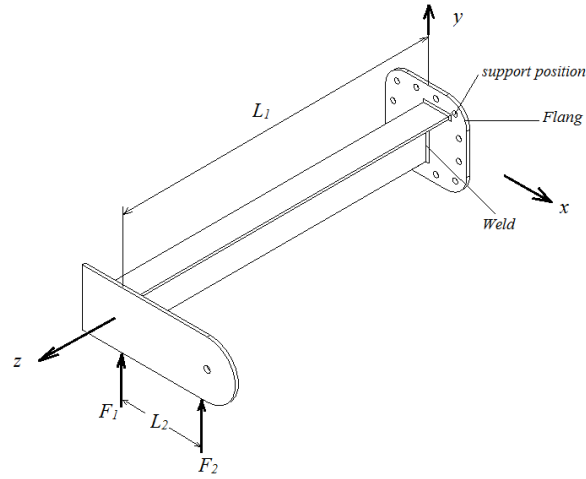
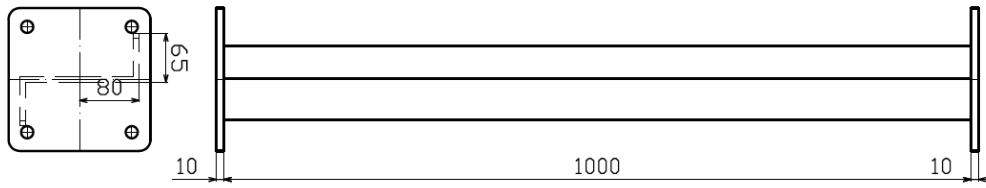




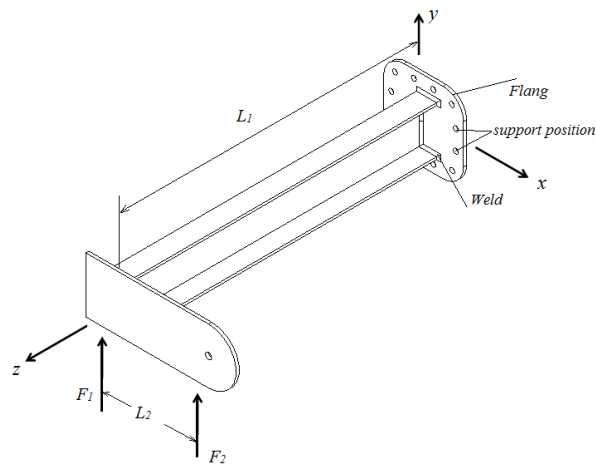
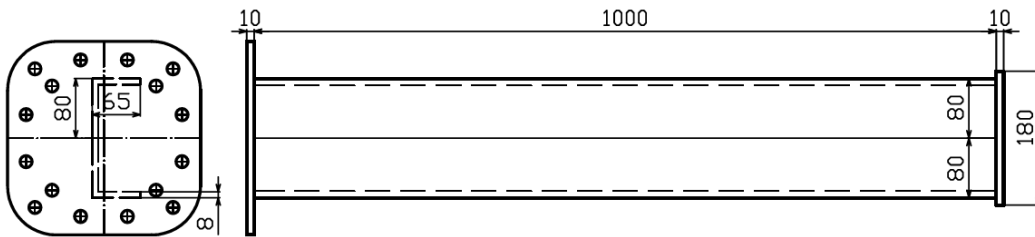
b- I beam profile



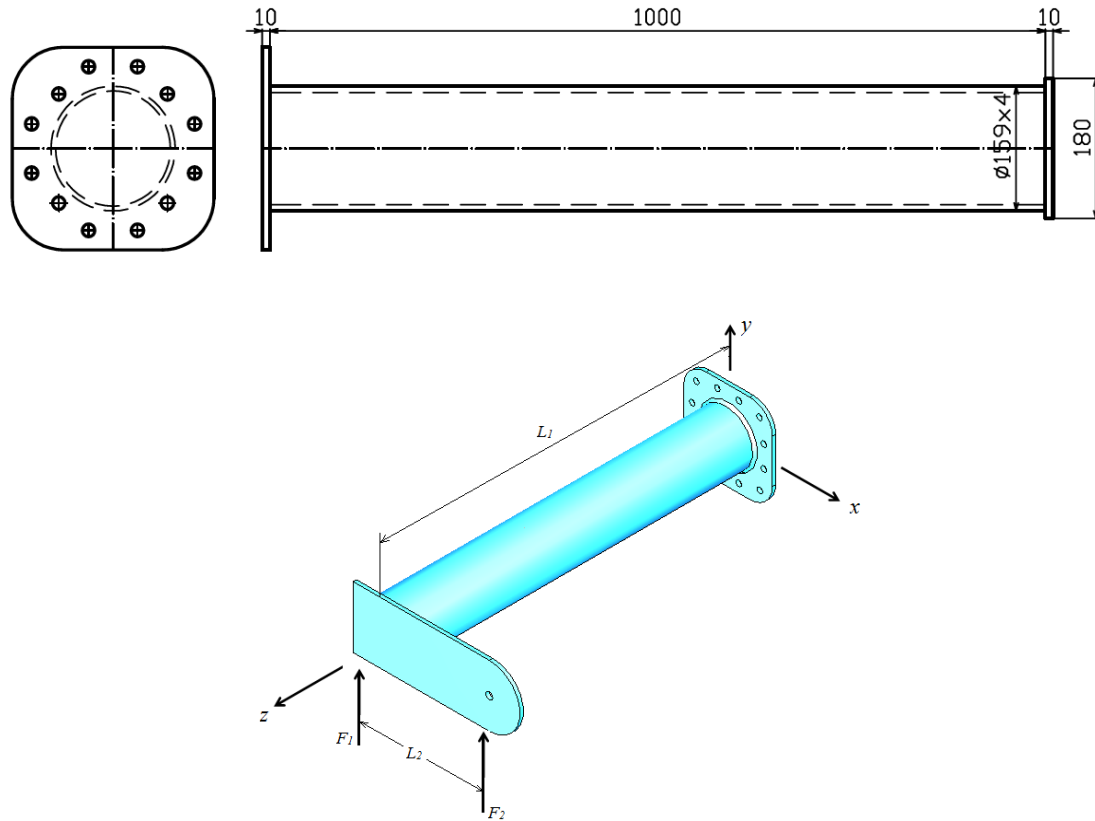
c- X beam profile



d- Z beam profile



e- C beam profile



f- Circular beam profile

Figure 2.3 Welded cantilever beams subjected to transverse loading.

A The effect of the force F_1

The forces acting on the all welded section joints due to the effect of the force F_1 are:

1-Direct shear stress (τ_{\parallel, F_1}) due to load F_1

2-Bending stress due to bending moment ($M_{x, F_1} = F_1 \times L_1 = 10^7 Nmm$)

B The effect of the force F_2

Also for all specimens the forces acting on the welded joint due to the effect of the force F_2 are:

1- Direct shear stress (τ_{\parallel, F_2}) due to load F_2

2-Bending stress (σ_{M_x, F_2}) due to bending moment ($M_{x, F_2} = F_2 \times L_1 = 10^7 Nmm$)

3-Shear stress (τ_{M_t}) due to the turning moment ($M_t = F_2 \times L_2 = 3.1 \times 10^6 Nmm$)

2.3.1 Rectangular section

The joint, as shown in figure 2.4, is subjected to direct shear stress and the bending stress.

$$l = 160mm$$

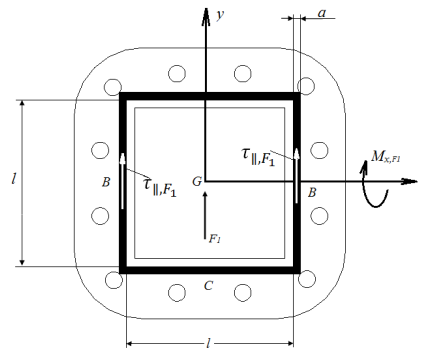


Figure 2.4 Rectangular section subjected to direct shear force and bending moment for fillet weld.

To find maximum stress in the weld at support

Solution

2.3.1.1 The effect of F_1

The loading involves direct shear plus bending, with the bending moment being

$$M_x = F_1 \times L_1$$

$$l = 160mm$$

$$\tau_{\parallel, F_1} = \frac{F_1}{2 \cdot a \cdot l} = \frac{10 \times 10^3}{(2)(5)(160)} = 6.25MPa$$

The rectangular moment of inertia about neutral bending x-axis consists of contributions made by the two vertical and two horizontal welds; that is,

$$I_x = 2I_v + 2I_h$$

The section modulus of rectangular weld section is $Z_X = \frac{I_X}{l/2} = \frac{2\left(\frac{al^3}{12} + al(l/2)^2\right)}{l/2}$

$$Z_X = a \left(l^2 + \frac{l^2}{3} \right) = 1.7 \times 10^5 \text{mm}^3$$

The (tensile) bending stress on the horizontal weld is,

$$\sigma_{M_x, F_1} = \frac{M_{x, F_1}}{Z_X} = \frac{10^7 \text{Nmm}}{1.7 \times 10^5 \text{mm}^3} = 58.8 \text{N/mm}^2$$

the stress magnitude σ_{F_1} is the Pythagorean combination

$$\sigma_{F_1} = \sqrt{\sigma_{M_x, F_1}^2 + \tau_{\parallel, F_1}^2} = \sqrt{(58.8)^2 + (6.25)^2} = 59.1 \text{MPa}$$

2.3.1.2 The effect of F_2

The welded joint, as shown in figure 2.5, is subjected to twisting moment (M_t), shear force F_2 as well as bending moment (M_{x, F_2}).

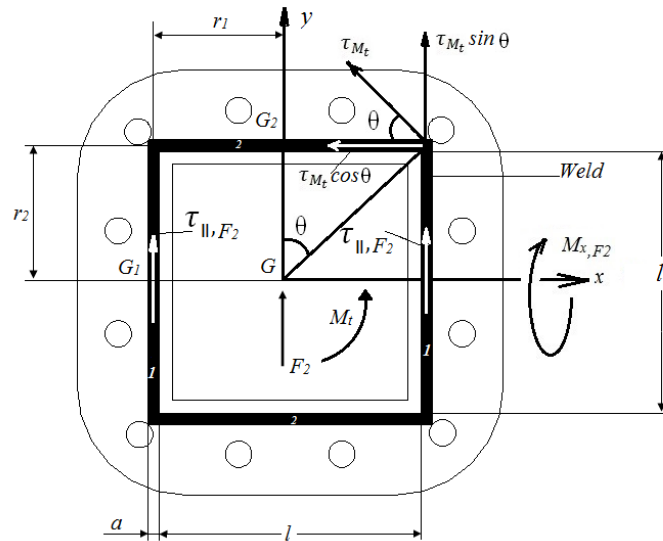


Figure 2.5 Rectangular section subjected to direct shear force, bending and twisting moment for fillet weld.

∴ direct shear stress,

$$\tau_{\parallel, F_2} = \frac{F_2}{2a \cdot l} = 6.25 \text{MPa}$$

The (tensile) bending stress on the horizontal weld is,

$$\sigma_{M_x, F_2} = \frac{M_{x, F_2}}{Z_w} = 58.8 \text{ MPa}$$

Note that the magnitudes of the stresses at the upper and lower horizontal weld are the same signs of the maximum normal stress indicated tension or compression, while the sign of the maximum shear stress is of no consequence since design is based on the magnitude [47].

The moment at the support produces secondary shear or torsion stress of the welds, and this stress is given by the following equation:

$$\tau_{M_t} = \frac{M_t r_{\max}}{j_G}$$

Where, $r_{\max} = 82.5\sqrt{2} = 116.6 \text{ mm}$

And the polar moment of inertia about the centroid of the weld group G is

$$j_G = 2(j_{G1} + A_1 r_1^2) + 2(j_{G2} + A_2 r_2^2) = 2.86 \times 10^7 \text{ mm}^4$$

Where, the subscripts 1 and 2 are for vertical and horizontal welds respectively.

$$\tau_{M_t} = \frac{3.1 \times 10^6 \times 116.6}{2.86 \times 10^7} = 12.6 \text{ MPa}$$

It is clear that $\theta = 45^\circ$

$$\sigma_{F_2} = \sqrt{\sigma_{M_x, F_2}^2 + (\tau_{\parallel, F_2} + \tau_{M_t} \cos\theta)^2 + (\tau_{M_t} \sin\theta)^2} = 61.3 \text{ MPa}$$

2.3.2 I section

2.3.2.1 The effect of the force F_1

The joint, as shown in figure 2.6, is subjected to direct shear stress and the bending stress due to the effect of F_1 .

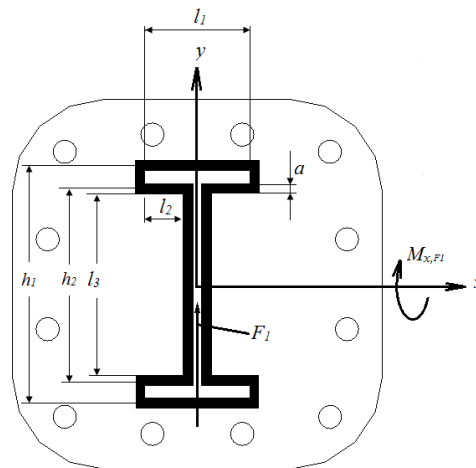


Figure 2.6 A beam of I cross section subjected to direct shear force and bending moment for fillet weld.

The shear stress due to the effect of the force F_1 is,

$$\tau_{\parallel, F_1} = \frac{F_1}{2al_3} = 7.59 \text{MPa}$$

The Bending stress due to bending moment ($M_{x, F_1} = F_1 \times L_1$)

$$I_x = \left(\frac{l_1 a^3}{12} + al_1 \frac{h_1^2}{4} \right) 2 + \left(\frac{l_2 a^3}{12} + al_2 \frac{h_2^2}{4} \right) 4 + \frac{al^3}{12} 2 = 1.2 \times 10^7 \text{mm}^4$$

$$y_{max} = 85 \text{mm}, Z_w = \frac{I_x}{y_{max}} = 1.4 \times 10^5 \text{mm}^3$$

$$\sigma_{M_{x, F_1}} = \frac{M_{x, F_1}}{Z_w} = 70.8 \text{MPa}$$

In order to find the resultant stress, the primary and secondary shear stresses are combined vectorially. The resultant stress due to the force F_1 is:

$$\sigma_{F_1} = \sqrt{\sigma_{M_{x, F_1}}^2 + \tau_{\parallel, F_1}^2} = 71.2 \text{MPa}$$

2.3.2.2 The effect of the force F_2

The joint, as shown in figure 2.7, is subjected to direct shear stress, bending stress and Shear stress due to the turning moment.

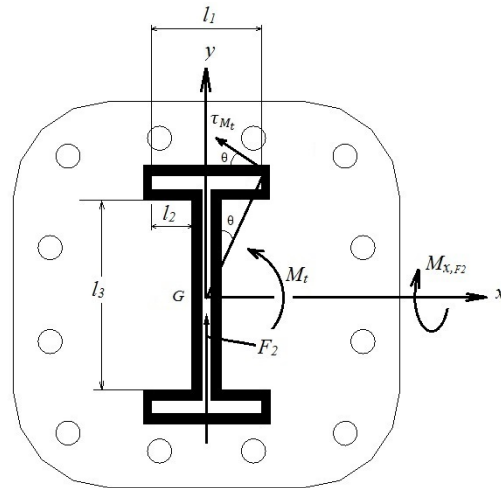


Figure 2.7 A beam of I cross- section subjected to direct shear force , bending and twisting moment for fillet weld.

The shear stress due to the effect of the force F_2

$$\tau_{\parallel, F_2} = \frac{F_2}{2al_3} = 7.59MPa$$

The Bending stress due to bending moment (M_{x, F_2}),

$$\sigma_{M_{x, F_2}} = \frac{M_{x, F_2}}{Z_w} = 70.8MPa$$

The Shear stress due to the turning moment is:

$$\tau_{M_t} = \frac{M_t \times r_{max}}{j_G} = 22.6MPa$$

Where, $l_3 = 131.8mm$, $r_{max} = 85mm$, $j_G = 1.3 \times 10^7 mm^4$, $\theta = 0$

The resultant stress due to the effect of the force F_2 is:

$$\sigma_{F_2} = \sqrt{\sigma_{M_{x, F_2}}^2 + (\tau_{M_t} \cos\theta)^2 + (\tau_{\parallel, F_2} + \tau_{M_t} \sin\theta)^2} = 77MPa$$

2.3.3 X section

2.3.3.1 The effect of the force F_1

The joint, as shown in figure 2.8, is subjected to direct shear stress and the bending stress.

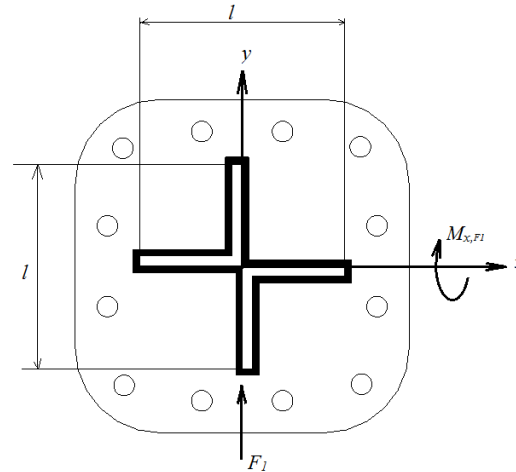


Figure 2.8 A beam of X cross section subjected to direct shear force and bending moment for fillet weld.

The shear stress due to the effect of the force F_1 is , $\tau_{\parallel,F_1} = \frac{F_1}{2al} = 6.25MPa$

The Bending stress due to bending moment (M_{x,F_1}) is:

$$\sigma_{M_{x,F_1}} = \frac{M_{x,F_1}}{Z_w} = 180.8MPa$$

Where, $l=160mm$, $y_{max} = 85mm$, $I_x = 4.7 \times 10^6mm^4$, $Z_w = 5.53 \times 10^4 mm^3$

In order to find the resultant stress, the primary and secondary shear stresses are combined vectorially. The resultant stress due to the force F_1 is

$$\sigma_{F_1} = \sqrt{\sigma_{M_{x,F_1}}^2 + \tau_{\parallel,F_1}^2} = 181MPa$$

2.3.3.2 The effect of the force F_2

The joint, as shown in figure 2.9, is subjected to direct shear stress , bending stress and Shear stress due to the turning moment.

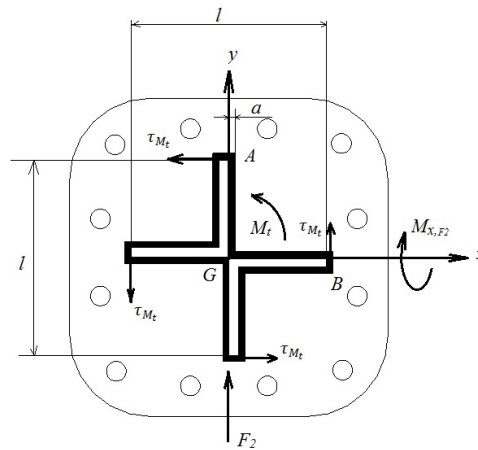


Figure 2.9 A beam of X cross- section subjected to direct shear force, bending and twisting moment for fillet weld.

The shear stress due to the effect of the force F_2 (τ_{\parallel,F_2}) and the bending stress ($\sigma_{M_{x,F_2}}$) due to bending moment (M_{x,F_2}) are 6.25MPa and 181MPa respectively.

The Shear stress due to the turning moment (M_t)

$$\tau_{M_t} = \frac{M_t \times r_{max}}{j_G} = 28MPa$$

Where, $r_{max} = 85mm$, $j_G = 9.4 \times 10^6 mm^4$

We note that the maximum stress is at point A. The resultant stress due to the effect of the force F_2

$$\sigma_{F_2} = \sqrt{\sigma_{M_{x,F_2}}^2 + \tau_{M_t}^2 + \tau_{\parallel,F_2}^2} = 183.8MPa$$

2.3.4 Z Section

2.3.4.1 The effect of the force F_1

The joint, as shown in figure 2.10, is subjected to direct shear stress and the bending stress.

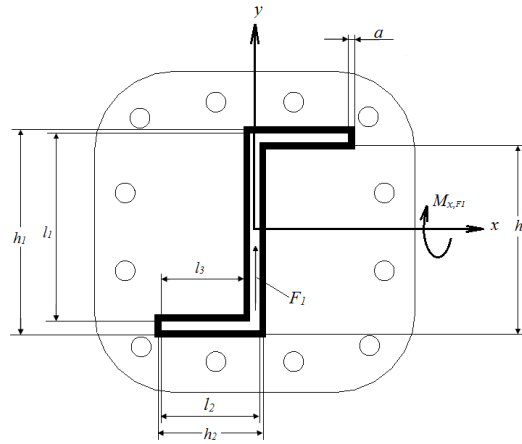


Figure 2.10 A beam of Z cross-section subjected to direct shear force and bending moment for fillet weld.

The shear stress due to the effect of the force F_1 ,

$$\tau_{\parallel, F_1} = \frac{F_1}{2al_1} = 6.25 \text{MPa}$$

The section is antisymmetrical with its centroid at the mid-point of the vertical web.

Therefore, the direct stress distribution is given by either of the equation below [48], where the point of interest has coordinates (0,80mm)

$$\sigma_{M_{x,F_1}} = \frac{M_{x,F_1}(I_{yy}y - I_{xy}x)}{I_{xx}I_{yy} - I_{xy}^2} = 149.1 \text{MPa}$$

Where, $l_1 = 160 \text{mm}$, $y_{\max} = 85 \text{mm}$, $I_x = 1.1 \times 10^7 \text{mm}^4$, $I_y = 2.3 \times 10^6 \text{mm}^4$

In order to find the resultant stress, the primary and secondary shear stresses are combined vectorially. The resultant stress due to the force F_1 is

$$\sigma_{F_1} = \sqrt{\sigma_{M_{x,F_1}}^2 + \tau_{\parallel, F_1}^2} = 149.2 \text{MPa}$$

2.3.4.2 The effect of the force F_2

The joint, as shown in figure 2.11, is subjected to direct shear stress, bending stress and Shear stress due to the turning moment.

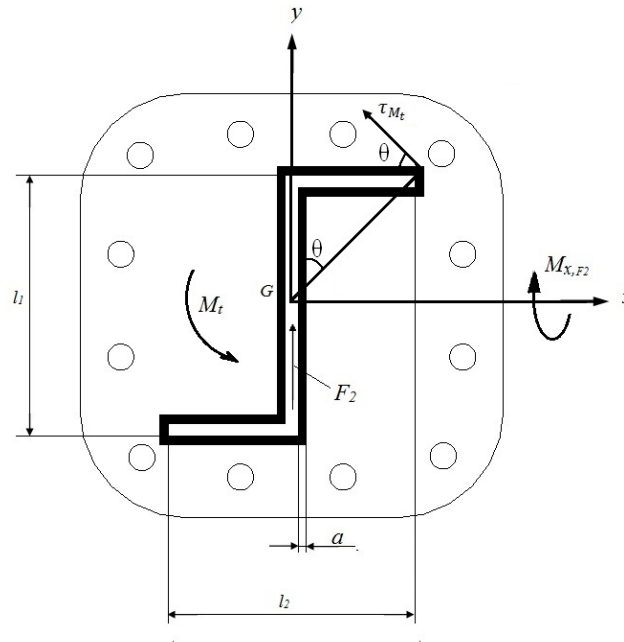


Figure 2.11 A beam of Z cross- section subjected to direct shear force , bending and twisting moment for fillet weld.

The shear stress due to the effect of the force F_2 , $\tau_{\parallel, F_2} = \frac{F_2}{2al_1} = 6.25MPa$

The Bending stress due to bending moment (M_{x, F_2}), $\sigma_{M_{x, F_2}} = \frac{M_{x, F_2}}{Z_w} = 149.1MPa$

The Shear stress due to the turning moment (M_t), $\tau_{M_t} = \frac{M_t \times r_{max}}{j_G} = 19.38MPa$

Where, $l_1 = 160mm$, $y_{max} = 85mm$

, $I_x = 1.1 \times 10^7 mm^4$, $I_y = 2.3 \times 10^6 mm^4$, $j_G = 1.36 \times 10^7 mm^4$, $\theta = -2.7^\circ$

The resultant stress due to the effect of the force F_2 ,

$$\sigma_{F_2} = \sqrt{\sigma_{M_{x, F_2}}^2 + (\tau_{M_t} \cos\theta)^2 + (\tau_{\parallel, F_2} + \tau_{M_t} \sin\theta)^2} = 151.1MPa$$

2.3.5 C section

2.3.5.1 The effect of the force F_1

The joint, as shown in figure 2.12, is subjected to direct shear stress and the bending stress.

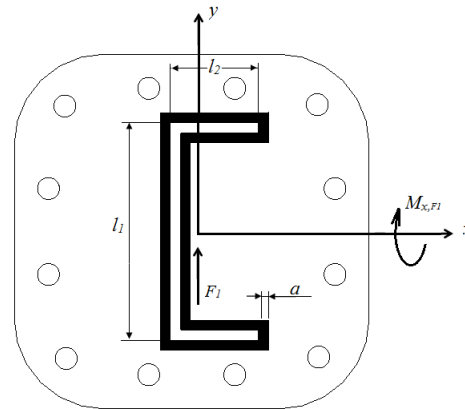


Figure 2.12 A beam of C cross-section subjected to direct shear force and bending moment for fillet weld.

The shear stress due to the effect of the force F_1 , $\tau_{\parallel, F_2} = \frac{F_2}{2al_1} = 6.25 \text{MPa}$

The Bending stress due to bending moment (M_{x, F_1}), $\sigma_{M_{x, F_1}} = \frac{M_{x, F_1}}{Z_w} = 72.7 \text{MPa}$

Where, $l_1 = 160 \text{mm}$, $y_{max} = 85 \text{mm}$, $I_x = 1.1 \times 10^7 \text{mm}^4$

In order to find the resultant stress, the primary and secondary shear stresses are combined vectorially. The resultant stress due to the force F_1 is

$$\sigma_{F_1} = \sqrt{\sigma_{M_{x, F_1}}^2 + \tau_{\parallel, F_1}^2} = 73 \text{MPa}$$

2.3.5.2 The effect of the force F_2

The joint, as shown in figure 2.13, is subjected to direct shear stress, bending stress and Shear stress due to the turning moment.

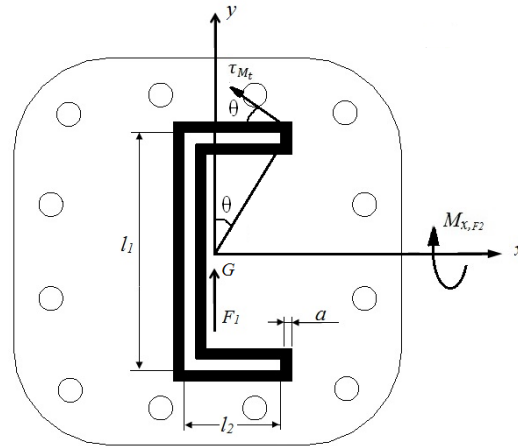


Figure 2.13 A beam of C cross- section subjected to direct shear force , bending and twisting moment for fillet weld.

The shear stress due to the effect of the force F_2 , $\tau_{\parallel, F_2} = \frac{F_2}{2al_1} = 6.25 \text{MPa}$

The Bending stress due to bending moment, $\sigma_{M_{x, F_2}} = \frac{M_{x, F_2}}{Z_w} = 72.7 \text{MPa}$

The Shear stress due to the turning moment, $\tau_{M_t} = \frac{M_t \times r_{max}}{j_G} = 21.9 \text{MPa}$

Where, $l_1 = 160 \text{mm}$, $y_{max} = 85 \text{mm}$, $I_x = 1.1 \times 10^7 \text{mm}^4$, $j_G = 1.2 \times 10^7 \text{mm}^4$, $\theta = 0^\circ$

The resultant stress due to the effect of the force F_2 is

$$\sigma_{F_2} = \sqrt{\sigma_{M_{x, F_2}}^2 + (\tau_{M_t} \cos \theta)^2 + (\tau_{\parallel, F_2} + \tau_{M_t} \sin \theta)^2} = 77.5 \text{MPa}$$

2.3.6 circular section

2.3.6.1 The effect of the force F_1

The joint, as shown in figure 2.14, are subjected to direct shear stress and the bending stress.

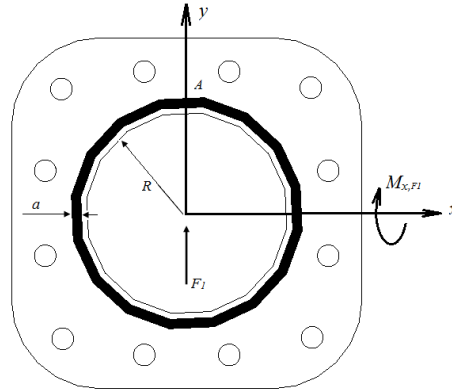


Figure 2.14 A beam of circular cross-section subjected to direct shear force and bending moment for fillet weld.

The shear stress due to the effect of the force F_1 , $\tau_{\parallel, F_1} = \frac{F_1}{2\pi a R_m} = 3.88 MPa$

The Bending stress due to bending moment, $\sigma_{M_{x,F_1}} = \frac{M_{x,F_1}}{Z_w} = 98 MPa$

Where, $R_m = 82mm$, $y_{max} = 84.5mm$, $I_x = 8.57 \times 10^6 mm^4$, $Z_w = 1.01 \times 10^5 mm^4$

In order to find the resultant stress, the primary and secondary shear stresses are combined vectorially. The resultant stress due to the force F_1 is

$$\sigma_{F_1} = \sqrt{\sigma_{M_{x,F_1}}^2 + \tau_{\parallel, F_1}^2} = 98.7 MPa$$

2.3.6.2 The effect of the force F_2

The joint, as shown in figure 2.15., are subjected to direct shear stress, bending stress and Shear stress due to the turning moment.

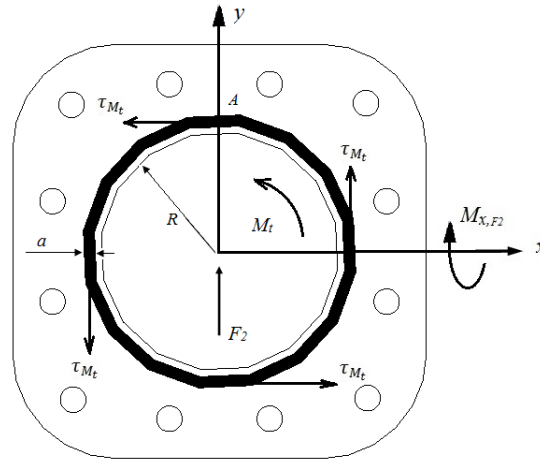


Figure 2.15. A beam of circular cross- section subjected to direct shear force , bending and twisting moment for fillet weld.

The shear stress due to the effect of the force F_2 , $\tau_{\parallel,F_2} = \frac{F_2}{2\pi a R_m} = 3.88 MPa$

The Bending stress due to bending moment, $\sigma_{M_{x,F_2}} = \frac{M_{x,F_2}}{Z_w} = 98 MPa$

The Shear stress due to the turning moment , $\tau_{M_t} = \frac{M_t \times r_{max}}{j_G} = 15.31 MPa$

Where, $R_m = 82 mm$, $y_{max} = 84.5 mm$, $I_x = 8.57 \times 10^6 mm^4$, $j_G = 1.7 \times 10^7 mm^4$, $Z_w = 1.01 \times 10^5 mm^3$, $\theta = 0^\circ$

The resultant stress due to the effect of the force F_2

$$\sigma_{F_2} = \sqrt{\sigma_{M_{x,F_2}}^2 + (\tau_{M_t} \cos\theta)^2 + (\tau_{\parallel,F_2} + \tau_{M_t} \sin\theta)^2} = 100.3 MPa$$

2.4. V Weld Case (b)

In this case, the weld thickness is equal to the beam thickness (it's similar to no weld). These specimens (Rectangular, I, X, Z, C and circular cross section) are welded to a support plate by means of bevel weld on their one end. The other ends are loaded by $F_1 = F_2 = 10 KN$, and the dimensions L_1 and L_2 are 1000mm and 310mm respectively.

A-The effect of the force F_1

The forces acting on the all welded section joints due to the effect of the force F_1 are:

1-Direct shear stress (τ_{\parallel,F_1}) due to load F_1

2-Bending stress due to bending moment ($M_{x,F_1} = F_1 \times L_1 = 10^7 Nmm$)

B- The effect of the force F2

Also for all specimens the forces acting on the welded joint due to the effect of the force F_2 are:

1- Direct shear stress (τ_{\parallel,F_2}) due to load F_2

2-Bending stress ($\sigma_{M_{x,F_2}}$) due to bending moment ($M_{x,F_2} = F_2 \times L_1 = 10^7 Nmm$)

3-Shear stress (τ_{M_t}) due to the turning moment ($M_t = F_2 \times L_2 = 3.1 \times 10^6 Nmm$)

2.4.1. Rectangular section

The data for rectangular section are : $l = 144mm$, $y_{max} = 82mm$, $r_{max} = 113.1mm$, $I_x = 1.8 \times 10^7 mm^4$, $J_G = 3.7 \times 10^7 mm^4$, $Z_w = 2.3 \times 10^5 mm^3$

The joint, as shown in figure 2.16, is subjected to direct shear stress and the bending stress.

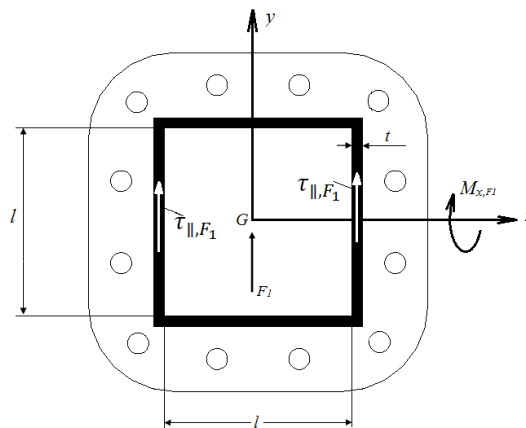


Figure 2.16 . A beam of rectangular cross-section subjected to direct shear force and bending moment for V weld.

2.4.1.1. The effect of F_1

The direct shear stress is, $\tau_{\parallel,F_1} = \frac{F_1}{2.a.l} = 4.3MPa$

The (tensile) bending stress on the horizontal weld is, $\sigma_{M_x,F1} = \frac{M_x,F1}{Z_X} = 45.5 \text{ N/mm}^2$

The stress magnitude σ_{F1} is the Pythagorean combination

$$\sigma_{F1} = \sqrt{\sigma_{M_x,F1}^2 + \tau_{\parallel,F1}^2} = 45.76 \text{ MPa}$$

2.4.1.2. The effect of F_2

The welded joint, as shown in figure 2.17, is subjected to twisting moment (M_t), shear force F_2 as well as bending moment ($M_x,F2$).

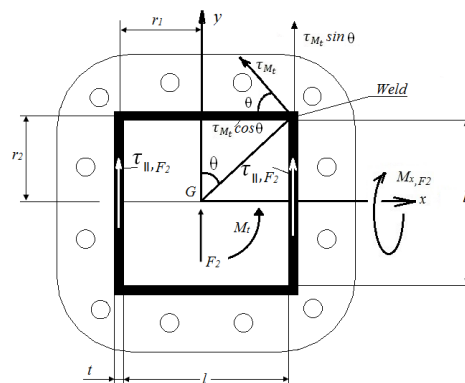


Figure 2.17. A beam of rectangular cross- section subjected to direct shear force , bending and twisting moment for V weld.

∴ direct shear stress is, $\tau_{\parallel,F2} = \frac{F_2}{2a.l} = 4.3 \text{ MPa}$

The (tensile) bending stress on the horizontal weld is, $\sigma_{M_x,F2} = \frac{M_x,F2}{Z_w} = 45.5 \text{ MPa}$

The moment at the support produces secondary shear or torsion stress of the welds, and this stress is given by the equation

$$\tau_{M_t} = \frac{M_t r_{\max}}{J_G} = 9.5 \text{ MPa}$$

It is clear that $\theta = 45^\circ$

$$\sigma_{F2} = \sqrt{\sigma_{M_x,F2}^2 + (\tau_{\parallel,F2} + \tau_{M_t} \cos\theta)^2 + (\tau_{M_t} \sin\theta)^2} = 47.7 \text{ MPa}$$

2.4.2 I section

The data for I section are : $l = 141.8mm$, $y_{max} = 80mm$, $r_{max} = 80mm$, $I_x = 9.1 \times 10^6 mm^4$, $J_G = 9.79 \times 10^6 mm^4$, $Z_w = 1.14 \times 10^5 mm^3$

2.4.2.1 The effect of the force F_1

The joint, as shown in figure 2.18., is subjected to direct shear stress and the bending stress. Due to the effect of F_1

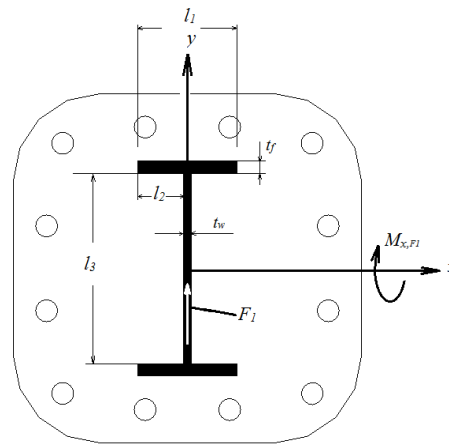


Figure 2.18. A beam of I cross-section subjected to direct shear force and bending moment for V weld.

The shear stress due to the effect of the force F_1 is , $\tau_{\parallel,F_1} = \frac{F_1}{2al_3} = 4.41MPa$

The Bending stress due to bending moment is, $\sigma_{M_x,F_1} = \frac{M_x,F_1}{Z_w} = 87.9MPa$

In order to find the resultant stress, the primary and secondary shear stresses are combined vectorially. The resultant stress due to the force F_1 is

$$\sigma_{F_1} = \sqrt{\sigma_{M_x,F_1}^2 + \tau_{\parallel,F_1}^2} = 88MPa$$

2.4.2.2. The effect of the force F_2

The joint, as shown in figure 2.19, is subjected to direct shear stress ,bending stress and Shear stress due to the turning moment.

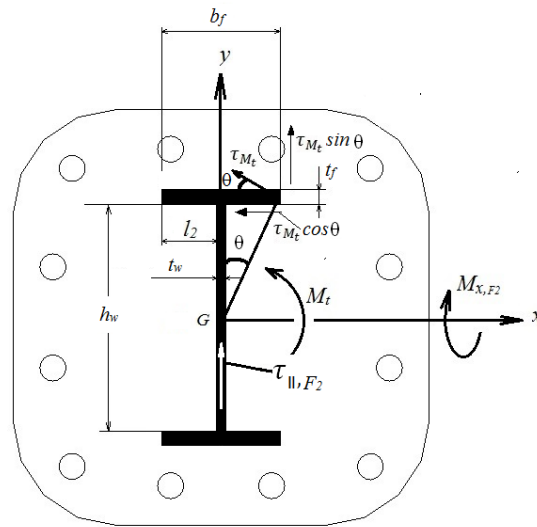


Figure 2.19. A beam of I cross- section subjected to direct shear force , bending and twisting moment for V weld.

The shear stress due to the effect of the force F_2 is, $\tau_{\parallel, F_2} = \frac{F_2}{2al_3} = 4.4MPa$

The Bending stress due to bending moment (M_{x, F_2}), $\sigma_{M_{x, F_2}} = \frac{M_{x, F_2}}{Z_w} = 87.9MPa$

The Shear stress due to the turning moment is, $\tau_{M_t} = \frac{M_t \times r_{max}}{j_G} = 27.9MPa$

Where, $\theta = 0$

The resultant stress due to the effect of the force F_2

$$\sigma_{F_2} = \sqrt{\sigma_{M_{x, F_2}}^2 + (\tau_{M_t} \cos \theta)^2 + (\tau_{\parallel, F_2} + \tau_{M_t} \sin \theta)^2} = 93.7MPa$$

2.4.3. X section

The data for X section are : $l = 160mm$, $y_{max} = 80mm$, $r_{max} = 80mm$, $I_x = 2.76 \times 10^6 mm^4$, $j_G = 5.5 \times 10^6 mm^4$, $Z_w = 3.45 \times 10^4 mm^3$

2.4.3.1. The effect of the force F_1

The joint, as shown in figure 2.20, is subjected to direct shear stress and the bending stress.

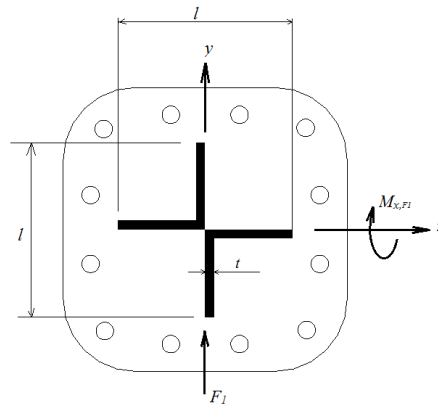


Figure 2.20 . A beam of X cross-section subjected to direct shear force and bending moment for V weld.

The shear stress due to the effect of the force F_1 is , $\tau_{\parallel,F_1} = \frac{F_1}{2al} = 3.9MPa$

The Bending stress due to bending moment , $\sigma_{M_{x,F_1}} = \frac{M_{x,F_1}}{Z_w} = 289.8MPa$

In order to find the resultant stress, the primary and secondary shear stresses are combined vectorially. The resultant stress due to the force F_1 is

$$\sigma_{F_1} = \sqrt{\sigma_{M_{x,F_1}}^2 + \tau_{\parallel,F_1}^2} = 289.9MPa$$

2.4.3.2. The effect of the force F_2

The joint, as shown in figure 2.21, is subjected to direct shear stress ,bending stress and Shear stress due to the turning moment.

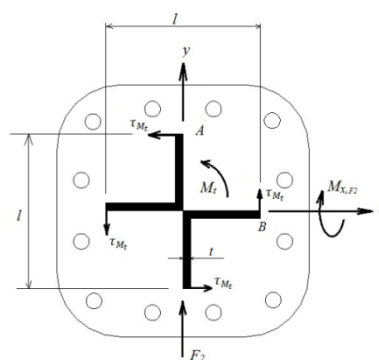


Figure 2.21. A beam of X cross- section subjected to direct shear force , bending and twisting moment for V weld.

The direct shear stress due to the effect of the force F_2 (τ_{\parallel, F_2}) and the bending stress (σ_{M_x, F_2}) due to bending moment (M_{x, F_2}) are $3.9MPa$ and $289.8MPa$, respectively.

The Shear stress due to the turning moment (M_t) is, $\tau_{M_t} = \frac{M_t \times r_{max}}{j_G} = 45MPa$

We note that the maximum stress is at point A. The resultant stress due to the effect of

the force F_2 is, $\sigma_{F_2} = \sqrt{\sigma_{M_x, F_2}^2 + \tau_{M_t}^2 + \tau_{\parallel, F_2}^2} = 293.4MPa$

2.4.4. Z Section

The following data area for Z section are : $l = 160mm$, $y_{max} = 80mm$, $r_{max} = 80mm$, $I_x = 8 \times 10^6 mm^4$, $I_y = 1.22 \times 10^6 mm^4$, $I_{xy} = -2.25 \times 10^6 mm^4$, $j_G = 9.2 \times 10^6 mm^4$,

2.4.4.1. The effect of the force F_1

The joint, as shown in figure 2.22, is subjected to direct shear stress and the bending stress.

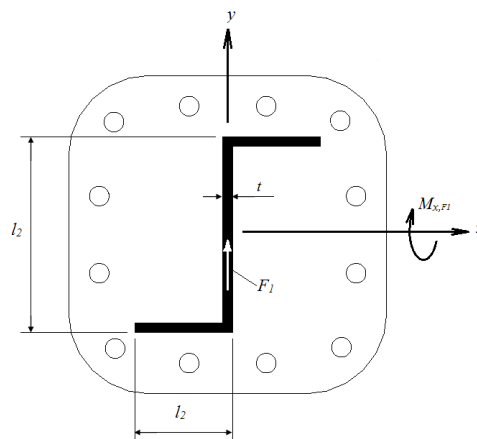


Figure 2.22 . A beam of Z cross-section subjected to direct shear force and bending moment for V weld.

The shear stress due to the effect of the force F_1 is, $\tau_{\parallel, F_1} = \frac{F_1}{2al_1} = 3.9MPa$

The section is antisymmetrical with its centroid at the mid-point of the vertical web.

Therefore, the direct stress distribution is given by the equation below [48], where the point of interest has coordinates (0,80mm)

$$\sigma_{M_{x,F_1}} = \frac{M_{x,F_1}(I_{yy}y - I_{xy}x)}{I_{xx}I_{yy} - I_{xy}^2} = 207.8MPa$$

In order to find the resultant stress, the primary and secondary shear stresses are combined vectorially. The resultant stress due to the force F_1 is

$$\sigma_{F_1} = \sqrt{\sigma_{M_{x,F_1}}^2 + \tau_{\parallel,F_1}^2} = 207.7MPa$$

2.4.4.2. The effect of the force F_2

The joint, as shown in figure 2.23, is subjected to direct shear stress ,bending stress and Shear stress due to the turning moment.

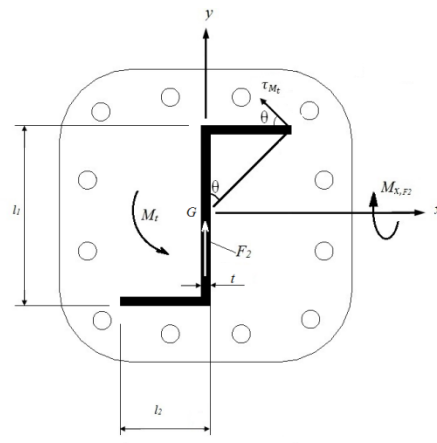


Figure 2.23. A beam of Z cross- section subjected to direct shear force , bending and twisting moment for V weld.

The shear stress due to the effect of the force F_2 , $\tau_{\parallel,F_2} = \frac{F_2}{2al_1} = 3.9MPa$

The Bending stress due to bending moment (M_{x,F_2}), $\sigma_{M_{x,F_2}} = 207.7MPa$

The Shear stress due to the turning moment (M_t), $\tau_{M_t} = \frac{M_t \times r_{max}}{j_G} = 26.9MPa$

Where , $\theta = -2.7^\circ$

The resultant stress due to the effect of the force F_2 ,

$$\sigma_{F_2} = \sqrt{\sigma_{M_{x,F_2}}^2 + (\tau_{M_t} \cos\theta)^2 + (\tau_{\parallel,F_2} + \tau_{M_t} \sin\theta)^2} = 209.5MPa$$

2.4.5. C section

The following data area for C section are : $l = 160mm$, $y_{max} = 80mm$, $r_{max} = 80mm$, $I_x = 8 \times 10^6 mm^4$, $j_G = 8.82 \times 10^6 mm^4$, $Z_w = 1 \times 10^5 mm^4$

2.4.5.1. The effect of the force F_1

The joint, as shown in figure 2.24, is subjected to direct shear stress and the bending stress.

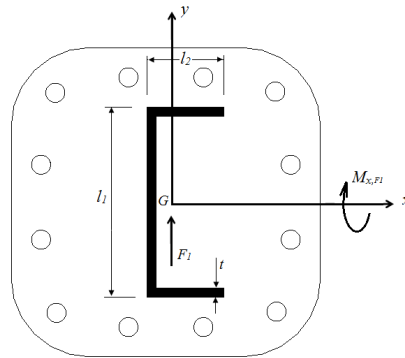


Figure 2.24 . A beam of C cross-section subjected to direct shear force and bending moment for V weld.

The shear stress due to the effect of the force F_1 , $\tau_{\parallel, F_1} = \frac{F_1}{2al_1} = 3.9MPa$

The Bending stress due to bending moment (M_{x, F_1}), $\sigma_{M_{x, F_1}} = \frac{M_{x, F_1}}{Z_w} = 100MPa$

In order to find the resultant stress, the primary and secondary shear stresses are combined vectorially. The resultant stress due to the force F_1 is

$$\sigma_{F_1} = \sqrt{\sigma_{M_{x, F_1}}^2 + \tau_{\parallel, F_1}^2} = 100.1MPa$$

2.4.5.2 The effect of the force F_2

The joint, as shown in figure 2.25, is subjected to direct shear stress ,bending stress and Shear stress due to the turning moment.

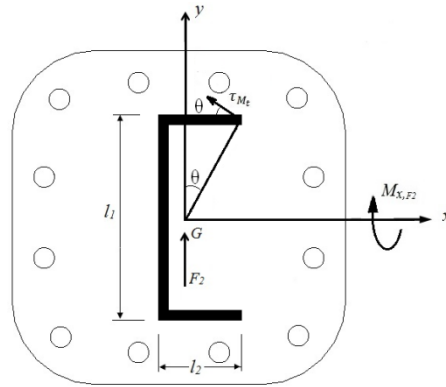


Figure 2.25. A beam of C cross- section subjected to direct shear force , bending and twisting moment for V weld.

The shear stress due to the effect of the force F_2 , $\tau_{\parallel, F_2} = \frac{F_2}{2al_1} = 3.9\text{MPa}$

The Bending stress due to bending moment, $\sigma_{M_{x,F_2}} = 100\text{MPa}$

The Shear stress due to the turning moment, $\tau_{M_t} = \frac{M_t \times r_{max}}{j_G} = 28.1\text{MPa}$

Where, $\theta = 0^\circ$

The resultant stress due to the effect of the force F_2 is

$$\sigma_{F_2} = \sqrt{\sigma_{M_{x,F_2}}^2 + (\tau_{M_t} \cos\theta)^2 + (\tau_{\parallel, F_2} + \tau_{M_t} \sin\theta)^2} = 104\text{MPa}$$

2.4.6 circular section

The following data area for circular section section are : $R_m = 77.25\text{mm}$, $y_{max} = 79.5\text{mm}$, $I_x = 6.45 \times 10^6\text{mm}^4$, $j_G = 1.29 \times 10^7\text{mm}^4$, $Z_w = 8.1 \times 10^4\text{mm}^4$

2.4.6.1 The effect of the force F_1

The joint, as shown in figure 2.26, are subjected to direct shear stress and the bending stress.

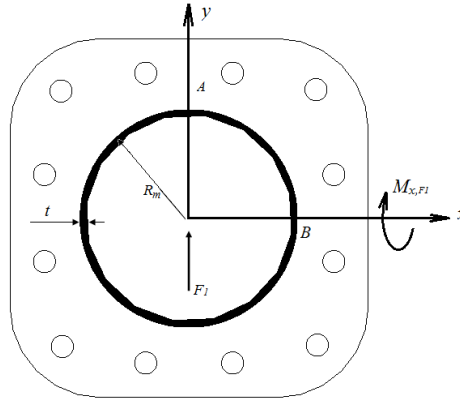


Figure 2.26 . A beam of circular cross-section subjected to direct shear force and bending moment for V weld.

The shear stress due to the effect of the force F_1 is $\tau_{\parallel,F_1} = \frac{F_1}{2\pi a R_m} = 4.58 MPa$

The Bending stress due to bending moment is $\sigma_{M_{x,F_1}} = \frac{M_{x,F_1}}{Z_w} = 123.26 MPa$

In order to find the resultant stress, the primary and secondary shear stresses are combined vectorially. The resultant stress due to the force F_1 is

$$\sigma_{F_1} = \sqrt{\sigma_{M_{x,F_1}}^2 + \tau_{\parallel,F_1}^2} = 123.3 MPa$$

2.4.6.2 The effect of the force F_2

The joint, as shown in figure 2.27, are subjected to direct shear stress, bending stress and Shear stress due to the turning moment.

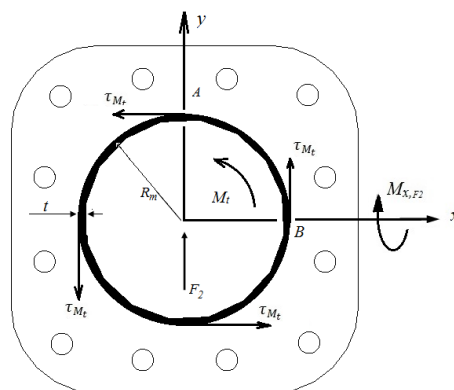


Figure 2.27. A beam of circular cross- section subjected to direct shear force , bending and twisting moment for V weld.

The shear stress due to the effect of the force F_2 , $\tau_{\parallel, F_2} = \frac{F_2}{2\pi a R_m} = 4.58 MPa$

The Bending stress due to bending moment, $\sigma_{M_x, F_2} = \frac{M_x F_2}{Z_w} = 123.26 MPa$

The Shear stress due to the turning moment, $\tau_{M_t} = \frac{M_t \times r_{max}}{j_G} = 19.1 MPa$

Where, $\theta = 0^\circ$

The resultant stress due to the effect of the force F_2

$$\sigma_{F_2} = \sqrt{\sigma_{M_x, F_2}^2 + (\tau_{M_t} \cos \theta)^2 + (\tau_{\parallel, F_2} + \tau_{M_t} \sin \theta)^2} = 124.8 MPa$$

Chapter 3

Three dimensional optical strain measurements

The measurement and analysis of the strain distribution is very important in civil and mechanical engineering, especially in the stress concentration problem in plastic and fracture mechanics. The traditional strain measurement technique can be divided into two types. Type 1: The relative displacement of two points will be measured. Then we can calculate the average strain between these two points by means of this relative displacement. The disadvantage of this method is that the surface strain distribution cannot be obtained. Type 2: A grid will be established on a sample surface before the deformation. We can measure the displacements of the grid after the deformation and analyze the strain distribution. The disadvantage of this method lies in its time consuming at analyzing the data. There are also precise measurement instrument, e.g. Raman-Spectroscopy and electrical speckle pattern interferometer, which can be used to measure the surface strain field without contact. But due to the expensive cost and the stability problem those methods cannot be widely used in the scientific research and engineering. A precise measurement of the surface strain distribution can be achieved with the help of the low-cost digital-image-correlation technique. It is an efficient tool to verify the result of the numerical calculation.

The fundamental theory of the digital-image-correlation technique is to compare the digital images before and after the deformation. Therefore, the “structural fleck” will be established on the sample surface before the deformation. The grayscale distribution offers an important character at recognizing the corresponding facets between before and after deformation. The relative position before and after the deformation can be obtained with the help of the grayscale distribution comparison. Then we can calculate the displacement vector and the strain in x- and y-direction, shear strain and von Mises strain[49].

3.1 Brief introduction to the Aaramis system

Aaramis is a non-contact optical 3D deformation measuring system. Aaramis analyzes, calculates and documents deformations. The graphical representation of the measuring results provides an optimum understanding of the behavior of the measuring object. Aaramis recognizes the surface structure of the measuring object in digital camera images and allocates coordinates to the image pixels. The first image in the measuring project represents the undeformed state of the object. After or during the deformation of the measuring object, further images are recorded. Then, Aaramis compares the digital images and calculates the displacement and deformation of the object characteristics. If the measuring object has only a few object characteristics, like it is the case with homogeneous surfaces, you need to prepare such surfaces by means of suitable methods, for example apply a stochastic color spray pattern, Stochastic pattern, see figure 3.1 [50].

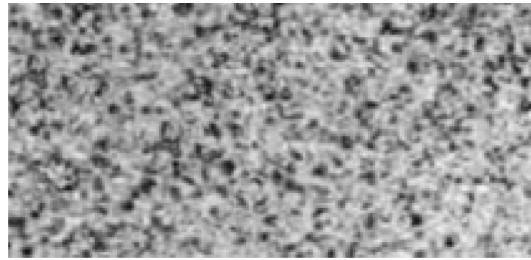


Figure 3.1 Stochastic pattern.

Aaramis is particularly suitable for three-dimensional deformation measurements under static and dynamic load in order to analyze deformations and strain of real components. One of the fields of application is verification of FE models

New products are designed and optimized with numerical simulation methods. Material parameters and components deformation behavior have a significant influence on the accuracy of simulation calculations and their reliability. Therefore Aramis is used for the validation of numerical simulations by calculating the differences between experimental measurements and FE data.

3.2 Main hardware and software components

- Sensor with two cameras (only for 3D setup).
- Stand for secure and steady hold of the sensor.
- Sensor controller for power supply of the cameras and to control image recording.
- High-performance PC system.
- Aaramis application software v6.1 and GOM Linux 10 system software or higher.

3.3 Principle of deviation measurements

In general, the Aaramis sensor unit is operated on a stand in order to optimally position the sensor with respect to the specimen. For a 3D measurement setup, two cameras are used (stereo setup) that are calibrated prior to measuring. The specimen needs to be within the resulting measuring volume (calibrated 3D space). After creating the measuring project in the software, images are recorded (monochrome, right camera, left camera) in various load stages of the specimen. After the area to be evaluated is defined (computation mask) and a start point is determined, the measuring project is computed. During computation, Aaramis observes the deformation of the specimen through the images by means of various square or rectangular image details (facets). The following figure 3.2 shows 15 x 15 pixel facets with a 2 pixel overlapping area in stage 0.

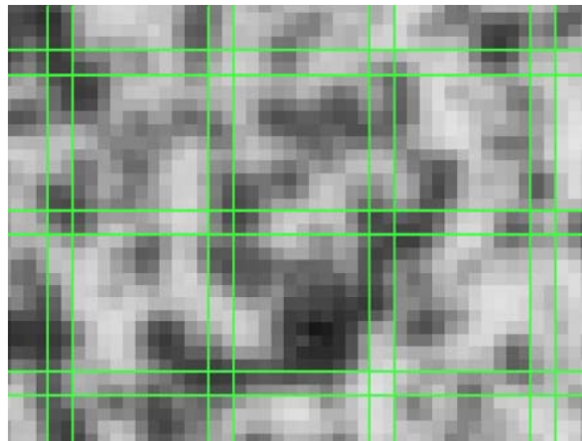


Figure 3.2. 5x15 facets with 2 pixels overlapping

You may adjust the facet size in pixels in the software. In the different load stages, the facets are identified and followed by means of the individual gray level structures. In the

following, we show a pair of facets (15 x 15 pixels) of the right and left camera, the gray values of which were observed through six deformation stages (Stage 0 to Stage 5). Stage 0 is the undeformed reference state and Stage 5 is the final deformation state. In these images, the white dashed line visualizes the undeformed state in order to make clear the factual relation between facets and deformation.

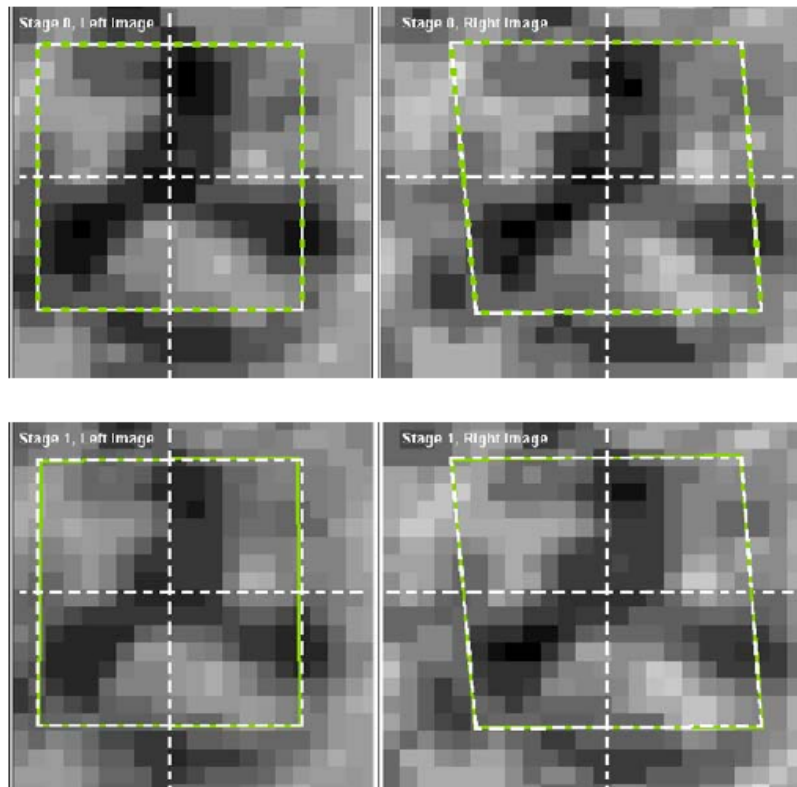


Figure 3.3. Relation between facets and deformation.

The system determines the 2D coordinates of the facets from the corner points of the green facets and the resulting centers. Using photogrammetric methods, the 2D coordinates of a facet, observed from the left camera and the 2D coordinates of the same facet, observed from the right camera, lead to a common 3D coordinate.

After successful computation, the data may undergo a postprocessing procedure in order to reduce measuring noise or suppress other local perturbations.

The measuring result is now available as 3D view. All further result representations like statistical data, sections, reports, etc. are derived thereof.

3.4 Facet computation

Using a single facet (enlarged representation) as example, we explain the computation principle for a 3D point through several deformation stages.

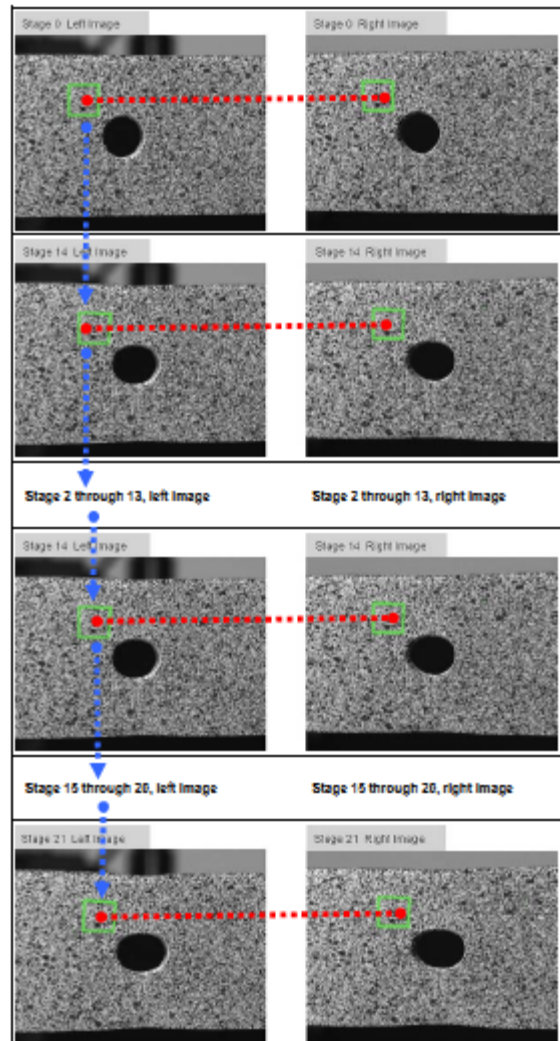


Figure 3.4. Computation principle

- The facet computation requires start points in all stages.



Figure 3.5. Start point definition (automatically or manually)

- The size of the green facet results from the facet field definition when creating the project.
- Computation is started in Stage 0, Left Image.
- Due to the start point definition, the software in principle knows the position of the facets and their adjacent facets in the 2D image. By identifying the individual spray pattern of a facet in the right and left image, the facet quadrangle is optimized. From the resulting 2D image coordinates of the facet (central point of the facet) in the right and left camera image, the software now calculates the 3D position of the facet.
- After the computation of the 3D positions of one stage, the software automatically continues with the next stage. Here as well, in principle the position of the facet is known because of the start point definition. Now, computation of the 3D position of the facet starts again.
- The strain computation results from the displacements of the 3D points.

3.5 Steps to carry out a typical measuring procedure

- Determination of measuring volume and preparation of the specimen. Prior to start measuring, make sure the measuring object fits into the selected measuring volume in all its deformation stages.
- Specimen preparation if the specimen has only little surface structure.
- Calibration of the measuring volume in case of a 3D measuring project.
- Creating a new project (2D or 3D) in the software and defining the project parameters (Facets, Strain, Keywords, Stage Parameter...).

- Adjusting the image recording mode, e.g. simple or fast measurement.
- Recording images during measurement (e. g. tensile test).
- Defining the computation mask in the measuring images, so that only deviation relevant areas of the specimen will be computed.
- Defining a start point for the computation process.
- Compute project.
- Selecting the result representation (Major Strain, Minor Strain, ...).
- Transformation of the project into a defined coordinate system.
- Data post processing to suppress unwanted measuring noise, interpolate missing 3D points, emphasize local effects .
- Defining analysis elements, sections or stage points for evaluation.
- Documentation of the results (creating reports, export).

3.6 Calibration

Calibration is a measuring process during which the measuring system with the help of calibration objects is adjusted, such that the dimensional consistency of the measuring system is ensured.

3.6.1 Calibration objects

For the Aaramis measuring system, two different calibration objects are used, calibration panels for small measuring volumes and calibration crosses for large measuring volumes. Calibration panels are also available cube-shaped in order to calibrate particularly small measuring volumes (10x8 to 66x44 mm). They are available in different sizes. Depending on the type of the system and the size they may differ slightly in their appearance. Calibration objects are equipped with so called reference points.

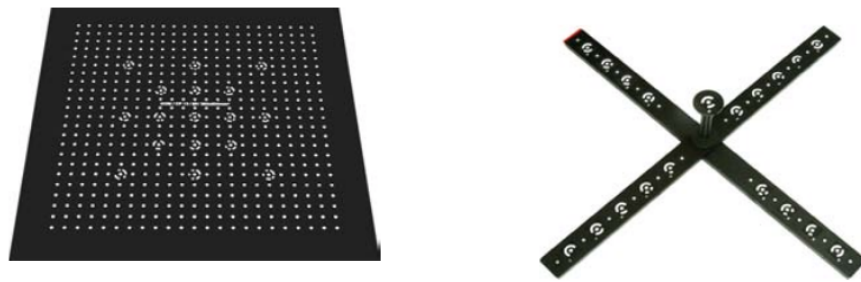


Figure 3.6. Calibration panel and calibration cross

The calibration object contains the scale bar information. Depending on the type, a calibration panel has one or two scale bars. A scale bar is the specified distance between two specific points. A calibration cross always has two scale bars (one scale bar on each cross section) [50].

3.6.2 When is calibration required?

- Before starting measurements for the first time, the respective measuring volume needs to be calibrated.
- Also, if the adjustment of the camera lenses or the position of the cameras with respect to each other is changed (e.g. when changing the camera support to a different length), the system requires calibration again.
- If the Aaramis system shows many yellow facets in the camera images after computation, the system might be decalibrated.

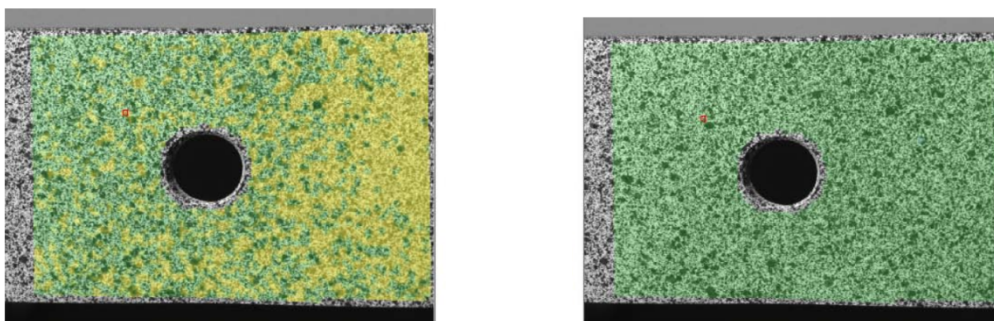


Figure 3.7. Camera image of a stage in a decalibrated state.

The system automatically creates yellow image areas (yellow facets) if the intersection error of a 3D point (facet) is larger than 0.3 pixels (factory-adjusted setting). The average intersection error of all 3D points should not be larger than 0.1 pixels.

3.6.3 Background information about calibration theory

During calibration, the sensor configuration is determined. This means that the distance of the cameras and the orientation of the cameras to each other are determined. In addition, the image characteristics of the lenses are determined (e.g. focus, lens distortions). Based on these settings, the software calculates from the reference points of the calibration object in the 2D camera image their 3D coordinates. The calculated 3D coordinates are then “calculated back” again into the 2D camera images. For the position of the reference points, this results in the so-called reference point deviation (intersection error)[50].

3.7 Measuring

3.7.1 Selecting the correct measuring volume

The measuring volume depends on the size of the measuring object or on the size of the area you would like to analyze. Choose a measuring volume in which the measuring object or the measuring area fills the entire image as best as possible. Ensure that the measuring object or the measuring area remains within the measuring volume in all deformation stages! If it is necessary to adapt the measuring volume, you need to readjust and calibrate the sensor again.

3.7.2 Preparing a specimen

The surface structure is important for carrying out a measurement. The specimen’s surface must meet the following requirements:

- The surface of the measuring object must have a pattern in order to clearly allocate the pixels in the camera images (facets). Thus, a pixel area in the reference image can be allocated to the corresponding pixel area in the target image.
- The surface pattern must be able to follow the deformation of the specimen. The surface pattern must not break early.
- The optimum specimen surface is smooth. Highly structured surfaces may cause problems in facet identification and 3D point computation.
- The pattern on the object should show a good contrast because otherwise such an allocation (matching) does not work.

- The surface pattern must be dull. Reflections cause a bad contrast and brightness differences between the right and left camera which prevent the facet computation in the areas of reflection.
- On one hand, the size of the surface characteristics should be small enough to allow a fine raster of calculation facets during evaluation. On the other hand, the pattern should be large enough to be completely resolved by the camera.
- Best suitable are stochastic patterns which are adapted to the measuring volume, camera resolution and facet size. In addition, for calculation, it is advantageous if the patterns do not have larger areas of constant brightness, e.g. large spots. Structures with changing gray values as they occur with random patterns are more appropriate. The left figure shows a pattern that is not really suitable. The right figure shows a good and clearly better pattern [50].

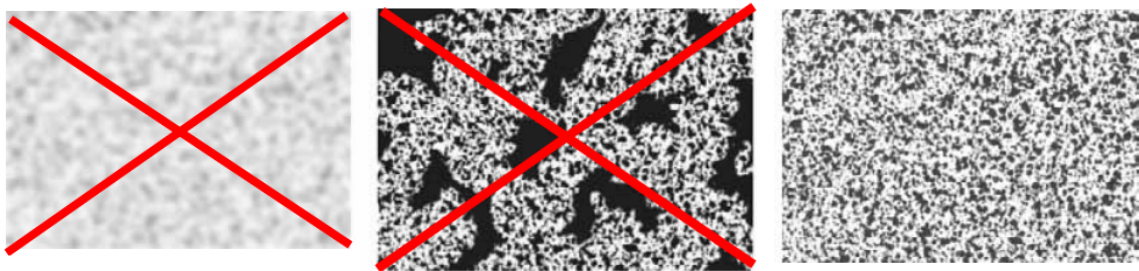


Figure 3.8 a) Unsuitable low contrast stochastic pattern

b) High contrast stochastic pattern with disturbing large spots

c) Good high contrast stochastic pattern

3.7.3 Spraying a stochastic pattern

Before you start spraying, make sure the surface of the specimen is free of grease and oil. In a first step, you need to apply a white and dull base layer. In a second step, spray a black stochastic pattern. In order to check if your spray pattern is suitable for your measuring volume, specific reference patterns are available for the measuring volumes.

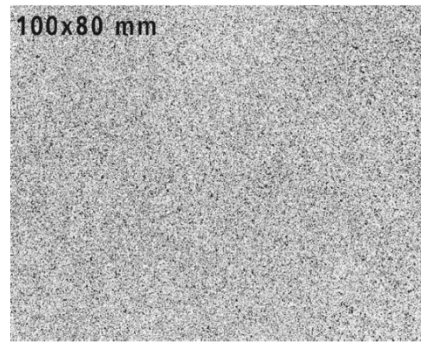


Figure 3.9. Spray pattern reference

To compare the spray patterns, use your computer screen and the spray pattern reference for the volume 100x80 mm, regardless of the real measuring area. If you do not have an original spray pattern reference, you may also use this page of the user manual [50].

- Position your specimen with the spray pattern in the measuring distance in front of the camera.
- On your computer screen, adjust the window of the camera image to the same dimensions as the spray pattern reference 100x80 mm (see figure 3.10).

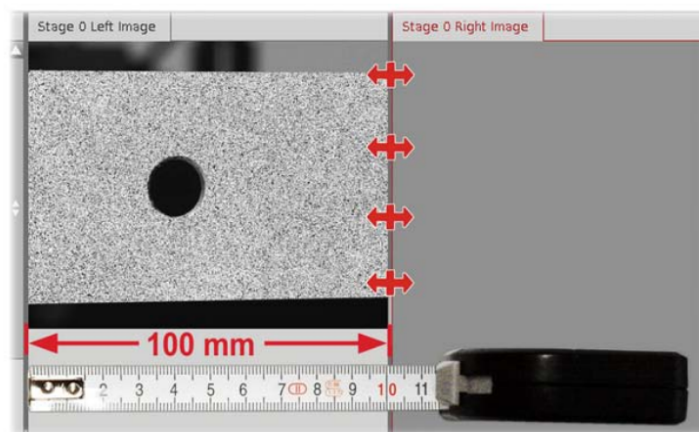


Figure 3.10 Window set to 100mm

- Compare the pattern of the camera image with the spray pattern reference for volume 100x80mm.

3.7.4 Computations

After having recorded an image series, explains the strain computation, and shows corresponding 3D representations.

3.8 Facets

Aramis observes the deformation of the specimen through the images by means of various square or rectangular facets. Figure 3.11 shows 15x15 pixel facets with a facet step of 13 pixels (corresponds to a 2 pixel overlapping area, default setting).

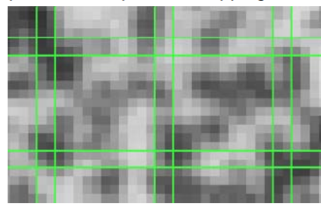


Figure 3.11.A 15x15 pixel facets with a facet step of 13 pixels

3.8.1 Facet shapes

The facet shape (square, rectangular, quadrangular) influences the computability of the measuring project. Square and rectangular facets in the reference stage are always aligned according to the x-y orientation of the 2D image.

3.8.2 Rectangular facets

For strain measurements where the specimen is subject to high levels of strain, use rectangular facets according to the figure below in order to get evaluable facet fields.

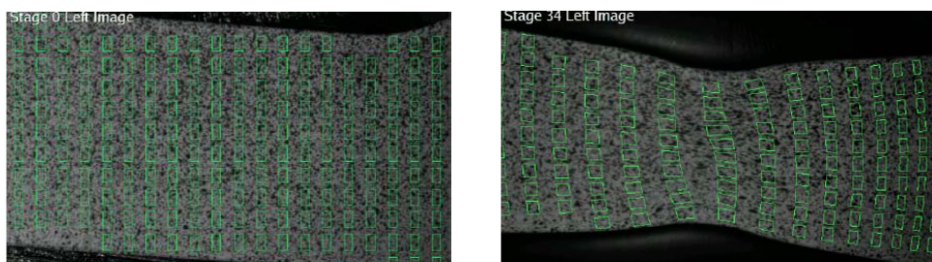


Figure 3.12 a- Undeformed state

b-Deformed state with considerable material necking

3.8.3 Quadrangular facets

If, in case of quadrangular specimens you would like to create valid facets up to the edge, you may create a facet field manually which follows the specimen's geometry. The individual facets result within this field. The x-y orientation is based on this field as well. As computation here is only done within the facet field, it is not necessary to mask the specimen.

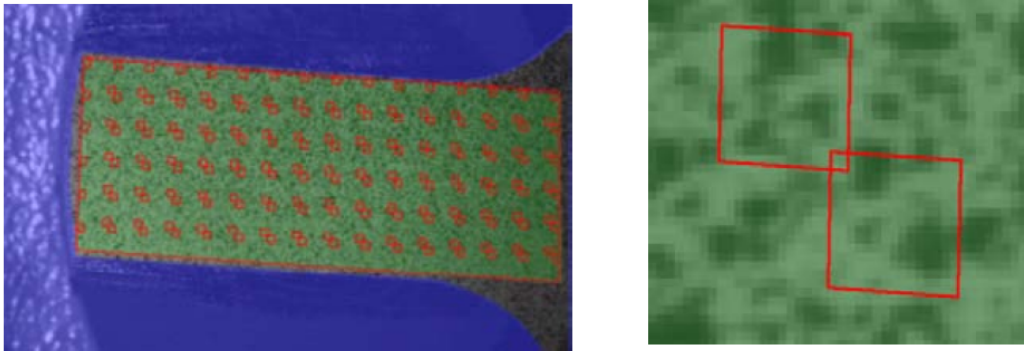


Figure 3.13. a- Undeformed state with quadrangular facet field b- individual facets in a quadrangular facet field

3.9 Computation masks

Computation masks allow the software to carry out facet computations in defined areas of the 2D camera images only. To define computation masks, the software provides extensive tools.

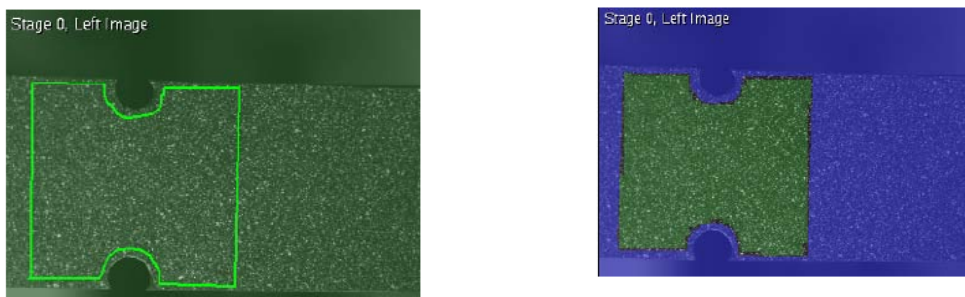


Figure 3.14. a- Computation mask during definition b- Finished computation mask (only the green area will be computed)

Only areas on a specimen that are relevant for deformation shall be calculated. Thus, for example, fixtures, backgrounds, specimen edges and contour jumps are not included in the computation.

As the 3D computation of the measuring points is based on facets that need to be seen from the right and left camera with the individual facet pattern, a correct 3D computation and strain computation is not possible for specimen edges and contour jumps in specimens [50].

Figure 3.15 shows measuring images of tensile test specimen with circular hole.

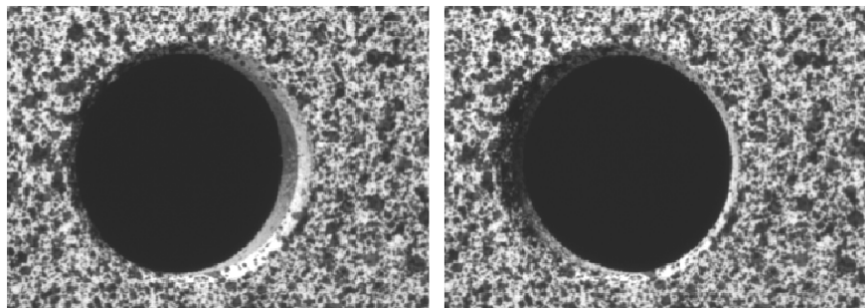


Figure 3.15. Tensile test specimen with circular hole

The images show a tensile test specimen with a hole in stage 1 of a strain measuring project seen from the left and right camera. While the surface pattern almost looks the same, considerable differences result at the hole edges due to the different camera locations.

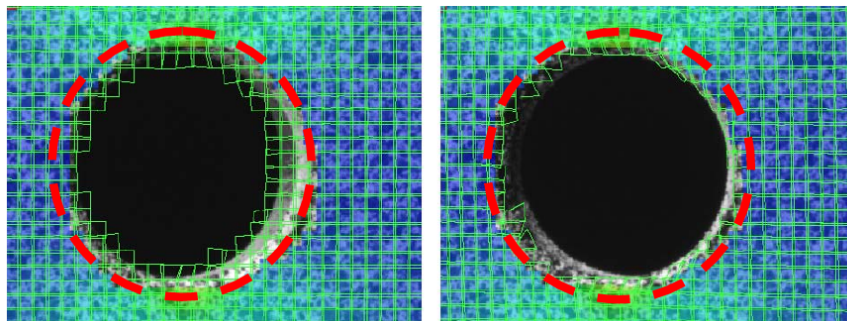


Figure 3.16 strain of red framed area cannot be computed.

The red framed area shows strain which cannot be computed correctly because of the mentioned problems.

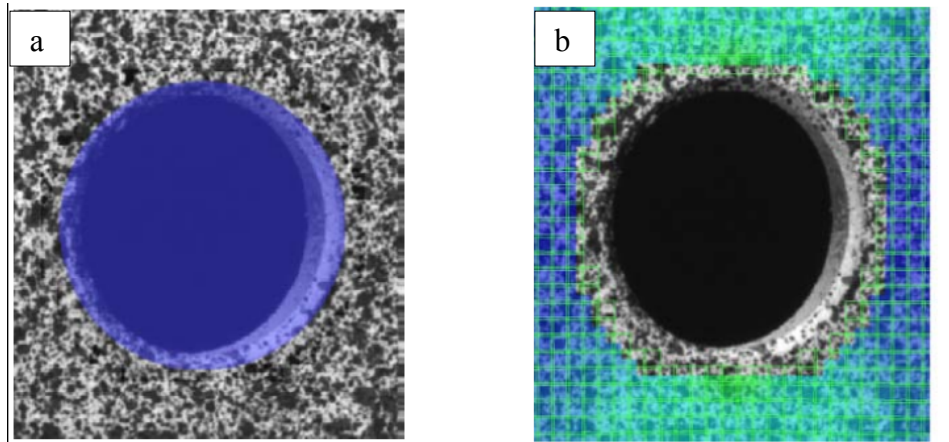


Figure 3.17. The image shows a tensile test specimen with hole and a computation mask.

a) In the blue area, facets will not be computed

b) Excluding the facet problems in the edge region.

3.10 Start point

A start point is used to calculate facet. The start point creation may fail in the following stages because the facet content shows only little stochastic pattern structure figure.

Also it can fall back on a well perceptible stochastic pattern structure figure.

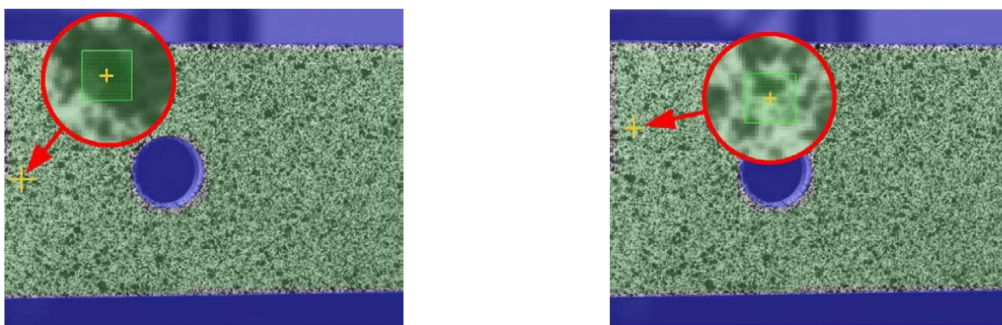


Figure 3.18 Example of a Poor Start Point

3.11 Strain computation

For strain computation, Aaramis distinguishes between two methods, linear strain and spline strain computation. In Aaramis measuring projects normally only, linear strain computation is used. For specimen of small curvature radii, the spline strain computation method can be used.

3.11.1 Linear strain

Principle of a specimen in the undeformed (left) and deformed (right) state is shown in figure 3.19. The strain is computed in connection with the surrounding measuring points which are directly derived from the facets.

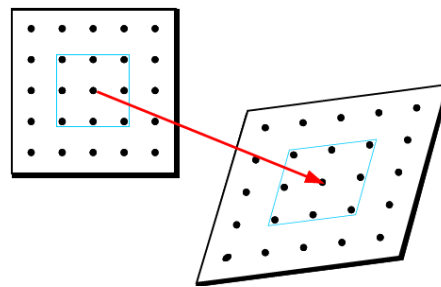


Figure 3.19. A specimen in the undeformed (left) and deformed (right) state

3.11.2 Spline strain

Figure 3.20 shows a specimen in the undeformed (left) and deformed (right) state. The black points are measuring points which are directly derived from the facets. The white points were interpolated from the black points using the spline function. Here, strain computation also considers the interpolated (white) points [50].

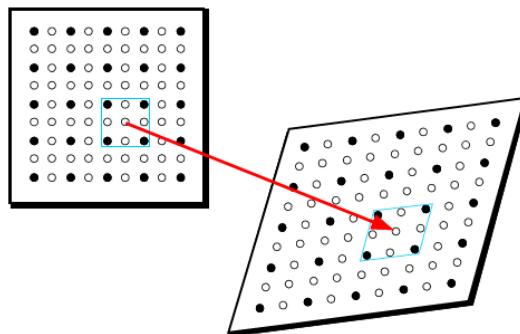


Figure 3.20 A specimen in the undeformed (left) and deformed (right) state.

Chapter 4

Finite element method

The finite element method is a numerical method for solving problems of engineering and mathematical physics. Typical problem areas of interest in engineering and mathematical physics that are solvable by use of the finite element method include structural analysis, heat transfer, fluid flow, mass transport, and electromagnetic potential [51].

The finite element method became popular with the advancements in digital computers since they allow engineers to solve large systems of equations quickly and efficiently. The finite element method is a useful tool for the solution of many types of engineering problems such as the analysis of the structures, heat transfer and fluid flow. The method is also used in the design of air frames, ships, electric motors, heat engines and spacecraft.

In most structural analysis applications, it is necessary to compute displacements and stresses at various points of interest. The finite element method is a valuable tool for studying the behavior of structures. The finite element model can be created by dividing the structure into a number of finite elements. Each element is interconnected by nodes. The selection of elements for modeling the structure depends upon the behavior and geometry of the structure being analyzed. The modeling pattern, which is generally called mesh for the finite element method, is very important part of the modeling process. The results obtained from the analysis depend upon the selection of the finite elements and the mesh size. Although the finite element model does not behave exactly like the actual structure, it is possible to obtain sufficiently accurate results for most practical applications. Once the finite element model has been created, the equilibrium equations can easily be solved using digital computers. The deflections at each node of the finite element model are obtained by solving the equilibrium equations. The stresses and strains then can be obtained from the stress-strain and strain-displacement relations. The finite element method is ideally suited for implementation on a computer with the advancements in digital computers, the finite element method is becoming the method of choice for solving many engineering problems, and is extensively used for structural

analysis. The structure can be discretized using frame elements, plane elements, plate elements, or shell elements according to the behavior of the structure. The structure can also be modeled by combining different types of elements to approximate different aspects of structural behavior.

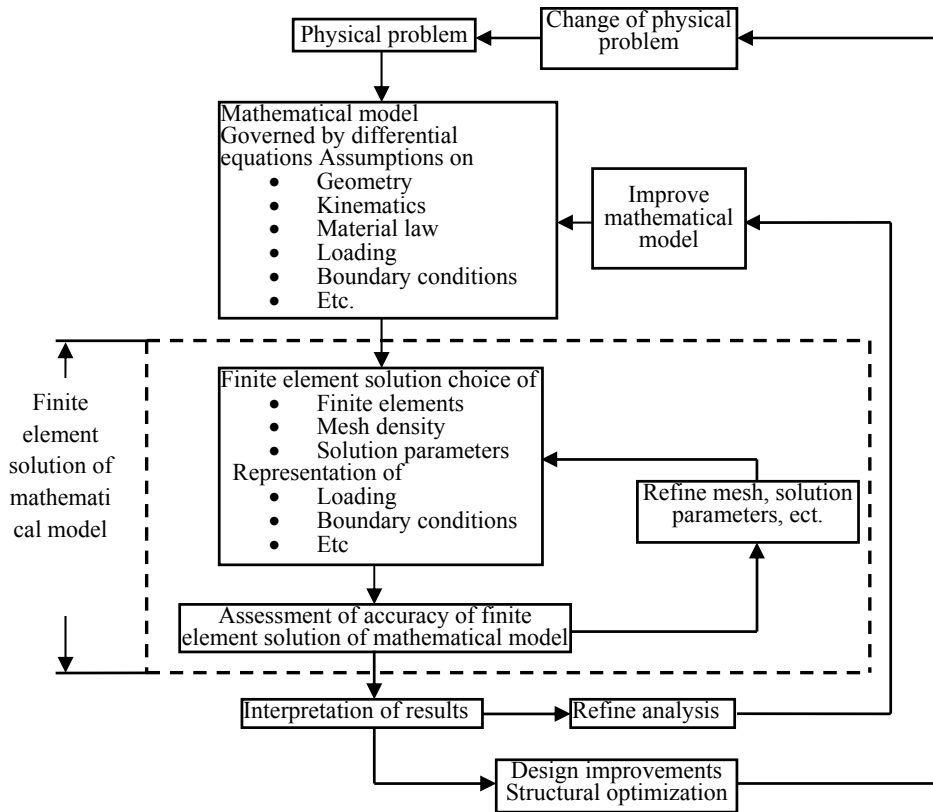


Figure4.1. The process of finite element analysis [52].

4.1 Physical problems, mathematical models and the finite element solution

The finite element method is used to solve physical problems in engineering analysis and design. Figure 4.1 summarizes the process of finite element analysis. The physical problem typically involves an actual structure or structural component subjected to certain loads. The idealization of the physical problem to a mathematical model requires certain assumptions that together lead to differential equations governing the mathematical model. The finite element analysis solves this mathematical model.

It is clear that the finite element solution will solve only the selected mathematical model and that all assumption in a model will be reflected in the predicted response. We cannot expect any more information in the prediction of physical phenomena than the

information contained in the mathematical model. Hence the choice of appropriate mathematical model is crucial and completely determines the insight into the actual physical problem that we can obtain by the analysis [52].

4.2 General steps of the finite element method

In the finite element method, the actual continuum or body of matter, such as a solid, liquid, or gas, is represented as an assemblage of subdivisions called finite elements. These elements are considered to be interconnected at specified joints called nodes or nodal points. The nodes usually lie on the element boundaries where adjacent elements are considered to be connected. Since the actual variation of the field variable (e.g., displacement, stress, temperature, pressure, or velocity) inside the continuum is not known, we assume that the variation of the field variable inside a finite element can be approximated by a simple function. These approximating functions (also called interpolation models) are defined in terms of the values of the field variables at the nodes. When field equations (like equilibrium equations) for the whole continuum are written, the new unknowns will be the nodal values of the field variable. By solving the field equations, which are generally in the form of matrix equations, the nodal values of the field variable will be known. Once these are known, the approximating functions define the field variable throughout the assemblage of elements.

4.2.1 Step 1 Discretize and select the element types

This step involves dividing the body into an equivalent system of finite elements with associated nodes and choosing the most appropriate element type to model most closely the actual physical behavior. The choice of elements used in a finite element analysis depends on the physical makeup of the body under actual loading conditions and on how close to the actual behavior the analyst wants the results to be.

Many practical problems in engineering are either extremely difficult or impossible to solve by conventional analytical methods. Such methods involve finding mathematical equations which define the required variables. For example, the distribution of stresses and displacements in a solid component might be required [53].

The finite element method is used to solve physical problems in engineering analysis and design. Figure 4.1 summarizes the process of finite element analysis. The physical

problem typically involves an actual structure or structural component subjected to certain loads. The idealization of the physical problem to a mathematical model requires certain assumption that together leads to differential equations governing the mathematical model. Since the finite element solution technique is a numerical procedure. Judgment concerning the appropriateness of one-, two-, or three-dimensional idealizations is necessary. Moreover, the choice of the most appropriate element for a particular problem is one of the major tasks that must be carried out by the designer/analyst. Elements that are commonly employed in practice are shown in figures 4.2-5.



Figure 4.2 . A bar or beam element a) Simple two-noded line element
b) The higher-order line element

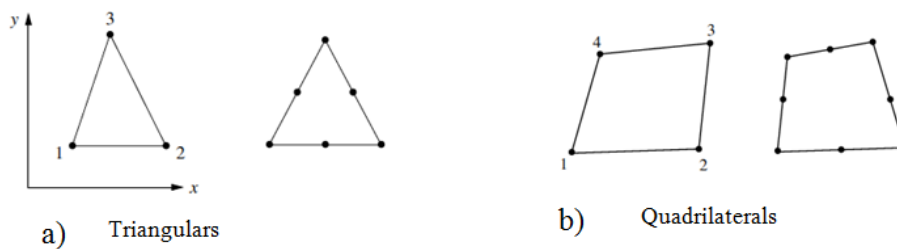


Figure 4.3. Simple two-dimensional elements with corner nodes
a) Triangular Elements b) Quadrilateral elements

The following elements typically used to represent three-dimensional stress state

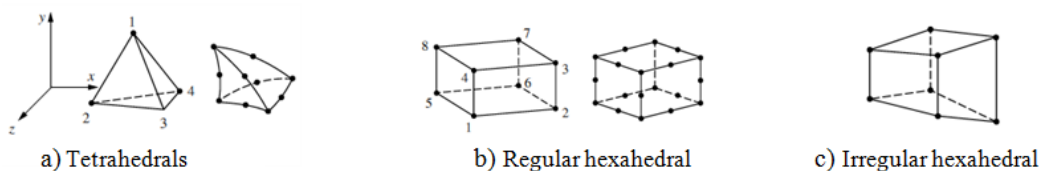


Figure 4.4. Simple three-dimensional elements and higher-order three-dimensional elements with intermediate nodes along edges
a) Tetrahedral Elements
b) Regular hexahedral
c) Irregular hexahedral

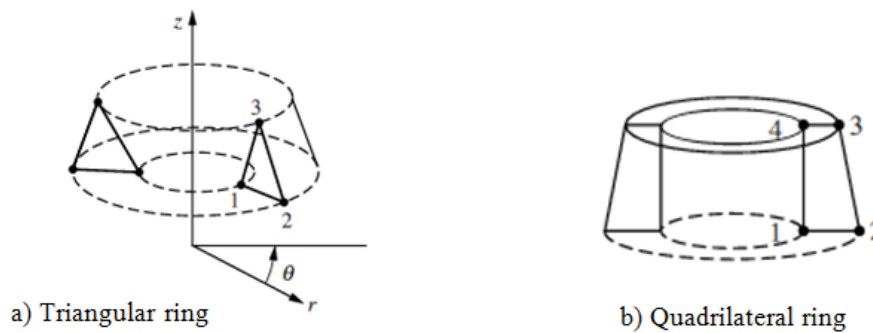


Figure 4.5 Simple axisymmetric used for axisymmetric problems

a) Triangular ring

b) Quadrilateral ring

4.2.2 Step 2 Selection of a proper interpolation or displacement model

This step involves choosing a displacement function within each element. The function is defined within the element using the nodal values of the element. Linear, quadratic, and cubic polynomials are frequently used functions because they are simple to work with in finite element formulation. However, trigonometric series can also be used. For a two-dimensional element, the displacement function is a function of the coordinates in its plane (say, the x-y plane). The functions are expressed in terms of the nodal unknowns (in the two-dimensional problem, in terms of an x and a y component). The same general displacement function can be used repeatedly for each element. Hence the finite element method is one in which a continuous quantity, such as the displacement throughout the body, is approximated by a discrete model composed of a set of piecewise-continuous functions defined within each finite domain or finite element [51].

4.2.3. Step 3 Define the strain displacement and stress strain relationships

Strain/displacement and stress/strain relationships are necessary for deriving the equations for each finite element. In addition, the stresses must be related to the strains through the stress/strain law generally called the constitutive law. The ability to define the material behavior accurately is most important in obtaining acceptable results.

4.2.4. Step 4 Derive the element stiffness matrix and equations

From the assumed displacement model, the element stiffness matrix $[K^e]$ of element e is to be derived by using either equilibrium conditions or a suitable variational principle.

We now present alternative methods used in finite element analysis.

4.2.4. 1 Direct equilibrium method

According to this method, the stiffness matrix and element equations relating nodal forces to nodal displacements are obtained using force equilibrium conditions for a basic element, along with force/deformation relationships. Because this method is most easily adaptable to line or one-dimensional elements (spring, bar, and beam elements).

4.2.4.2 Work or energy methods

To develop the stiffness matrix and equations for two- and three-dimensional elements, it is much easier to apply a work or energy method. The principle of virtual work (using virtual displacements), the principle of minimum potential energy, and Castigliano's theorem are methods frequently used for the purpose of derivation of element equations.

The principle of virtual work is applicable for any material behavior, whereas the principle of minimum potential energy and Castigliano's theorem are applicable only to elastic materials. Furthermore, the principle of virtual work can be used even when a potential function does not exist. The principle of minimum potential energy probably is the best known of the three energy methods.

4.2.4.3 Methods of weighted residuals

The methods of weighted residuals are useful for developing the element equations; particularly popular is Galerkin's method. These methods yield the same results as the energy methods wherever the energy methods are applicable. They are especially useful when a functional such as potential energy is not readily available. The weighted residual methods allow the finite element method to be applied directly to any differential equation. Using any of the methods will produce the equations to describe the behavior of an element. These equations are written conveniently in matrix form as

$$\begin{Bmatrix} f_1 \\ f_2 \\ f_3 \\ f_4 \\ \vdots \\ f_n \end{Bmatrix} = \begin{bmatrix} k_{11} & k_{12} & k_{13} & k_{14} & \cdots & k_{1n} \\ k_{21} & k_{22} & k_{23} & k_{24} & \cdots & k_{2n} \\ k_{31} & k_{32} & k_{33} & k_{34} & \cdots & k_{3n} \\ k_{41} & k_{42} & k_{43} & k_{44} & \cdots & k_{4n} \\ \vdots & \vdots & \vdots & \vdots & \ddots & \vdots \\ k_{n1} & k_{n2} & k_{n3} & k_{n4} & \cdots & k_{nn} \end{bmatrix} \begin{Bmatrix} u_1 \\ u_2 \\ u_3 \\ u_4 \\ \vdots \\ u_n \end{Bmatrix}$$

or in compact matrix form as

$$\{f\} = [k]\{u\} \tag{4.1}$$

Where $\{f\}$ is the vector of element nodal forces, $[k]$ is the element stiffness matrix (normally square and symmetric), and $\{u\}$ is the vector of unknown element nodal degrees of freedom or generalized displacements, n . Here generalized displacements may include such quantities as actual displacements, slopes, or even curvatures.

4.2.5. Step 5 Assemble the element equations to obtain the global or total equations and introduce boundary conditions

In this step the individual element nodal equilibrium equations generated in step 4 are assembled into the global nodal equilibrium equations.

The final assembled or global equation written in matrix form is,

$$\{F\} = [K]\{u\} \quad (4.2)$$

Here $\{F\}$ is the vector of global nodal forces, $[K]$ is the structure global or total stiffness matrix, (for most problems, the global stiffness matrix is square and symmetric) and $\{u\}$ is now the vector of known and unknown structure nodal degrees of freedom or generalized displacements. It can be shown that at this stage, the global stiffness matrix $[K]$ is a singular matrix because its determinant is equal to zero. To remove this singularity problem, we must invoke certain boundary conditions (or constraints or supports) so that the structure remains in place instead of moving as a rigid body [51].

4.2.6 Step 6 Solve for the unknown degrees of freedom (or generalized displacements)

Equation (4.2) is modified to account for the boundary conditions, is a set of simultaneous algebraic equations that can be written in expanded matrix form as

$$\begin{Bmatrix} F_1 \\ F_2 \\ F_3 \\ \vdots \\ F_n \end{Bmatrix} = \begin{bmatrix} K_{11} & K_{12} & K_{13} & \dots & K_{1n} \\ K_{21} & K_{22} & K_{23} & \dots & K_{2n} \\ K_{31} & K_{32} & K_{33} & \dots & K_{3n} \\ \vdots & \vdots & \vdots & \ddots & \vdots \\ K_{n1} & K_{n2} & K_{n3} & \vdots & K_{nn} \end{bmatrix} \begin{Bmatrix} u_1 \\ u_2 \\ u_3 \\ \vdots \\ u_n \end{Bmatrix} \quad (4.3)$$

Where now n is the structure total number of unknown nodal degrees of freedom. These equations can be solved for the displacements u by using an elimination method (such as Gauss's method) or an iterative method (such as the Gauss–Seidel method). The

$\{u\}$ are called the primary unknowns, because they are the first quantities determined using the stiffness (or displacement) finite element method.

4.2.7 Step 7 Computation of element strains and stresses

From the known nodal displacements $\{u\}$, the element strains and stresses (or moment and shear force) can be computed by using the necessary equations of solid or structural mechanics.

4.2.8 Step 8 Interpret the results

The final goal is to interpret and analyze the results for use in the design/analysis process. Determination of locations in the structure where large deformations and large stresses occur is generally important in making design/analysis decisions. Postprocessor computer programs help the user to interpret the results by displaying them in graphical form.

4.3 Advantages of the finite element method

The finite element method has a number of advantages that have made it very popular. They include the ability to

- 1-Model irregularly shaped bodies quite easily.
- 2-Handle general load conditions without difficulty.
3. Model bodies composed of several different materials because the element equations are evaluated individually.
4. Handle unlimited numbers and kinds of boundary conditions.
5. Vary the size of the elements to make it possible to use small elements where necessary.
6. Alter the finite element model relatively easily and cheaply.
7. Include dynamic effects.
8. Handle nonlinear behavior existing with large deformations and nonlinear materials.

The finite element method of structural analysis enables the designer to detect stress, vibration, and thermal problems during the design process and to evaluate design changes before the construction of a possible prototype. Thus confidence in the acceptability of the prototype is enhanced. Moreover, if used properly, the method can reduce the number of prototypes that need to be built [51].

4.4 Guidelines on element layout

4.4.1 Mesh refinement

Use a relatively fine (coarse) discretization in regions where you expect a high (low) gradient of strains and/or stresses. Regions to watch out for high gradients are:

- Near entrant corners, or sharply curved edges.
- In the vicinity of concentrated (point) loads, concentrated reactions, cracks and cutouts.
- In the interior of structures with abrupt changes in thickness, material properties or cross sectional areas [54].

Figure 4.6 shows some situations where a locally refined finite element discretization.

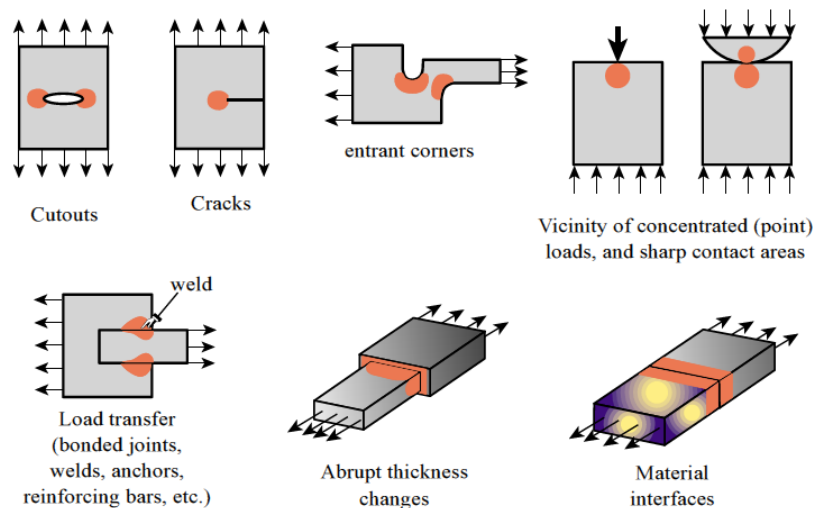


Figure 4.6. Some situations where a locally refined finite element discretization (in the red-colored areas) is recommended.

4.4.2 Element aspect ratios

When discretizing two and three dimensional problems, try to avoid finite elements of high aspect ratios: elongated or “skinny” elements, as the ones illustrated in figure 4.7. As a rough guideline, elements with aspect ratios exceeding 3 should be viewed with caution and those exceeding 10 with alarm.

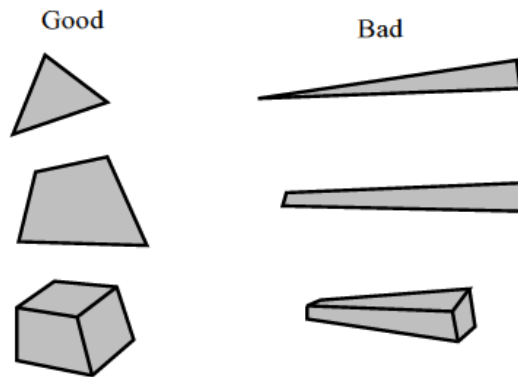


Figure 4.7. Elements of good and bad aspect ratios.

4.4.3. Physical interfaces

A physical interface, resulting from example from a change in material, should also be an interelement boundary. That is, elements must not cross interfaces. See figure 4.8.

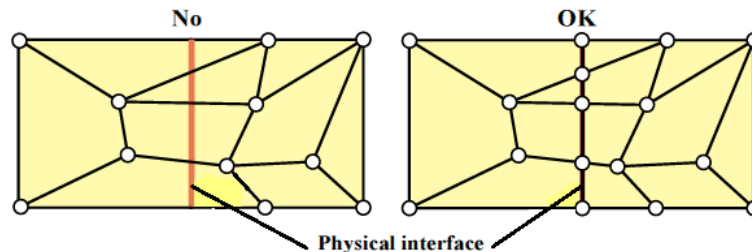


Figure 4.8 Illustration of the rule that elements should not cross material interfaces.

4.4.4. Preferred shapes

In two-dimensional FE modeling, if you have a choice between triangles and quadrilaterals with similar nodal arrangement, prefer quadrilaterals. Triangles are quite convenient for mesh generation, mesh transitions, rounding up corners, and the like. But sometimes triangles can be avoided altogether with some thought. In three dimensional FE modeling, prefer strongly bricks over wedges, and wedges over tetrahedra. The latter should be used only if there is no viable alternative. The main problem with tetrahedral

and wedges is that they can produce wrong stress results even if the displacement solution looks reasonable [54].

The aim of this section is not to provide a detailed description of FE theory which can be found in many textbooks but to give a brief outline of the basic principles involved to enable the reader with little or no knowledge of the FE method to have some appreciation of the method in relation to simple problems and the procedure by which more complex FE models are constructed and analyzed. Brief characteristics of the elements used within the work in this thesis will also be discussed.

To simplify the explanation of the theory a two-dimensional plate problem will be considered, taking one element from that. It can be appreciated that for larger problems, the formulation can be simply built up by repetition.

4.5 Plane stress and plane strain stiffness equations

Two-dimensional (planar) elements are defined by three or more nodes in a two-dimensional plane (that is, x-y). The elements are connected at common nodes and/or along common edges to form continuous structures such as those shown in figure 4.3 [51].

Membrane elements are among the simplest elements to develop. These elements are used for analyzing structures subjected to inplane forces. Assuming that the structure is in the xy plane, the displacements at any point of the structure are u , the translation in the x direction and v , the translation in the y direction. The stresses of interest are the normal stresses σ_x and σ_y and the shearing stress τ_{xy} . The normal stress in the direction perpendicular to the plane of structure is considered to be zero. Membrane elements are used to model the behavior.

We begin this section to give a reader some idea about with the development of the stiffness matrix for a basic two-dimensional or plane finite element, called the constant-strain triangular element. We consider the constant-strain triangle (CST) stiffness matrix because its derivation is the simplest among the available two-dimensional elements. The element is called a CST because it has a constant strain throughout it. We will derive the CST stiffness matrix by using the principle of minimum potential energy because the energy formulation is the most feasible for the development of the equations for both two- and three-dimensional finite elements.

4.5.1 Basic concepts of plane stress and plane strain

4.5.1.1 Plane stress

Plane stress is defined to be a state of stress in which the normal stress (σ_z) and the shear stresses (τ_{xz}, τ_{yz}) directed perpendicular to the plane are assumed to be zero. Generally, members that are thin (those with a small z dimension compared to the in-plane x and y dimensions) and whose loads act only in the x - y plane can be considered to be under plane stress. Plane stress analysis, which includes problems such as plates with holes, fillets, such as illustrated in figure 4.9.

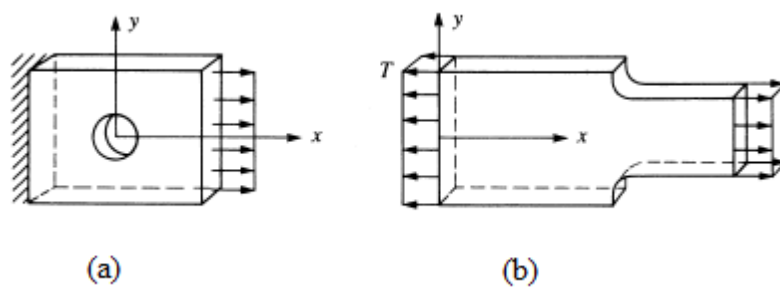


Figure 4.9. Plane stress problems: (a) Plate with hole; (b) Plate with fillet

4.5.1.2 Plane strain

Plane strain is defined to be a state of strain in which the strain normal to the x - y plane ϵ_z and the shear strains γ_{xz} and γ_{yz} are assumed to be zero. The assumptions of plane strain are realistic for long bodies (say, in the z direction) with constant cross-sectional area subjected to loads that act only in the x and/or y directions and do not vary in the z direction. Some plane strain examples are shown in figure 4.10. In these examples, only a unit thickness (1 mm. or 1 m) of the structure is considered because each unit thickness behaves identically (except near the ends).

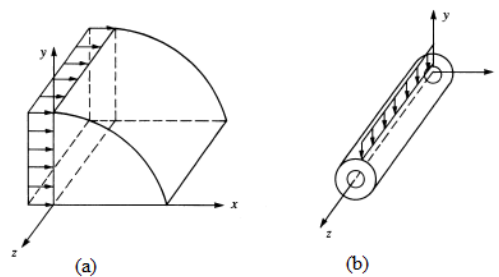


Figure 4.10. Plane strain problems: (a) dam subjected to horizontal loading; (b) pipe subjected to a vertical load

4.5.2 Two-dimensional state of stress and strain

Consider an infinitesimal element of the two-dimensional state of stress in the xy plane with thickness t along the z direction subjected to inplane stresses as shown in figure 4.11. The infinitesimal element has normal and shear stresses σ_x , σ_y , τ_{xy} and τ_{yx} .

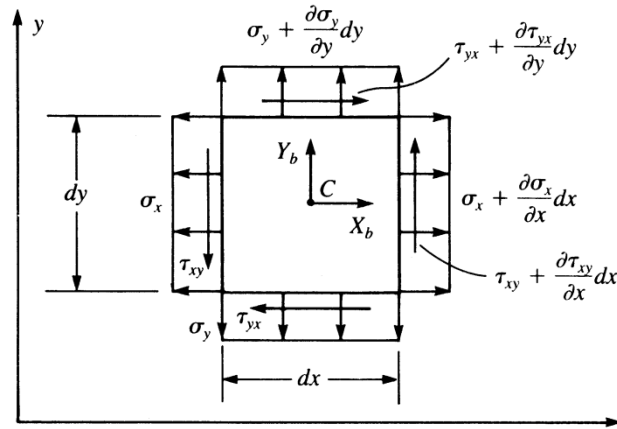


Figure 4.11. Plane differential element subjected to stresses

The equilibrium of forces in x direction ($\sum F_x = 0$) after simplifying and canceling terms, we obtain

$$\frac{\partial \sigma_x}{\partial x} + \frac{\partial \tau_{yx}}{\partial y} + X_b = 0 \quad (4.4)$$

Similarly, the equilibrium of forces in y direction ($\sum F_y = 0$)

$$\frac{\partial \sigma_y}{\partial y} + \frac{\partial \tau_{xy}}{\partial x} + Y_b = 0 \quad (4.5)$$

Equilibrium of moments of the element results in τ_{xy} being equal in magnitude to τ_{yx} ;

$$\tau_{xy} = \tau_{yx} \quad (4.6)$$

The three independent stresses can be represented by the vector column matrix as follows:

$$\{\sigma\} = \begin{Bmatrix} \sigma_x \\ \sigma_y \\ \tau_{xy} \end{Bmatrix} \quad (4.7)$$

Figure 4.12 shows an infinitesimal element used to represent the general two-dimensional state of strain at some point in a structure. The element is shown to be displaced by amounts u and v in the x and y directions at point A.

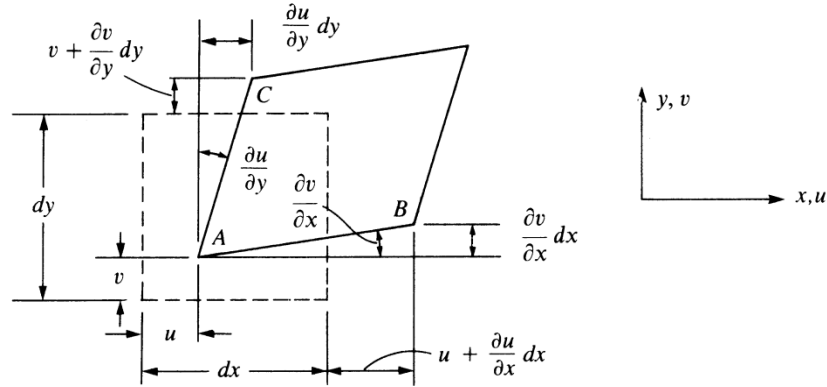


Figure 4.12. Displacements and rotations of lines of an element in the x-y plane.

From the general definitions of normal and shear strains and the use of figure 4.12, we get;

$$\varepsilon_{xx} = \frac{\partial u_x}{\partial x} \quad \varepsilon_{yy} = \frac{\partial u_y}{\partial y} \quad \varepsilon_{xy} = \frac{1}{2} \left(\frac{\partial u_x}{\partial y} + \frac{\partial u_y}{\partial x} \right) \quad (4.8)$$

The strains given by Eqs. (6.1.4) can be generally represented as the vector column matrix,

$$\{\varepsilon\} = \begin{Bmatrix} \varepsilon_x \\ \varepsilon_y \\ \varepsilon_{xy} \end{Bmatrix} \quad (4.9)$$

4.5.3 Stress/strain relationships

The three-dimensional stress/strain relationship for isotropic materials are given by [55],

$$\begin{aligned} \varepsilon_x &= \frac{1}{E} (\sigma_x - \nu \sigma_y - \nu \sigma_z) \\ \varepsilon_y &= \frac{1}{E} (\sigma_y - \nu \sigma_x - \nu \sigma_z) \\ \varepsilon_z &= \frac{1}{E} (\sigma_z - \nu \sigma_x - \nu \sigma_y) \\ \gamma_{xy} &= \frac{\tau_{xy}}{G}, \quad \gamma_{yz} = \frac{\tau_{yz}}{G}, \quad \gamma_{zx} = \frac{\tau_{zx}}{G} \end{aligned} \quad (4.10)$$

The stress/strain relationships for isotropic materials for plane stress can be derived as follows:

As we mentioned in previous sections that for plane stress, the following stresses are zero,

$$\sigma_z = \tau_{xz} = \tau_{yz} = 0 \quad (4.11)$$

The shear strains are:

$$\gamma_{xz} = \gamma_{yz} = 0 \quad \text{but} \quad \varepsilon_z \neq 0$$

For plane stress conditions, we then have

$$\begin{Bmatrix} \sigma_x \\ \sigma_y \\ \tau_{xy} \end{Bmatrix} = [D] \begin{Bmatrix} \varepsilon_x \\ \varepsilon_y \\ \gamma_{xy} \end{Bmatrix} \quad (4.12)$$

$$[D] = \frac{E}{1-\nu^2} \begin{bmatrix} 1 & \nu & 0 \\ \nu & 1 & 0 \\ 0 & 0 & \frac{1-\nu}{2} \end{bmatrix}$$

Where, $[D]$ is called the stress/strain matrix (or constitutive matrix), E is the modulus of elasticity, and ν is Poisson's ratio.

For plane strain, we assume the following strains to be zero,

$$\varepsilon_z = \gamma_{xz} = \gamma_{yz} = 0 \quad (4.13)$$

Applying Eq. (4.13) to the three-dimensional stress/strain relationship Eq. (4.10), the shear stresses $\tau_{xz} = \tau_{yz} = 0$, but $\sigma_z \neq 0$. The stress/strain matrix then becomes,

$$[D] = \frac{E}{(1+\nu)(1-2\nu)} \begin{bmatrix} 1-\nu & \nu & 0 \\ \nu & 1-\nu & 0 \\ 0 & 0 & \frac{1-2\nu}{2} \end{bmatrix} \quad (4.14)$$

4.6. Finite element theory

The aim of this section is to provide some description of FE theory and to give a brief outline of the basic principles involved to enable the reader with little or no knowledge of the FE method to have some appreciation of the method in relation to some problems and the procedure by which more complex FE models are constructed and analyzed. Brief characteristics of the elements used within the work in this thesis will also be discussed. To simplify the explanation of the theory a two-dimensional plate problem will be considered, taking one element from that.

4.6.1. Constant strain triangle

The simplest triangular plane stress element is the constant strain triangle (CST). We use triangular elements because boundaries of irregularly shaped bodies can be closely

approximated in this way .This element has two inplane degrees of freedom at each node for a total of six degrees of freedom per element. The constant strain triangle is widely used for various analysis purposes. The nodes of the CST element are numbered in a counterclockwise direction as shown in figure. 4.13. Remember that a consistent numbering procedure for the whole body is necessary to avoid problems in the calculations such as negative element areas.

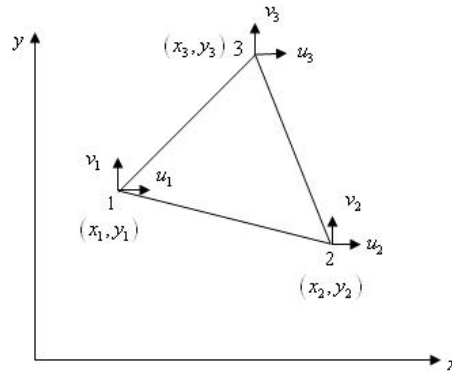


Figure 4.13. Constant Strain Triangle (CST).

Here (x_1, y_1) , (x_2, y_2) and (x_3, y_3) are the known nodal coordinates of nodes 1; 2, and 3, respectively. The procedure for deriving the stiffness matrix of the constant strain triangle element is as follows [58],

The nodal displacement matrix is given by

$$\{\delta\} = \begin{Bmatrix} \delta_1 \\ \delta_2 \\ \delta_3 \end{Bmatrix} = \begin{Bmatrix} u_1 \\ v_2 \\ u_1 \\ v_2 \\ u_1 \\ v_2 \end{Bmatrix} \quad (4.15)$$

The assumed displacement field can be written as,

$$\begin{aligned} u(x, y) &= a_1 + a_2x + a_3y \\ v(x, y) &= a_4 + a_5x + a_6y \end{aligned} \quad (4.16)$$

Where $u(x, y)$ and $v(x, y)$ describe displacements at any interior point (x, y) of the element. The above equations can be written in matrix form as,

$$\begin{Bmatrix} u \\ v \end{Bmatrix} = \begin{bmatrix} 1 & x & y & 0 & 0 & 0 \\ 0 & 0 & 0 & 1 & x & y \end{bmatrix} \begin{Bmatrix} a_1 \\ a_2 \\ a_3 \\ a_4 \\ a_5 \\ a_6 \end{Bmatrix} \quad (4.17)$$

Or $\{U(x, y)\} = [X]\{a\}$

From strain-displacement relationships the following results can be obtained,

$$\varepsilon_x = \frac{\partial u}{\partial x} = a_2,$$

$$\varepsilon_y = \frac{\partial v}{\partial y} = a_6,$$

And,

$$\gamma_{xy} = \frac{\partial u}{\partial y} + \frac{\partial v}{\partial x} = a_3 + a_5 \quad (4.18)$$

The element is called the constant strain triangle, because it is clear from the above equations that the term a_2 represents a constant strain in the x direction, and the term a_6 represents a constant strain in the y direction. Also the term $a_3 + a_5$ represents a uniform shear strains. The terms a_1 and a_4 represents rigid body translation.

To obtain the a's in Eqs. (4.17), we begin by substituting the coordinates of the nodal points into Eqs. (4.17) to yield

$$\begin{aligned} u_1 &= u(x_1, y_1) = a_1 + a_2x_1 + a_3y_1 \\ v_1 &= v(x_1, y_1) = a_4 + a_5x_1 + a_6y_1 \\ u_2 &= u(x_2, y_2) = a_1 + a_2x_2 + a_3y_2 \\ v_2 &= v(x_2, y_2) = a_4 + a_5x_2 + a_6y_2 \\ u_3 &= u(x_3, y_3) = a_1 + a_2x_3 + a_3y_3 \\ v_3 &= v(x_3, y_3) = a_4 + a_5x_3 + a_6y_3 \end{aligned} \quad (4.19)$$

We can put Eqs. (4.19) in matrix form as

$$\begin{Bmatrix} u_1 \\ v_1 \\ u_2 \\ v_2 \\ u_3 \\ v_3 \end{Bmatrix} = \begin{bmatrix} 1 & x_1 & y_1 & 0 & 0 & 0 \\ 0 & 0 & 0 & 1 & x_1 & y_1 \\ 1 & x_2 & y_2 & 0 & 0 & 0 \\ 0 & 0 & 0 & 1 & x_2 & y_2 \\ 1 & x_3 & y_3 & 0 & 0 & 0 \\ 0 & 0 & 0 & 1 & x_3 & y_3 \end{bmatrix} \begin{Bmatrix} a_1 \\ a_2 \\ a_3 \\ a_4 \\ a_5 \\ a_6 \end{Bmatrix} \quad (4.20)$$

$$\{u\} = [C]\{a\} \quad (4.21)$$

Where, $[C] = \begin{bmatrix} 1 & x_1 & y_1 & 0 & 0 & 0 \\ 0 & 0 & 0 & 1 & x_1 & y_1 \\ 1 & x_2 & y_2 & 0 & 0 & 0 \\ 0 & 0 & 0 & 1 & x_2 & y_2 \\ 1 & x_3 & y_3 & 0 & 0 & 0 \\ 0 & 0 & 0 & 1 & x_3 & y_3 \end{bmatrix} \quad (4.22)$

It should be noted that all the terms in matrix $[C]$ are known since they simply consist of the coordinates of the element nodes.

The coefficients $\{a\}$ are obtained by inverting Equation (4.21),

$$\{a\} = [C]^{-1}\{u\} \quad (4.23)$$

From equation (4.17),

$$\{U(x, y)\} = [X]\{a\} \quad (4.24)$$

Thus,

$$\{U(x, y)\} = [X][C]^{-1}\{u\} \quad (4.25)$$

Where, $[X][C]^{-1}$ represents the shape functions $[N]$.

Hence,

$$[N] = [X][C]^{-1} \quad (4.26)$$

Then, Equation (4.25) becomes

$$\{U(x, y)\} = [N]\{u\} \quad (4.27)$$

Inverting the $[C]$ matrix in Equation (4.21) and solving for $\{a\}$ gives,

$$\begin{Bmatrix} a_1 \\ a_2 \\ a_3 \\ a_4 \\ a_5 \\ a_6 \end{Bmatrix} = \frac{1}{2A^e} \begin{bmatrix} x_2y_3 - x_3y_2 & 0 & -x_1y_3 + x_3y_1 & 0 & x_1y_2 - x_2y_1 & 0 \\ y_2 - y_3 & 0 & y_3 - y_1 & 0 & y_1 - y_2 & 0 \\ x_3 - x_2 & 0 & x_1 - x_3 & 0 & x_2 - x_1 & 0 \\ 0 & x_2y_3 - x_3y_2 & 0 & -x_1y_3 + x_3y_1 & 0 & x_1y_2 - x_2y_1 \\ 0 & y_2 - y_3 & 0 & y_3 - y_1 & 0 & y_1 - y_2 \\ 0 & x_3 - x_2 & 0 & x_1 - x_3 & 0 & x_2 - x_1 \end{bmatrix} \begin{Bmatrix} u_1 \\ v_1 \\ u_2 \\ v_2 \\ u_3 \\ v_3 \end{Bmatrix} \quad (4.28)$$

Where, A^e is the area of the triangle element and can be expressed as,

$$A^e = \frac{1}{2} \begin{vmatrix} 1 & x_1 & y_1 \\ 1 & x_2 & y_2 \\ 1 & x_3 & y_3 \end{vmatrix} \quad (4.29)$$

$$A^e = \frac{1}{2} [(x_2y_3 - x_3y_2) - (x_1y_3 - x_3y_1) + (x_1y_2 - x_2y_1)] \quad (4.30)$$

by combining Equations (6.2.8) and (6.2.9), we can obtain the shape functions as follows;

$$\{N\} = \begin{bmatrix} 1 & x & y & 0 & 0 & 0 \\ 0 & 0 & 0 & 1 & x & y \end{bmatrix} \times \frac{1}{2A^e} \begin{bmatrix} x_2y_3 - x_3y_2 & 0 & -x_1y_3 + x_3y_1 & 0 & x_1y_2 - x_2y_1 & 0 \\ y_2 - y_3 & 0 & y_3 - y_1 & 0 & y_1 - y_2 & 0 \\ x_3 - x_2 & 0 & x_1 - x_3 & 0 & x_2 - x_1 & 0 \\ 0 & x_2y_3 - x_3y_2 & 0 & -x_1y_3 + x_3y_1 & 0 & x_1y_2 - x_2y_1 \\ 0 & y_2 - y_3 & 0 & y_3 - y_1 & 0 & y_1 - y_2 \\ 0 & x_3 - x_2 & 0 & x_1 - x_3 & 0 & x_2 - x_1 \end{bmatrix} \quad (4.30)$$

Equation (4.30) can be written in a simple form as follows;

$$[N] = \begin{bmatrix} N_1(x, y) & 0 & N_2(x, y) & 0 & N_3(x, y) & 0 \\ 0 & N_1(x, y) & 0 & N_2(x, y) & 0 & N_3(x, y) \end{bmatrix} \quad (4.31)$$

Where,

$$\begin{Bmatrix} N_1(x, y) \\ N_2(x, y) \\ N_3(x, y) \end{Bmatrix} = \frac{1}{2A^e} \begin{bmatrix} (x_2y_3 - x_3y_2) + x(y_2 - y_3) + y(x_3 - x_2) \\ (-x_1y_3 + x_3y_1) + x(y_3 - y_1) + y(x_1 - x_3) \\ (x_1y_2 - x_2y_1) + x(y_1 - y_2) + y(x_2 - x_1) \end{bmatrix} \quad (4.32)$$

The displacements can now be rewritten in terms of the shape functions as,

$$\begin{Bmatrix} u \\ v \end{Bmatrix} = \begin{Bmatrix} u(x, y) \\ v(x, y) \end{Bmatrix} = \begin{bmatrix} N_1(x, y) & 0 & N_2(x, y) & 0 & N_3(x, y) & 0 \\ 0 & N_1(x, y) & 0 & N_2(x, y) & 0 & N_3(x, y) \end{bmatrix} \begin{Bmatrix} u_1 \\ v_2 \\ u_1 \\ v_2 \\ u_1 \\ v_2 \end{Bmatrix} \quad (4.33)$$

The normal and shearing strains can be obtained from the strain-displacement relationships,

$$\begin{aligned} \varepsilon_x &= \frac{\partial u}{\partial x} = \frac{\partial}{\partial x} \sum_{i=1}^3 (N_i(x, y) u_i) \\ \varepsilon_{xy} &= \frac{\partial v}{\partial y} = \frac{\partial}{\partial y} \sum_{i=1}^3 (N_i(x, y) v_i) \\ \gamma_{xy} &= \left(\frac{\partial u}{\partial y} + \frac{\partial v}{\partial x} \right) = \frac{\partial}{\partial y} \sum_{i=1}^3 (N_i(x, y) u_i) + \frac{\partial}{\partial x} \sum_{i=1}^3 (N_i(x, y) v_i) \end{aligned} \quad (4.34)$$

The above equations can be written in matrix form as,

$$\begin{Bmatrix} \varepsilon_x \\ \varepsilon_y \\ \gamma_{xy} \end{Bmatrix} = \frac{1}{2A^e} \begin{bmatrix} \frac{\partial N_1}{\partial x} & 0 & \frac{\partial N_2}{\partial x} & 0 & \frac{\partial N_3}{\partial x} & 0 \\ 0 & \frac{\partial N_1}{\partial y} & 0 & \frac{\partial N_2}{\partial y} & 0 & \frac{\partial N_3}{\partial y} \\ \frac{\partial N_1}{\partial y} & \frac{\partial N_1}{\partial x} & \frac{\partial N_2}{\partial y} & \frac{\partial N_2}{\partial x} & \frac{\partial N_3}{\partial y} & \frac{\partial N_3}{\partial x} \end{bmatrix} \begin{Bmatrix} u_1 \\ v_2 \\ u_1 \\ v_2 \\ u_1 \\ v_2 \end{Bmatrix} \quad (4.35)$$

Eq.4.35 can be rewritten as follows,

$$\{\varepsilon_x(x, y)\}_{3 \times 1} = [B(x, y)]_{3 \times 6} \{u_i\}_{6 \times 1} \quad (4.36)$$

By taking the derivatives of the shape functions (Equation 4.32) with respect to x and y , gives the strain-displacement matrix [B],

$$[B(x, y)] = \frac{1}{2A^e} \begin{bmatrix} y_2 - y_3 & 0 & y_3 - y_1 & 0 & y_1 - y_2 & 0 \\ 0 & x_3 - x_2 & 0 & x_1 - x_3 & 0 & x_2 - x_1 \\ x_3 - x_2 & y_2 - y_3 & x_1 - x_3 & y_3 - y_1 & x_2 - x_1 & y_1 - y_2 \end{bmatrix} \quad (4.37)$$

The stiffness matrix of the element $[k^e]$ can be found by using the strain-displacement matrix [B] and the material matrix [D],

4.6.2 Plate bending element

The plate element is one of the more important structural elements and is used to model and analyze such structures as pressure vessels, chimney stacks, and automobile parts. A plate can be considered the two-dimensional extension of a beam in simple bending. Both beams and plates support loads transverse or perpendicular to their plane and through bending action (see figure 4.14). A plate is flat (if it was curved, it would become a shell). A beam has a single bending moment resistance, while a plate resists bending about two axes and has a twisting moment [51].

The plate surfaces are at $z = \pm t/2$, and its midsurface is at $z = 0$. The assumed basic geometry of the plate is as follows:

- (1) The plate thickness is much smaller than its inplane dimensions b and c (that is, $t \ll b$ or c). (If t is more than about one-tenth the span of the plate, then transverse shear deformation must be accounted for and the plate is then said to be thick.)
- (2) The deflection w is much less than the thickness t (that is, $w \ll t$).

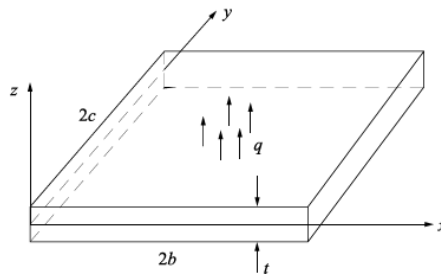


Figure 4.14. Thin plate subjected to transverse loading.

4.6.2.1 Finite elements for plates

A plate is a thin solid and might be modeled by 3D solid elements (figure 4.15 -a). But a solid element is wasteful of d.o.f, as it computes transverse normal stress and transverse shear stress, all of which are considered negligible in a thin plate [56].

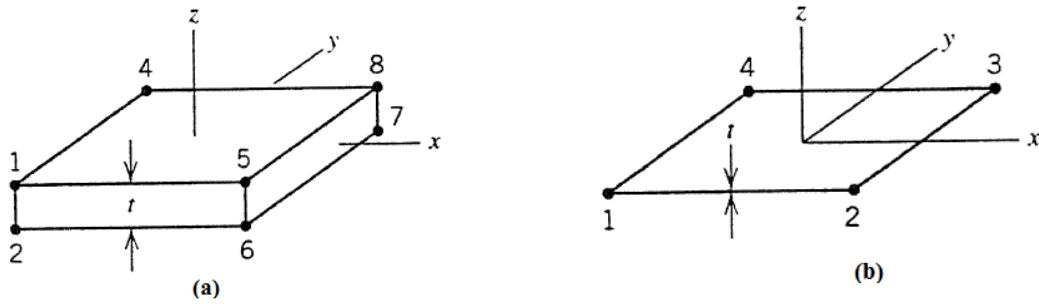


Figure 4.15 (a) A 3D solid element (b) Plate Element.

In figure 4.15- b, thickness t may appear to be zero, but it is used in formulating element stiffness matrices.

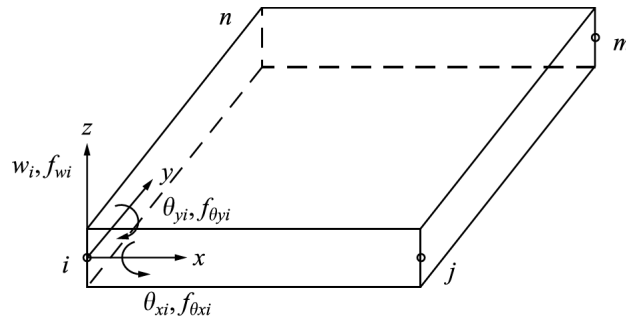


Figure 4.16. Rectangular plate element with nodal degrees of freedom

The flat-plate bending element has three degrees of freedom at each node, namely two rotations and the transverse deflection. The lateral deflection is denoted by w , the rotation about x -axis is denoted by θ_x and the rotation about y -axis is denoted by θ_y . The element has twelve degrees of freedom as shown in figure 4.16. The nodal displacement matrix at node i is given by

$$\{\delta_i\} = \begin{Bmatrix} w_i \\ \theta_{xi} \\ \theta_{yi} \end{Bmatrix} \quad (4.42)$$

The two slopes θ_x and θ_y the rotations are related to the lateral displacement w by the expressions,

$$\theta_x = +\frac{\partial w}{\partial y} \text{ and } \theta_y = -\frac{\partial w}{\partial x} \quad (4.43)$$

The total element displacement matrix is now given by,

$$\{\delta\} = \begin{Bmatrix} \delta_i \\ \delta_j \\ \delta_m \\ \delta_n \end{Bmatrix} \quad (4.44)$$

Since the element has 12 degrees of freedom, 12 undetermined constants must be employed in the polynomial expression chosen to represent w . A suitable function is given in Eq 4.45,

$$w = a_1 + a_2x + a_3y + a_4x^2 + a_5xy + a_6y^2 + a_7x^3 + a_8x^2y + a_9xy^2 + a_{10}y^3 + a_{11}x^3y + a_{12}xy^3 \quad (4.45)$$

We can get the constants a_0 through a_{11} by expressing the 12 simultaneous equations linking the values of w and its slopes at the nodes when the coordinates take up their appropriate values. First, we write,

$$\{\delta\} = \begin{Bmatrix} w_i \\ \theta_{xi} \\ -\theta_{yi} \\ w_j \\ \theta_{xj} \\ \vdots \\ \vdots \end{Bmatrix} = \begin{bmatrix} 1 & x & y & x^2 & xy & y^2 & x^3 & x^2y & xy^2 & y^3 & x^3y & xy^3 \\ 0 & 0 & 1 & 0 & x & 2y & 0 & x^2 & 2xy & 3y^2 & x^3 & xy^2 \\ 0 & -1 & 0 & -2x & -y & 0 & -3x^2 & -2xy & -y^2 & 0 & -3x^2y & -y^3 \\ \vdots & & & & & & & & & & & \\ \vdots & \dots \end{bmatrix} \times \begin{Bmatrix} a_1 \\ a_2 \\ a_3 \\ a_4 \\ a_5 \\ a_6 \\ a_7 \\ a_8 \\ a_9 \\ a_{10} \\ a_{11} \\ a_{12} \end{Bmatrix} \quad (4.46)$$

or in simple matrix form the degrees of freedom matrix is,

$$\{\psi\} = [P]_{3 \times 12} \{a\}_{12 \times 1} \quad (4.47)$$

Next, we evaluate Eq. (4.46) at each node point as follows;

$$\begin{aligned}
 & \begin{pmatrix} w \\ + \frac{\partial w}{\partial y} \\ \frac{\partial w}{\partial x} \end{pmatrix} \\
 &= \begin{bmatrix} 1 & x & y & x^2 & xy & y^2 & x^3 & x^2y & xy^2 & y^3 & x^3y & xy^3 \\ 0 & 0 & 1 & 0 & x & 2y & 0 & x^2 & 2xy & 3y^2 & x^3 & xy^2 \\ 0 & -1 & 0 & -2x & -y & 0 & -3x^2 & -2xy & -y^2 & 0 & -3x^2y & -y^3 \end{bmatrix} \\
 & \times \begin{pmatrix} a_1 \\ a_2 \\ a_3 \\ a_4 \\ a_5 \\ a_6 \\ a_7 \\ a_8 \\ a_9 \\ a_{10} \\ a_{11} \\ a_{12} \end{pmatrix} \\
 & \tag{4.48}
 \end{aligned}$$

Equation (4.48) can be written in a simple form as follows,

$$\{\delta\} = [C]\{a\} \tag{4.49}$$

Where, $[C]$ is the 12×12 matrix. Therefore, the constants (a's) can be solved for by

$$\{a\} = [C]^{-1}\{\delta\} \tag{4.50}$$

$$\text{Equation (4.47) can now be written as } \{\psi\} = [P][C]^{-1}\{\delta\} \tag{4.51}$$

$$\text{Or } r\{\psi\} = [N]\{\delta\} \tag{4.52}$$

Where, $[N] = [P][C]^{-1}$ is the shape function matrix. The strain (curvature)/displacement and stress (moment)/curvature relationships are given by [51],

$$\{\kappa\} = \begin{pmatrix} \kappa_x \\ \kappa_y \\ \kappa_{xy} \end{pmatrix} = \begin{pmatrix} -2a_4 - 6a_7x - a_8y - \\ -2a_6 - 2a_9x - 6a_{10}y - 6a_{12}xy \\ -2a_5 - 4a_8x - 4a_9y - 6a_{11}x^2 - 6a_{12}y^2 \end{pmatrix} \tag{4.52}$$

Eq. (4.52) can be expressed in matrix form as follows,

$$\{\kappa\} = [Q]\{a\} \tag{4.53}$$

Where, $[Q]$ is the coefficient matrix multiplied by the a's in Eq. (4.52). Using Eq. (4.50) for $\{a\}$, we express the curvature matrix as,

$$\{\kappa\} = [B]\{\delta\} \tag{4.54}$$

Where,

$$[B] = [Q][C]^{-1} \tag{4.55}$$

The moment/curvature matrix for a plate is given by

$$\{M\} = \begin{Bmatrix} M_x \\ M_y \\ M_{xy} \end{Bmatrix} = [D] \begin{Bmatrix} \kappa_x \\ \kappa_y \\ \kappa_{xy} \end{Bmatrix} = [D][B]\{\delta\} \quad (4.56)$$

Where the [D] matrix is the constitutive matrix given for isotropic materials by

$$[D] = \frac{Et^3}{12(1-\nu^2)} \begin{bmatrix} 1 & \nu & 0 \\ \nu & 1 & 0 \\ 0 & 0 & \frac{1-\nu}{2} \end{bmatrix} \quad (4.57)$$

The Element Stiffness Matrix can be derived by the usual form of the stiffness matrix as

$$[k^e]_{12 \times 12} = \iint [B]^T [D] [B] dx dy \quad (4.58)$$

Where $[k^e]$ is a rectangular element stiffness matrix.

The surface force matrix due to distributed loading q acting per unit area in the z direction is obtained using the standard equation, see [51].

$$\{F_s\} = \iint [N_s]^T q dx dy \quad (4.59)$$

For an element of dimensions $2b \times 2c$ subjected to a uniform q acting over the surface, Eq. (4.59) yields the forces and moments at node i as

$$\begin{Bmatrix} f_{w_i} \\ f_{\theta_{xi}} \\ f_{\theta_{yi}} \end{Bmatrix} = 4qcb \begin{Bmatrix} 1/4 \\ -c/12 \\ b/12 \end{Bmatrix} \quad (4.60)$$

Similarly for the nodes j, m and n . The element equations can be written as follows,

$$\begin{Bmatrix} f_{w_i} \\ f_{\theta_{xi}} \\ f_{\theta_{yi}} \\ \vdots \\ f_{\theta_{yn}} \end{Bmatrix} = \begin{bmatrix} k_{11} & k_{12} & k_{13} & k_{14} & \cdots & k_{1,12} \\ k_{21} & k_{22} & k_{23} & k_{24} & \cdots & k_{2,12} \\ k_{31} & k_{32} & k_{33} & k_{34} & \cdots & k_{3,12} \\ k_{41} & k_{42} & k_{43} & k_{44} & \cdots & k_{4,12} \\ \vdots & \vdots & \vdots & \vdots & \ddots & \vdots \\ k_{12,1} & k_{12,2} & k_{12,3} & k_{12,4} & \cdots & k_{12,12} \end{bmatrix} \begin{Bmatrix} w_i \\ \theta_{xi} \\ \theta_{yi} \\ \vdots \\ \theta_{yn} \end{Bmatrix} \quad (4.61)$$

The rest of the steps, including assembling the global equations, applying boundary conditions, and solving the equations for the nodal displacements and slopes (note three degrees of freedom per node).

4.7 Shells

4.7.1 Shell element

Flat shell elements are obtained by combining plate elements with plate stress elements.

The geometry of a shell is defined by its thickness and its midsurface which is curved

surface in space. Load is carried by a combination of membrane action and bending action. A thin shell can be very strong if membrane action dominates. A shell of a given shape can carry a variety of distributed loadings by membrane action alone.

4.7.2 Finite elements for shells

The most direct way to obtain a shell element is to combine a membrane element and a bending element. Thus a simple triangular shell element can be obtained by combining the plane stress triangle with the plate bending triangle. The resulting element is flat and has five or six degrees of freedom per node, depending on whether or not the shell-normal rotation θ_{zi} at node i is present in plane stress element. A quadrilateral shell element can be produced in similar way, by combining quadrilateral plane and plate elements. The shell element can also be formulated using the usual method of defining shape functions, substituting into the constitutive equations, and thus obtaining the element matrices.

Advantages of a flat element include simplicity of element formulation, simplicity in the description of element geometry, and the elements ability to represent a rigid body motion without strain. Disadvantage includes the representation of a smoothly curved shell surface by flat or slightly warped facets, so that there are fold lines where elements meet. There is discretization error associated with the lack of coupling between membrane and bending actions within individual elements. Membrane – bending coupling arises globally because adjacent elements are not coplanar: membrane force in one element is transferred to neighboring element with an element normal component, which produces bending. Discretization error can be reduced by using smaller elements. Common advice is that a flat shell element should span no more than roughly 10° of the arc of the actual shell [56].

Since the plate structure can be treated as a special case of the shell structure, it is common practice to use a shell element offered in a commercial FE package to analyze plate structures. Shell structures are usually curved. We assume that the shell structure is divided into shell elements that are flat. The curvature of the shell is then followed by changing the orientation of the shell elements in space. Therefore, if the curvature of the shell is very large, a fine mesh of elements has to be used [57].

There are six DOFs at a node for a shell element: three translational displacements in the x, y and z directions, and three rotational deformations with respect to the x, y and z

axes. Figure 4.17 shows the middle plane of a rectangular shell element and the DOFs at the nodes. The generalized displacement vector for the element can be written as

$$\{\delta_e\} = \begin{cases} \delta_{e1} \\ \delta_{e2} \\ \delta_{e3} \\ \delta_{e4} \end{cases} \begin{matrix} \text{node1} \\ \text{node2} \\ \text{node3} \\ \text{node4} \end{matrix} \quad (4.62)$$

$$\{\delta_{ei}\} = \begin{cases} u_i \\ v_i \\ w_i \\ \theta_{xi} \\ \theta_{yi} \\ \theta_{zi} \end{cases} \begin{matrix} \text{displacement in } x - \text{direction} \\ \text{displacement in } y - \text{direction} \\ \text{displacement in } z - \text{direction} \\ \text{rotation in } x - \text{direction} \\ \text{rotation in } y - \text{direction} \\ \text{rotation in } z - \text{direction} \end{matrix} \quad (4.63)$$

Where, δ_{ei} ($i = 1, 2, 3, 4$) are the displacement vector at node i .

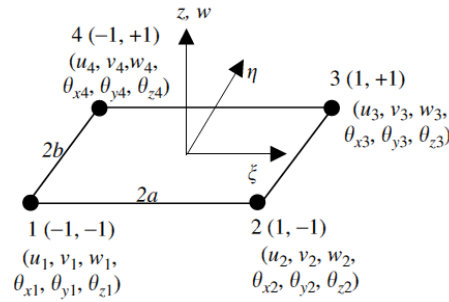


Figure 4.17. The middle plane of a rectangular shell element.

The stiffness matrix for the shell element can be formulated by combining the element stiffness matrix for membrane and element stiffness matrix for bending.

The membrane stiffness matrix can thus be expressed in the following form using sub-matrices according to the nodes:

$$[k_e^m] = \begin{bmatrix} k_{11}^m & k_{12}^m & k_{13}^m & k_{14}^m \\ k_{21}^m & k_{22}^m & k_{23}^m & k_{24}^m \\ k_{31}^m & k_{32}^m & k_{33}^m & k_{34}^m \\ k_{41}^m & k_{42}^m & k_{43}^m & k_{44}^m \end{bmatrix} \begin{matrix} \text{node1} \\ \text{node2} \\ \text{node3} \\ \text{node4} \end{matrix} \quad (4.64)$$

Where, the superscript m stands for the membrane matrix. Each sub-matrix will have a dimension of 2×2 , since it corresponds to the two DOFs u and v at each node.

The stiffness matrix for a rectangular plate element is used for the bending effects, corresponding to DOFs of w , and θ_x, θ_y . The bending stiffness matrix can thus be expressed in the following form using sub-matrices according to the nodes [57]:

$$[k_e^b] = \begin{bmatrix} k_{11}^b & k_{12}^b & k_{13}^b & k_{14}^b \\ k_{21}^b & k_{22}^b & k_{23}^b & k_{24}^b \\ k_{31}^b & k_{32}^b & k_{33}^b & k_{34}^b \\ k_{41}^b & k_{42}^b & k_{43}^b & k_{44}^b \end{bmatrix} \begin{matrix} \text{node1} \\ \text{node2} \\ \text{node3} \\ \text{node4} \end{matrix} \quad (4.65)$$

Where, the superscript b stands for the bending matrix. Each bending sub-matrix has a dimension of 3×3

The stiffness matrix for the shell element in the local coordinate system is then formulated by combining equations. (4.64) and (4.65):

$$[k_e] = \begin{bmatrix} k_{11}^m & 0 & 0 & k_{12}^m & 0 & 0 & k_{13}^m & 0 & 0 & k_{14}^m & 0 & 0 \\ 0 & k_{11}^b & 0 & 0 & k_{12}^b & 0 & 0 & k_{13}^b & 0 & 0 & k_{14}^b & 0 \\ 0 & 0 & 0 & 0 & 0 & 0 & 0 & 0 & 0 & 0 & 0 & 0 \\ k_{21}^m & 0 & 0 & k_{22}^m & 0 & 0 & k_{23}^m & 0 & 0 & k_{24}^m & 0 & 0 \\ 0 & k_{21}^b & 0 & 0 & k_{22}^b & 0 & 0 & k_{23}^b & 0 & 0 & k_{24}^b & 0 \\ 0 & 0 & 0 & 0 & 0 & 0 & 0 & 0 & 0 & 0 & 0 & 0 \\ k_{31}^m & 0 & 0 & k_{32}^m & 0 & 0 & k_{33}^m & 0 & 0 & k_{34}^m & 0 & 0 \\ 0 & k_{31}^b & 0 & 0 & k_{32}^b & 0 & 0 & k_{33}^b & 0 & 0 & k_{34}^b & 0 \\ 0 & 0 & 0 & 0 & 0 & 0 & 0 & 0 & 0 & 0 & 0 & 0 \\ k_{41}^m & 0 & 0 & k_{42}^m & 0 & 0 & k_{43}^m & 0 & 0 & k_{44}^m & 0 & 0 \\ 0 & k_{41}^b & 0 & 0 & k_{42}^b & 0 & 0 & k_{43}^b & 0 & 0 & k_{44}^b & 0 \\ 0 & 0 & 0 & 0 & 0 & 0 & 0 & 0 & 0 & 0 & 0 & 0 \end{bmatrix} \quad (4.66)$$

The stiffness matrix for a rectangular shell matrix has a dimension of 24×24 . Note that in Eq. (4.66), the components related to the DOF θ_z , are zeros. This is because there is no θ_z in the local coordinate system. If these zero terms are removed, the stiffness matrix would have a reduced dimension of 20×20 . However, using the extended 24×24 stiffness matrix will make it more convenient for transforming the matrix from the local coordinate system into the global coordinate system [57].

Chapter 5

Finite element modeling of the welded joints using beam elements

The purpose of this chapter is to develop a finite element model and obtain the analysis result that can be compared with analytical and experimental data. Hence, in most structural analysis applications, it is necessary to compute displacements and stresses at various points of interest. The finite element method is a very valuable tool for studying the behavior of structures. The finite element model is created by dividing the structure into a number of finite elements. Each element is interconnected by nodes. The selection of elements for modeling the structure depends upon the behavior and geometry of the structure being analyzed.

There are always situations where the models contain regions with complexity in geometry such as fillet welds which are extensively used in various fields such as in construction industry. Therefore, it is important to be able to represent the mechanical capacity of fillet-welded structures in numerical analyses for design purposes. Here a numerical investigation was undertaken on the performance of a series of fillet-welded connections in steel.

Accuracy and efficiency are two major concerns in any finite element analysis that are forcing engineers and design analysts to seek reliable and accurate yet economical methods to determine the behavior of structural components. These element types (beams, plates and shells) produce more computationally efficient models, thus reducing analyses time and cost. They also require less data and are easier to construct than solid models.

Beam elements allow for bending and stretching and are most useful in modelling of whole structure. They are available within Abaqus[59] in two different formats, in-plane (two displacement degrees of freedom and one in-plane rotational degree of freedom) and three dimensional where all six degrees of freedom are active. Numerical analyses were performed using the Abaqus[59]. The connections were modelled with beam and shell elements, see Figure 5.1. The beam and weld were modelled as beam element, while base plate was modelled using shell element.

In the modeling certain assumption were made to simplify the model. Parent metal and welded metal had the same material properties which are steel ($E = 210 \times 10^3 MPa, \nu = 0.3$)

5.1 Fillet weld

The stiffness of the welds in the fillet welded joints can be represented by increasing the thickness of the beam in the region of welded joints. Coupling of beams and shells has been considered and used in this thesis. Based on this technique for analyzing the stress variation over the cross-section of an interface, the Coupling constraint technique can be generated by Abaqus[59].

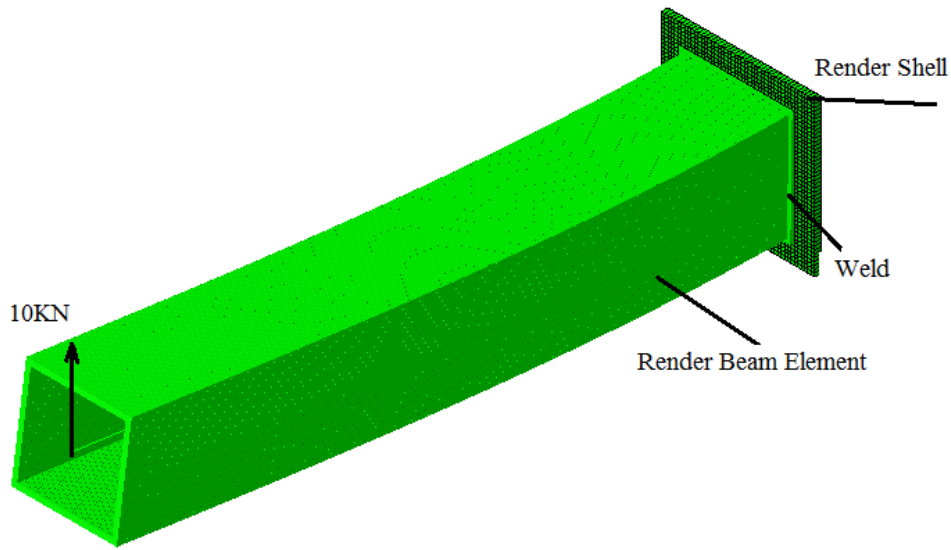
5.1.1 Finite element results of beam shell coupling of fillet weld in case of bending.

Beam elements require less data and are easier to construct than solid models and are thus especially suitable for conceptual design evaluation and optimization.

5.1.1.1 Rectangular Section

Figure 5.1 shows a cantilever rectangular hollow beam under the given loading of 10KN acting upward at the free end. Coupling of beam elements and shell elements were used with a full integration scheme.

Figure 5.2 shows that the finite element results of stress in the fillet weld is 55MPa, and the displacement at the free end is 1mm. From chapter 2, the analytical results of this beam is 59MPa. We can see that the finite element results are in good agreement with the analytical results. We can see that the analytical solution can be replaced by beam element solution to represent the fillet weld.



ODB: BeamShellCouplingWeld.odb Abaqus/Standard 6.10-1 Tue Jul 02 11:55:02
 Step: Step-1 Central Europe Daylight Time 2013
 Increment 1: Step Time = 1.000
 Deformed Var: U Deformation Scale Factor: +1.045e+02

Figure 5.1. General view of the Beam-shell coupling of rectangular section

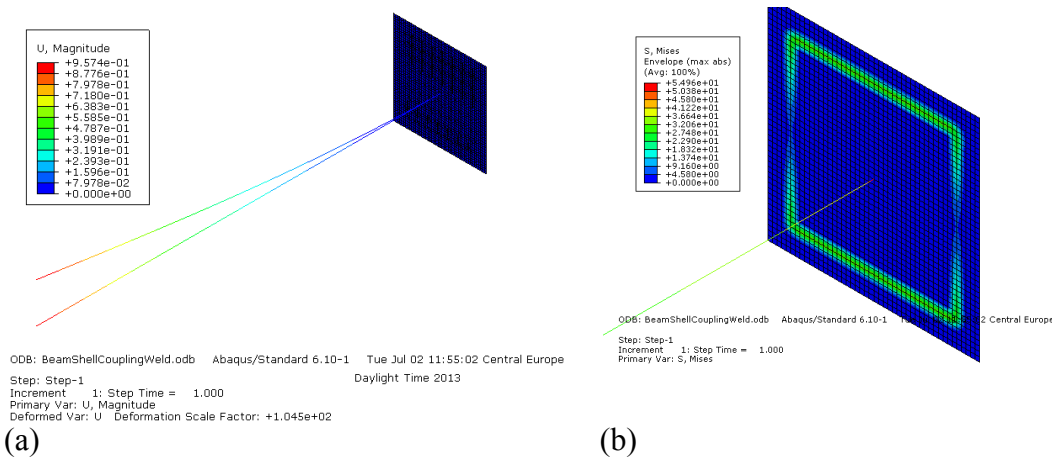


Figure 5.2. FE Results for a rectangular section a) Displacement b) Von Mises Stress

5.1.1.2 I section

Figure 5.3 shows a cantilever beam of I section profile under the given loading of 10kN acting upward at the free end. Coupling of beam elements and shell elements were used with a full integration scheme.

Figure 5.4 shows that the finite element results of stress in the fillet weld is 72.7MPa, and the displacement magnitude at the free end is 2.1mm. From chapter 2, the analytical

results of this beam is 71.2MPa. We can see that the finite element results verify the analytical solution. It is clear that the analytical solution can be replaced by beam element solution to represent the fillet weld.

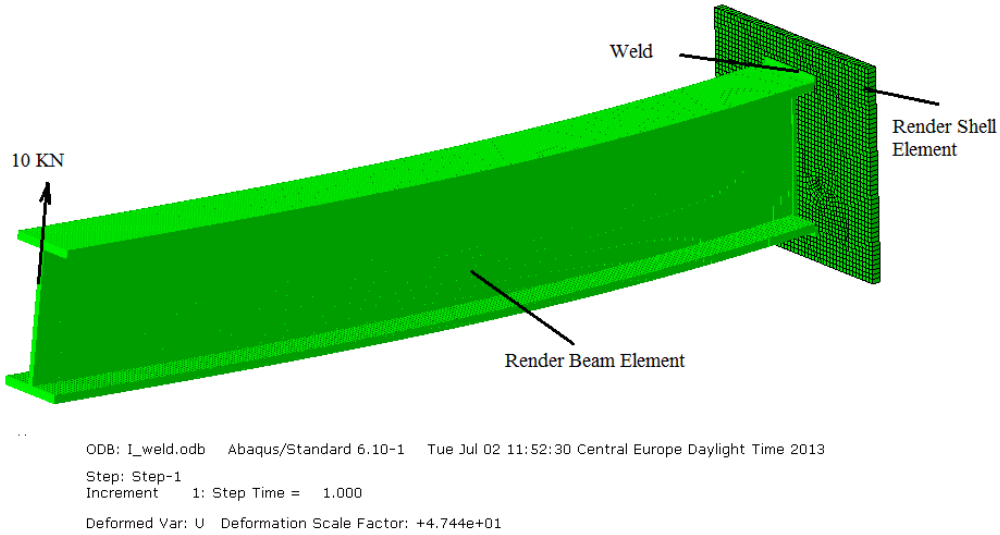


Figure 5.3. General view of the Beam-shell coupling of I- section

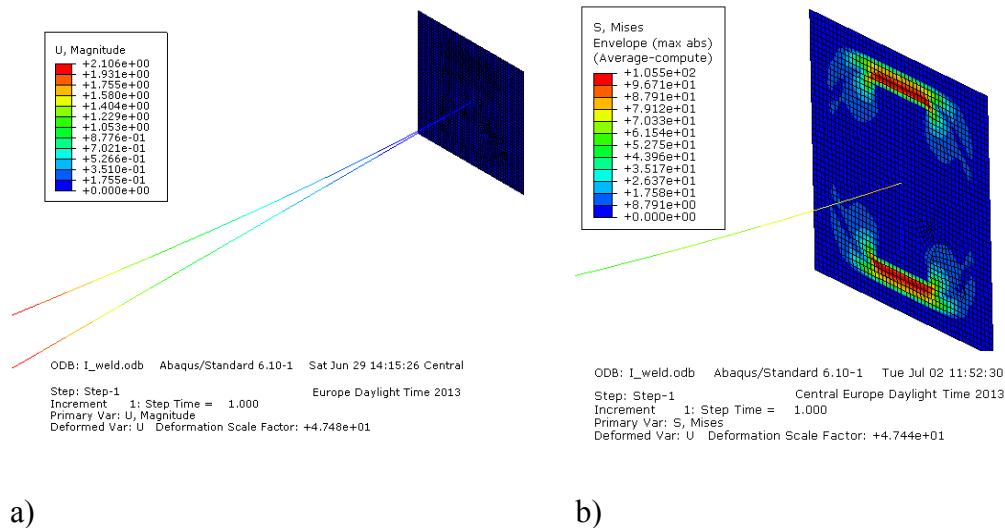


Figure 5.4. FE Results for a I- section a) Displacement b) Von Mises Stress

5.1.1.3. C- section

Figure 5.5 shows a cantilever beam of C section profile under the given loading of 10KN acting upward at the free end. Coupling of beam elements and shell elements were used with a full integration scheme.

Figure 5.6 shows that the finite element results of stress in the fillet weld is 78.8MPa, and the displacement magnitude at the free end is 3.3mm. From chapter 2, the analytical results of this beam is 73 MPa. We can see that the finite element results verify the analytical solution. It is clear that the analytical solution can be replaced by beam element solution to represent the fillet weld.

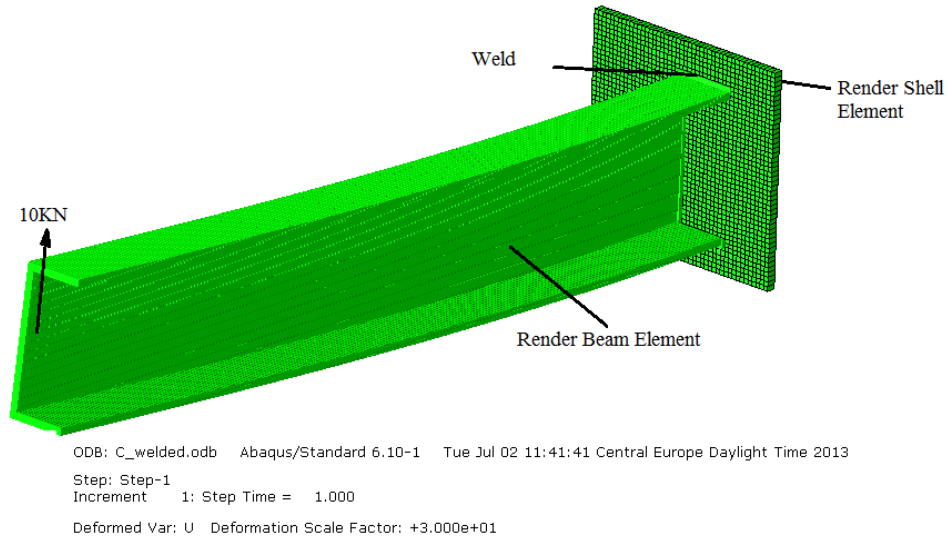
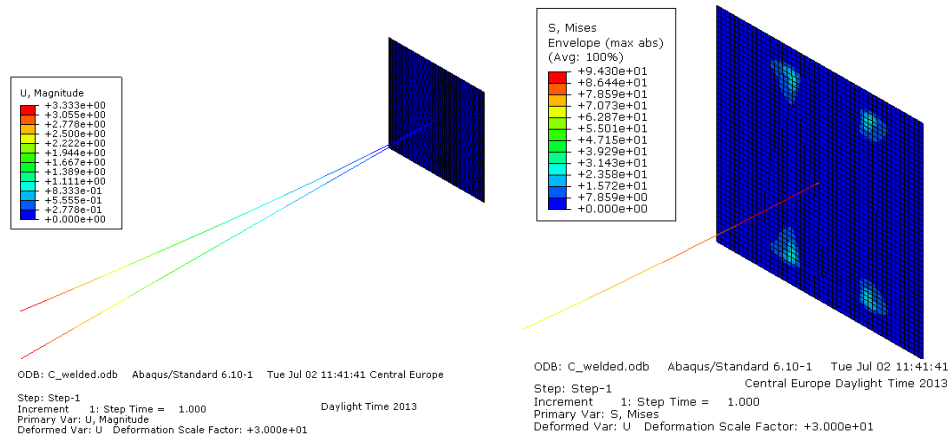


Figure 5.5. General view of the Beam-shell coupling of C- section



a)

b)

Figure 5.6. FE Results for a C- section a) Displacement b) Von Mises Stress

5.1.1.4 Circular- section

Figure 5.7 shows a cantilever beam of circular section profile under the given loading of 10KN acting upward at the free end. Coupling of beam elements and shell elements were used with a full integration scheme.

Figure 5.8 shows that the finite element results of stress in the fillet weld is 94.4MPa, and the displacement magnitude at the free end is 2.8mm. From chapter 2, the analytical results of this beam is 98.7 MPa. It is clear that the finite element results verify the analytical solution. We can see that the analytical solution can be replaced by beam element solution to represent the fillet weld.

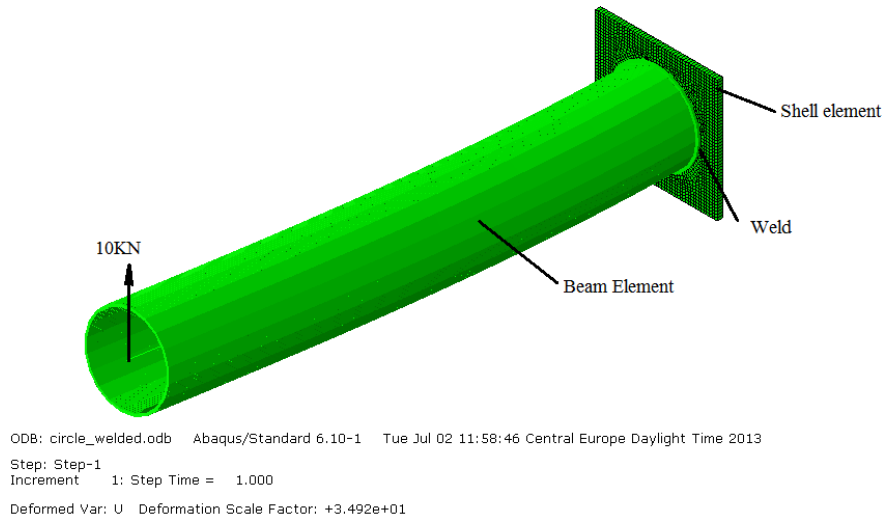


Figure 5.7. General view of the Beam-shell coupling of Circular- section

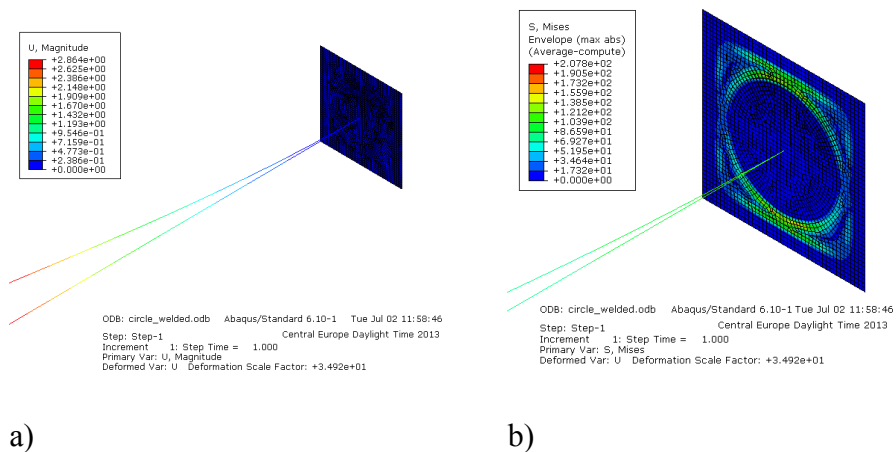


Figure 5.8. FE Results for a Circular- section a) Displacement b) Von Mises Stress

5.1.1.5 Z- section

Figure 5.9 shows a cantilever beam of Z section profile under the given loading of 10KN acting upward at the free end. Coupling of beam elements and shell elements were used with a full integration scheme.

Figure 5.10 shows that the finite element results of stress in the fillet weld is 156.5MPa, and the displacement magnitude at the free end is 9.9 mm. From chapter 2, the analytical result of this beam is 149.2MPa. It is clear that the finite element results verify the analytical solution. We can see that the analytical solution can be replaced by beam element solution to represent the fillet weld.

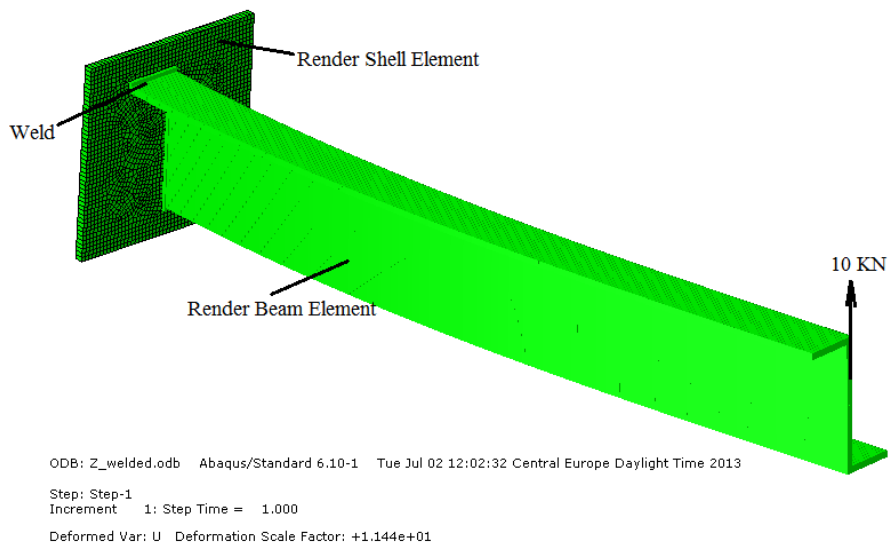


Figure 5.9. General view of the Beam-shell coupling of Z- section

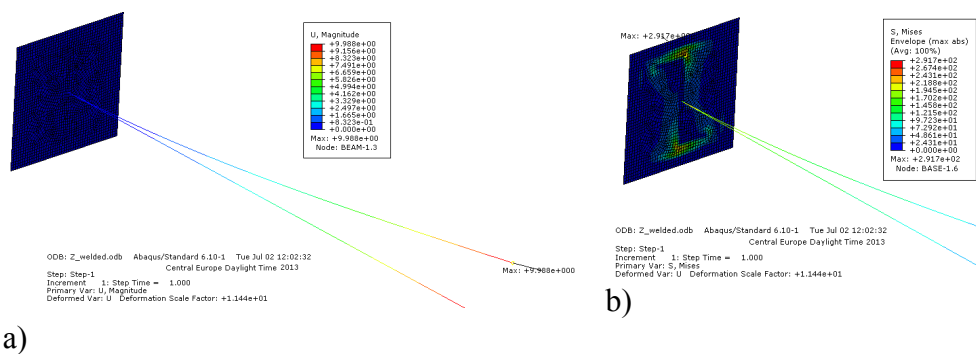


Figure 5.10. FE Results for a Z- section a) Displacement b) Von Mises Stress

5.1.1.6 X- section

Figure 5.11 shows a cantilever beam of X section profile under the given loading of 10KN acting upward at the free end. Coupling of beam elements and shell elements were used.

Figure 5.12 shows that the finite element results of stress in the fillet weld is 207.1MPa, and the displacement magnitude at the free end is 7.6 mm. From chapter 2, the analytical result of this beam is 181 MPa. It is clear that the finite element results verify the analytical solution. It can be seen that the analytical solution can be replaced by beam element solution to represent the fillet weld.

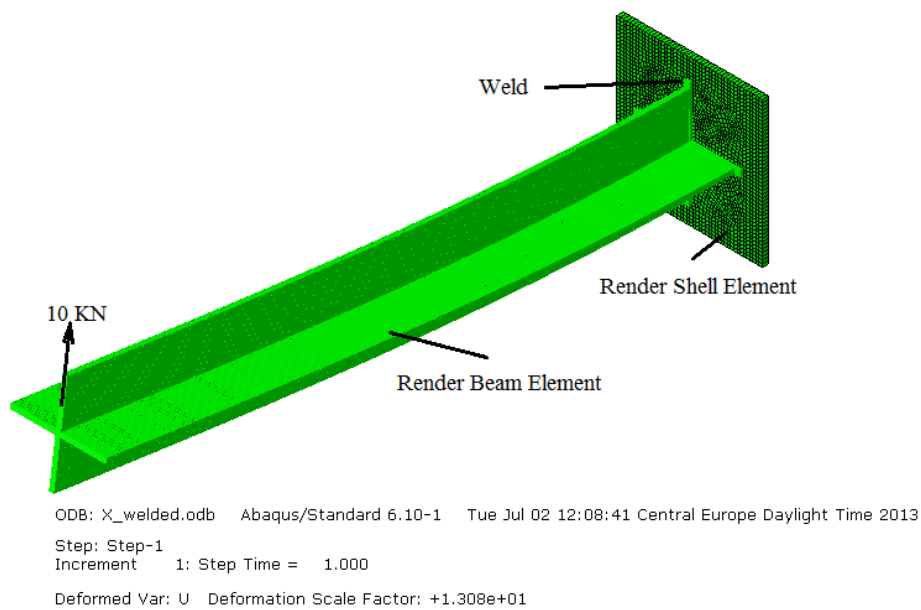


Figure 5.11. General view of the Beam-shell coupling of X- section

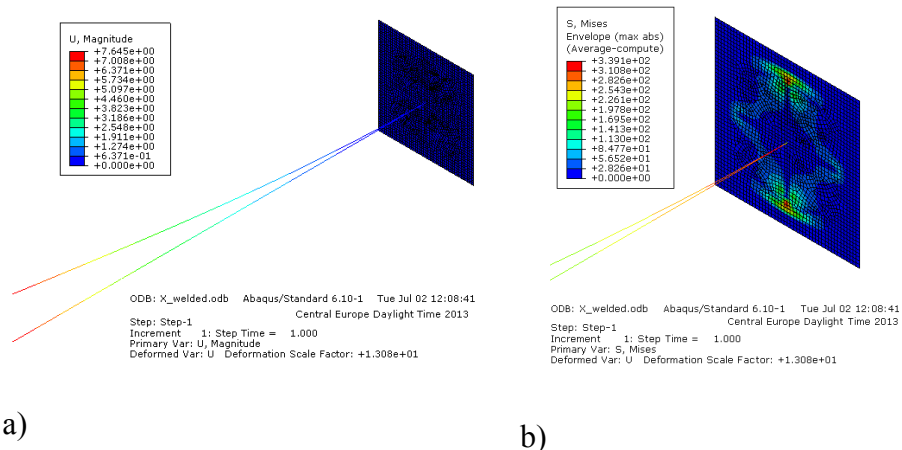


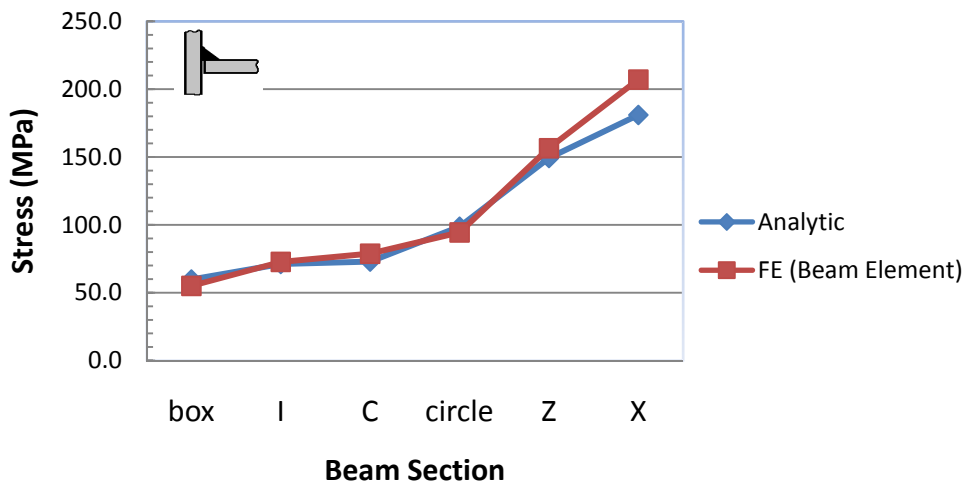
Figure 5.12. FE Results for a X- section a) Displacement b) Von Mises Stress

We can summarize the numerical results in Figures 5.1-12, in the following table:

Table. 5.1 Analytical and FE Results of beams of fillet weld (Bending Moment)

Specimen Fillet joint	Analytic Stress (MPa)	FE (Beam Element) Stress (MPa)
box	59.1	55.0
I	71.2	72.7
C	73.0	78.8
circle	98.7	94.4
Z	149.2	156.5
X	181.0	207.1

Numerical analyses were carried out to represent the mechanical performance of the welded beam-sections under bending. The study is summarized and concluded as follows. The predicted stress curves are in good agreement with the analytical results for all six cases of the beam members. As can be seen from the test Figures 5.13 the finite element results verify the analytical results.



Figures 5.13 stress of Analytic and finite Element Results of Various Beam Sections of fillet weld (Bending)

5.1.2 Finite element results of beam shell coupling of fillet weld in case of twisting

Figure 5.14 shows a cantilever beam of rectangular section profile under the given loading of 10KN acting upward at the free end. Coupling of beam elements and shell elements were used.

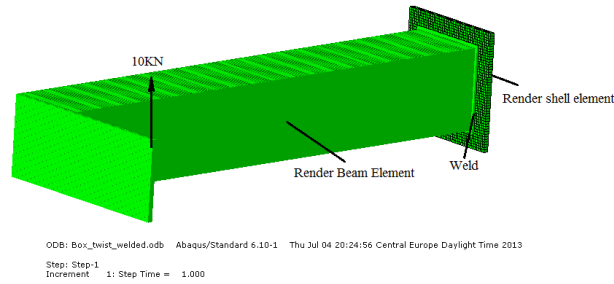


Figure 5.14. General view of the beam-shell coupling of rectangular cross- section (twisting)

The finite element and analytical results of box, I, C, circular, Z and X of fillet weld in case of twisting were summarized in figure 5.15.

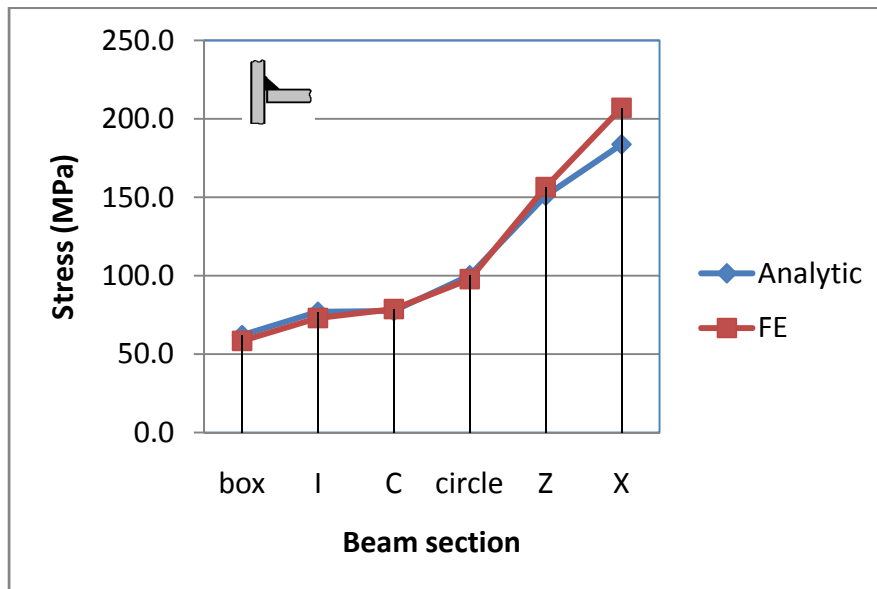


Figure 5.15. Stress of analytic and finite element results of various beam sections of fillet weld (twisting)

It is seen from Figure 5.15 that the predicted stress curves are in good agreement with the analytical results for all six cases of the beam members in case of twisting. It is observed from the same figure that the largest stress is found at the X beam cross section while the box beam profile has the smallest stress.

5.2. V welded joint

In this case, the weld thickness is equal to the beam thickness. Coupling of beams and shells has been considered and implemented in this section. The Coupling constraint technique of beam to shell can be generated by Abaqus [59].

5. 2.1 Finite element results of beam shell coupling of V-welded joint in case of bending.

Figure 5.16 shows a cantilever beam of rectangular section profile under the given loading of 10KN acting upward at the free end. Coupling of beam elements and shell elements were used.

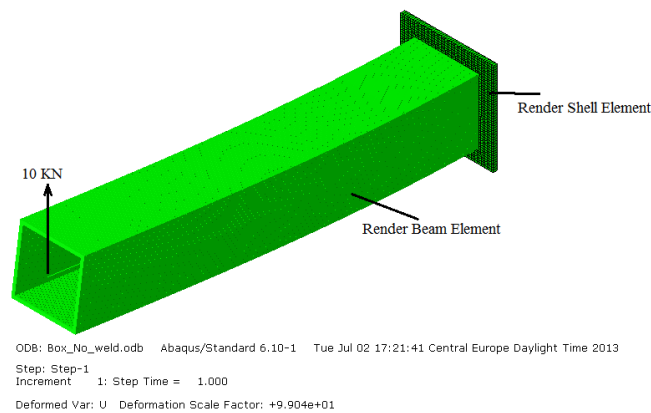
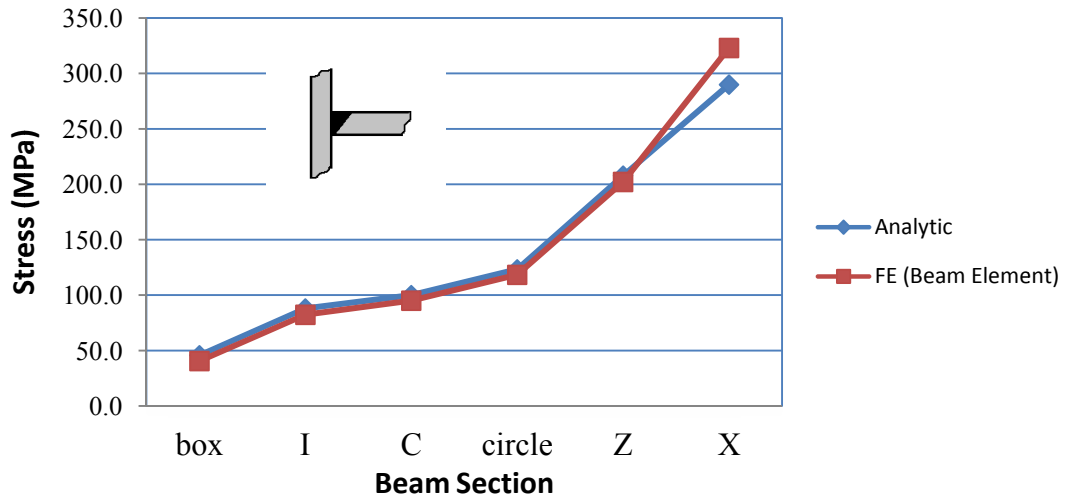


Figure 5.16. General view of the Beam-shell coupling of Rectangular- section of V welded joint

Figure 5.17 shows the summary of the finite element and analytical results of box, I, C, circular, Z and X of fillet weld in case of twisting.

Table 5.2 shows that the finite element results of stress in the fillet weld are varied from 40.5MPa for box beam profile and 323MPa for X beam profile. From chapter 2, the analytical results of stress in the fillet weld are varied from 45.8MPa for box beam profile and 290MPa for X beam profile. It is clear that the finite element results verify the analytical solution. It can be seen that the analytical solution can be replaced by beam element solution to represent the fillet weld.



Figures 5.17 stress of analytic and finite element results of various beam sections of V weld (Bending)

Table. 5.2 Analytical and FE Results of beams of V weld (Bending Moment).

Specimen	Analytic	FE (Beam Element)
V joint	Stress MPa	Stress MPa
box	45.8	40.5
I	88.0	82.3
C	100.1	95.0
circle	123.3	118.3
Z	207.8	202.1
X	289.9	323.0

5. 2.2 Finite element results of beam shell coupling of V-welded joint in case of twisting.

Figure 5.18 shows the summary of the finite element and analytical results of box, I, C, circular, Z and X of V weld in case of twisting.

Table 5.3 shows that the finite element results of stress in the V weld are varied from 43MPa for box beam profile and 323.8MPa for X beam profile. From chapter 2, the analytical results of stress in the fillet weld are varied from 47MPa for box beam profile and 293MPa for X beam profile. It is clear that the finite element results verify the analytical solution. It can be seen that the analytical solution can be replaced by beam element solution to represent the fillet weld.

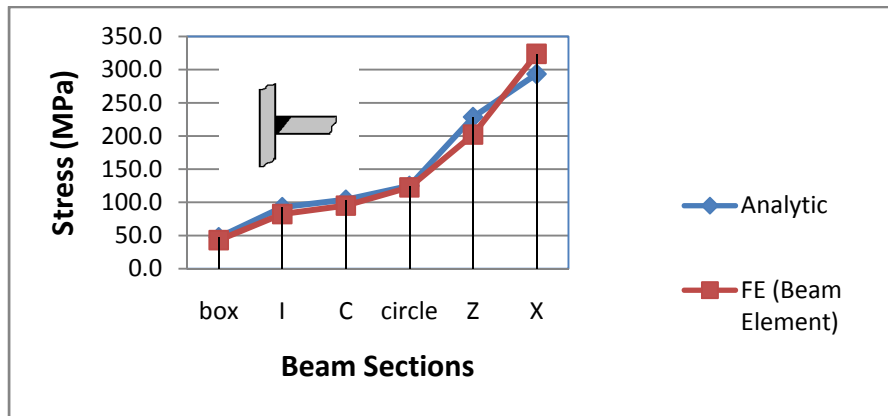


Figure 5.18 stress of Analytic and finite Element Results of Various Beam Sections of V weld for twisting moment

Table. 5.3 Analytical and FE Results of beams of V weld (twisting moment)

Specimen V joint	Analytic Stress (MPa)	FE (Beam Element) Stress (MPa)
box	47.4	43.0
I	92.8	82.3
C	104.0	95.0
circle	124.8	122.5
Z	228.6	202.1
X	293.4	323.8

5.4 Comparison

5.4.1 Comparison between V and fillet welded joints in case of bending.

Figure 5.19 shows the comparison between V and fillet welded joints of box, I, C, circular, Z and X of V weld in case of bending.

It is seen from Figure 5.19-20 and Table. 5.3 that for rectangular beam profile ,stress was minimized about 36% in case of using V weld while for the other sections , the stress was increased from 11.7% for I beam profile to 55% for X beam profile in case of using V weld .

Figure 5.19 shows the comparison between V and fillet welded joints of box, I, C, circular, Z and X of V weld in case of bending.

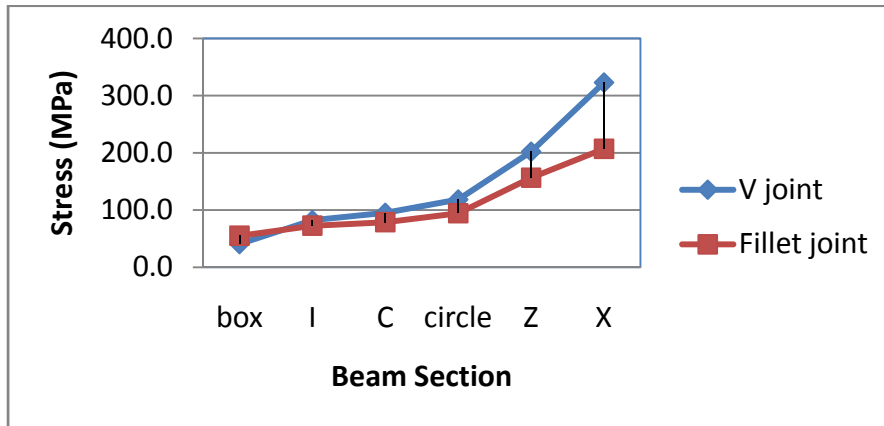


Figure 5.19 finite Element Results of Various Beam Sections of V weld and fillet weld of bending moment.

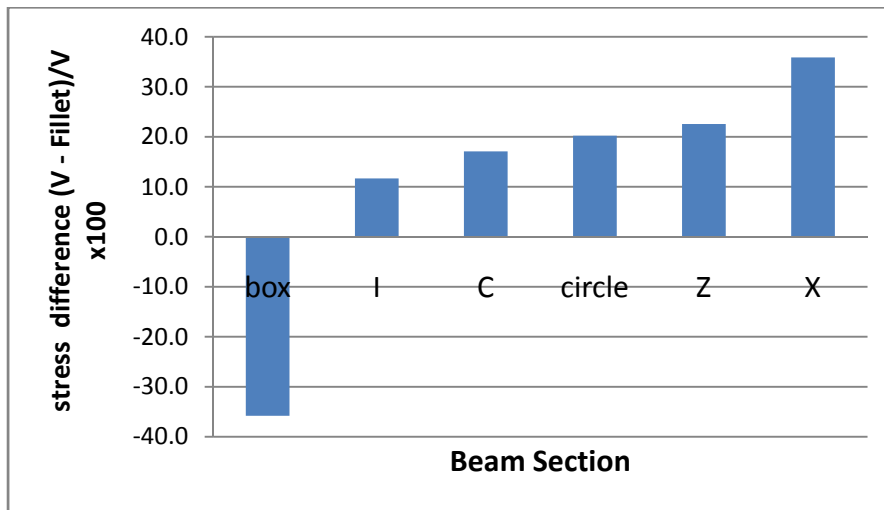


Figure 5.20. Stress change of various beam sections (bending)

Table. 5.3. FE Results of V and fillet joints of bending.

Specimen (Bending)	FE Results, Stress of V Joint (MPa)	FE Results, stress of Fillet Joint (MPa)
box	40.5	55.0
I	82.3	72.7
C	95.0	78.8
circle	118.3	94.4
Z	202.1	156.5
X	323.0	207.1

5.4.2 Comparison between V and fillet welded joints in case of twisting.

It is observed from figures. 5.21-22 that the largest stress is found at the X beam cross section. Also, it is shown from these figures that Fillet welds is better for beam sections I, C, Circular, Z and X. we can see also the stress was increased from 11.7% for I section to 55% for X section in case of using V weld instead of fillet weld. This means: these cross sections are recommended to be welded using fillet weld while a rectangular cross section is recommended to be welded by using V weld .

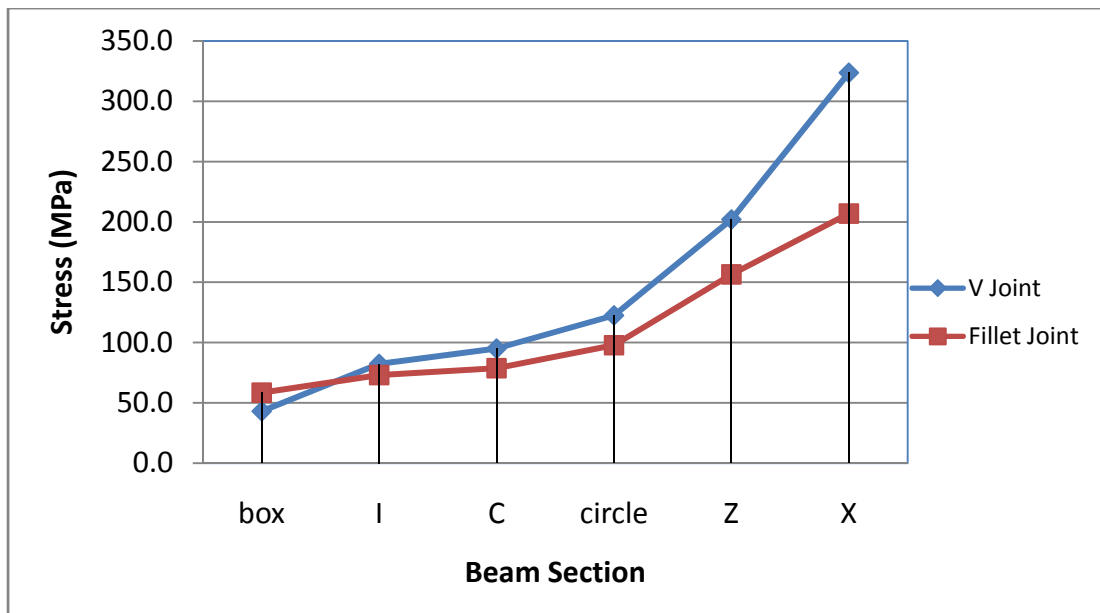


Figure 5.21. Finite element results of various beam sections of fillet and V weld (twisting)

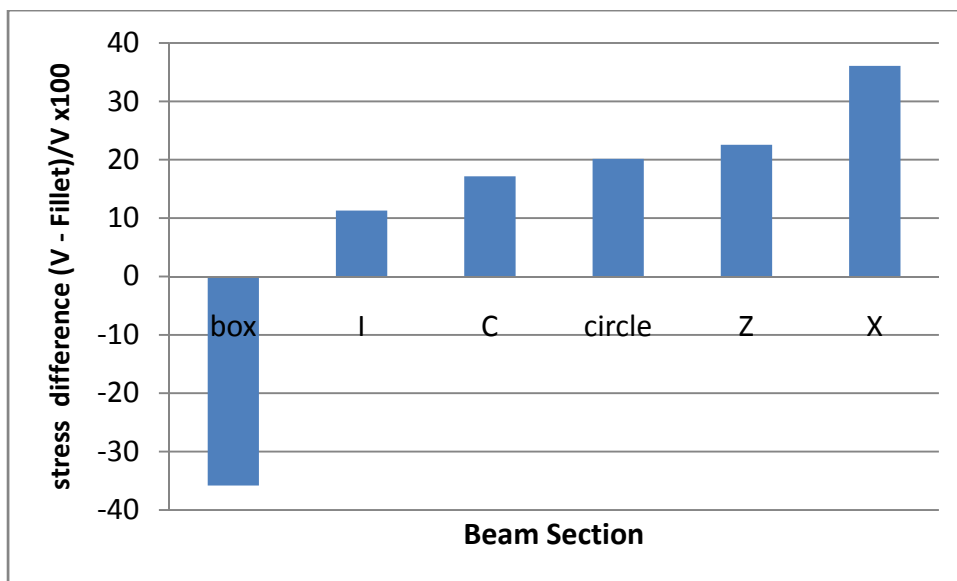


Figure 5.22. Stress change of various beam sections (twisting)

5.5 Discussion

The finite element simulations were performed for all the six specimens. The numerical analyses were carried out to represent the mechanical performance of the fillet weld and V weld beam-sections under bending. The study is summarized and concluded as follows. The predicted stress curves are in good agreement with the analytical results for all six cases of the beam members. The finite element results verify the analytical results.

Also, the results show that V weld gives high stress for sections I,C , Circular, Z, and X cross sections while a rectangular cross section gives lower stress when it welded by using V joint.

Based on numerical simulation beam element technique for V and fillet welded joints, we can conclude that the analytical approach can be replaced by using a beam element numerical approach.

Chapter 6

V-weld modeling using solid and shell elements

This chapter focuses on the development of a predictive methodology for V welded structures using shell and solid element. However, three-dimensional finite element analysis of complete structural hollow sections can be complex and time-consuming. Due to the complex nature of the finite element analysis codes, this method has limited application. It can be used in research area but cannot be widely used by structural engineers in their real-world projects. Therefore, there is a need to develop a simplified modeling method that can be implemented by using commonly available commercial software and easily employed.

Finite element models with different modeling techniques and meshing with various size and types of elements were created and analyzed. In the modeling certain assumption were made to simplify the model. Parent metal and welded metal had the same material properties which are steel ($E = 210 \times 10^3 MPa, \nu = 0.3$)

6.1 V-weld modelling using solid elements

Modelling welds with deformable solid elements are widely used because of its simplicity in modelling work and its accuracy in results since the stiffness of welds can be modelled accurately. In solid element models, the geometry and stiffness of the welds in a welded joint can easily be represented by using solid elements, see Figure 6.1. But, three-dimensional finite element analysis of a complete structural hollow sections can be complex and time-consuming.

Three-dimensional finite element analysis of complete structural hollow sections can be complex and time-consuming. Therefore, there is a need to develop a simplified modeling method that can be implemented by using commonly available commercial software and easily employed.

When modeling the welds with solid elements in shell element models, a special technique is necessary to connect these two different types of elements. The reason for that is the fact that solid elements have three degrees of freedom in each node while shell elements have five degrees of freedom in each node. The bending moments from

shell elements need to be transferred to solid elements. There are a couple of techniques available to perform it. One method when connecting the solid elements to the shell elements is using shell-to-solid-coupling see figure 6.1. However this procedure can be done automatically by Abaqus[59], a finite element software.

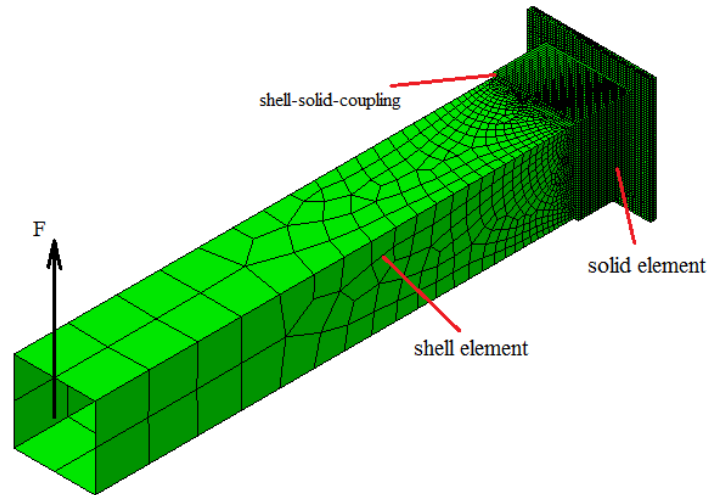


Figure 6.1 Modelling of the V-weld with coupling of shell and solid elements.

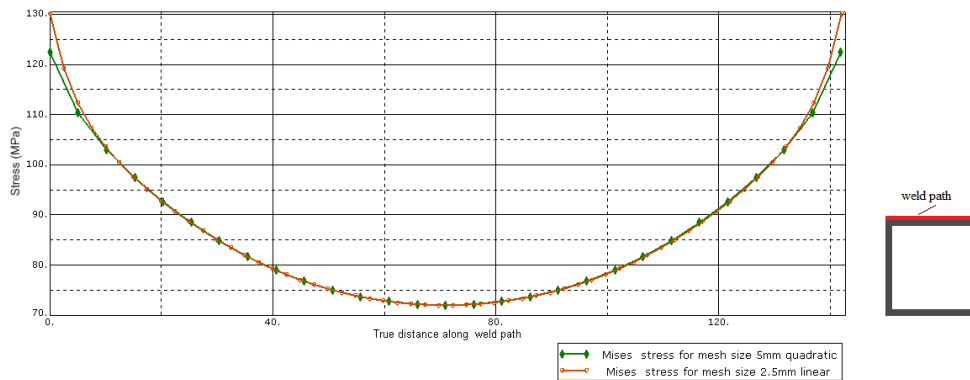


Figure 6.2 Stress distribution along weld path for different mesh size and shape function.

Figure 6.2 shows that the data of interest are substantially independent of the mesh and/or the polynomial degree of elements. Generally, good agreement of the stress distribution was obtained between the mesh size 5mm with quadratic polynomial and mesh size 2.5mm with linear polynomial.

6.1.1 Finite element results of solid element model of V- weld in case of bending.

6.1.1.1 Rectangular cross-section

Figures 6.3-4 show the stress distribution of top and vertical welds of a cantilever rectangular hollow section joint under the given loading of 10KN acting upward at the free end, respectively. Solid elements and shell elements were used in this analysis.

The figures show that the stress components S33, S13 and S23 are small compared with S11, S22 and S12. We conclude that the model can be modeled by using shell elements. Also, the figures show stress concentrations in the edges of the box profile. The distribution cannot be captured by using theoretical formula or by using beam elements.

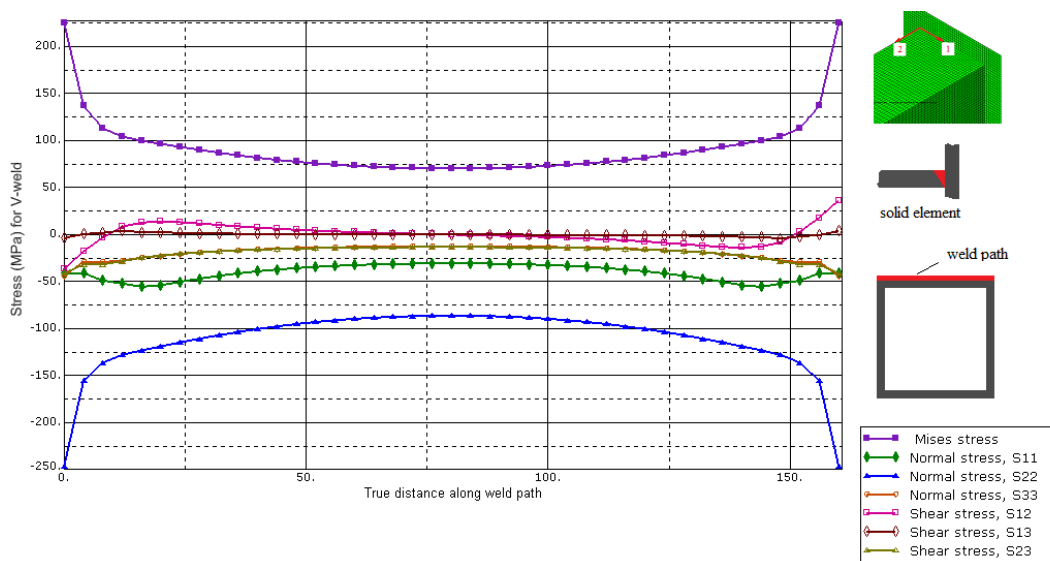


Figure 6.3. Stress distribution along horizontal weld path of box profile –bending.

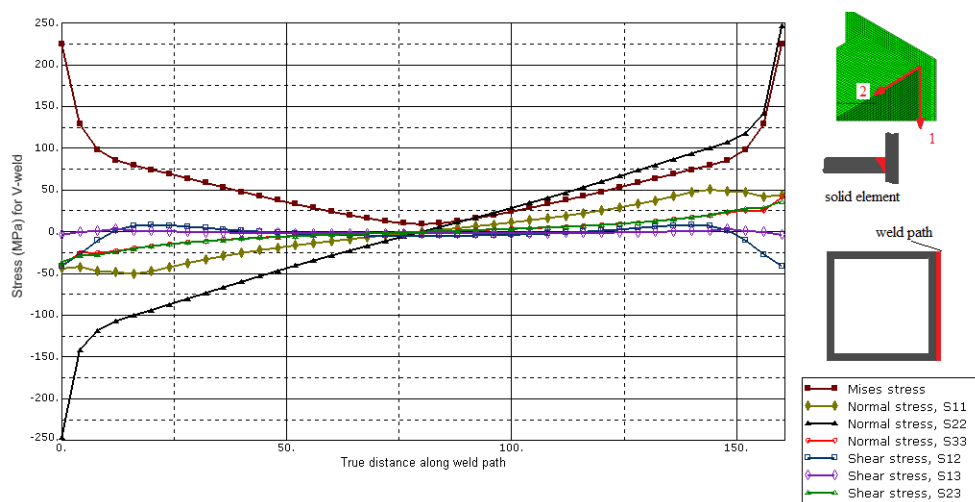


Figure 6.4 . Stress distribution along vertical weld path of box section-bending.

6.1.1.2 I section

Figures 6.5-6 illustrate the stress distribution of top and vertical welds of a cantilever beam of I profile under the given loading of 10KN acting upward at the free end, respectively. Solid elements were used to model welded joints and the area near welded joints while shell elements were used away from welded joints.

Also, we can see that the stress components S33, S13 and S23 are small compared with S11, S22 and S12. We conclude that the model can be modeled by using shell elements. Also, the figures show stress concentrations in the edges of the box profile. The distribution cannot be captured by using theoretical formula or by using beam elements.

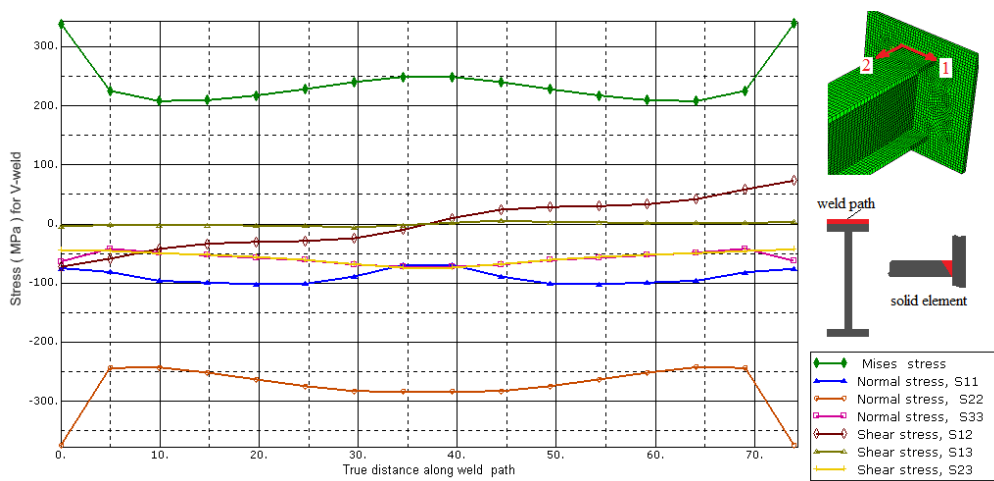


Figure 6.5 . Stress distribution along horizontal weld path of I section-bending.

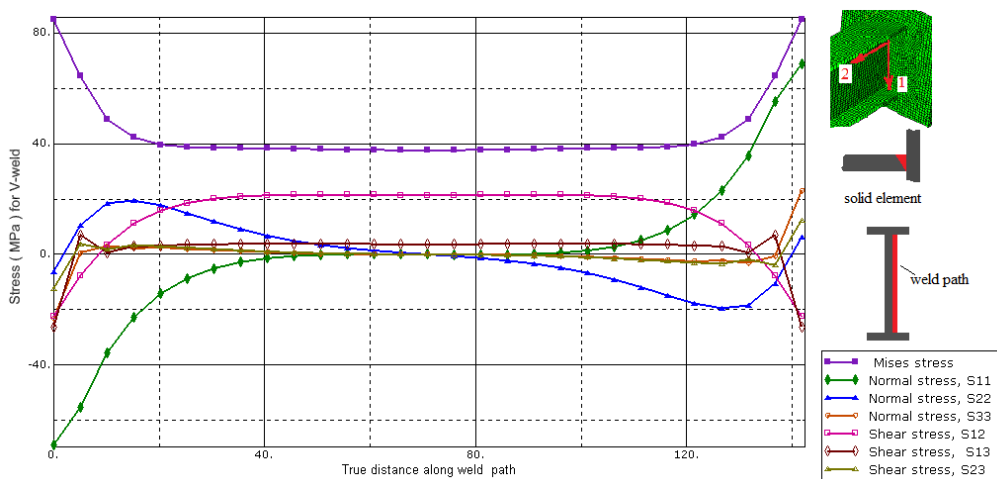


Figure 6.6 . Stress distribution along vertical weld path of I section-bending.

6.1.1.3 C section

Figure 6.7 shows the stress distribution in case of bending on the C profile for solid elements of top weld. Also, we can see that the stress components S33, S13 and S23 are small compared with S11, S22 and S12. We conclude that the model can be modeled by using shell elements. The figures show stress concentrations in the side of the stiffened edge of the C profile.

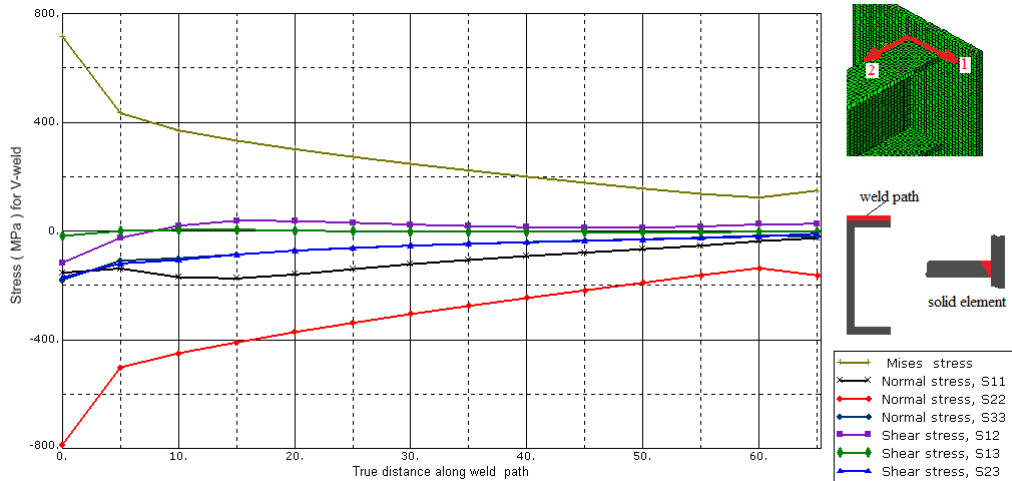


Figure 6.7 . Stress distribution along horizontal weld path of C section-bending.

6.1.1.4 Circular section

The stress distribution in case of bending on the circular profile for solid elements of top weld is shown in figure 6.8. Also, we can see that the stress components S33, S13 and S23 are small compared with S11, S22 and S12. We conclude that the model can be modeled by using shell elements.

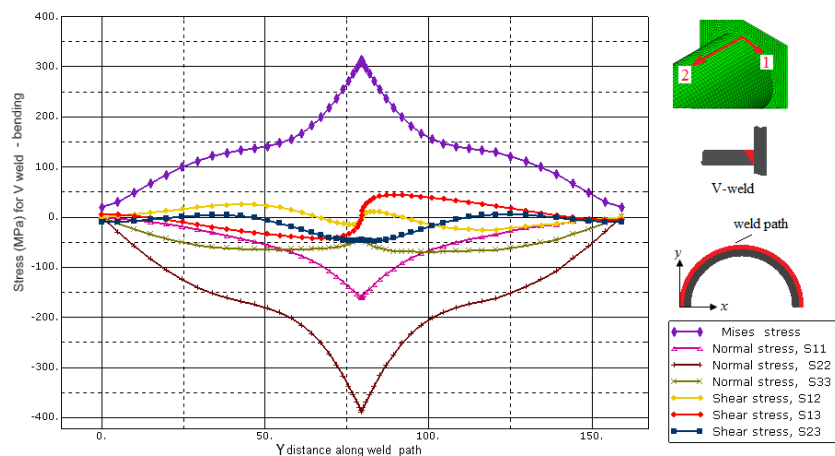


Figure 6.8 . Stress distribution along top weld path of circular section-bending.

6.1.1.5 Z – section

The stress distribution in case of bending on the Z profile for solid elements of top weld is shown in figure 6.9. Also, we can see that the stress components S33, S13 and S23 are small compared with S11, S22 and S12. We conclude that the model can be modeled by using shell elements. The figures show stress concentrations in the side of the stiffened edge of the Z profile.

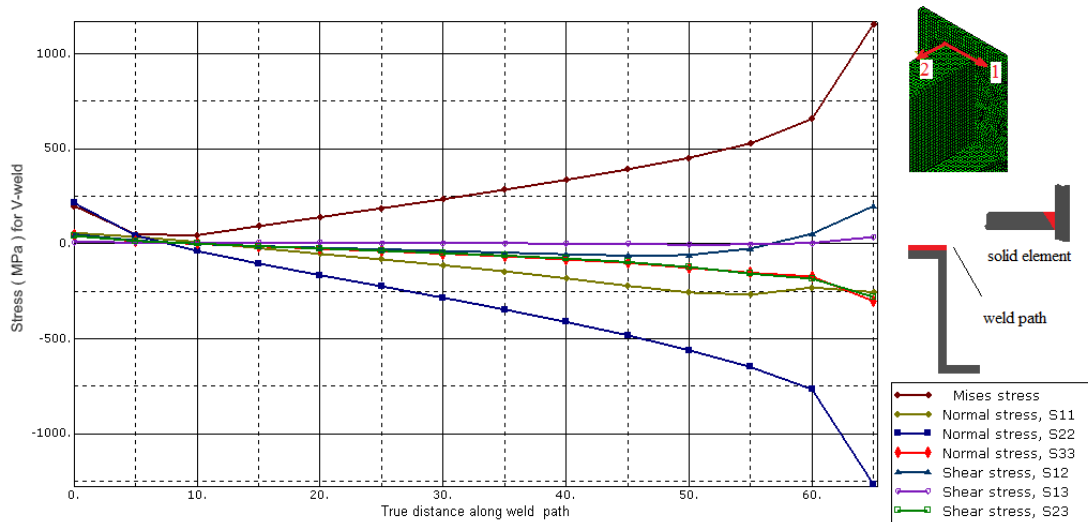


Figure 6.9 . Stress distribution along horizontal weld path ofZ section-bending.

6.1.1.6 X – section

The stress distribution in case of bending on the X profile for solid elements on the weld path is shown in figure 6.10. Also, we can see that the stress components S33, S13 and S23 are small compared with S11, S22 and S12. We conclude that the model can be modeled by using shell elements. The figures show stress concentrations in the top of the X profile.

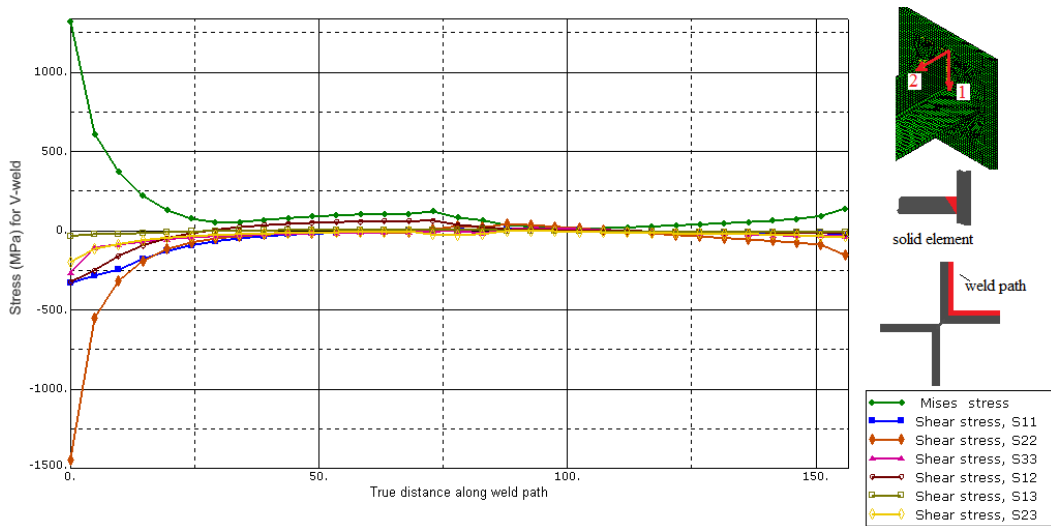


Figure 6.10 . Stress distribution along horizontal weld path of X section-bending.

6.1.2 Finite element results of solid element model of V- weld in case of twisting.

6.1.2.1 Rectangular cross-section

Figures 6.11 show the stress distribution of top weld of a cantilever rectangular hollow section joint under the given loading of 10KN acting upward at the free end. Solid elements and shell elements were used in this analysis. The figure shows stress concentrations in the side of the stiffened edges of the box profile.

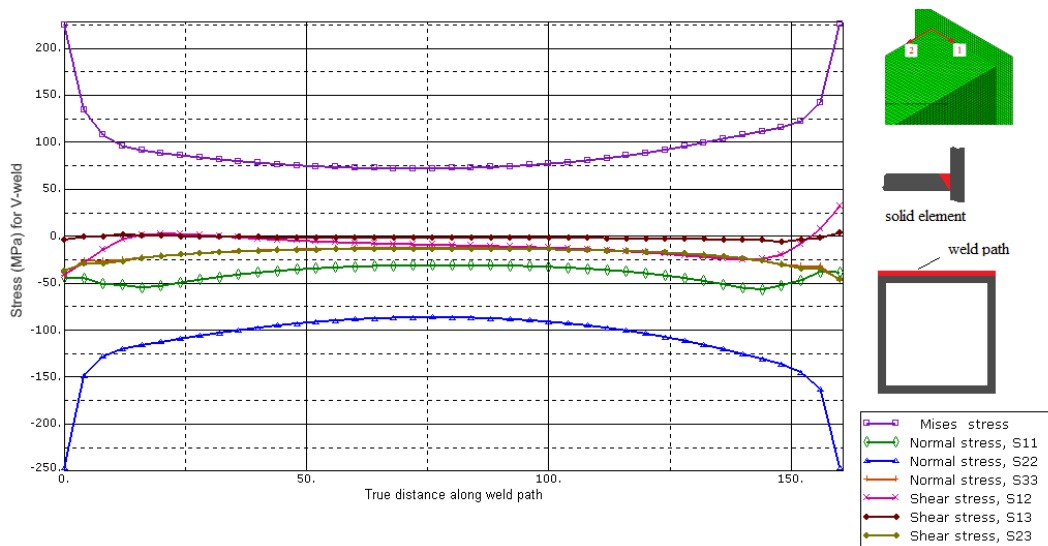


Figure 6.11 . Stress distribution along horizontal weld path of box section-twisting.

6.1.2.2 I-section

Figures 6.12 illustrate the stress distribution of top weld of a cantilever beam of I profile under the given loading of 1KN acting upward at the free end. Solid elements were used

to model welded joints and the area near welded joints while shell elements were used away from welded joints. The figure shows stress concentrations in the edges of the I profile.

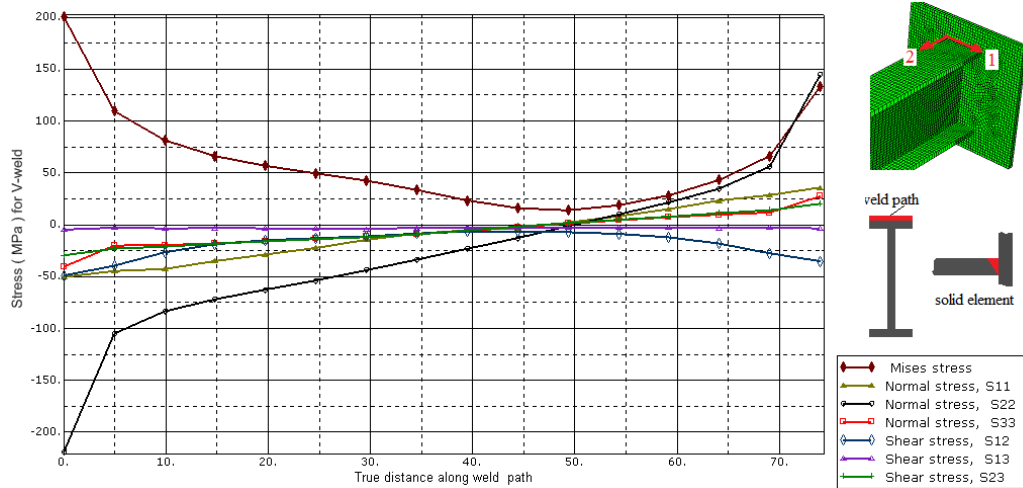


Figure 6.12. Stress distribution along horizontal weld path of I section-twisting.

6.1.2.3 C-section

Figures 6.13 illustrate the stress distribution of top weld of a cantilever beam of C profile under the given loading of 1KN acting upward at the free end. The figure shows stress concentrations in the stiffened edge of the C profile

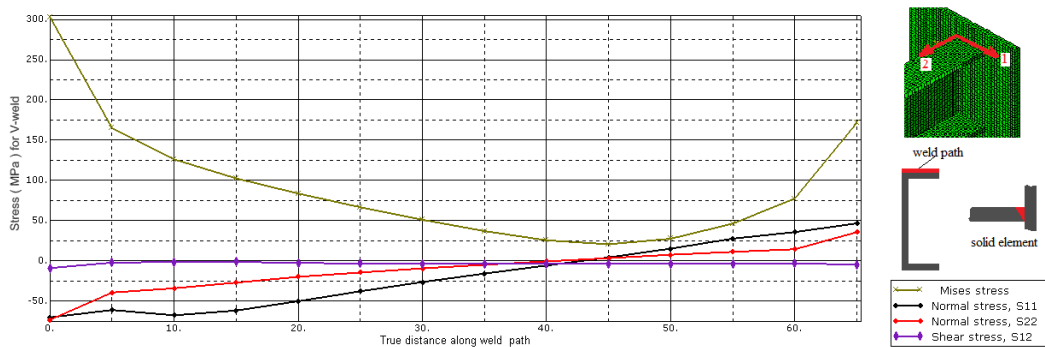


Figure 6.13 . Stress distribution along horizontal weld path of C section-twisting.

6.1.2.4 Circular-section

Figure 6.14 shows the stress distribution of top weld of a cantilever beam of circular profile under the given loading of 10KN acting upward at the free end. We can see that the stress distribution is maximum on top of the pipe.

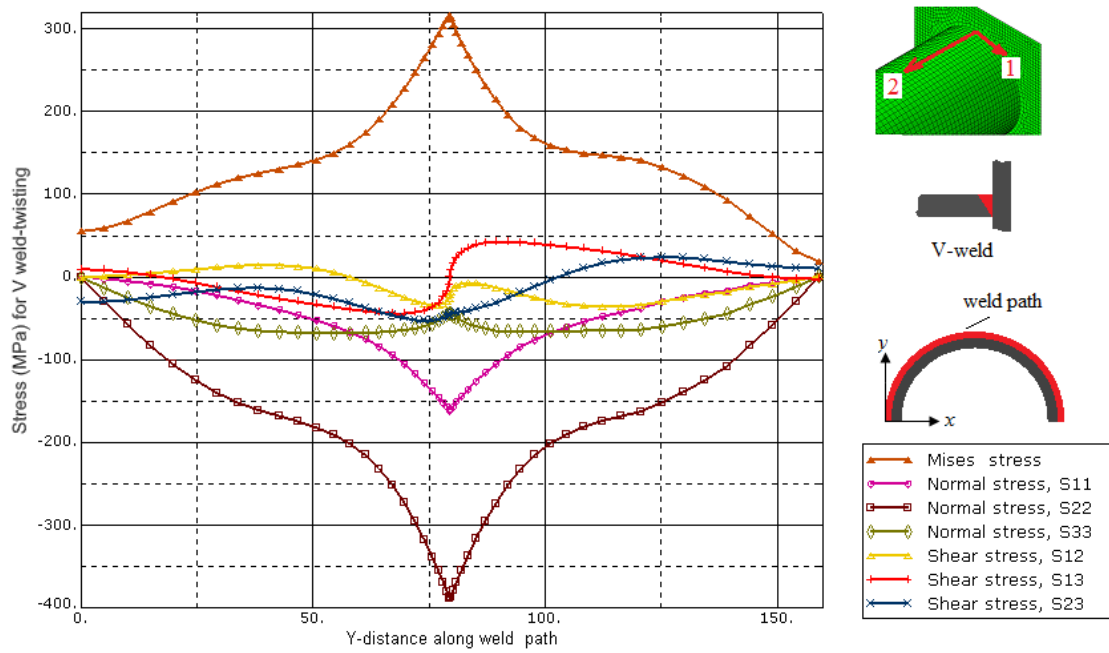


Figure 6.14 . Stress distribution along top weld path of circular section-twisting.

6.1.2.5 Z-section

Figure 6.15 illustrates the stress distribution of top weld of a cantilever beam of Z profile under the given loading of 1KN acting upward at the free end. Solid elements were used to model welded joints and the area near welded joints while shell elements were used away from welded joints. The figure shows stress concentrations in the edges of the Z profile.

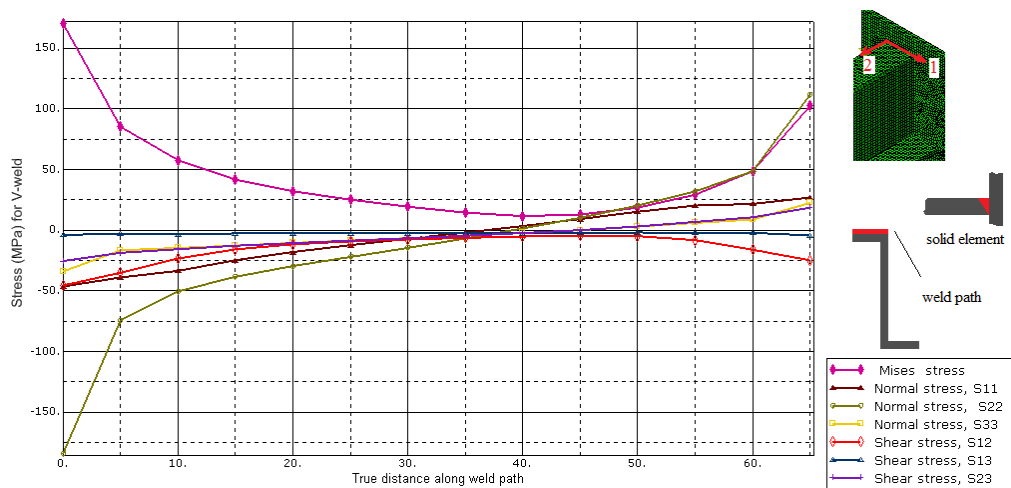


Figure 6.15. Stress distribution along horizontal weld path of Z section-twisting.

6.1.2.6 X-section

Figure 6.16 illustrates the stress distribution of top weld of a cantilever beam of X profile under the given loading of 1KN acting upward at the free end. Solid elements were used to model welded joints and the area near welded joints while shell elements were used away from welded joints. The figure shows stress concentrations in the top edge of the X profile.

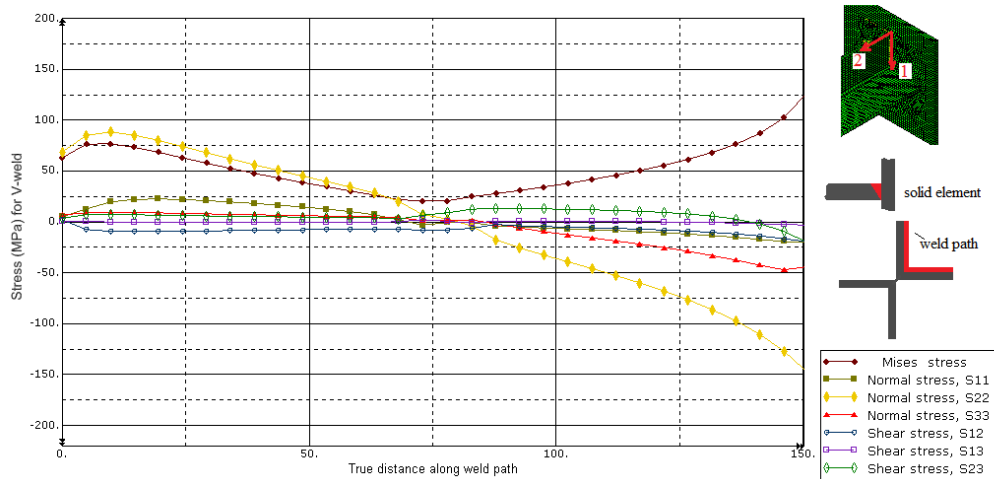


Figure 6.16. Stress distribution along weld path of the X section - twisting.

6.2 V-Weld modelling using shell elements

Shell elements with specified thickness in the intersection region of welded joints can be used to represent the stiffness of the welds in V-welded joints as shown in figure 6.17. In this analysis, the weld thickness is equal to the plate thickness as shown in figure below.

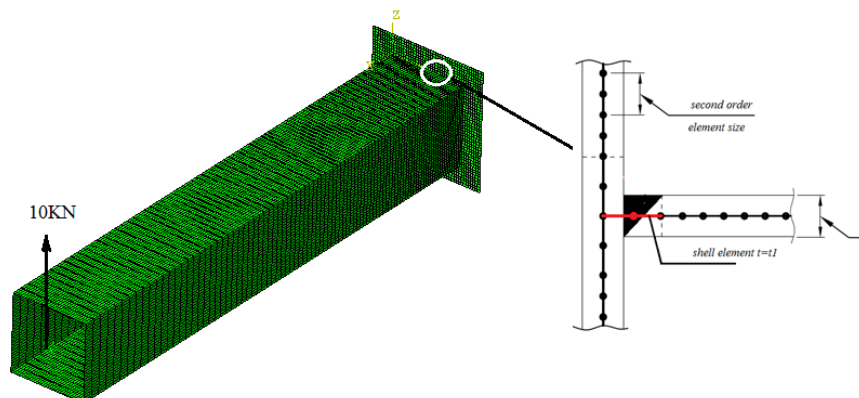


Figure. 6.17 Modelling welds using shell elements.

6.2.1 Finite Element Results of Shell element model of V- weld in case of bending.

6.2.1.1 Rectangular cross-section

Figures 6.18 and 6.19 show the stress distribution of top and vertical weld of a cantilever rectangular hollow section joint under the given loading of 10KN acting upward at the free end, respectively. Shell elements were used in this analysis. The figures show stress concentrations in the side of the stiffened edges of the box profile

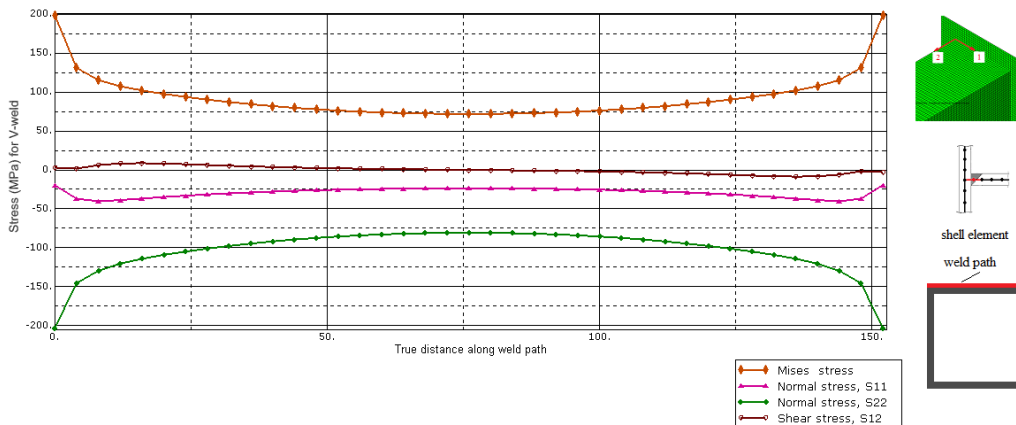


Figure 6.18. Stress distribution along horizontal weld of rectangular box-bending.

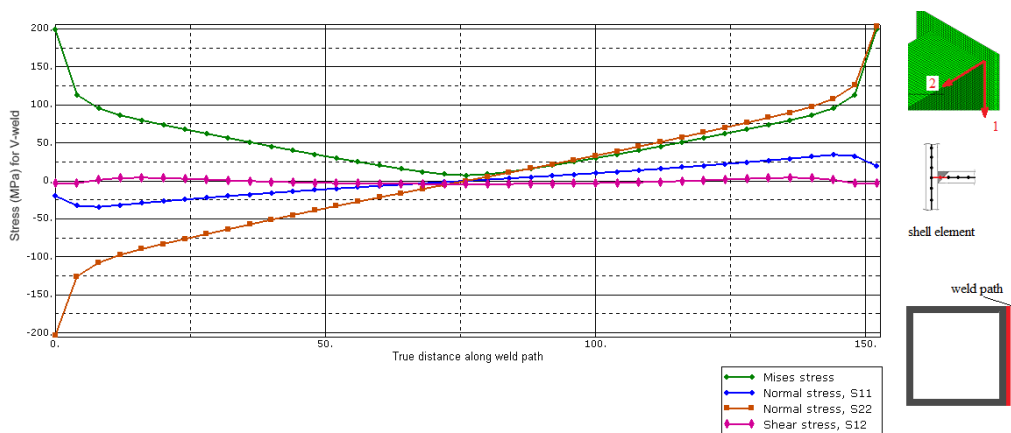


Figure 6.19. Stress distribution along vertical weld path of rectangular box-bending.

6.2.1.2 I cross-section

Figures 6.20 and 6.21 show the stress distribution of top and vertical weld of a cantilever I section joint under the given loading of 10KN acting upward at the free end, respectively. Shell elements were used in this analysis. The figure shows stress concentrations in the side of the edges of I profile.

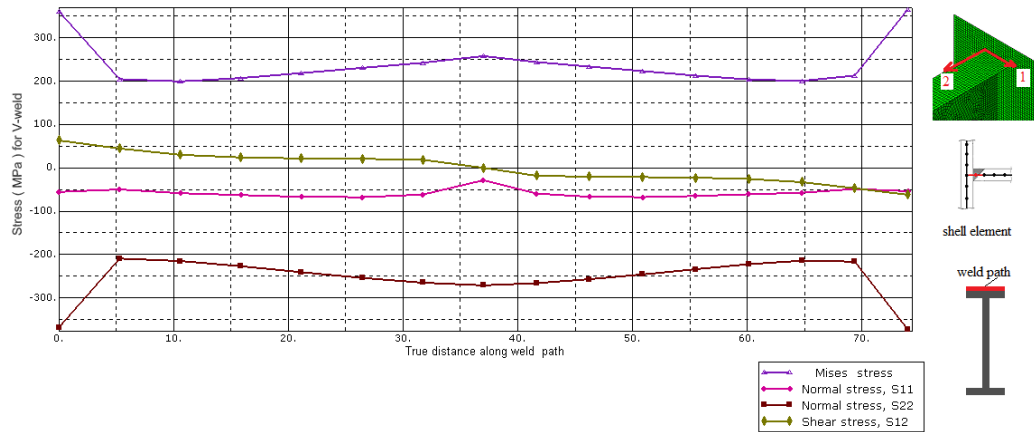


Figure 6.20. Stress distribution along horizontal weld path of I section-bending.

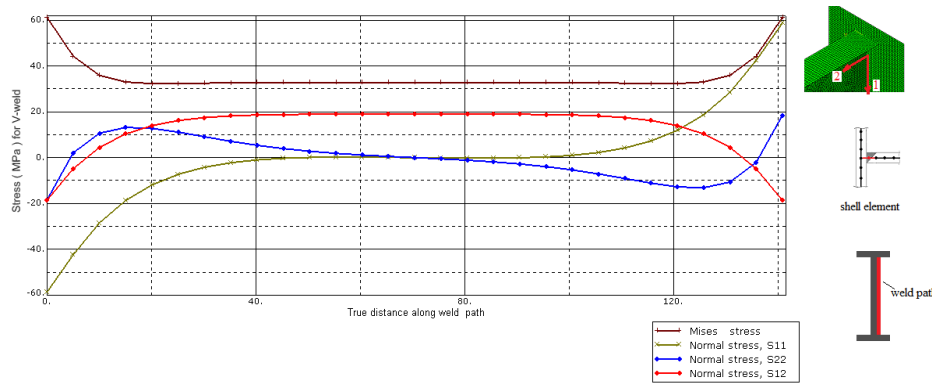


Figure 6.21 Stress distribution along vertical weld path of I section- bending.

6.2.1.3 C cross-section

Figures 6.22 and 6.23 show the stress distribution of top and vertical weld of a cantilever C section joint under the given loading of 10KN acting upward at the free end, respectively. Shell elements were used in this analysis. The figure shows stress concentrations in the side of the stiffened edge of the C profile.

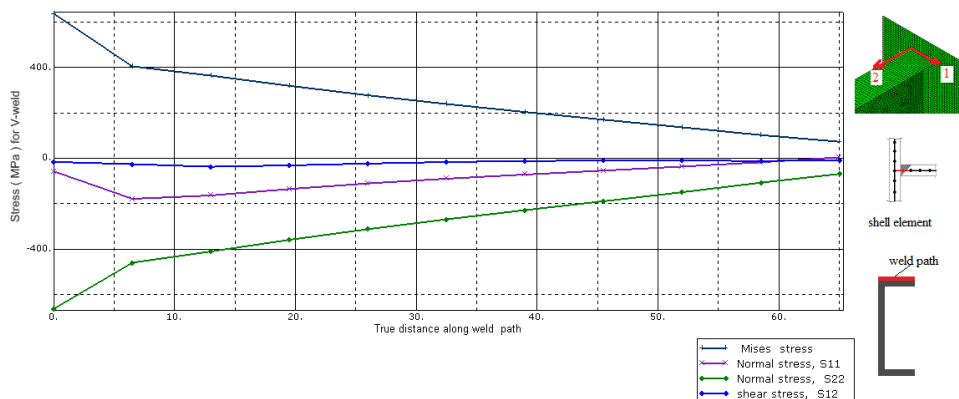


Figure 6.22. Stress distribution along horizontal weld path of C section-bending.

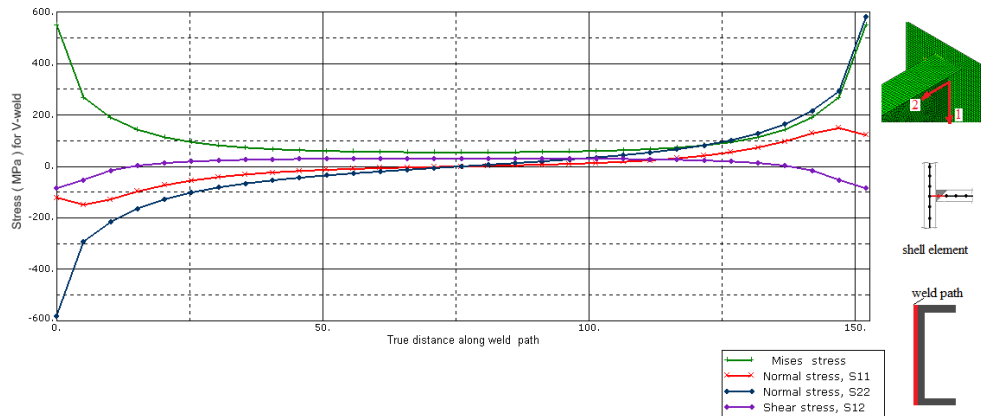


Figure 6.23 Stress distribution along vertical weld path of C section-bending.

6.2.1.4 Circular cross-section

Figures 6.24 and 6.25 show the stress distribution of top and vertical weld of a cantilever C section joint under the given loading of 10K N acting upward at the free end, respectively. Shell elements were used in this analysis. The figure shows stress concentrations on the top of the pipe.

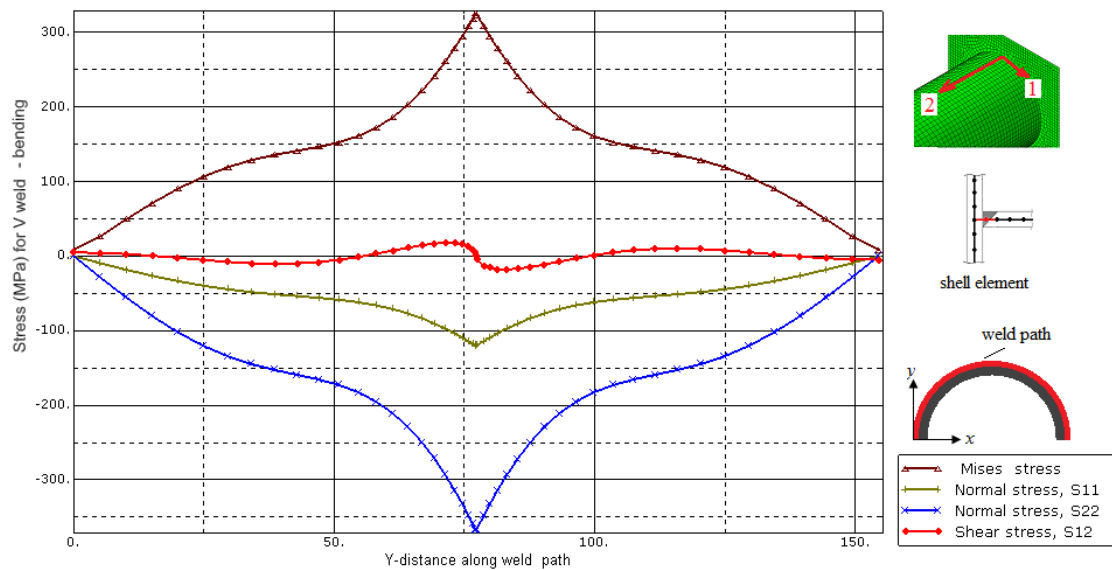


Figure 6.24. Stress distribution along top weld path of Circular section-bending.

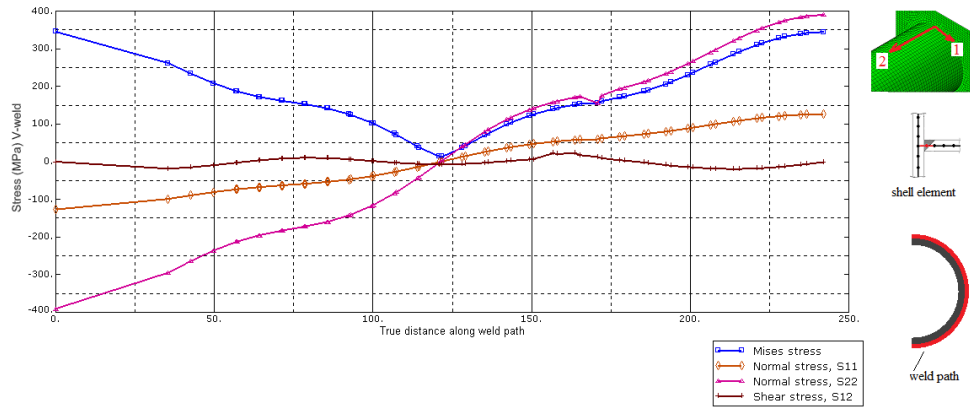


Figure 6.25 Stress distribution along vertical weld path of Circular section-bending.

6.2.1.5 Z cross-section

Figures 6.26 and 6.27 show the stress distribution of top and vertical weld of a cantilever Z section joint under the given loading of 10KN acting upward at the free end, respectively. Shell elements were used in this analysis. The figure shows stress concentrations in the side of the stiffened edge of the Z profile.

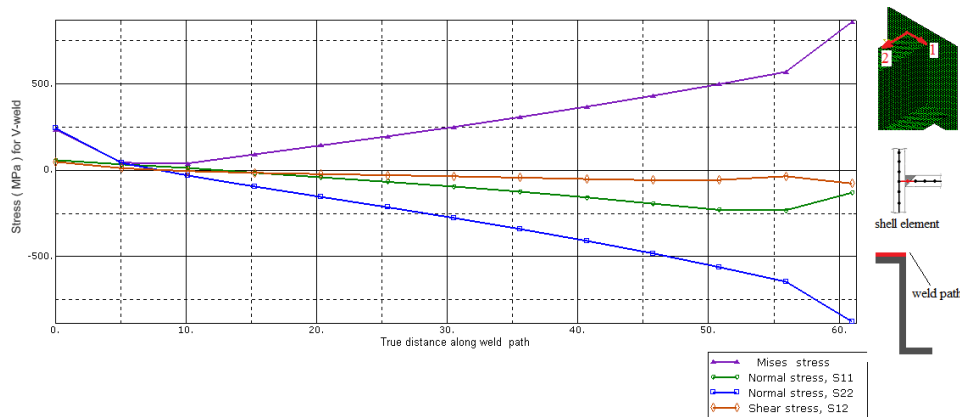


Figure 6.26. Stress distribution along horizontal weld path of Z section-bending.

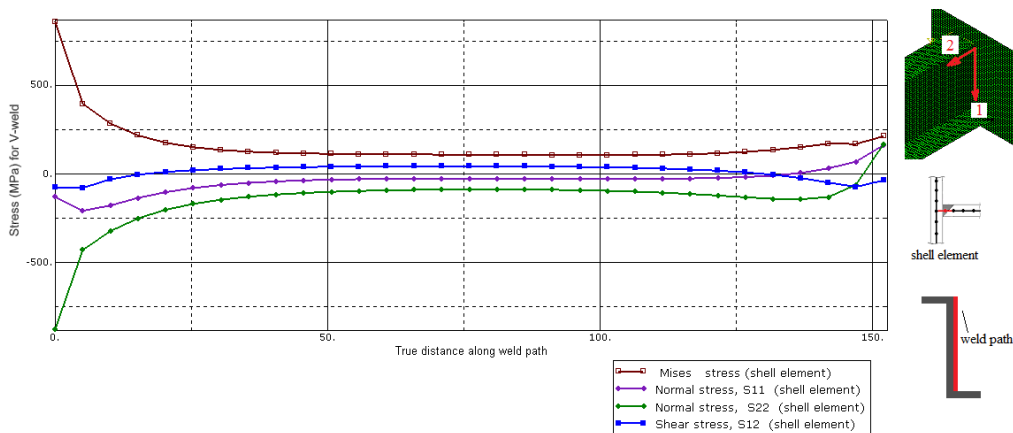


Figure 6.27 Stress distribution along vertical weld path of Z section-bending.

6.2.1.6 X cross-section

Figure 6.28 shows the stress distribution on the weld path of a cantilever X section joint under the given loading of 10KN acting upward at the free end. Shell elements were used in this analysis. The figure shows stress concentrations on the top of the X profile.

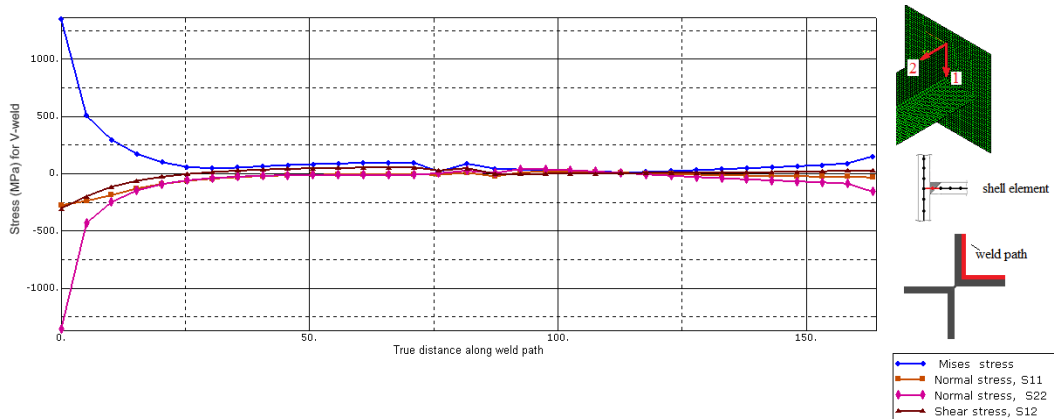


Figure 6.28. Stress distribution along weld path of X section -bending

6.2.2 Finite element results of shell element model of V- weld in case of twisting.

6.2.2.1 Rectangular section

Figures 6.29 and 6.30 show the stress distribution of top and vertical of weld path of a cantilever box section joint under the given loading of 10KN acting upward at the free end, respectively. Shell elements were used in this analysis. The figures show stress concentrations in the side of the stiffened edges of the box profile.

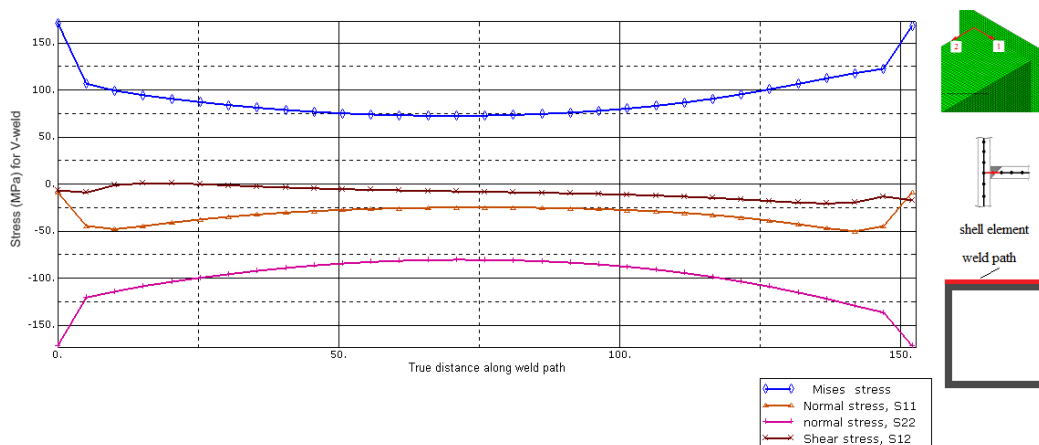


Figure 6.29. Stress distribution along horizontal weld path of box profile-twisting.

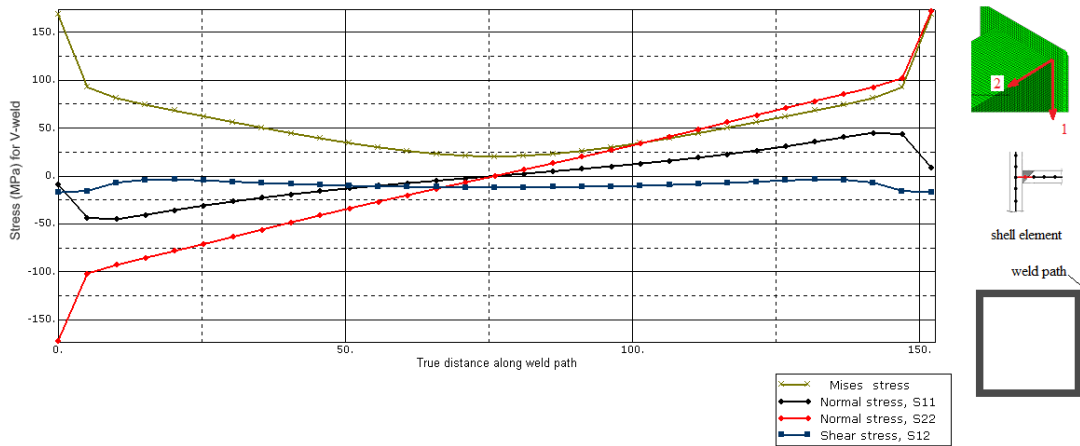


Figure 6.30. Stress distribution along vertical weld path of box profile -twisting.

6.2.2.2 I section

Figure 6.31 and 6.32 show the stress distribution of top and vertical of weld path of a cantilever I section joint under the given loading of 1KN acting upward at the free end. Shell elements were used in this analysis. The figure shows stress concentrations in the side of the stiffened edges of the I profile.

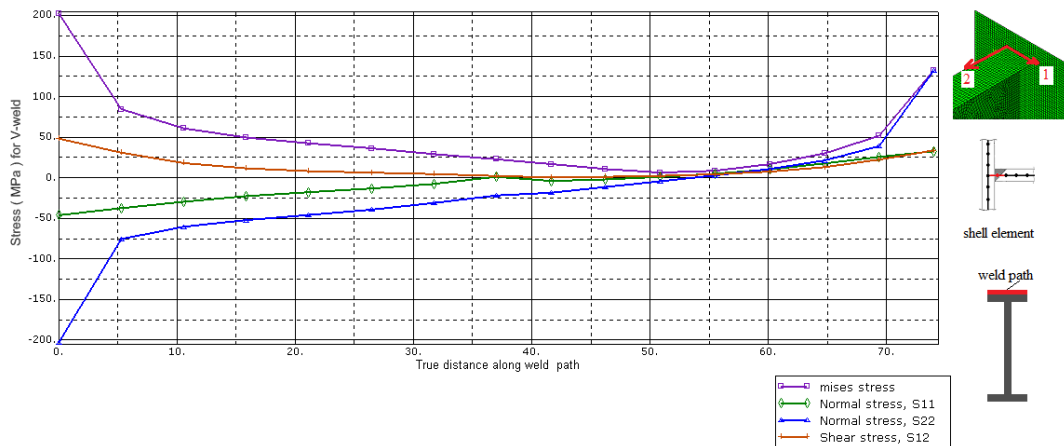


Figure 6.31. Stress distribution along horizontal weld path of I section-twisting.

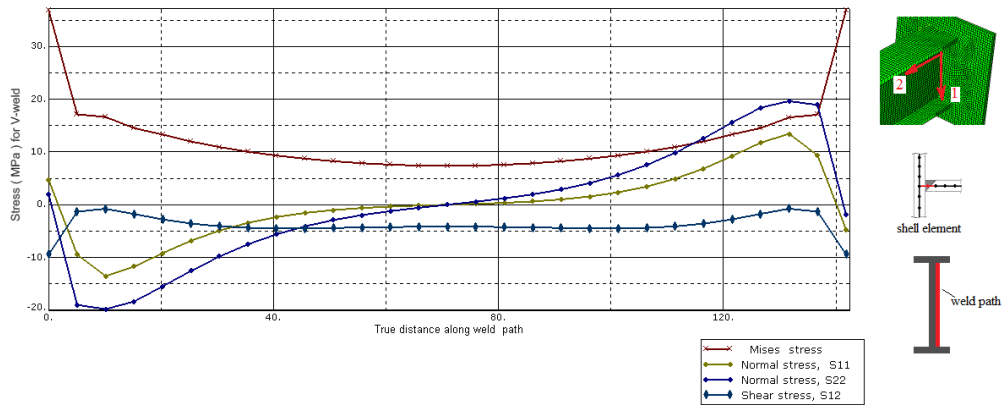


Figure 6.32. Stress distribution along vertical weld path of I section-twisting.

6.2.2.3 C section

Figure 6.33 and 6.34 show the stress distribution of top and vertical of weld path of a cantilever C section joint under the given loading of 1KN acting upward at the free end, respectively. Shell elements were used in this analysis. The figure shows stress concentrations in the side of the stiffened edge of the C profile.

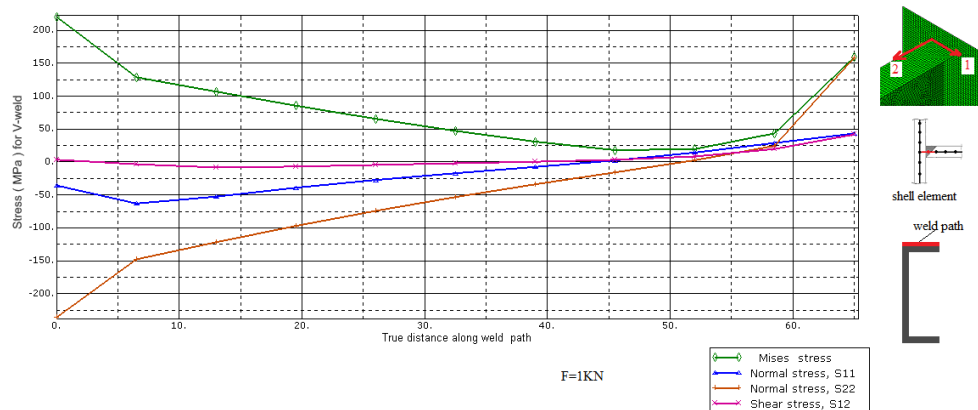


Figure 6.33. Stress distribution along horizontal weld path of C section-twisting.

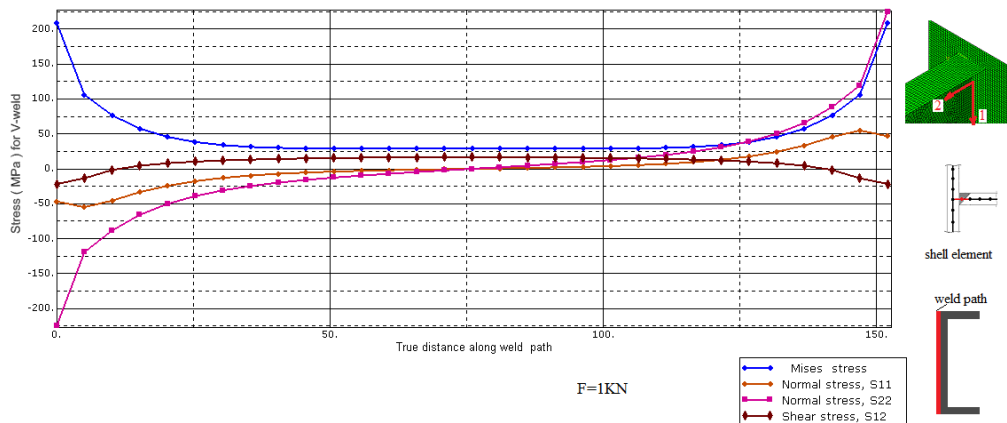


Figure 6.34. Stress distribution along vertical weld path of C section-twisting.

6.2.2.4 Circular section

Figure 6.35 and 6.36 show the stress distribution of top and vertical of weld path of a cantilever C section joint under the given loading of 10KN acting upward at the free end, respectively. Shell elements were used in this analysis. The figure shows stress concentrations on the top of the pipe.

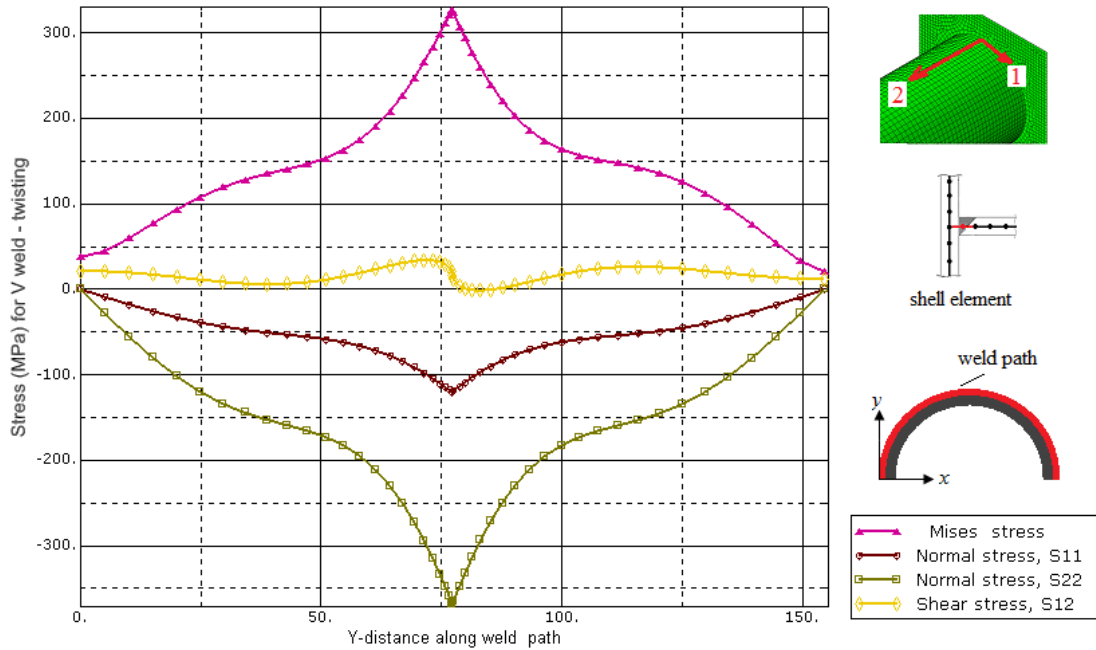


Figure 6.35. Stress distribution along top weld path of Circular section-twisting.

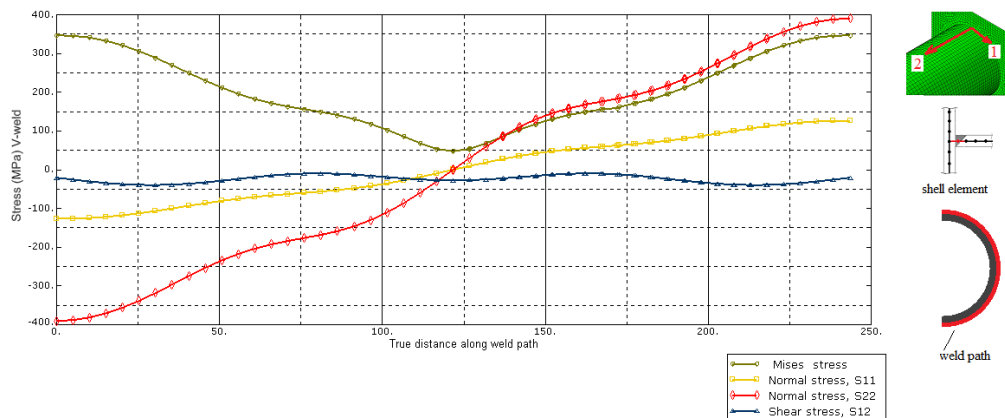


Figure 6.36. Stress distribution along vertical weld path of circular section-twisting.

6.2.2.5 Z section

Figure 6.37 and 6.38 show the stress distribution of top and vertical of weld path of a cantilever Z section joint under the given loading of 1KN acting upward at the free end, respectively. Shell elements were used in this analysis. The figure shows stress concentrations in the edge of the Z profile.

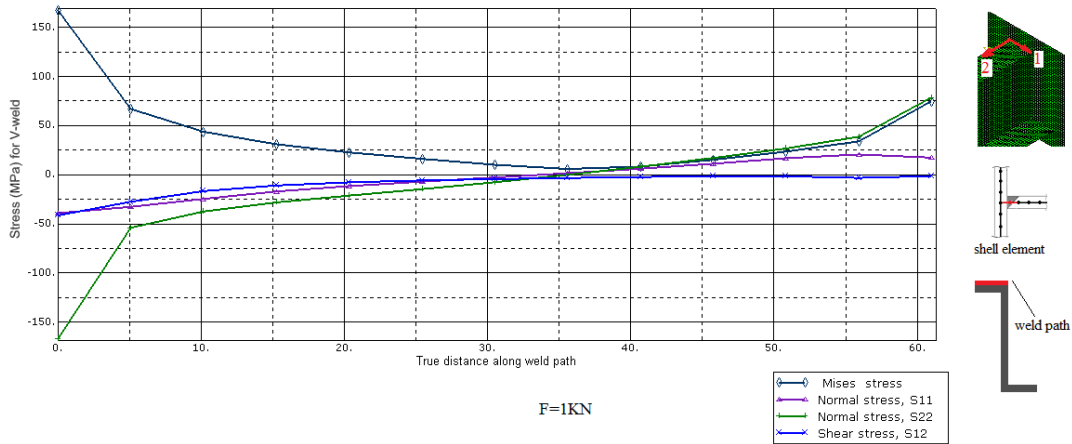


Figure 6.37. Stress distribution along horizontal weld path of Z section-twisting.

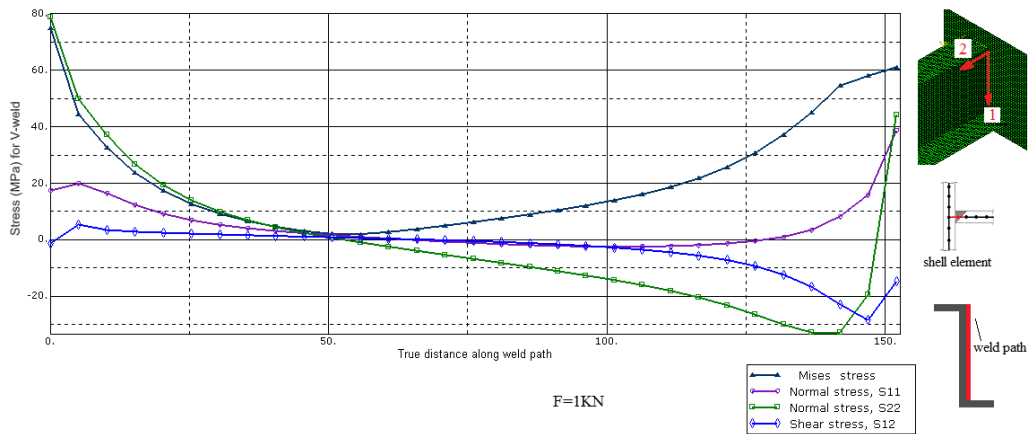


Figure 6.38. Stress distribution along vertical weld path of Z section-twisting.

6.2.2.6 X section

Figure 6.39 shows the stress distribution along weld path of a cantilever X section joint under the given loading of 1KN acting upward at the free end. Shell elements were used in this analysis. The figure shows stress concentrations in the edges of the X profile.

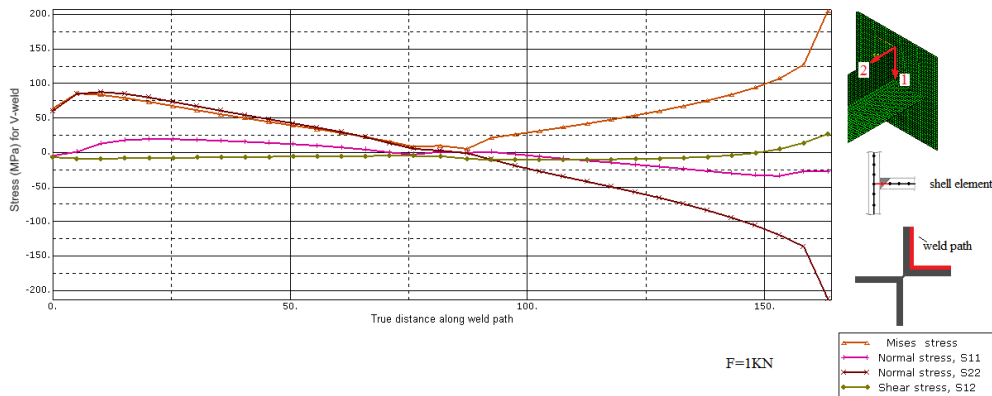


Figure 6.39. Stress distribution along weld path for X section-twisting.

6.3 Comparison between shell and solid elements

6.3.1 Case (a) Bending

6.3.1.1 Rectangular cross-section

Figure 6.40 shows the stress distribution for shell and solid elements along weld path of a cantilever box section joint under the given loading of 10KN acting at the free end. It is clear that stress curves of solid element are in good agreement with stress curves of shell element.

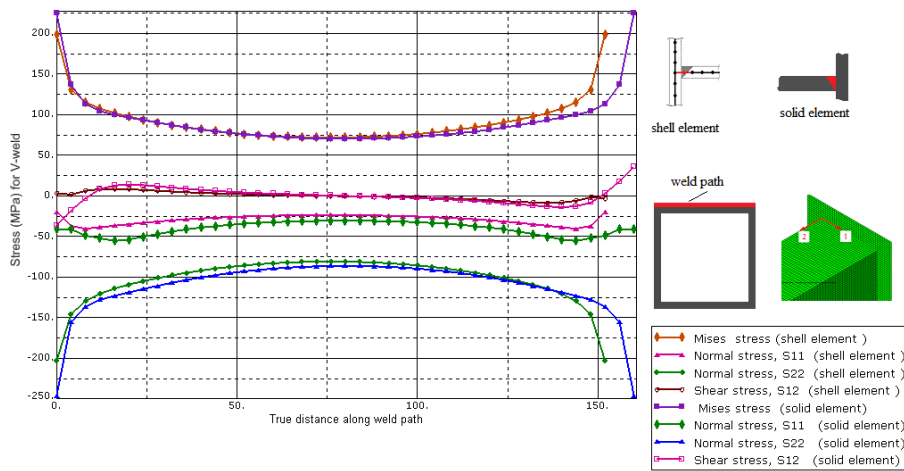


Figure 6.40 . Comparison of stress distribution between shell and solid elements along horizontal weld for box section-bending.

6.3.1.2 I- section

Figure 6.41 shows the stress distribution for shell and solid elements along weld path of a cantilever I section joint under the given loading of 1KN acting at the free end. We can see that stress curves of shell element are in good agreement with stress curves of solid element.

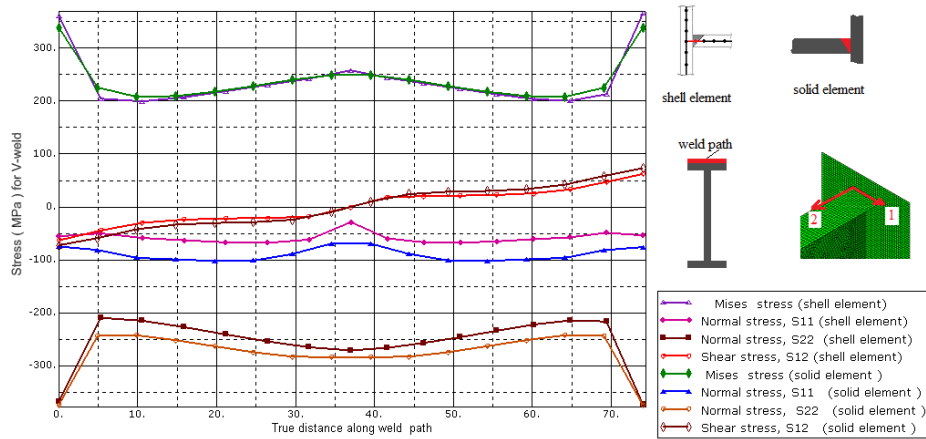


Figure 6.41 . Comparison of stress distribution between shell and solid elements along horizontal weld path of I section-bending.

6.3.1.3 C- section

Figure 6.42 shows the stress distribution for shell and solid elements along weld path of a cantilever C section joint under the given loading of 1KN acting at the free end. We can see that stress curves of shell element are in good agreement with stress curves of solid element.

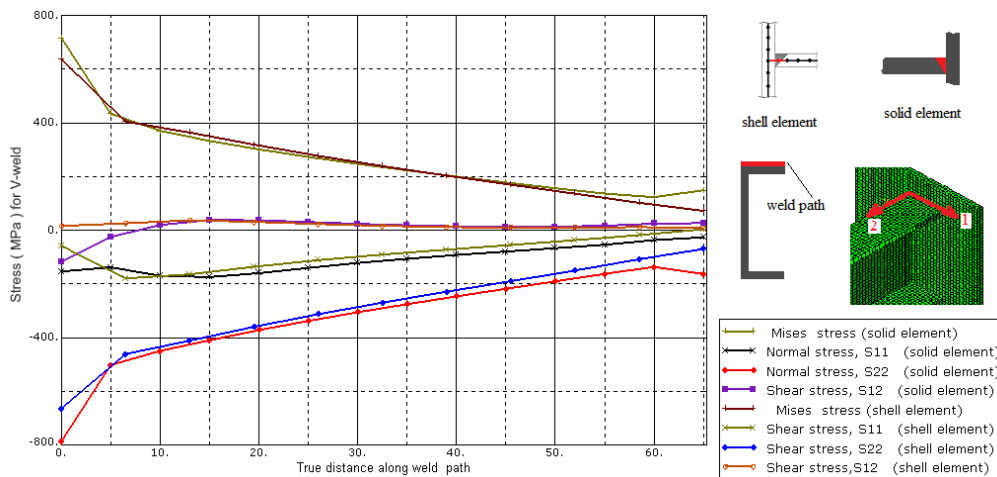


Figure 6.42 . Comparison of stress distribution between shell and solid elements along horizontal weld path of C section-bending.

6.3.1.4 Circular- section

Figure 6.43 shows the stress distribution for shell and solid elements along weld path of a cantilever circular section joint under the given loading of 10KN acting at the free

end. We can see that stress curves of shell element are in good agreement with stress curves of solid element.

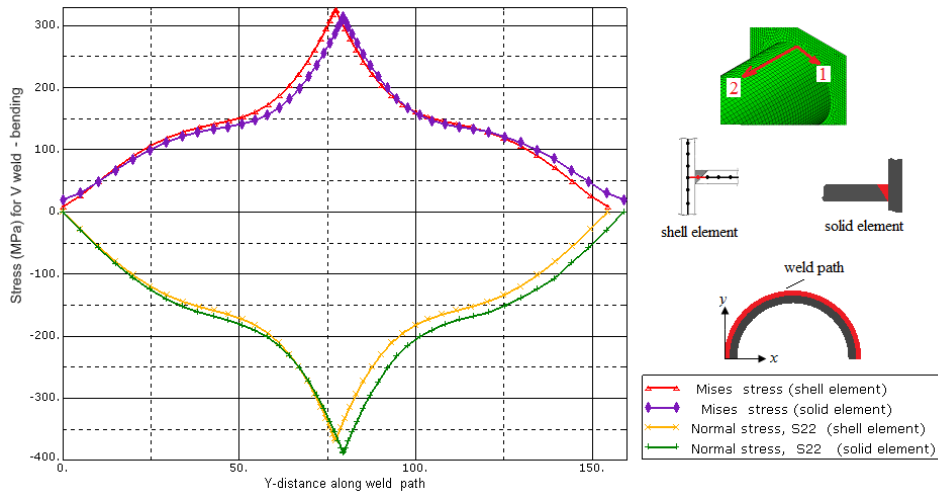


Figure 6.43 . Comparison of stress distribution between shell and solid elements along top weld of circular section-bending.

6.3.1.5 Z- section

Figure 6.44 shows the stress distribution for shell and solid elements along weld path of a cantilever Z section joint under the given loading of 1KN acting at the free end. We can see that stress curves of shell element are in good agreement with stress curves of solid element.

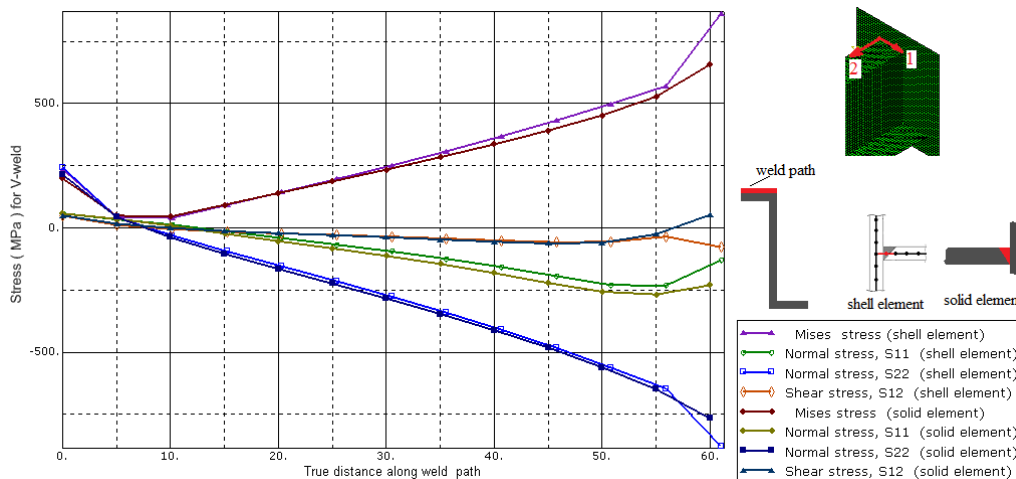


Figure 6.44 . Comparison of stress distribution between shell and solid elements along horizontal weld path of Z section-bending.

6.3.1.6 X - section

Figure 6.45 shows the stress distribution for shell and solid elements along weld path of a cantilever X section joint under the given loading of 1KN acting at the free end. We can see that stress curves of shell element are in good agreement with stress curves of solid element.

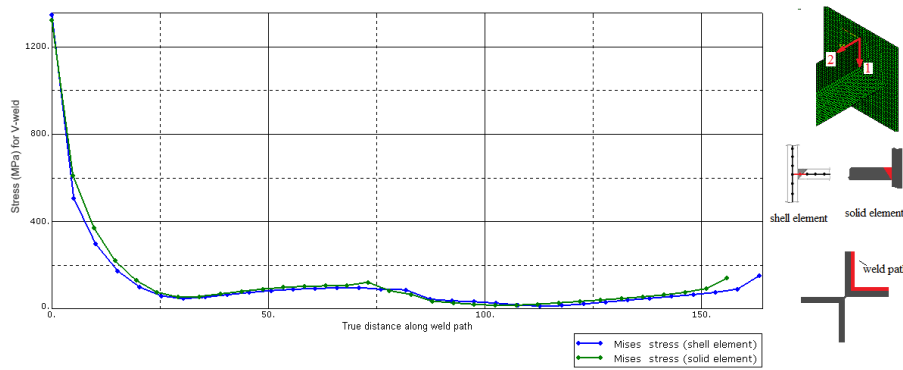


Figure 6.45. Comparison of stress distribution between shell and solid elements along top weld path of X section -bending.

6.3.2 Case (b) Twisting

6.3.2.1 Box- section

Figure 6.46 shows the stress distribution for shell and solid elements along weld path of a cantilever box section joint under the given loading of 10KN acting at the free end. We can see that stress curves of shell element are in good agreement with stress curves of solid element.

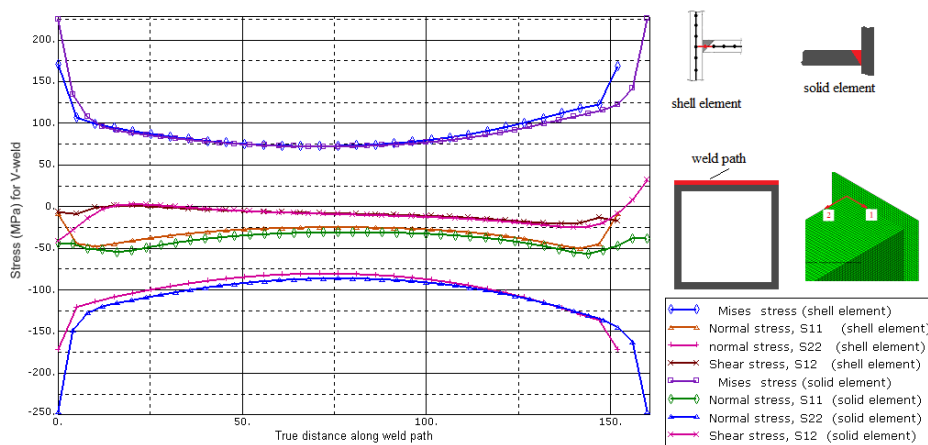


Figure 6.46 . Comparison of stress distribution between shell and solid elements along horizontal weld of box section -twisting.

6.3.2.2 I - section

Figure 6.47 shows the stress distribution for shell and solid elements along weld path of a cantilever I section joint under the given loading of 1KN acting at the free end. We can see that stress curves of shell element are in good agreement with stress curves of solid element.

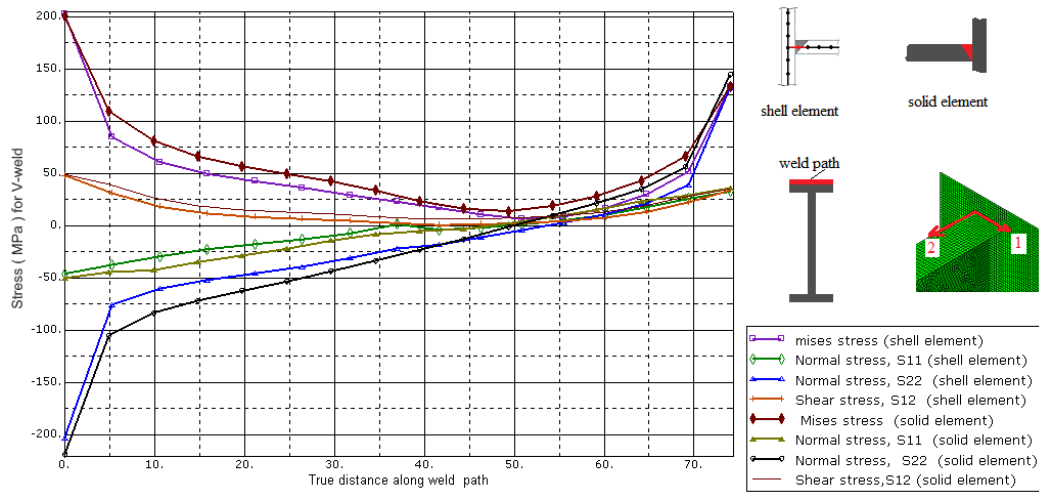


Figure 6.47 . Comparison of stress distribution between shell and solid elements along horizontal weld path of I section-twisting.

6.3.2.3 C - section

Figure 6.48 shows the stress distribution for shell and solid elements along weld path of a cantilever C section joint under the given loading of 1KN acting at the free end. It is clear that stress curves of shell element are in good agreement with stress (shell curves) of solid element.

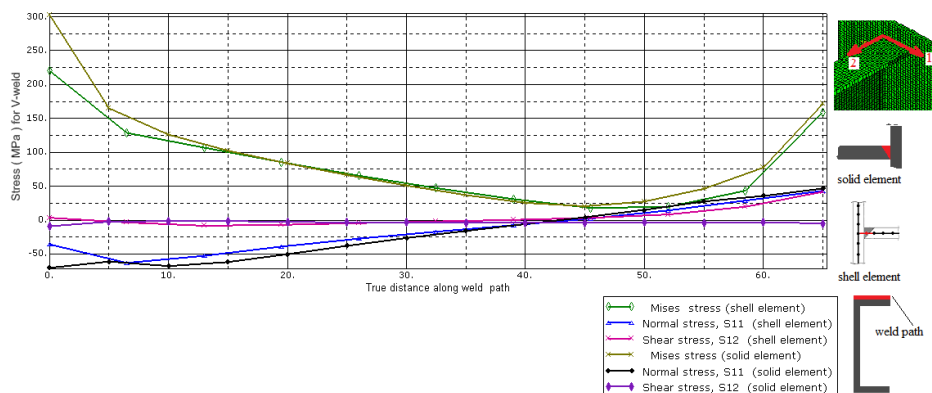


Figure 6.48 . Comparison of stress distribution between shell and solid elements along horizontal weld path of C section-twisting.

6.3.2.4 Circular - section

Figure 6.49 shows the stress distribution for shell and solid elements along weld path of a cantilever beam of circular section joint under the given loading of 10KN acting at the free end. We can see that stress curves of shell element are in good agreement with stress curves of solid element.

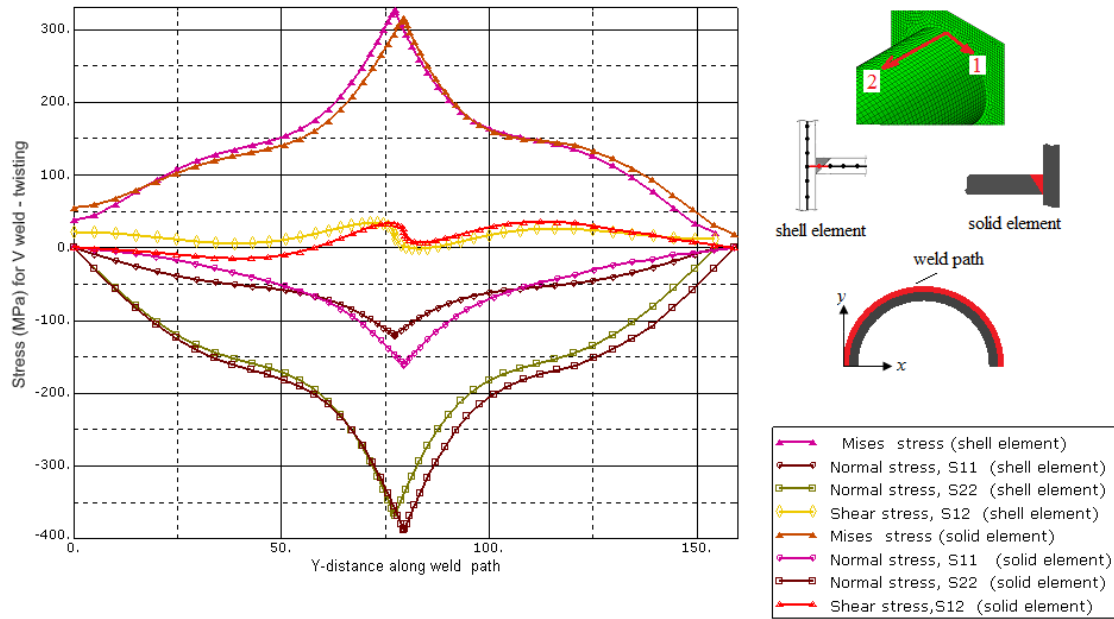


Figure 6.49 . Comparison of stress distribution between shell and solid elements along top weld path of circular section-twisting.

6.3.2 .5 Z - section

Figure 6.50 shows the stress distribution for shell and solid elements along weld path of a cantilever beam of Z section joint under the given loading of 1KN acting at the free end. We can see that stress curves of shell element are in good agreement with stress curves of solid element.

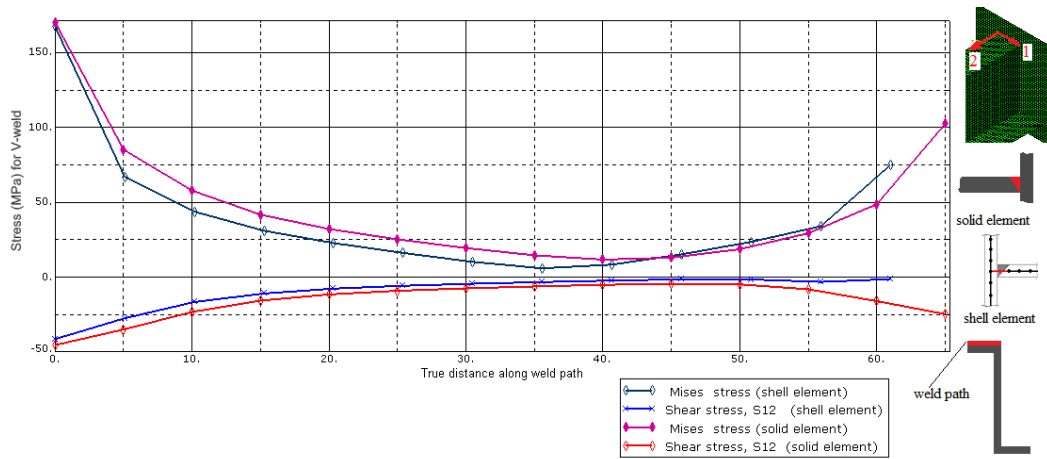


Figure 6.50. Comparison of stress distribution between shell and solid elements along horizontal weld path of Z section-twisting.

6.3.2.6 X - section

Figure 6.51 shows the stress distribution for shell and solid elements along weld path of a cantilever beam of X section joint under the given loading of 1KN acting at the free end. We can see that stress curves of shell element are in good agreement with stress curves of solid element.

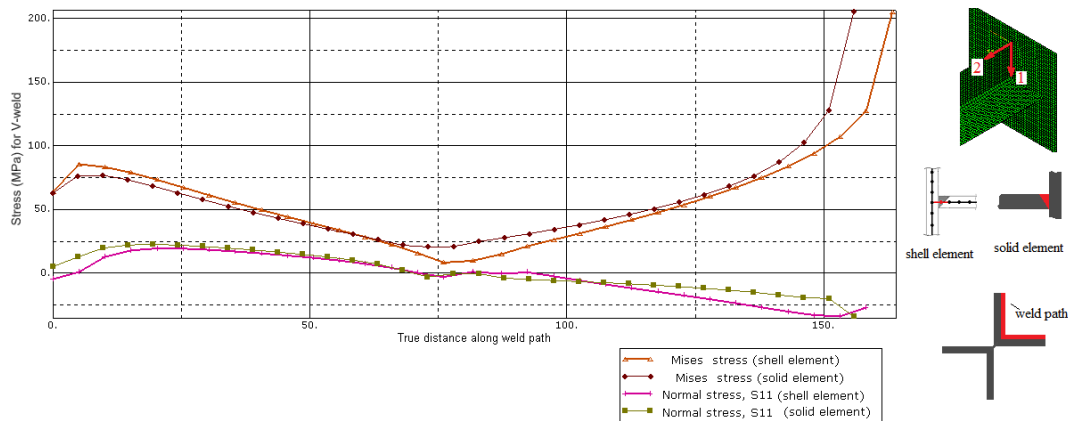


Figure 6.51 . Comparison of stress distribution between shell and solid elements along weld path of X section-twisting

6.4 Discussion

The numerical modeling of the v-welded joint connection was performed using Abaqus [59], the commercial finite element package. The developed FE model is based on the assumption of linear elasticity and small strains/displacements. Shell and solid elements

have been used for modeling both the beams and the welds in this study. Quadratic solid elements (20-noded) with three translational degrees-of-freedom at each node and quadratic shell elements (8-noded) with 6 degrees-of-freedom at each node were used to model the weld and the beam structure in order to accurately capture any non-linear stress gradients on the weld path. The study is summarized and concluded that stress curves of solid element are in good agreement with stress curves of shell element.

From the FEA results of the solid element model, a generally linear stress distribution across the thickness of the beams is observed. Therefore, the use of shell elements for the analysis of the beam-joint connection is appropriate.

The results show that the normal stresses in the 1 or 2-direction are the highest at the weld path (top of the path) on the top surface, and at horizontal weld path of the beam. It can be observed that the 1 or 2-direction component of normal stress causes the most damage. The values of the Von-Mises equivalent stresses are very close to the values of the stresses in the 1 or 2-direction (absolute value). This is expected as the stresses in the 1 or 2-direction are much larger than the other components of stress.

This means that the strains and stresses normal to the weld (i.e., 1 or 2 -direction in this study) are mainly responsible for plasticity/crack initiation and propagation.

Also the results show that the stress concentrations increase in the stiffened areas.

Chapter 7

Fillet weld modeling using solid and shell elements

This chapter focuses on the development of a predictive methodology for fillet welded structures using shell and solid element. However, three-dimensional finite element analysis of complete structural hollow sections can be complex and time-consuming. Due to the complex nature of the finite element analysis codes, this method has limited application. It can be used in research area but cannot be widely used by structural engineers in their real-world projects. Therefore, there is a need to develop a simplified modeling method that can be implemented by using commonly available commercial software and easily employed.

Finite element models with different modeling techniques and meshing with various size and types of elements were created and analyzed. In the modeling certain assumption were made to simplify the model. Parent metal and welded metal had the same material properties which are steel ($E = 210 \times 10^3 MPa, \nu = 0.3$)

7.1 Fillet weld modelling using solid elements

Modelling welds with deformable solid elements are widely used because of its simplicity in modelling work and its accuracy in results since the stiffness of welds can be modelled accurately. In solid element models, the geometry and stiffness of the welds in a welded joint can easily be represented by using solid elements, see Figure 7.1. But, three-dimensional finite element analysis of a complete structural hollow sections can be complex and time-consuming.

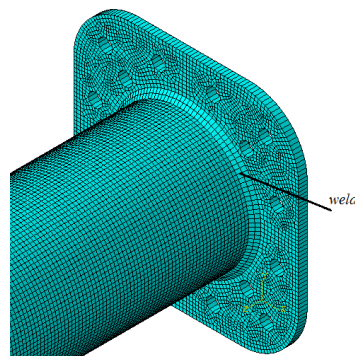


Figure 7.1 Modelling of the welds with solid elements.

Three-dimensional finite element analysis of complete structural hollow sections can be complex and time-consuming.

7.1.1 Finite element results of solid element model of fillet-weld in case of bending.

7.1.1.1 Rectangular cross-section

Figures 7.2 shows the stress distribution in top weld path of a cantilever rectangular hollow section joint under the given loading of 10K N acting upward at the free end. Solid elements and shell elements were used in this analysis.

The figure shows that the stress components S33, S13 and S23 are small compared with S11, S22 and S12. We conclude that the model can be modeled by using shell elements. Also, the figures show stress concentrations in the edges of the box profile. The distribution cannot be captured by using theoretical formula or by using beam elements.

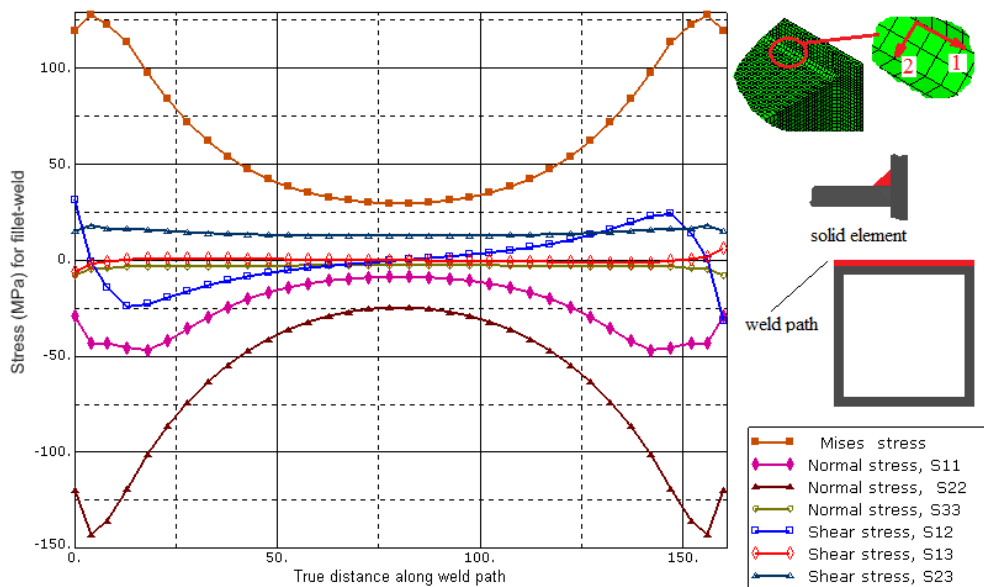


Figure 7.2 .Stress distribution along horizontal weld path of box profile-bending.

7.1.1.2 I-section

Figure7.3 shows the stress distribution in top weld path of a cantilever beam of I profile under the given loading of 10KN acting upward at the free end. Solid elements and shell elements were used in this analysis. The figure shows that the stress components S33, S13 and S23 are small compared with S11, S22 and S12. We conclude that the model can be modeled by using shell elements.

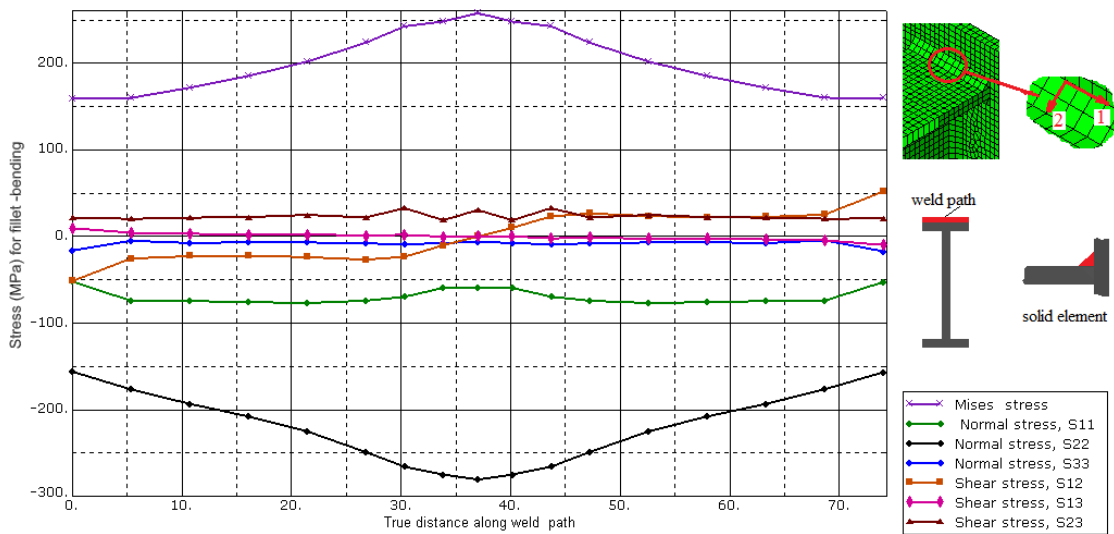


Figure 7.3 .Stress distribution along horizontal weld path of I section-bending.

7.1.1.3 C-section

Figure 7.4 shows the stress distribution in top weld path of a cantilever beam of C profile under the given loading of 10KN acting upward at the free end. Solid elements and shell elements were used in this analysis. The figure shows that the stress components S33, S13 and S23 are small compared with S11, S22 and S12. We conclude that the model can be modeled by using shell elements.

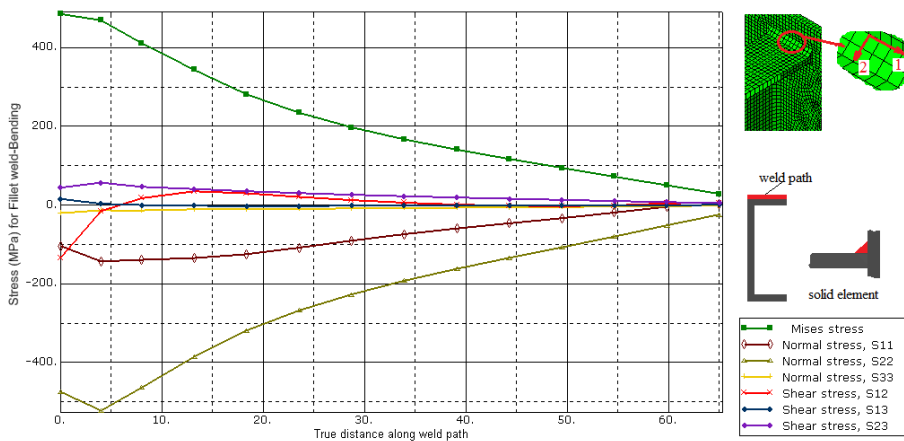


Figure 7.4 .Stress distribution along horizontal weld of C section-bending.

7.1.1.4 Circular-section

Figure 7.5 shows the stress distribution in top weld path of a cantilever beam of circular profile under the given loading of 10KN acting upward at the free end. Solid and shell elements were used in this analysis.

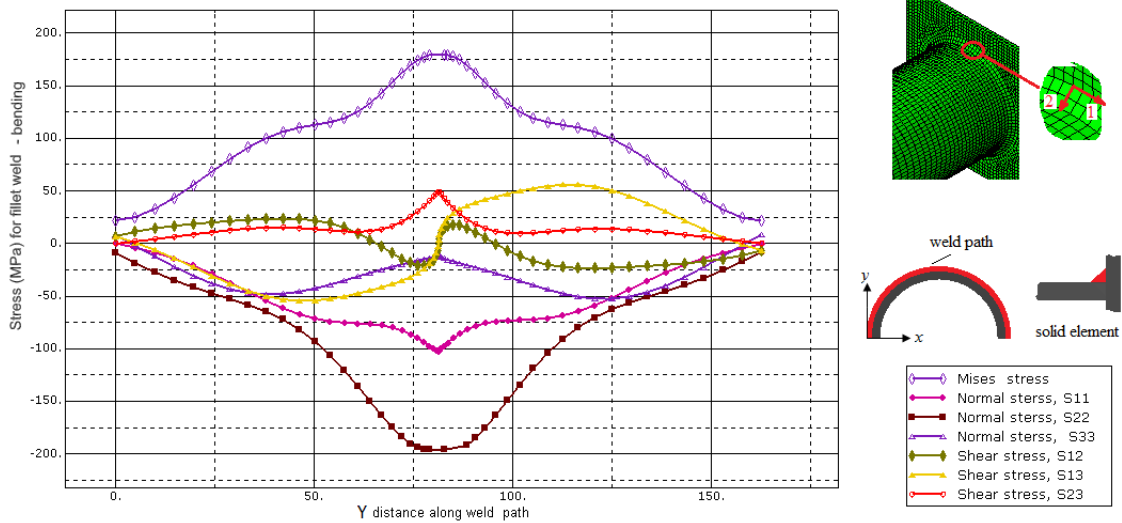


Figure 7.5 .Stress distribution along top weld path of circular section-bending. The results show stress concentration on the top of the v-weld.

7.1.1.5 Z-section

Figure 7.6 shows the stress distribution in top weld path of a cantilever beam of Z profile under the given loading of 10KN acting upward at the free end. Solid elements and shell elements were used in this analysis. The figure shows that the stress components S33, S13 and S23 are small compared with S11, S22 and S12. We conclude that the model can be modeled by using shell elements.

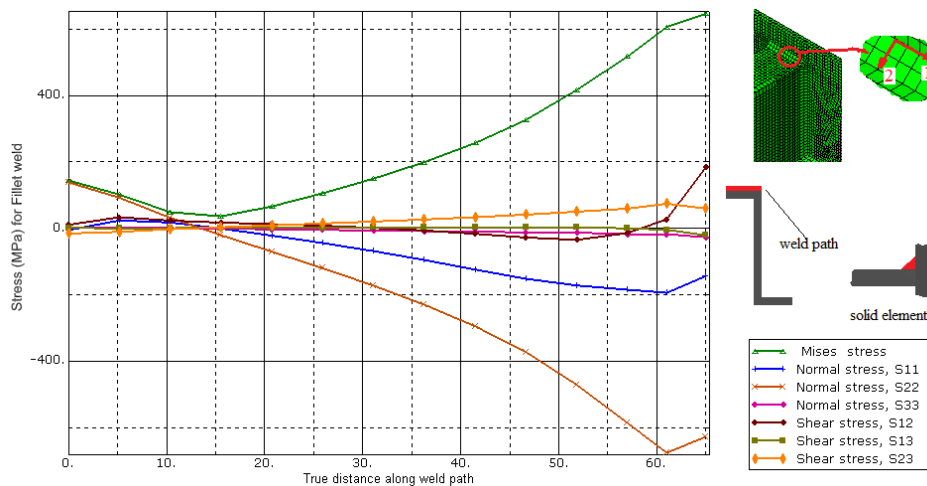


Figure 7. 6.Stress distribution along horizontal weld path of Z section-bending.

7.1.1.6 X-section

Figure 7.7 shows the stress distribution in top weld path of a cantilever beam of Z profile under the given loading of 10KN acting upward at the free end. Solid elements and shell

elements were used in this analysis. The figure shows that the stress components S33, S13 and S23 are small compared with S11, S22 and S12. We conclude that the model can be modeled by using shell elements.

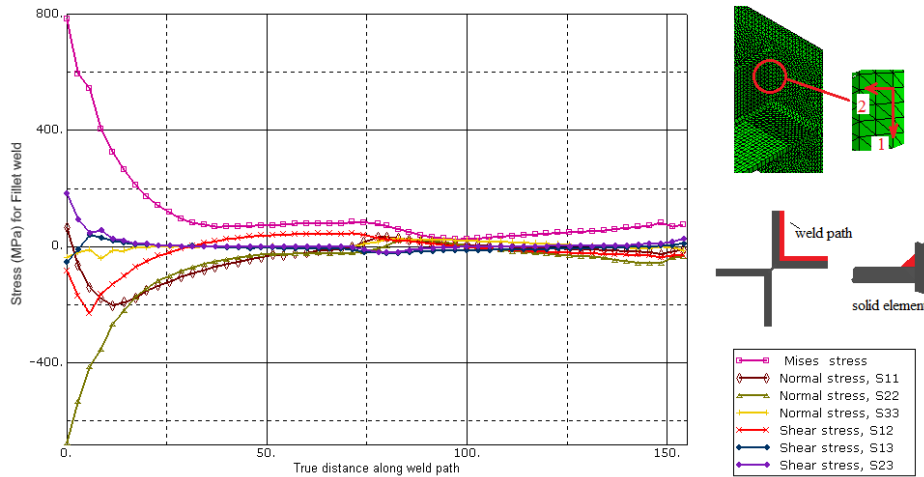


Figure 7. 7.Stress distribution along weld of X section-bending.

7.1.2 Finite element results of solid element model of fillet- weld in case of twisting.

7.1.2.1 Rectangular cross-section

Figure 7.8 shows the stress distribution in top weld path of a cantilever beam of box profile under the given loading of 10KN acting at the free end. Solid elements and shell elements were used in this analysis. It is clear that the normal stress S22 is maximum. Also, there is stress concentration in the edges of the weld.

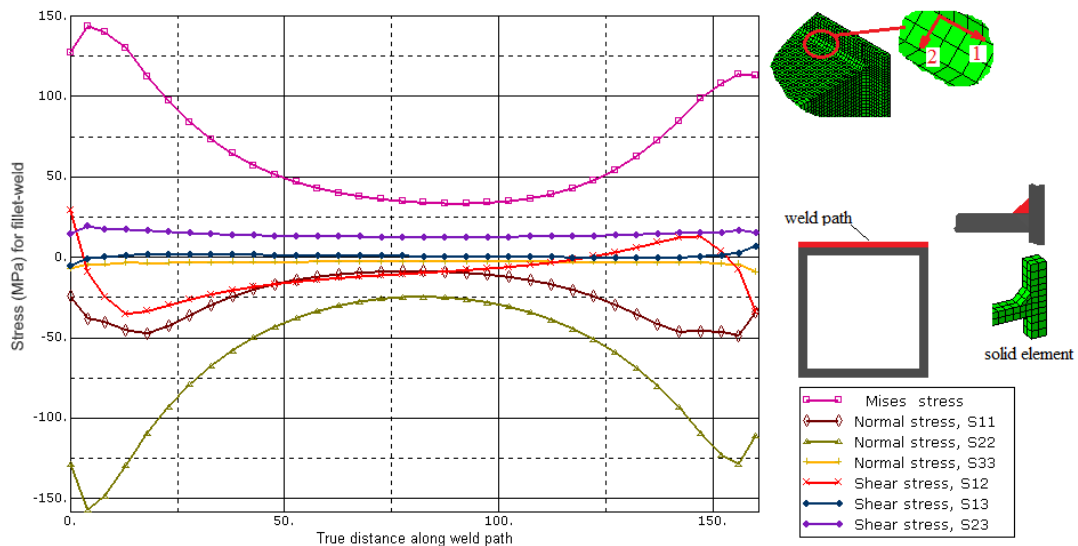


Figure 7.8 .Stress distribution along horizontal weld path of box section-twisting.

7.1.2.2 I-section

Figure 7.9 shows the stress distribution in top weld path of a cantilever beam of I profile under the given loading of 1KN acting at the free end. Solid elements and shell elements were used in this analysis. It is clear that the normal stress, S22 is maximum. Also, there is stress concentration in the edges of the weld.

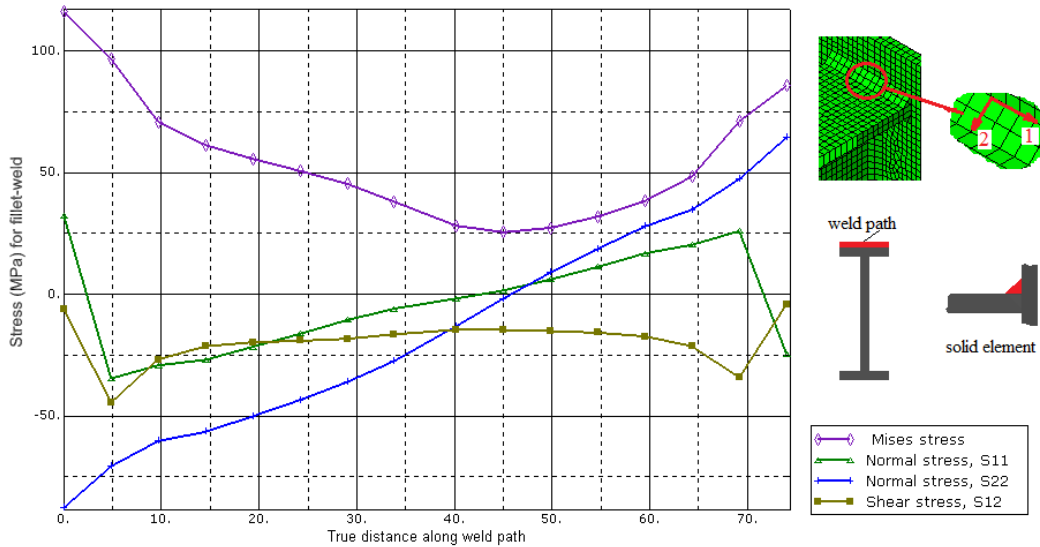


Figure 7.9 .Stress distribution along horizontal weld path of I section-twisting.

7.1.2.3 C-section

Figure 7.10 shows the stress distribution in top weld path of a cantilever beam of C profile under the given loading of 1KN acting at the free end. Solid elements and shell elements were used in this analysis. It is clear that the normal stress, S22 is maximum. Also, there is stress concentration in the edges of the weld.

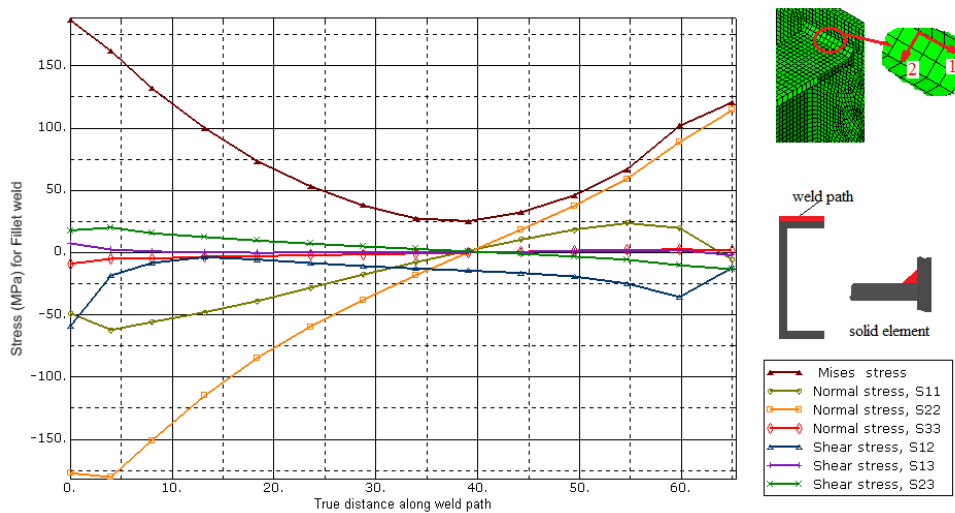


Figure 7.10 .Stress distribution along horizontal weld path of C section-twisting.

7.1.2.4 Circular -section

Figure 7.11 shows the stress distribution in top weld path of a cantilever beam of circular profile under the given loading of 10KN acting at the free end. Solid elements and shell elements were used in this analysis. It is clear that the normal stress, S22 is maximum. Also, there is stress concentration in the edges of the weld.

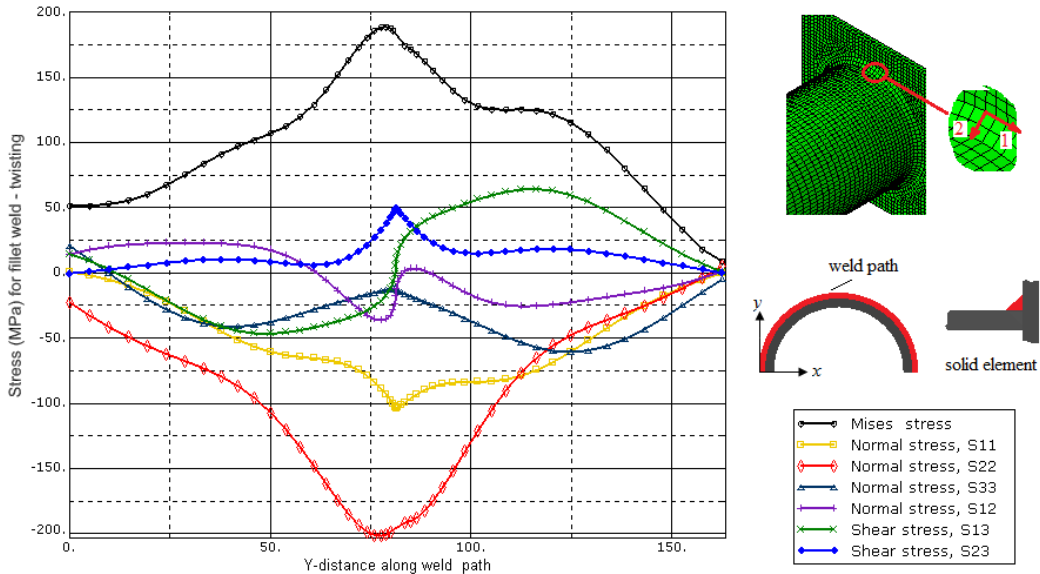


Figure 7. 11.Stress distribution along top weld of circular section-twisting.

7.1.2.5 Z –section

Figure 7.12 shows the stress distribution in top weld path of a cantilever beam of I profile under the given loading of 1KN acting at the free end. Solid elements and shell elements were used in this analysis. It is clear that the normal stress, S22 is maximum. Also, there is stress concentration in the edges of the weld.

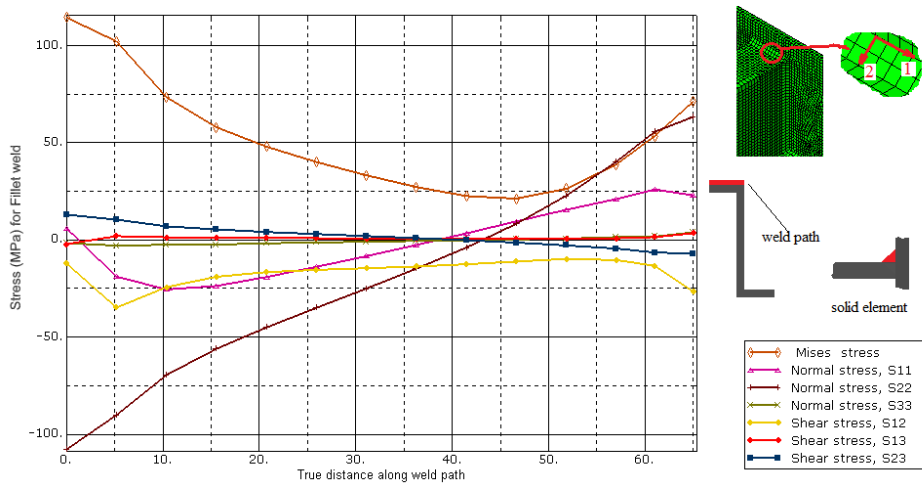


Figure 7. 12.Stress distribution along horizontal weld path of Z section-twisting.

7.1.2.6 X –section

Figure 7.13 shows the stress distribution along weld path of a cantilever beam of X profile under the given loading of 1KN acting at the free end. Solid elements and shell elements were used in this analysis. It is clear that the normal stress, S22 is maximum. Also, there is stress concentration on top of the weld.

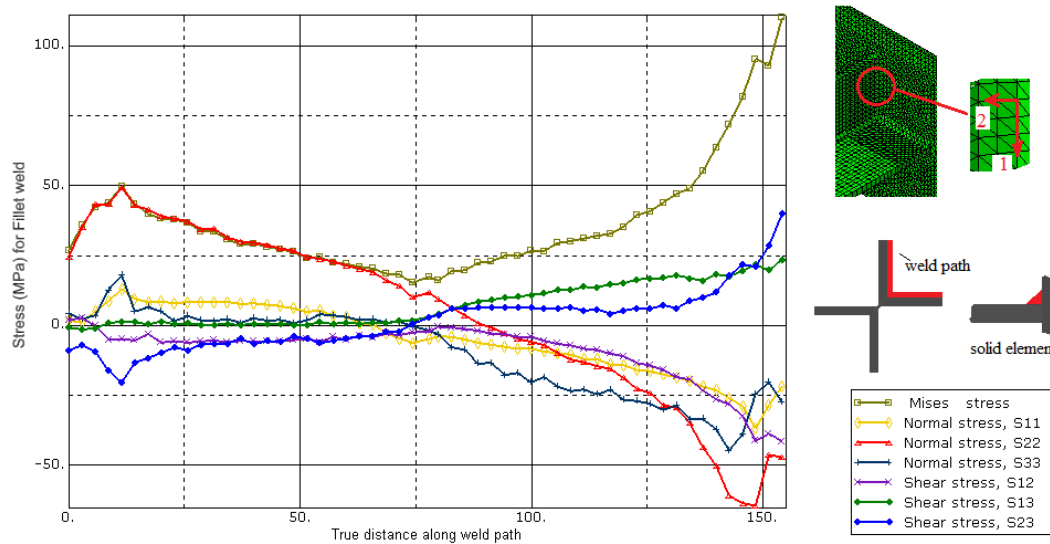


Figure 7.13 .Stress distribution along weld path of X section-twisting.

7.1.3 Discussion

All of the 6 components of the stress distributions (i.e., normal and shear) and the Von-Mises equivalent stresses at the connection are considered. It is important to examine these stresses in detail in order to obtain insight into the components of stress that cause the most damage. The dominating role of the normal stresses is in the 1 and 2 -direction in the thesis.

7.2 Fillet weld modeling using oblique shell elements

Shell elements generally have five degrees of freedom per node. Shell elements used in the analyses contained within this thesis contain six degrees of freedom per node. Shell elements are the main elements used in this section analysis.

In shell element models, the fillet welds in a welded joint can be represented using oblique shell elements. Both the stiffness and geometry of the welds can be correctly represented by utilizing this weld modelling technique. The attached plate should be joined to the main plate in the intersection as shown in Figure 7.14. The length of

inclined shell elements can be chosen as shown in this figure 7.14. The thickness of oblique shell elements can be defined same as the throat thickness of welds.

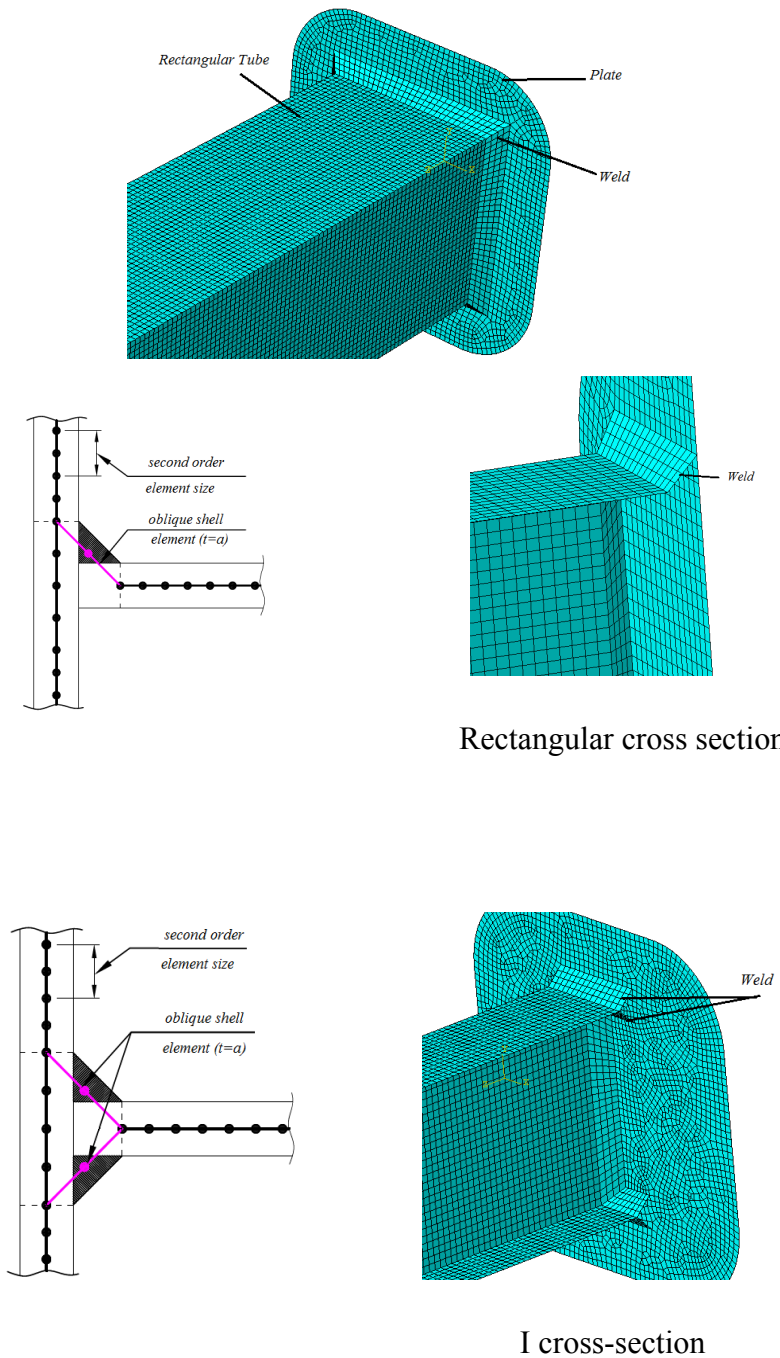


Figure 7.14 Weld modelling using oblique shell elements Shell Elements

7.2.1 Finite element results of shell element model of fillet- weld in case of bending.

7.2.1.1 Rectangular -section

Figure 7.15 shows the stress distribution in top weld path of a cantilever beam of box profile under the given loading of 10KN acting at the free end. Shell elements were used in this analysis. It is clear that the normal stress S22 is maximum. Also, there is stress concentration in the edges of the weld.

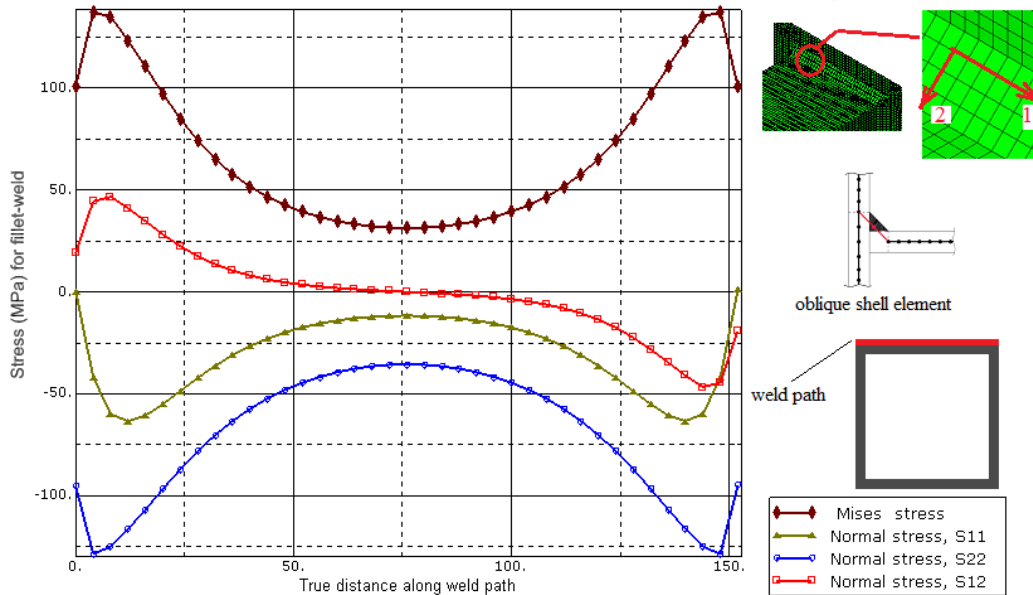


Figure 7.15 .Stress distribution along horizontal weld path of rectangular box-bending.

7.2.1.2 I-section

Figure 7.16 shows the stress distribution in top weld path of a cantilever beam of I profile under the given loading of 10KN acting at the free end. Shell elements were used in this analysis. It is clear that the normal stress S22 is maximum. Also, there is stress concentration in the stiffened area of the weld.

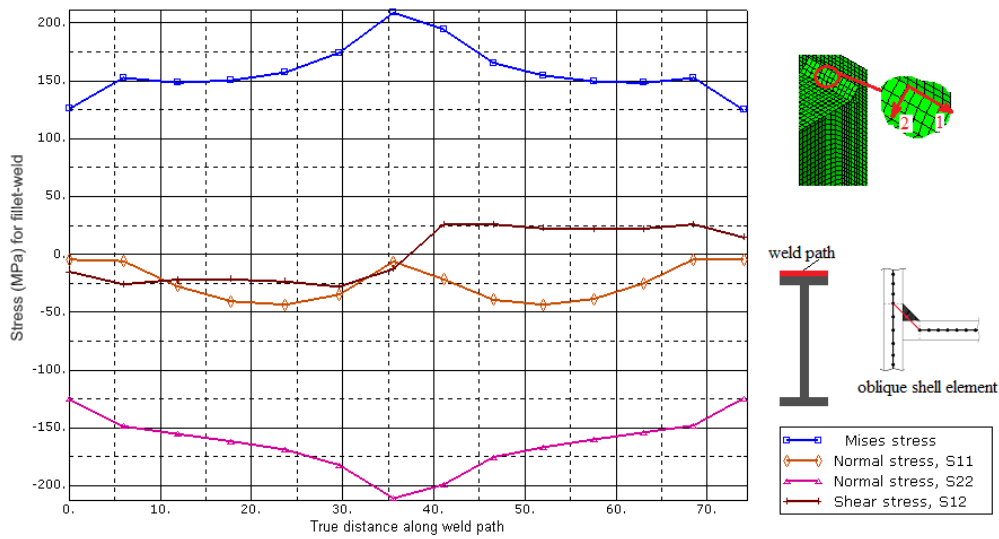


Figure 7.16 .Stress distribution along horizontal weld path of I section-bending.

7.2.1.3 C-section

Figure 7.17 shows the stress distribution in top weld path of a cantilever beam of C profile under the given loading of 10KN acting at the free end. Shell elements were used in this analysis. It is clear that the normal stress S22 is maximum. Also, there is stress concentration in the stiffened side of the weld.

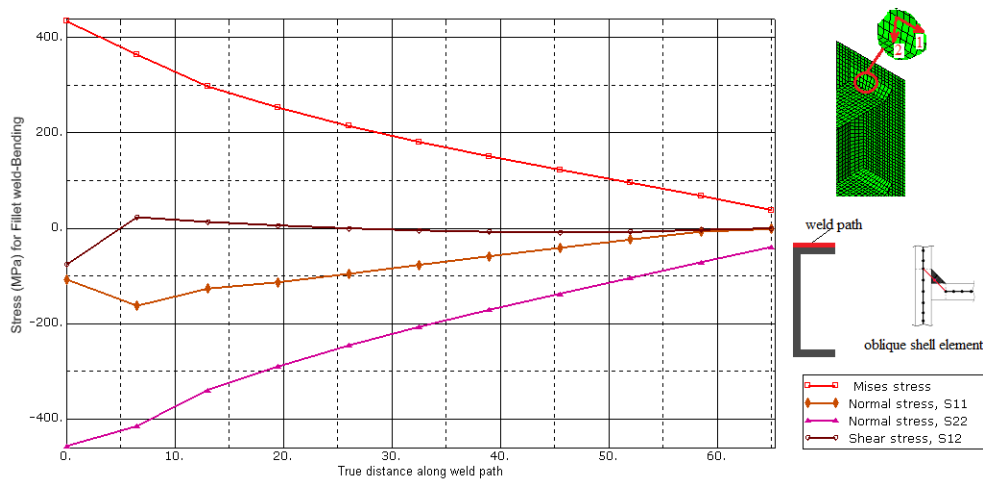


Figure 7.17 .Stress distribution along horizontal weld path of C section-bending.

7.2.1.4 Circular –section

Figure 7.18 shows the stress distribution in top weld path of a cantilever beam of circular profile under the given loading of 10KN acting at the free end. Shell elements were used in this analysis. It is clear that the normal stress S22 is maximum. Also, there is stress concentration in the top of the weld.

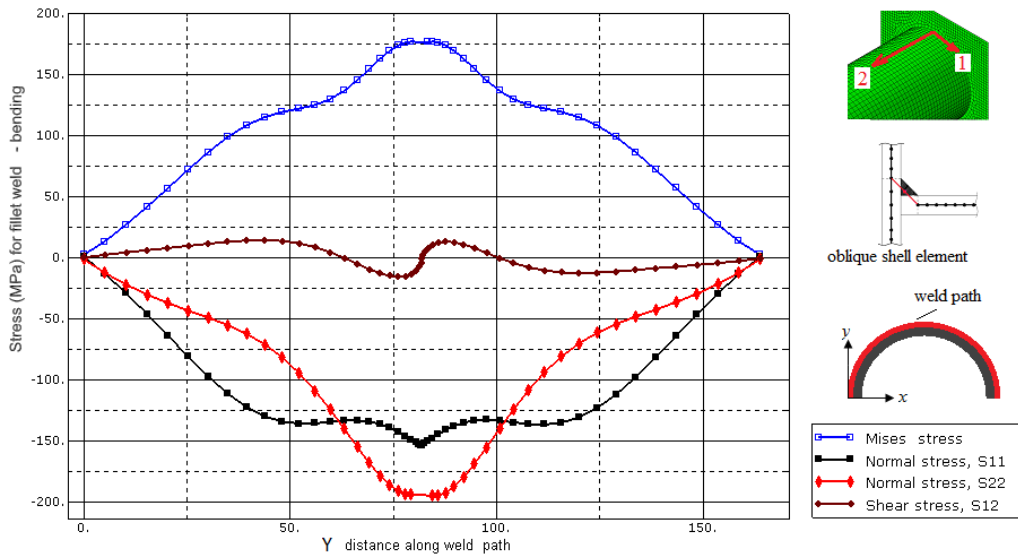


Figure 7.18 .Stress distribution along top weld path of cricular section-bending.

7.2.1.5 Z-section

Figure7.19 shows the stress distribution in top weld path of a cantilever beam of Z profile under the given loading of 10KN acting at the free end. Shell elements were used in this analysis. It is clear that the normal stress S22 is maximum. Also, there is stress concentration in the stiffened edge of the weld.

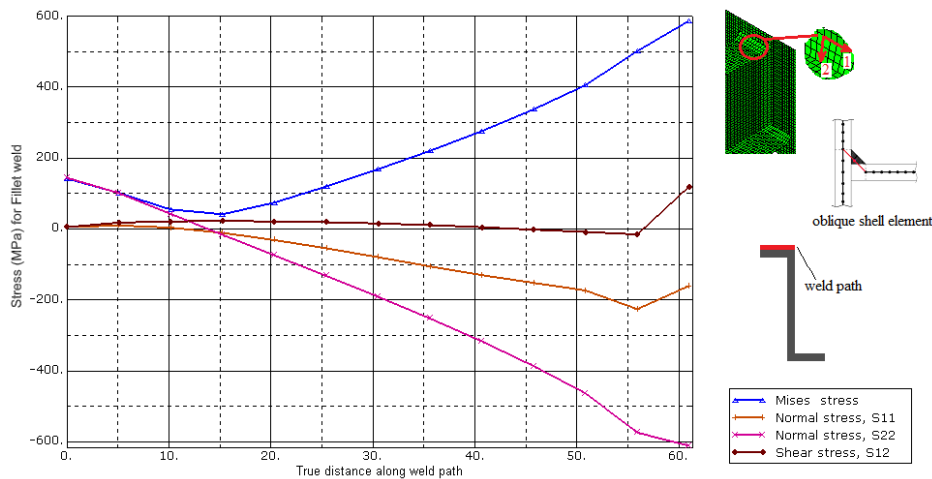


Figure 7.19 .Stress distribution along horizontal weld path of Z section -bending.

7.2.1.6 X-section

Figure7.20 shows the stress distribution in weld path of a cantilever beam of X profile under the given loading of 10KN acting at the free end. Shell elements were used in this

analysis. It is clear that the normal stress S22 is maximum. Also, there is stress concentration in the top area of the weld.

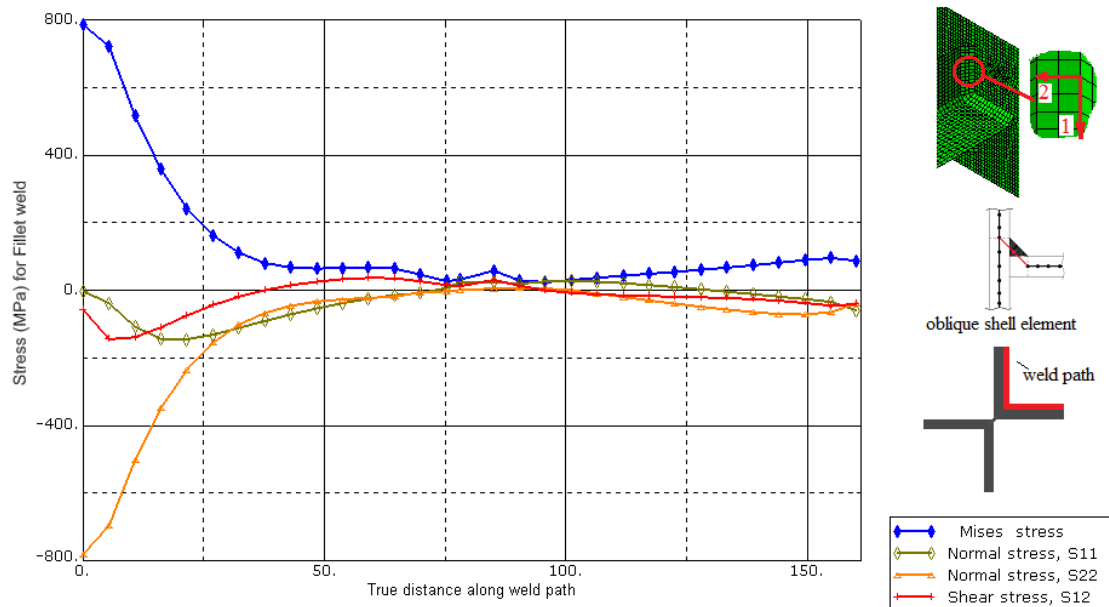


Figure 7. 20.Stress distribution along weld path of X section-bending.

The figure shows that the normal stresses in the 2-direction are the highest with a maximum value of approximately 800MPa at the weld path (top of the path) on the top surface, and 100 MPa at horizontal weld path of the beam. It can be observed that the 2-direction component of normal stress causes the most damage. The values of the Von-Mises equivalent stresses are very close to the values of the stresses in the 2-direction (absolute value). This is expected as the stresses in the 2-direction are much larger than the other components of stress.

This means that the strains and stresses normal to the weld (i.e., 1 or 2 -direction in this study) are mainly responsible for plasticity/crack initiation and propagation.

7.2.2 Finite element results of shell element model of fillet- weld in case of twisting.

7.2.2.1 Rectangular cross-section

Figure 7.21 shows the stress distribution in top weld path of a cantilever beam of box profile under the given loading of 10KN acting at the free end. Shell elements were used in this analysis. It is clear that the normal stress S22 is maximum. Also, there is stress concentration in the edges of the weld.

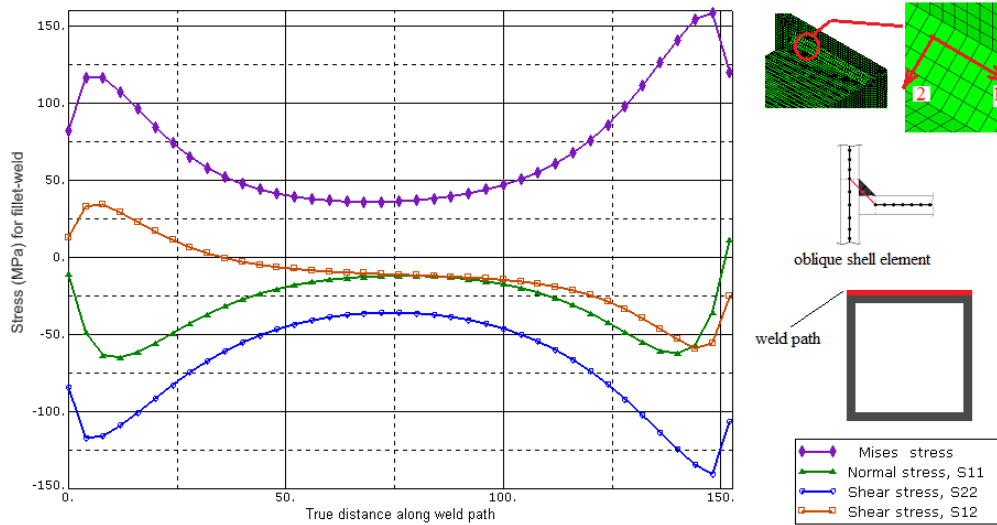


Figure 7.21 .Stress distribution along horizontal weld path of box section -twisting.

7.2.2.2 I-section

Figure 7.22 shows the stress distribution in top weld path of a cantilever beam of box profile under the given loading of 1KN acting at the free end. Shell elements were used in this analysis. It is clear that the normal stress S22 is maximum. Also, there is stress concentration in the edges of the weld.

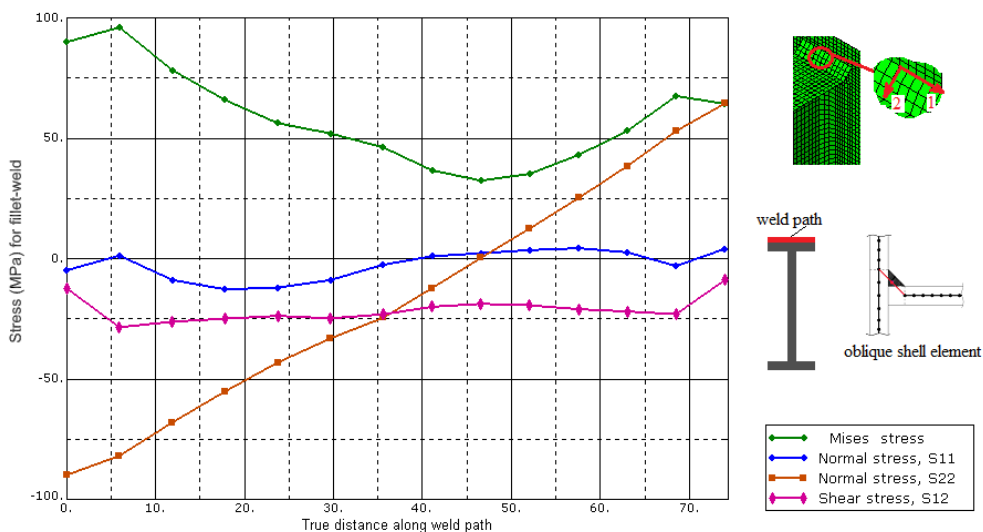


Figure 7.22 .Stress distributions along horizontal weld path of I section-twisting.

7.2.2.3 C-section

Figure 7.23 shows the stress distribution in top weld path of a cantilever beam of C profile under the given loading of 1KN acting at the free end. Shell elements were used

in this analysis. It is clear that the normal stress S22 is maximum. Also, there is stress concentration in the edges of the weld.

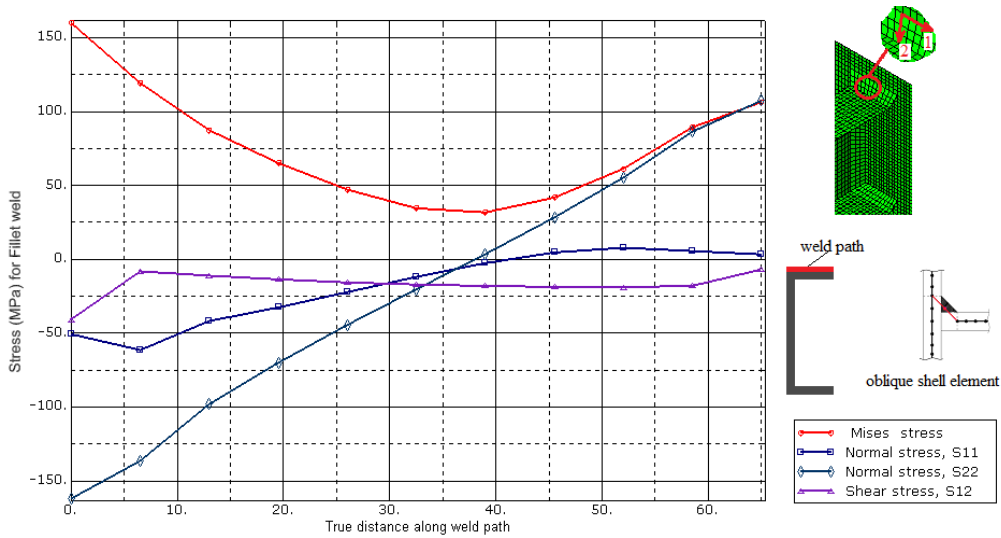


Figure 7.23 .Stress distribution along horizontal weld path of C section-twisting.

7.2.2.4 circular section

Figure 7.24 shows the stress distribution in top weld path of a cantilever beam of pipe profile under the given loading of 10KN acting at the free end. Shell elements were used in this analysis. It is clear that the normal stress S22 is maximum. Also, there is stress concentration in the top of the weld.

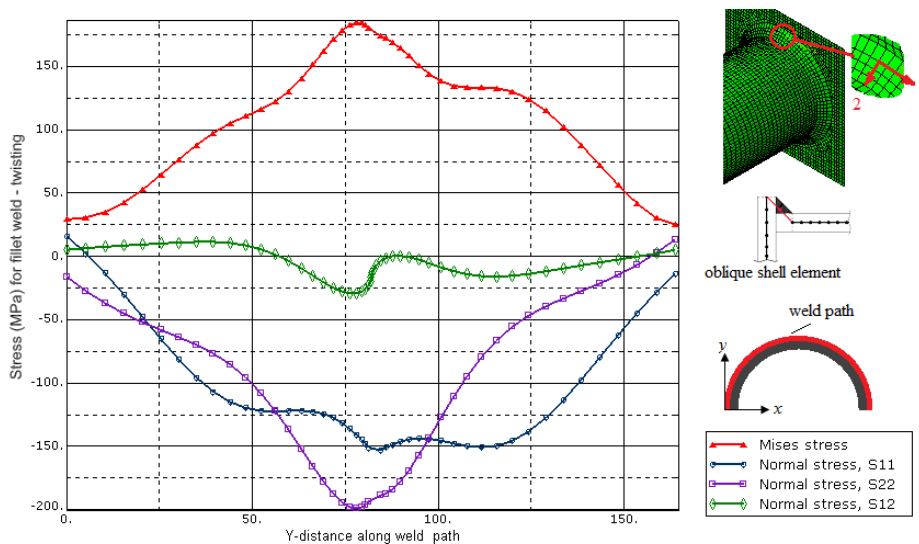


Figure 7.24 .Stress distribution along horizontal weld path of pipe section-twisting.

7.2.2.5 Z- section

Figure 7.25 shows the stress distribution in top weld path of a cantilever beam of Z profile under the given loading of 1KN acting at the free end. Shell elements were used in this analysis. It is clear that the normal stress S22 is maximum. Also, there is stress concentration in the edges of the weld.

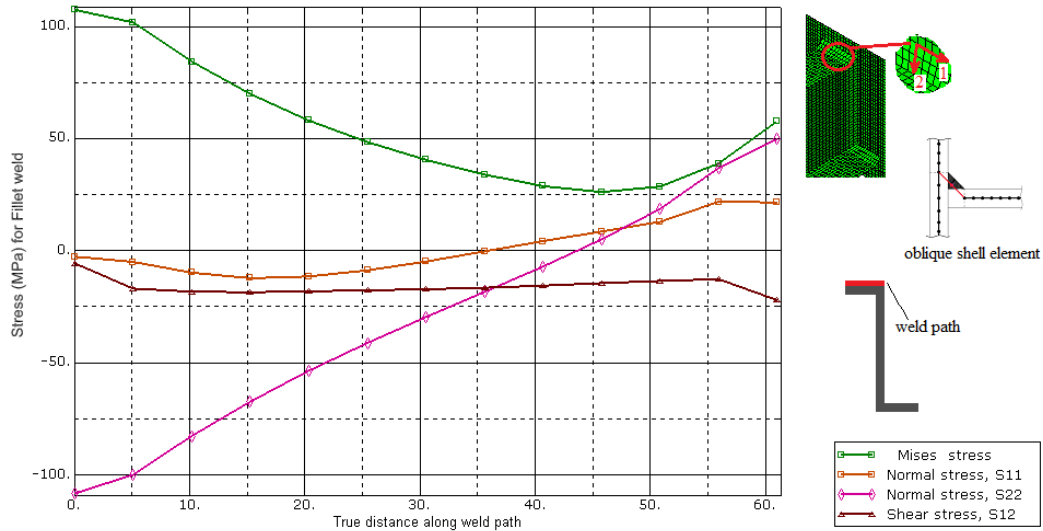


Figure 7.25 .Stress distribution along horizontal weld path of Z section-twisting.

7.2.2.6 X- section

Figure 7.26 shows the stress distribution in weld path of a cantilever beam of X profile under the given loading of 1KN acting at the free end. Shell elements were used in this analysis. It is clear that the normal stress S22 is maximum. Also, there is stress concentration in the edge of the weld.

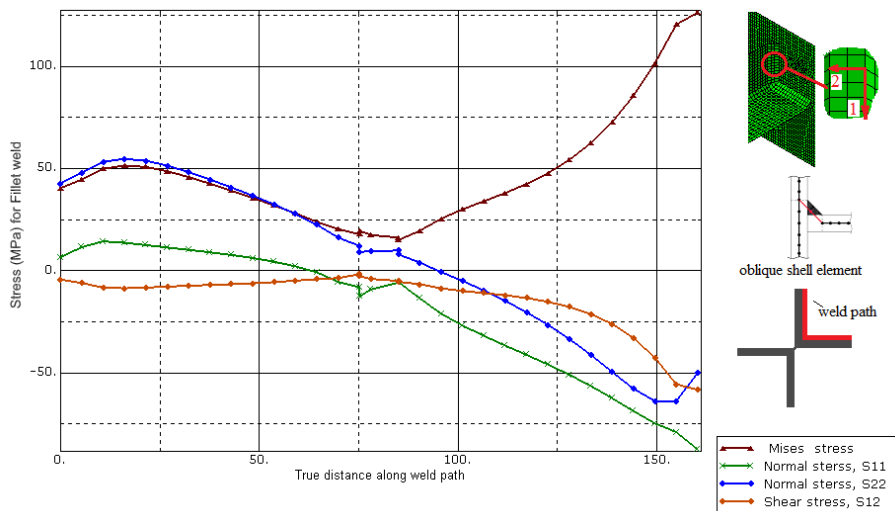


Figure 7.26 .Stress distribution along weld path of X section -twisting.

7.3 Comparison between solid and shell elements of fillet welds

7.3.1 Case(a) Bending

7.2.1.1 Rectangular cross-section

Figure 7.27 shows the stress distribution for shell and solid elements along weld path of a cantilever beam of box section joint under the given loading of 10KN acting at the free end. We can see that stress curves of shell element are in good agreement with stress curves of solid element.

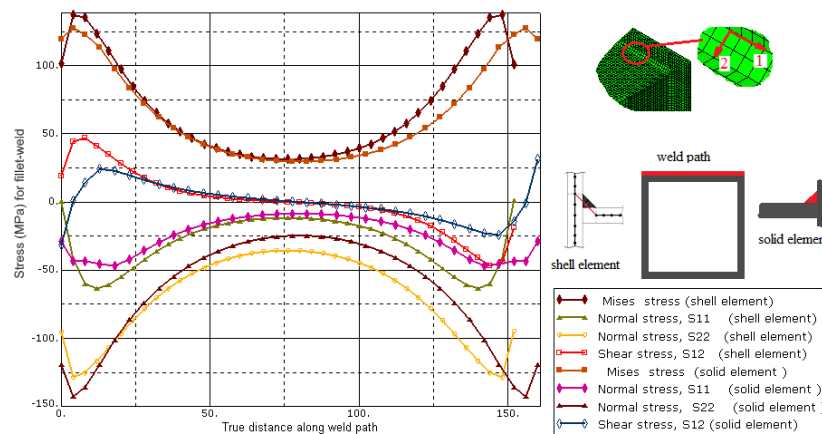


Figure 7.27 . Comparison of stress distribution between shell and solid elements along horizontal weld path of box section-bending.

7.3.1.2 I-section

Figure 7.28 shows the stress distribution for shell and solid elements along weld path of a cantilever beam of I section joint under the given loading of 1KN acting at the free end. We can see that stress curves of shell element are in good agreement with stress curves of solid element.

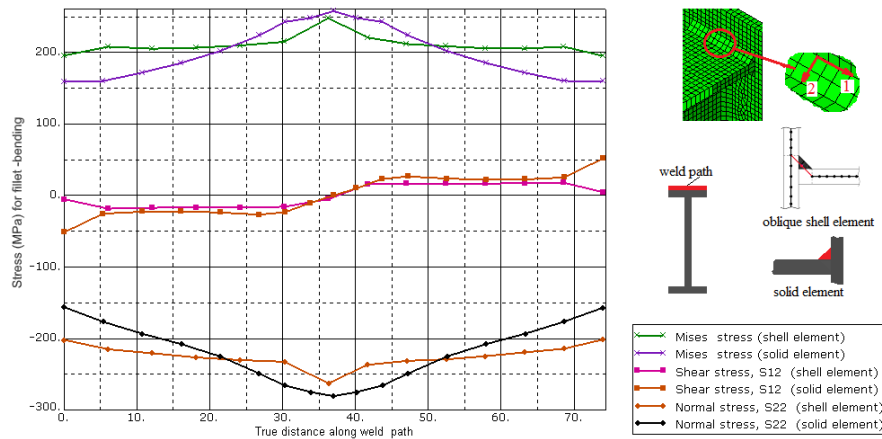


Figure 7.28 . Comparison of stress distribution between shell and solid elements along horizontal weld path of I section-bending.

7.3.1.3 C-section

Figure 7.29 shows the stress distribution for shell and solid elements along weld path of a cantilever beam of C section joint under the given loading of 1KN acting at the free end. We can see that stress curves of shell element are in good agreement with stress curves of solid element.

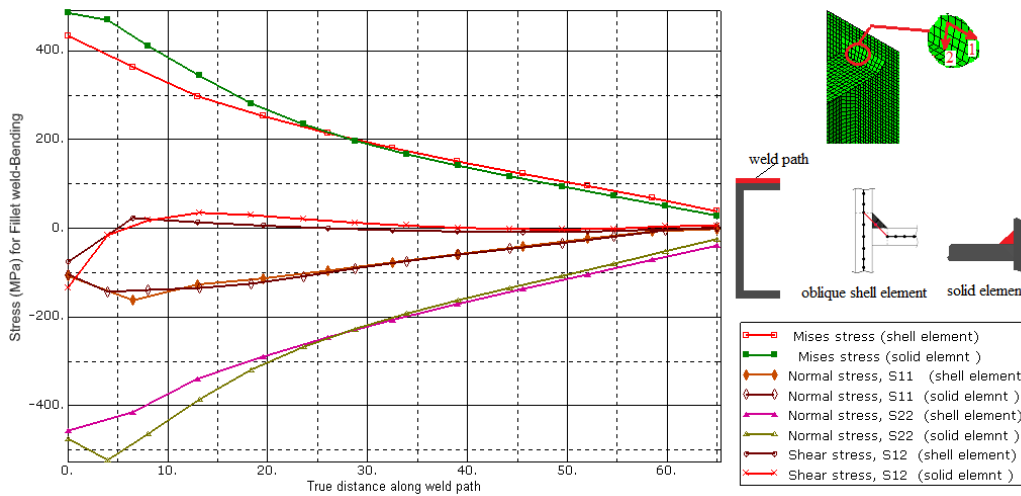


Figure 7.29 . Comparison of stress distribution between shell and solid elements along horizontal weld path of C section -bending.

7.3.1.4 Circular-section

Figure 7.30 shows the stress distribution for shell and solid elements along weld path of a cantilever beam of circular section joint under the given loading of 10KN acting at the

free end. We can see that stress curves of shell element are in good agreement with stress curves of solid element.

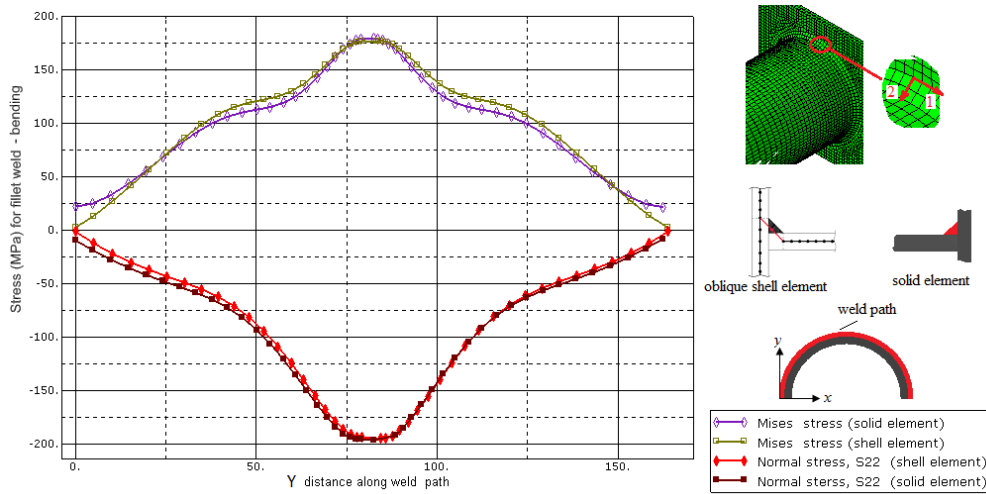


Figure 7.30 . Comparison of stress distribution between shell and solid elements along horizontal weld path of Circular section -bending.

7.3.1.5 Z-section

Figure 7.31 shows the stress distribution for shell and solid elements along weld path of a cantilever beam of Z section joint under the given loading of 1KN acting at the free end. We can see that stress curves of shell element are in good agreement with stress curves of solid element.

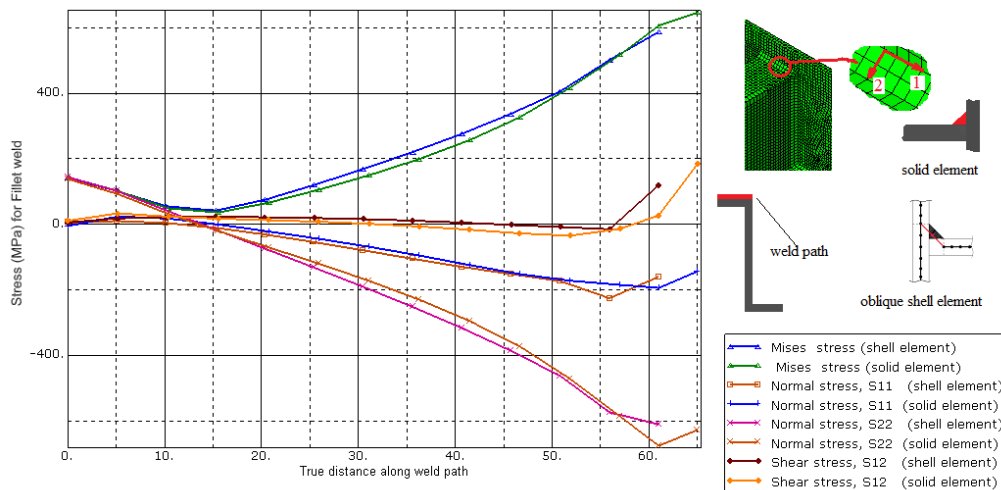


Figure 7.31 . Comparison of stress distribution between shell and solid elements along horizontal weld path of Z section-bending.

7.3.1.6 X-section

Figure 7.32 shows the stress distribution for shell and solid elements along weld path of a cantilever beam of X section joint under the given loading of 1KN acting at the free end. We can see that stress curves of shell element are in good agreement with stress curves of solid element.

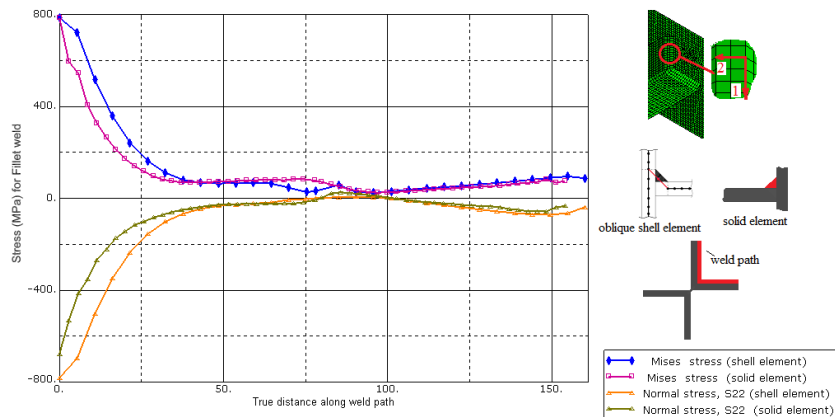


Figure 7.32 . Comparison of stress distribution between shell and solid elements along weld path of X section -bending.

7.3.2 Case (b) Twisting

7.3.2.1 Rectangular cross-section

Figure 7.33 shows the stress distribution for shell and solid elements along weld path of a cantilever beam of box section joint under the given loading acting at the free end. We can see that stress curves of shell element are in good agreement with stress curves of solid element.

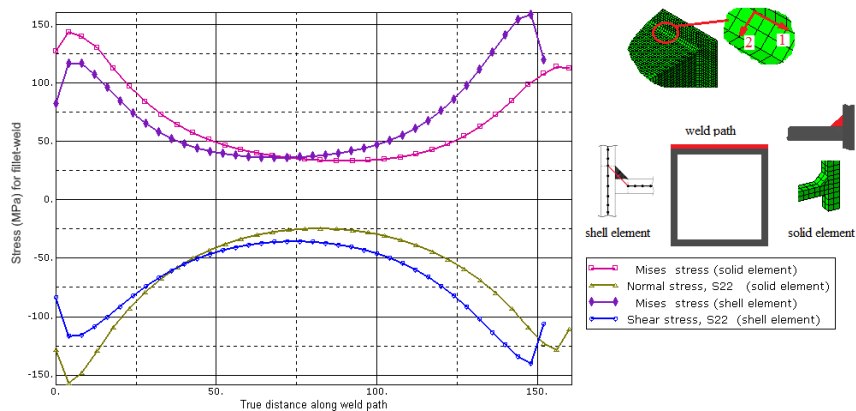


Figure 7.33 . Comparison of stress distribution between shell and solid elements along horizontal weld path of box section -twisting.

7.3.2.2 I-section

Figure 7.34 shows the stress distribution for shell and solid elements along weld path of a cantilever beam of I section joint under the given loading of 1KN acting at the free end. We can see that stress curves of shell element are in good agreement with stress curves of solid element.

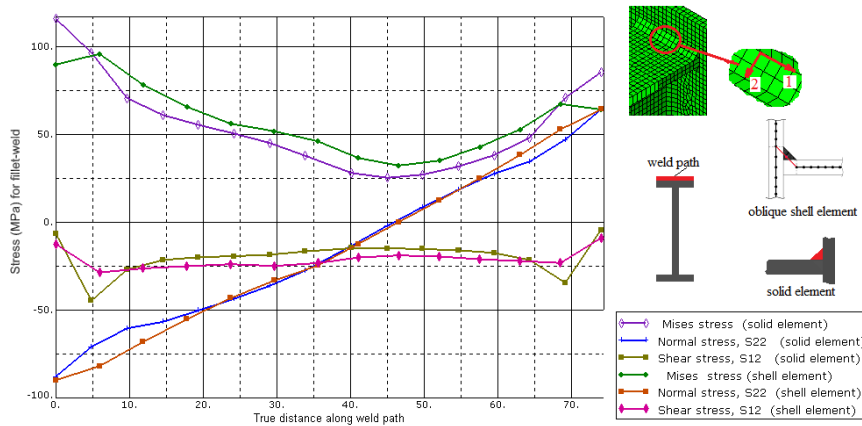


Figure 7.34 . Comparison of stress distribution between shell and solid elements along horizontal weld path of I section-twisting.

7.3.2.2 C-section

Figure 7.35 shows the stress distribution for shell and solid elements along weld path of a cantilever beam of C section joint under the given loading of 1KN acting at the free end. We can see that stress curves of shell element are in good agreement with stress curves of solid element.

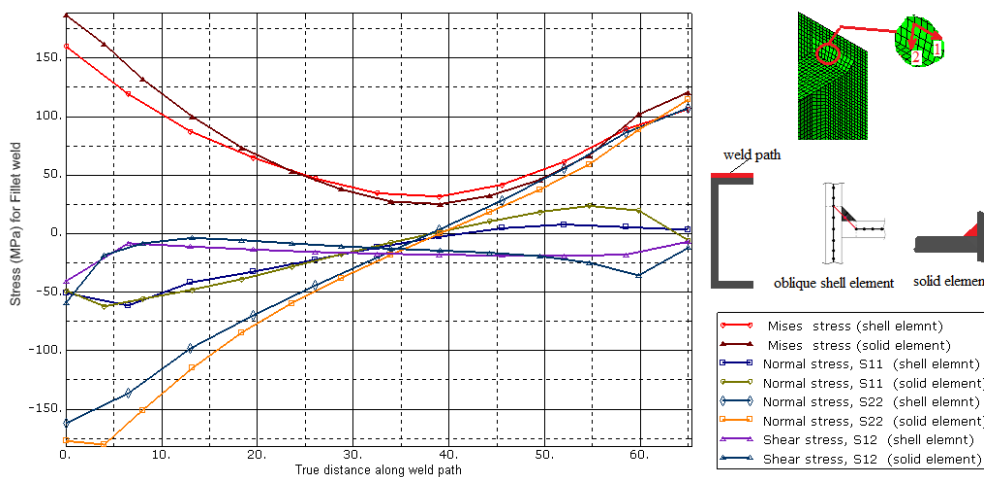


Figure 7.35 . Comparison of stress distribution between shell and solid elements along horizontal weld path of C section-twisting.

7.3.2.2 Circular-section

Figure 7.36 shows the stress distribution for shell and solid elements along weld path of a cantilever beam of circular section joint under the given loading of 10KN acting at the free end. We can see that stress curves of shell element are in good agreement with stress curves of solid element.

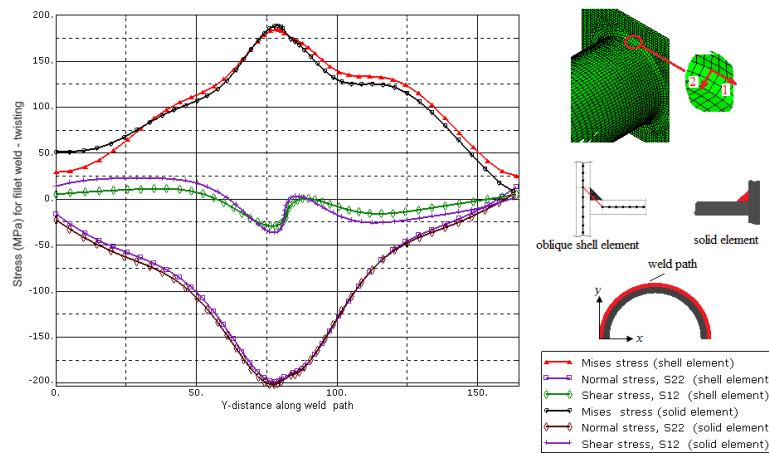


Figure 7.36 . Comparison of stress distribution between shell and solid elements along top weld path of circular section-twisting.

7.3.2.5 Z-section

Figure 7.37 shows the stress distribution for shell and solid elements along weld path of a cantilever beam of Z profile under the given loading of 1KN acting at the free end. We can see that stress curves of shell element are in good agreement with stress curves of solid element.

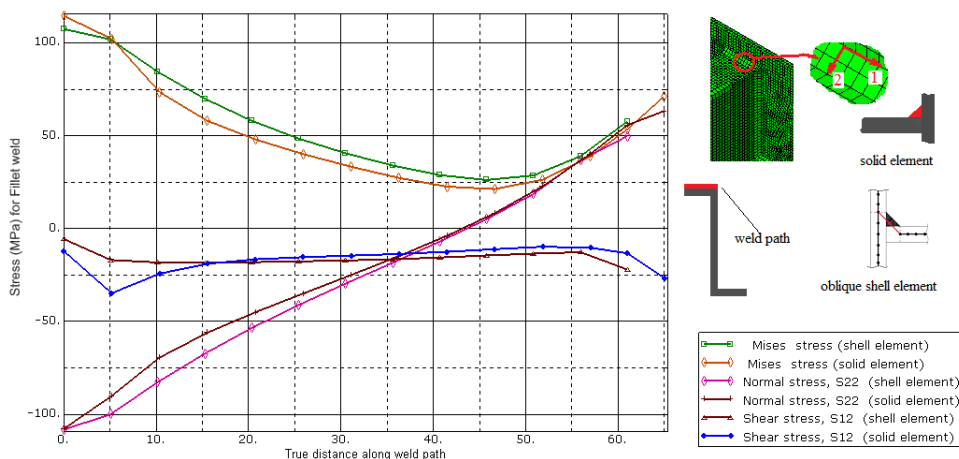


Figure 7. 37. Comparison of stress distribution between shell and solid elements along horizontal weld path of Z section-twisting.

7.3.2.6 X-section

Figure 7.38 shows the stress distribution for shell and solid elements along weld path of a cantilever beam of X profile under the given loading of 1KN acting at the free end. We can see that stress curves of shell element are in good agreement with stress curves of solid element.

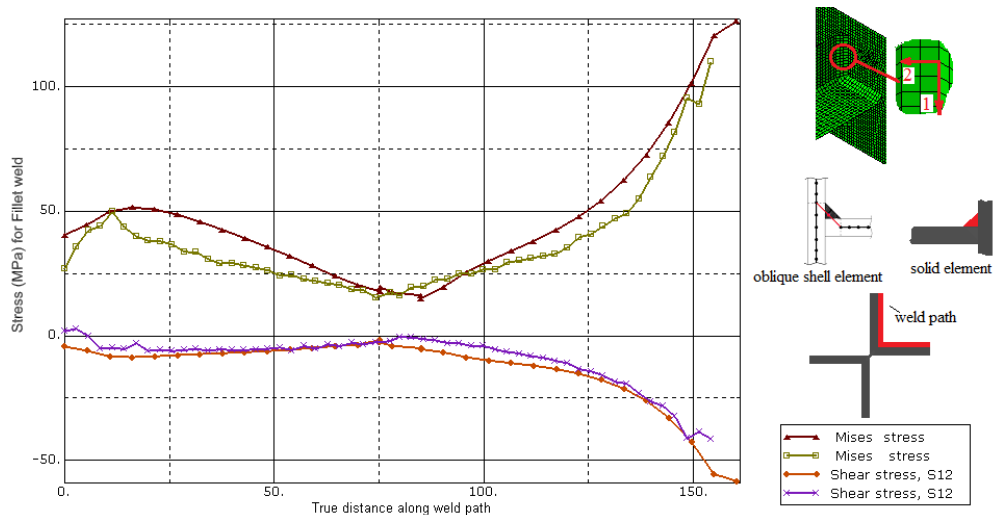


Figure 7.38 . Comparison of stress distribution between shell and solid elements along weld path of X section-twisting.

7.4 Comparison between V and fillet welds

This section introduces the comparison between fillet and V welds in case of bending for different beam sections.

7.4.1 Box section

The Comparison of Mises stress distribution of v-weld, fillet weld and beam along the top of weld path box profile in case of bending is shown in figure 7.39. The results show that the fillet weld has high stress gradient while v-weld has low stress gradient. The stress concentration at the edges of the v-weld is higher than the stress concentration of the fillet weld.

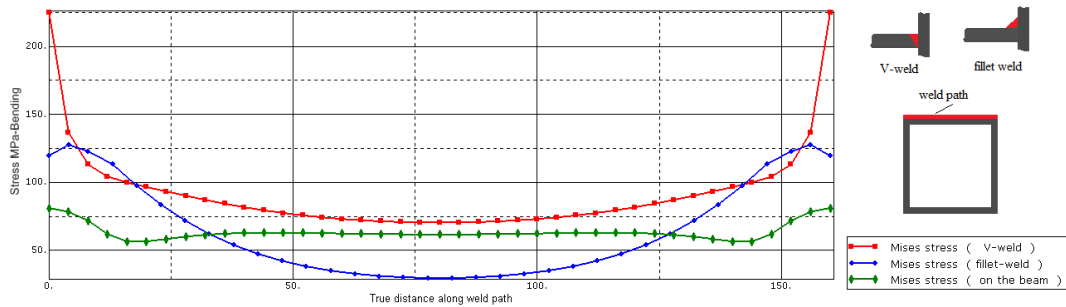


Figure 7.39 . Comparison of Mises stress distribution of v-weld ,fillet weld and beam along horizontal weld path of box profile-bending.

7.4.2 I section

It is seen from Figure 7.40 which represents Comparison of Mises stress distribution of v-weld, fillet weld and beam along weld path of I profile in case of bending. The v weld has higher stress concentration than the fillet weld. From this figure, we can conclude that the fillet weld is better than v-weld for I profile.

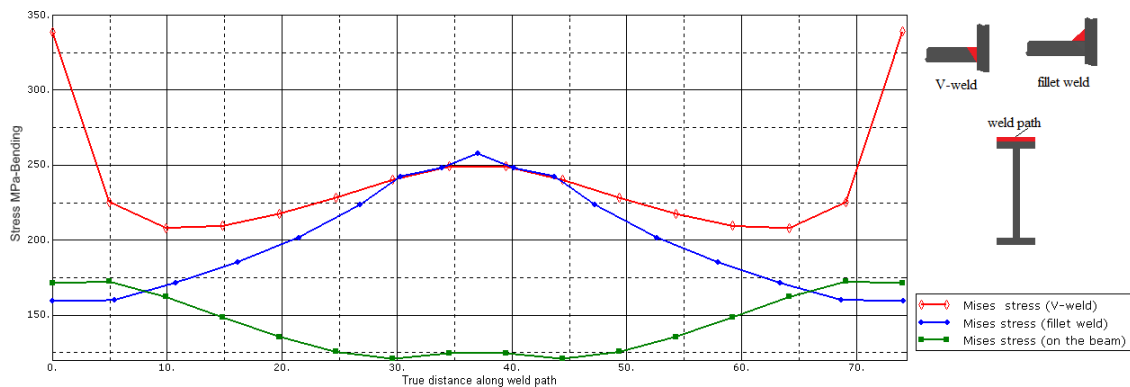


Figure 7.40 . Comparison of Mises stress distribution of v-weld ,fillet weld and beam along weld path of I profile-bending.

7.4.3 C section

Figure 7.41 shows the comparison of Mises stress distribution of v-weld ,fillet weld and beam along weld path of C profile in case of bending. We can see form this figure that v weld has higher stress than the fillet weld. This comparison leads us to conclude that the fillet weld is better that v-weld for C profile.

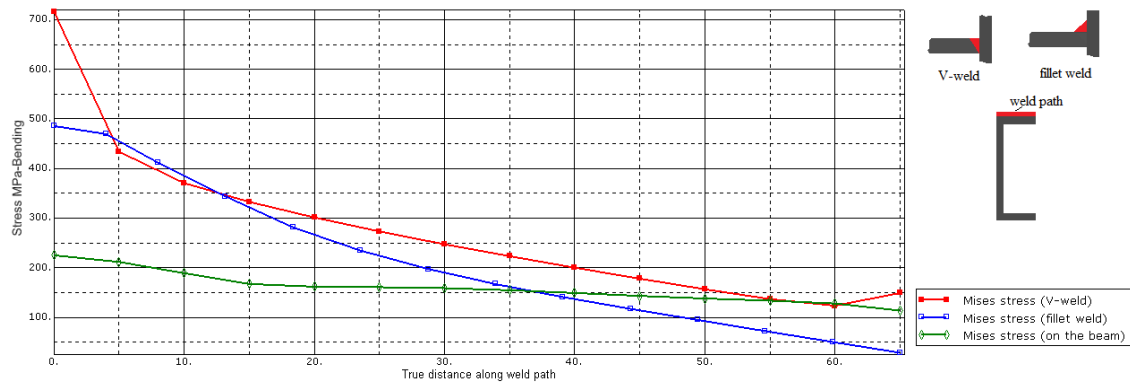


Figure 7.41 . Comparison of Mises stress distribution of v-weld ,fillet weld and beam along weld path of C profile-bending.

7.4.4 Circular section

Figure 7.42 shows the comparison of Mises stress distribution of v-weld ,fillet weld and beam along weld path of circular section profile in case of bending. It is clear from the figure that v-weld has high stress concentration while the fillet weld has lower stress concentration. This means fillet weld is better than v weld for this profile.

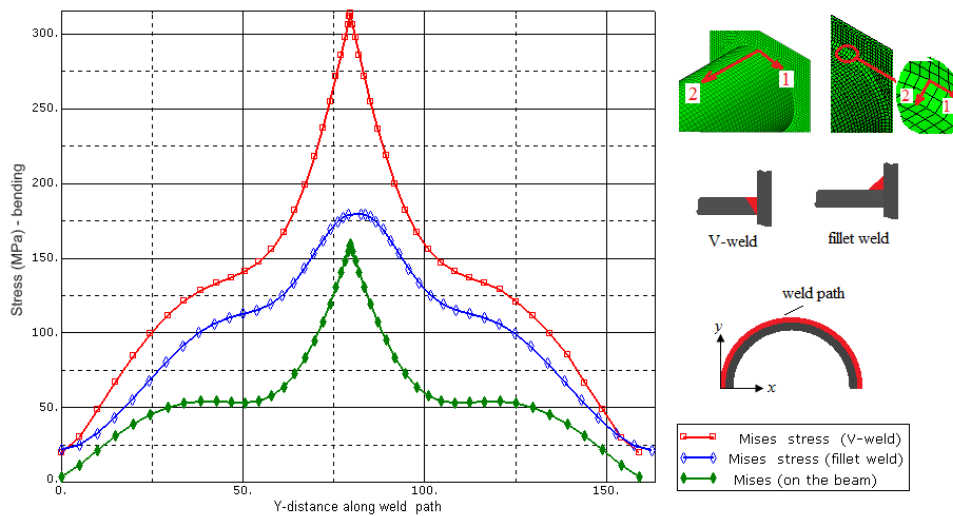


Figure 7.42 . Comparison of Mises stress distribution of v-weld ,fillet weld and beam along weld path of circular profile-bending.

7.4.5 Z section

Figure 7.43 shows the comparison of Mises stress distribution of v-weld ,fillet weld and beam along weld path of Z profile in case of bending. It is clear from the figure that v-

weld has high stress concentration while the fillet weld has lower stress concentration. This means fillet weld is better than v weld for Z profile.

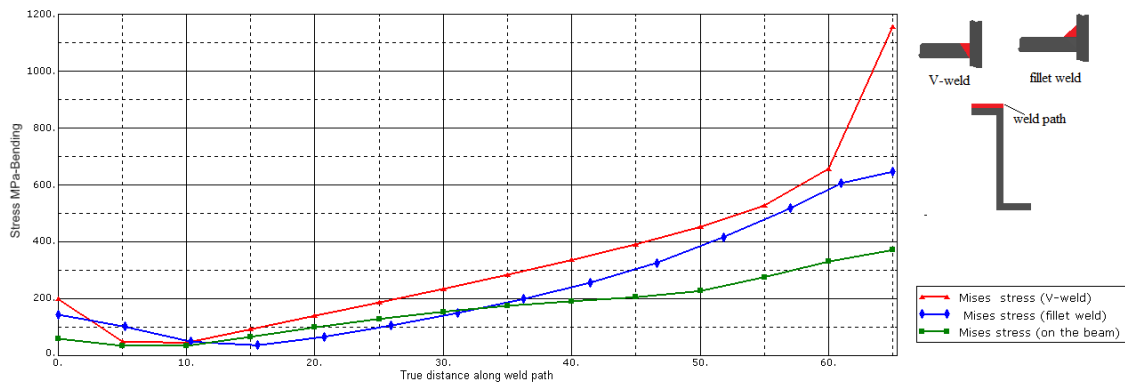


Figure 7.43 . Comparison of Mises stress distribution of v-weld ,fillet weld and beam along weld path of Z profile-bending.

7.4.6 X section

Figure 7.44 shows the comparison of Mises stress distribution of v-weld ,fillet weld and beam along weld path of X profile in case of bending. It is clear from the figure that v-weld has high stress concentration while the fillet weld has lower stress concentration. This means fillet weld is better than v weld for X profile.

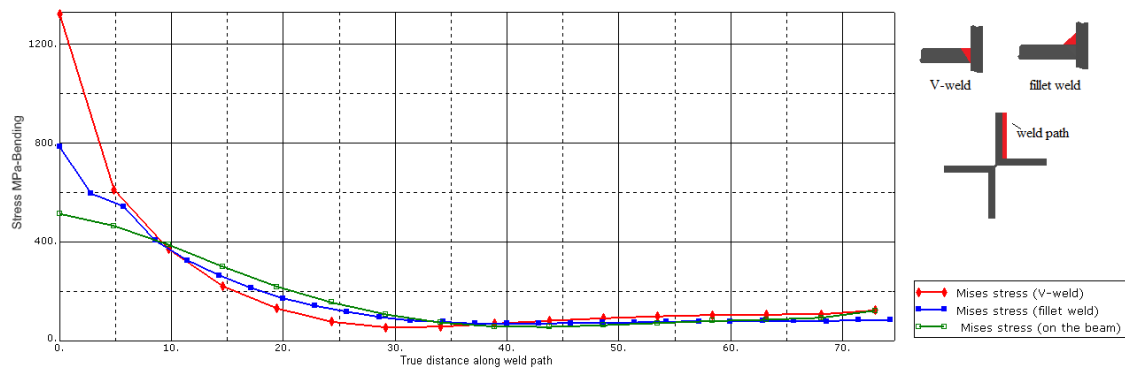


Figure 7.44 . Comparison of Mises stress distribution of v-weld ,fillet weld and beam along weld path of X profile-bending.

7.5 Discussion

The numerical modeling of the fillet welded joint connection was performed using Abaqus [59], the commercial finite element package. The developed FE model is based on the assumption of linear elasticity and small strains/displacements. Shell and solid elements have been used for modeling both the beams and the welds in this study.

Quadratic solid elements (20-noded) with three translational degrees-of-freedom at each node and quadratic shell elements (8-noded) with 6 degrees-of-freedom at each node were used to model the weld and the beam structure, in order to accurately capture any non-linear stress gradients on the beam. The study was summarised and concluded that stress curves of solid element are in good agreement with stress curves of shell element. The results show that the normal stresses in the 1 or 2-direction are the highest at the weld path (top of the path) on the top surface, and at horizontal weld path of the beam. It can be observed that the 1 or 2-direction component of normal stress causes the most damage. The values of the Von-Mises equivalent stresses are very close to the values of the stresses in the 1 or 2-direction (absolute value). This is expected as the stresses in the 1 or 2-direction are much larger than the other components of stress.

This means that the strains and stresses normal to the weld (i.e., 1 or 2 -direction in this study) are mainly responsible for plasticity/crack initiation and propagation.

The results of the box profile show that the fillet weld has high stress gradient while v-weld has low stress gradient. Stress concentrations at the weld ends in case of v-weld is higher than the fillet weld. The other sections profiles, I,C,Z,X and circular profiles, show that v weld has higher stress at edges than the fillet welds. We can conclude that the fillet welds are better than v-welds for these profiles. Also the results show that there are stress concentrations in the stiffened areas.

Chapter 8

Experimental results using digital image correlation (DIC)

To assess the effectiveness and accuracy of the modeling, the numerical and experimental results were compared to verify the validity of the developed FE models. Static loads were applied in the experiments. The same loads were also applied in the FE models. The experimental and FE displacements for both loading conditions and for all types of beam profiles were compared. The displacements obtained from the simulations and those from the experiments are depicted in graphs by Abaqus [59] and Armis [50] respectively. The results show that in general a good agreement exists between the experimental and numerical displacements. The finite element method was used to obtain results there not measured in the experiments like stresses and strains, giving insight into the welding that cannot be seen in the laboratory.

As the validity of the FE models were verified through the comparison of the FE and experimental displacements, the developed models were used to obtain a more thorough understanding of the stress distribution around the connection of the welded joints for the beams. It should be noted that with the existence of sharp corners at the weld toes, the elastic stress is theoretically infinite at these locations. This means that one cannot simply obtain the stresses at the weld toe from the FE results file, as they do not converge and are mesh sensitive.

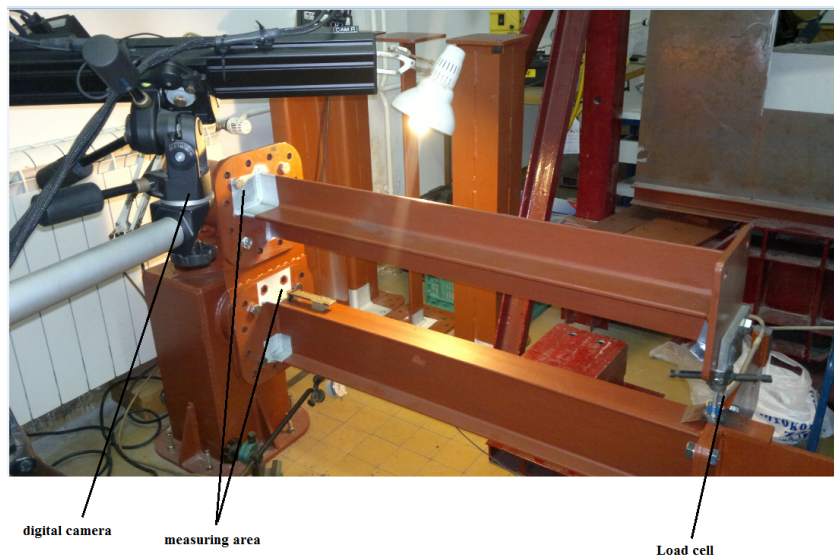


Figure 8.1. General view of experimental measuring using DIC.

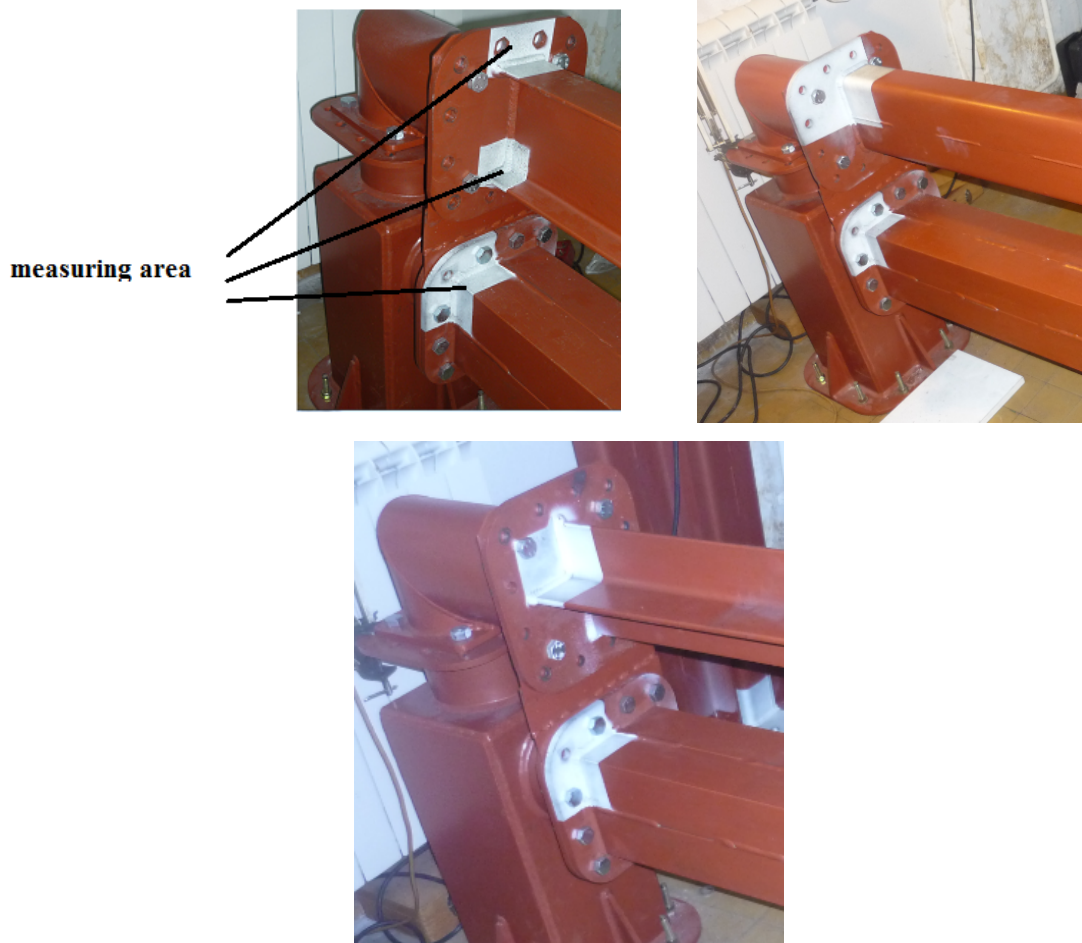


Figure.8.2 Shows the measuring areas (white regions) used in DIC.

8.1 Rectangular section

In the experimental study, a test fixture with a load cell is capable of applying static loads (see Figures 8.1-2), in order to verify the FEA results of the numerical study. It is clear that the measuring object has homogeneous surface, we need to prepare such surface by means of suitable methods. On this specimen, the corner surface was prepared by applying a stochastic color spray pattern (see chapter 3). The load was applied into 6 stages (see table 8.1). The maximum U_z displacement at the end of the beam is 1.75mm which corresponds to force 6.5KN.

Table 8.1 The input data for the box profile

Stage number	Displacement Uz mm
0	0
1	0.7
2	1.35
3	1.75
4	1.35
5	0.7
6	0

Figure.8.3 shows the partial view of a box beam profile test: description of 29mm length) which is considered to calculate the distribution of the displacement y by using the 3-D DIC .It is clear that the displacement y on the top surface of the box beam profile is 0.12mm

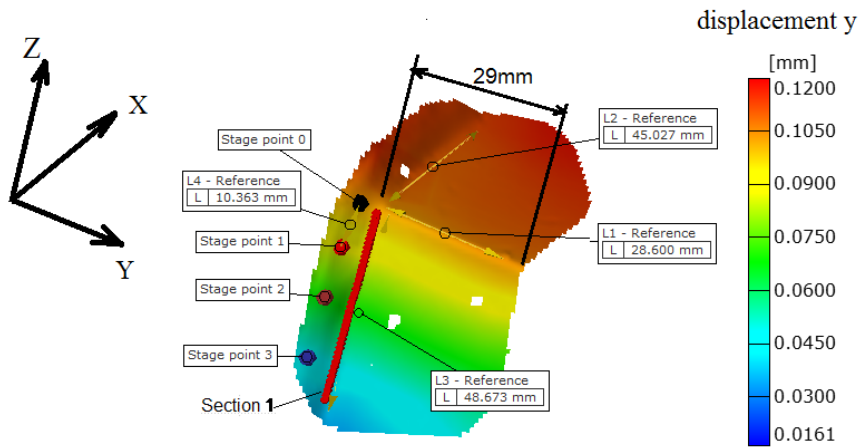


Figure.8.3 Partial view of the experimental results of the displacement y of 29mm length of the box profile.

Figure 8.4-a. shows the section length (see figure.8.3) versus displacement y. it is clear that there is linear distribution of y displacement along the section path. While figure 8.4-b shows four stage points along the vertical weld of the beam box profile. Each stage has linear distribution of the displacement y. Where the stage point 0 which is located at the top surface on the beam has maximum displacement.

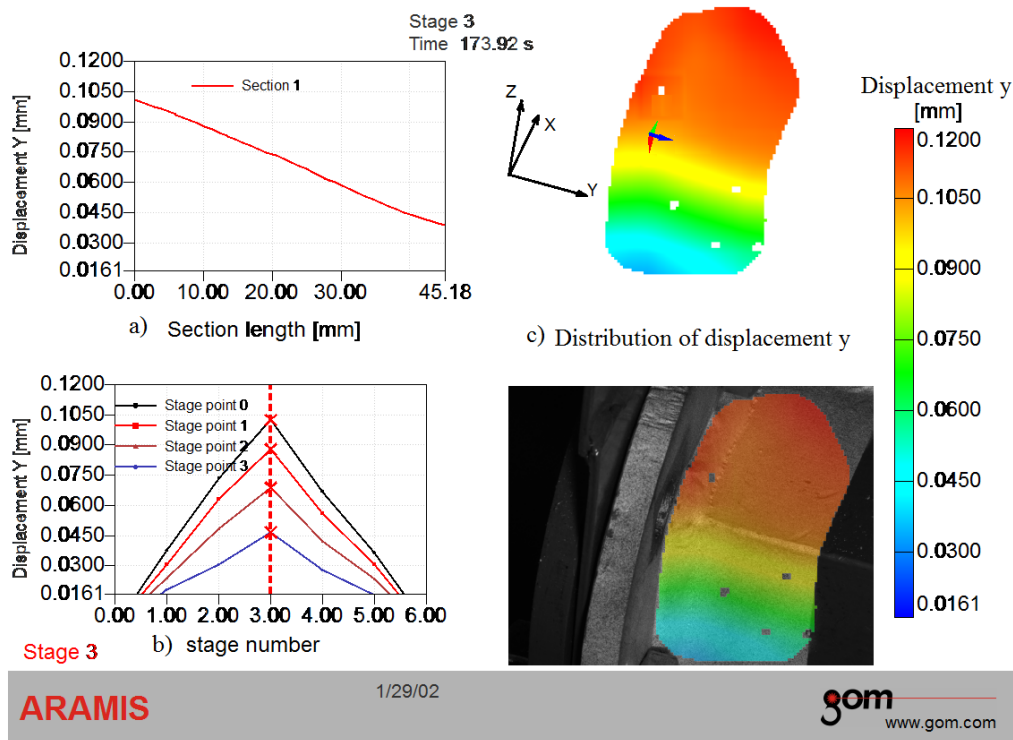


Figure.8.4 The experimental results of the displacement y of the box profile using aramis a) Section length versus displacement y b) Strain stage vs displacement y c) Distribution of displacement y.

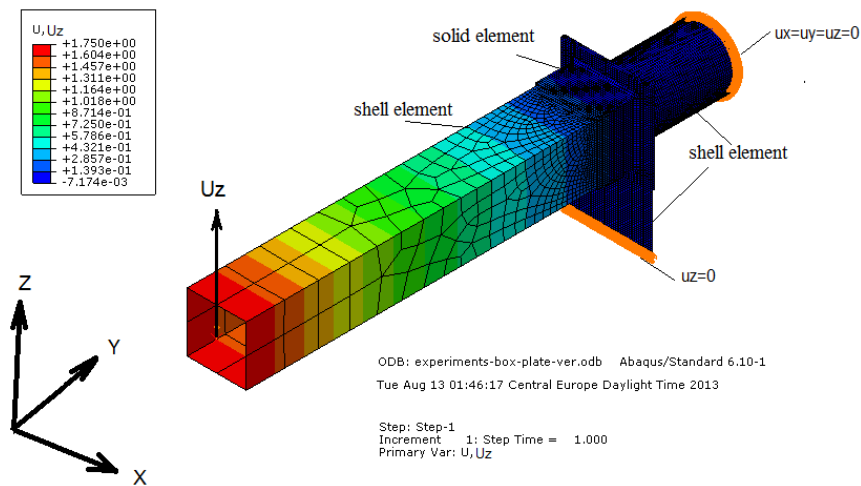


Figure 8.5. General view of the displacement distribution U_z of the box profile beam
 Figure 8.5. shows the general view of the displacement distribution U_z of the box profile beam. The applied force that makes deflection 1.75mm at the end of the beam is 6.5KN. Figure.8.6 shows partial view of the FE results of the displacement U_y of 29mm

of the box profile. The figure shows that the displacement distribution at the top of box beam is 0.11mm which is similar to the displacement that obtained from DIC (Aramis).

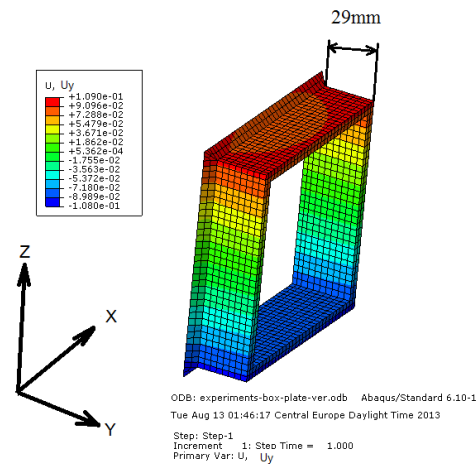


Figure.8.6 Partial view of the FE results of the displacement U_y of 29mm of the box profile.

Experimental and numerical results of the displacement U_y are shown in Figure 8.3-6. Generally, good agreement of the displacement distribution, U_y was obtained between the FE analyses and experiments.

8.2 I-section

The top surface of the I beam profile was prepared by applying a stochastic color spray pattern (see figure 8.2). The load was applied into 6 stages (see table 8.2). The maximum U_z displacement at the end of the beam is 3mm which corresponds to force 8.5KN.

Table 8.2 The input data for the I profile.

Stage number	Displacement U_z mm
0	0
1	1
2	2
3	3
4	2
5	1
6	0

Figure.8.7 shows the partial view of a I beam profile test: description of 30mm length which is considered to calculate the distribution of the displacement z by using the 3-D DIC .It is clear that the displacement z on the top surface at the end of 30mm of the I beam profile is 0.16mm.

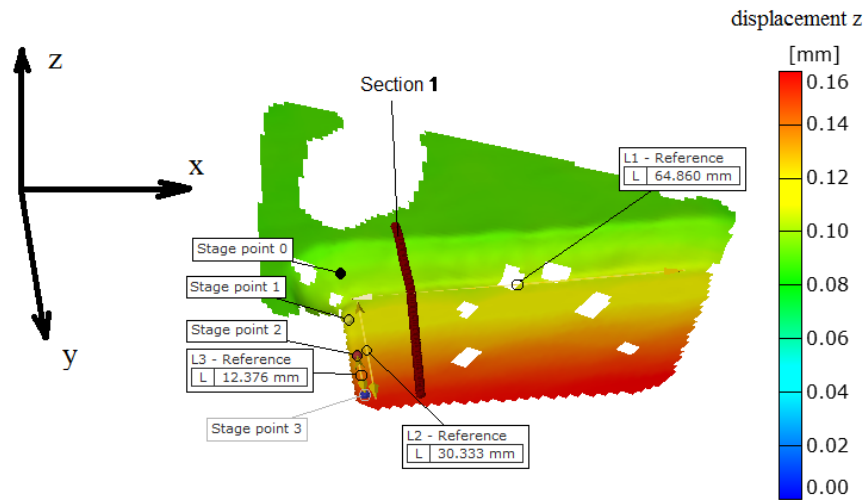


Figure.8.7 Partial view of the experimental results of the displacement z of 30mm length of the I profile.

Figure 8.8-a. shows the section length (see figure.8.7) versus displacement z . It is clear that there is linear distribution of z displacement along the section path. While figure 8.4-b shows four stage points, where stage point 0 is located on the weld and stage point 3 on 30mm apart on the top surface of the I beam profile(see figure 8.7). We can see that each stage has linear distribution of the displacement z . Stage point 0 has minimum displacement (.09mm) because it is near the support while stage point 3 has the maximum displacement (0.15mm) because it is locate about 30mm form stage point 0 (see figure8.7).

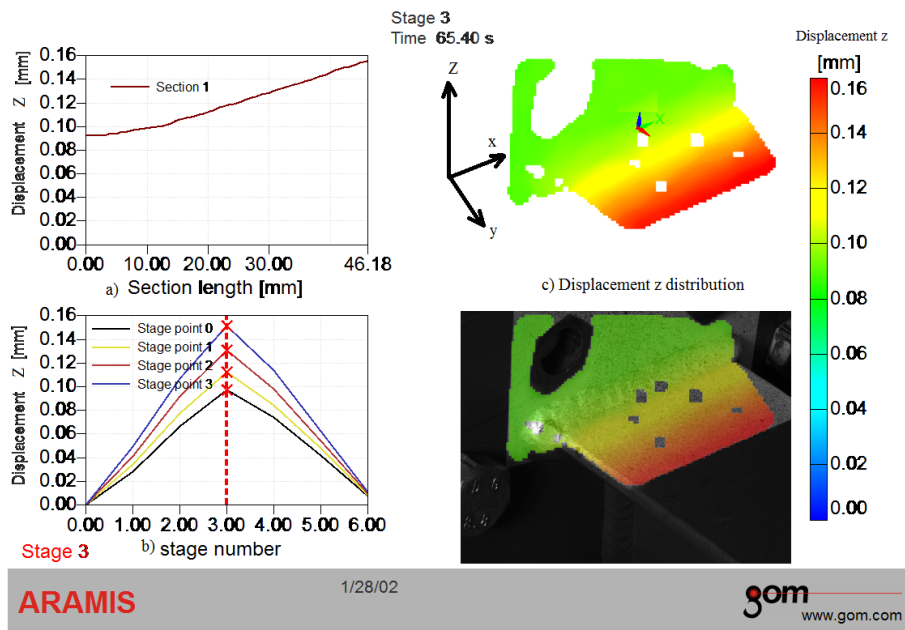


Figure.8.8 The experimental results of the displacement z of the I profile using aramis.
 a) Section length versus displacement y b) Strain stage vs displacement y c) Distribution of displacement y.

Figure 8.9 shows the general view of the displacement distribution U_z of the I beam profile. The applied force that makes deflection 3mm at the end of the beam is 8.5KN. Figure.8.10 shows partial view of the FE results of the displacement U_z of 30mm of I beam profile. The figure shows that the displacement distribution at the top of box beam is 0.155mm which is similar to the displacement that obtained from DIC (aramis).

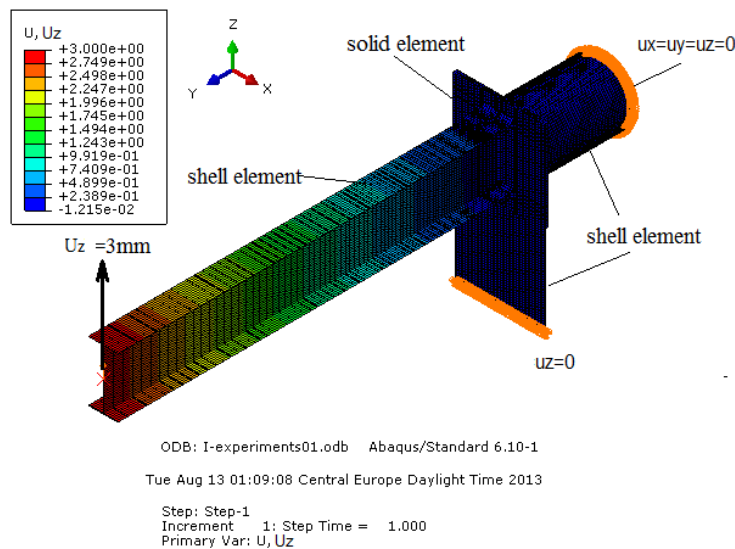


Figure 8.9. General view of the displacement distribution U_z of the I profile beam.

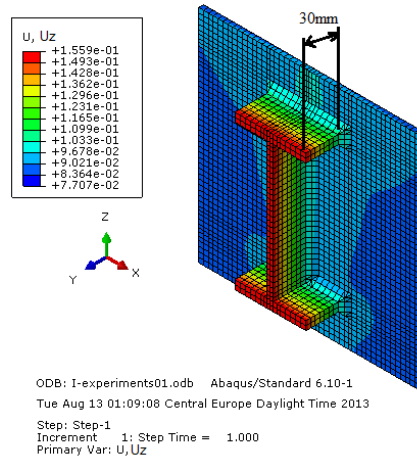


Figure.8.10 Partial view of the FE results of the displacement U_z of 30mm of the box profile.

Experimental and numerical results of the displacement U_z are shown in Figure 8.7,10. Generally, good agreement of the displacement distribution, U_z was obtained between the FE analyses and experiments.

8.3 C-section

The corner top surface of the C beam profile was prepared by applying a stochastic color spray pattern. The load was applied into 8 stages (see table 8.3). The maximum U_z displacement at the end of the beam is 4mm which corresponds to force 8.6KN.

Table 8.3. The input data for the C profile.

Stage number	Displacement U_z mm
0	0
1	1
2	2
3	3
4	4
5	3
6	2
7	1
8	0

Figure.8.11 shows the partial view of a C beam profile test: description of 53mm length which is considered to calculate the distribution of the displacement z by using the 3-D

DIC .It is clear that the displacement z on the top surface at the end of 53mm of the C beam profile is 0.35mm.

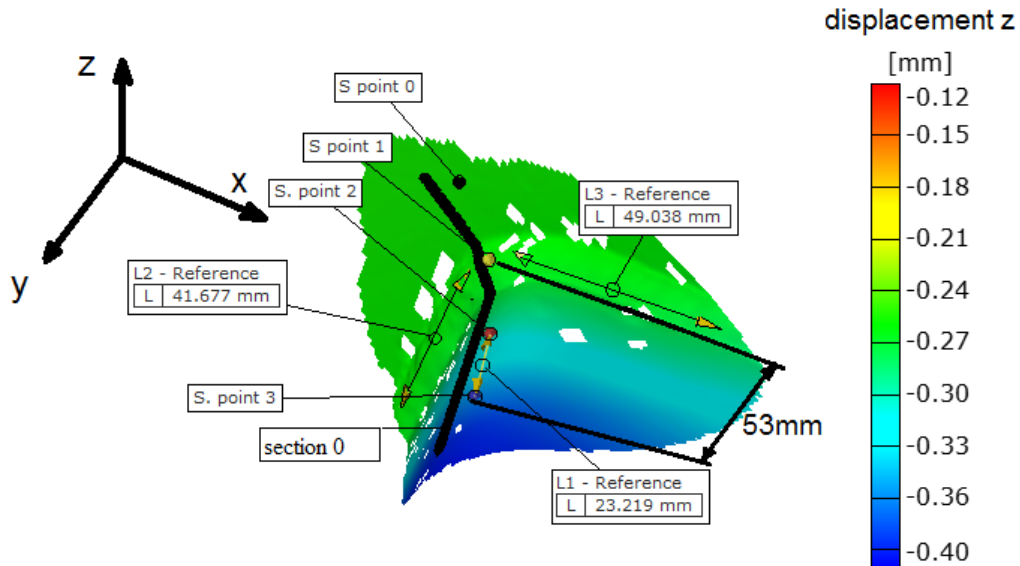


Figure.8.11 Partial view of the experimental results of the displacement z of 53mm length of the C profile.

Figure 8.12-a. shows the section length (see figure.8.11) versus displacement z. It is clear that there is linear distribution of z displacement along the section path. While figure 8.4-b shows four stage points, where the point 0 is located on the flange and point 3 is locate 53mm from the flange (see figure 8.11). We can see that each stage has linear distribution of the displacement z. Stage point 0 has displacement (.24mm) because it is near the support while point 3 has displacement (0.34mm) because it is locate about 53mm form point 0 (see figure8.11).

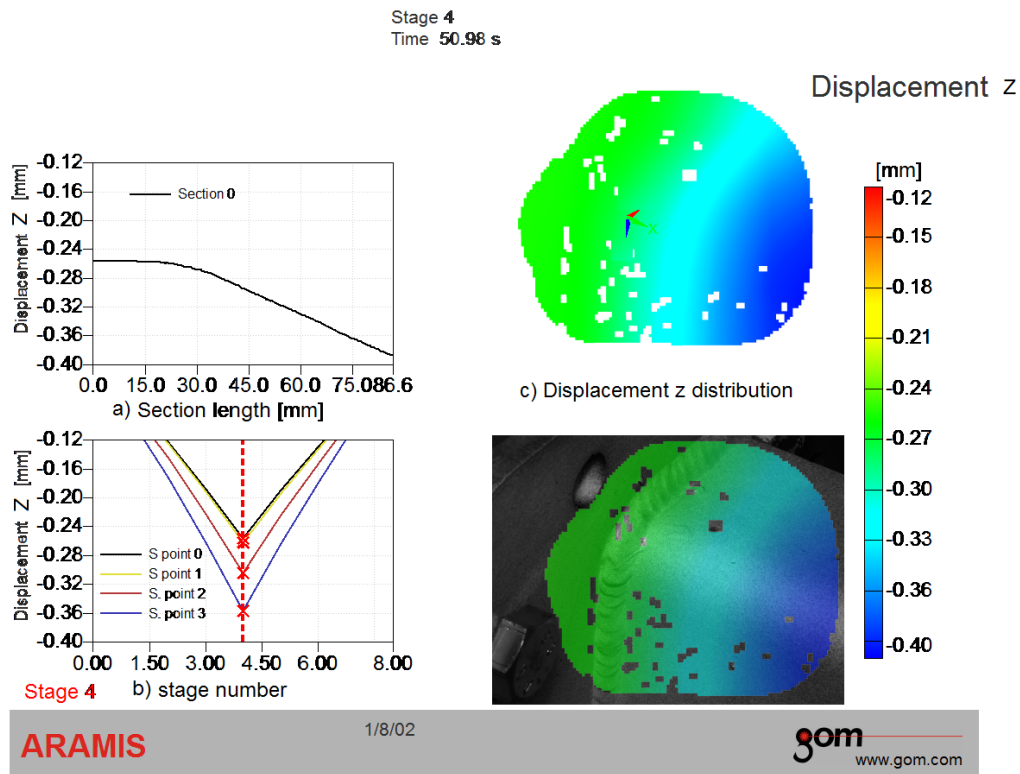


Figure.8.12 The experimental results of the displacement z of the C profile using aramis. a) Section length versus displacement z b) Strain stage vs displacement z c) Distribution of displacement z.

Figure 8.13 shows the general view of the displacement distribution U_z of the C beam profile. The applied force that makes deflection 4mm at the end of the beam is 8.6KN. Figure.8.14 shows partial view of the FE results of the displacement U_z of 53mm of the C beam profile. The figure shows that the displacement distribution at distance 53mm from the flange is 0.303mm (see figure 8.11) which is similar to the displacement that obtained from DIC (Aramis).

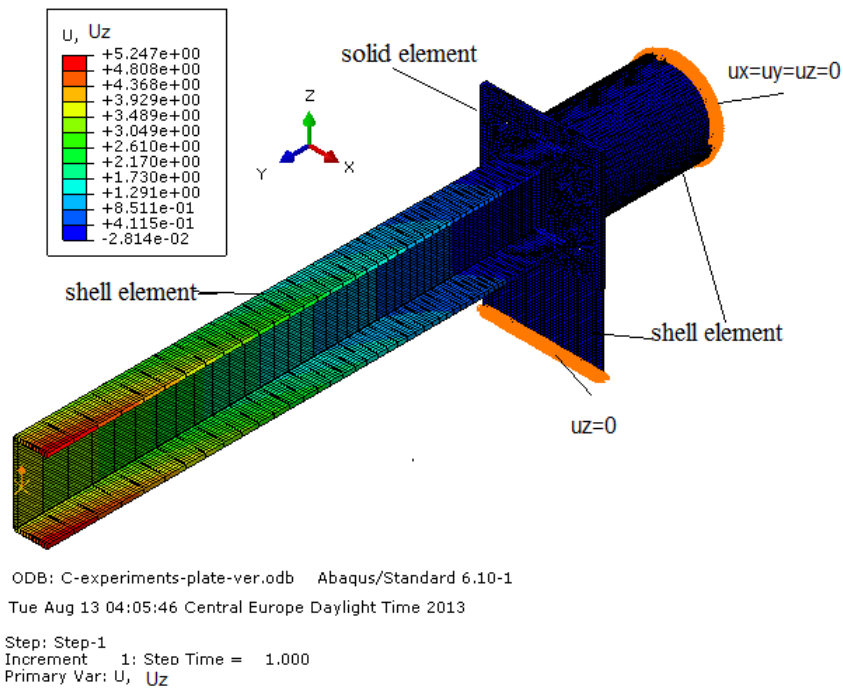


Figure 8.13. General view of the displacement distribution U_z of the C profile beam

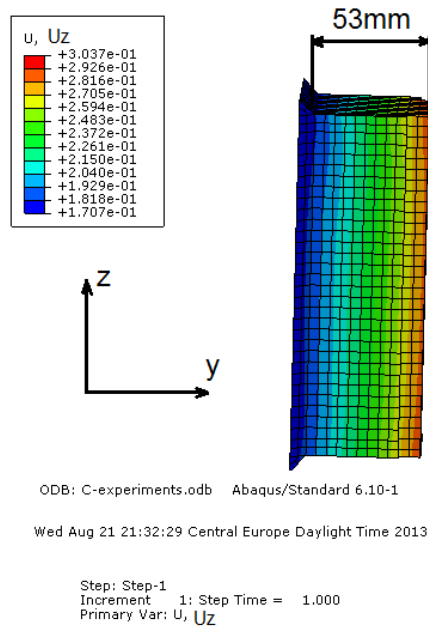


Figure.8.14 Partial view of the FE results of the displacement U_z of 53mm of the C profile.

Experimental and numerical results of the displacement U_z are shown in Figure 8.11 and figure 8.14, respectively. Generally, good agreement of the displacement distribution, U_z was obtained between the FE analyses and experiments.

8.4 Z-Section

The corner top surface of the Z beam profile was prepared by applying a stochastic color spray pattern. The load was applied into 8 stages (see table 8.4). The maximum U_z displacement at the end of the beam is 4mm which corresponds to force 5.3KN.

Table 8.4 The input data for the Z profile.

Stage number	Displacement U_z mm
0	0
1	1
2	2
3	3
4	4
5	3
6	2
7	1
8	0

Figure.8.15 shows the partial view of a Z beam profile test: description of 38mm length which is considered to calculate the distribution of the displacement z by using the 3-D DIC .It is clear that the displacement z on the top surface at 38mm from the flange of the Z beam profile is 0.288mm.

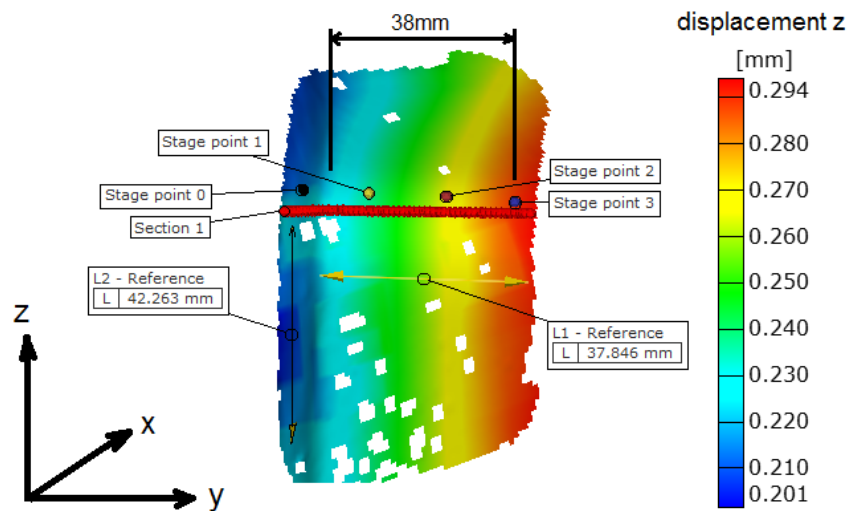


Figure.8.15 Partial view of the experimental results of the displacement z of 38mm length of the Z beam profile.

Figure 8.16-a. shows the section length (see figure.8.15) versus displacement z . It is clear that there is linear distribution of z displacement along the section path. While figure 8.4-b shows four stage points, where the point 0 is located on the flange and point 3 is located 38mm from the flange (see figure 8.15). We can see that each stage has linear distribution of the displacement z . Stage point 0 has displacement (.2mm) because it is near the support while point 3 has displacement (0.288mm) because it is located about 38mm from point 0 (see figure 8.15).

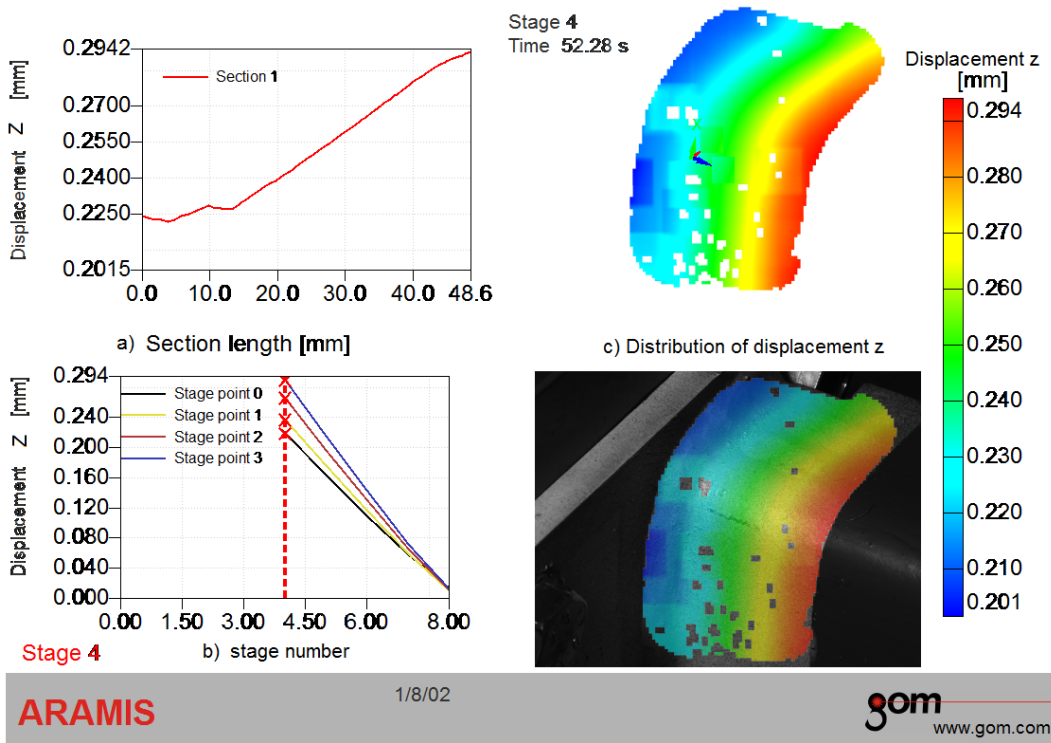


Figure.8.16 The experimental results of the displacement z of the Z profile using aramis. a) Section length versus displacement z b) Strain stage versus displacement z c) Distribution of displacement z.

Figure 8.17 shows the general view of the displacement distribution U_z of the Z beam profile. The applied force that makes deflection 4mm at the end of the beam is 5.3KN. Figure.8.18 shows partial view of the FE results of the displacement U_z of 38mm of the Z beam profile. The figure shows that the displacement distribution at distance 38mm from the flange is 0.24mm which is close to the displacement that obtained from DIC (Aramis).

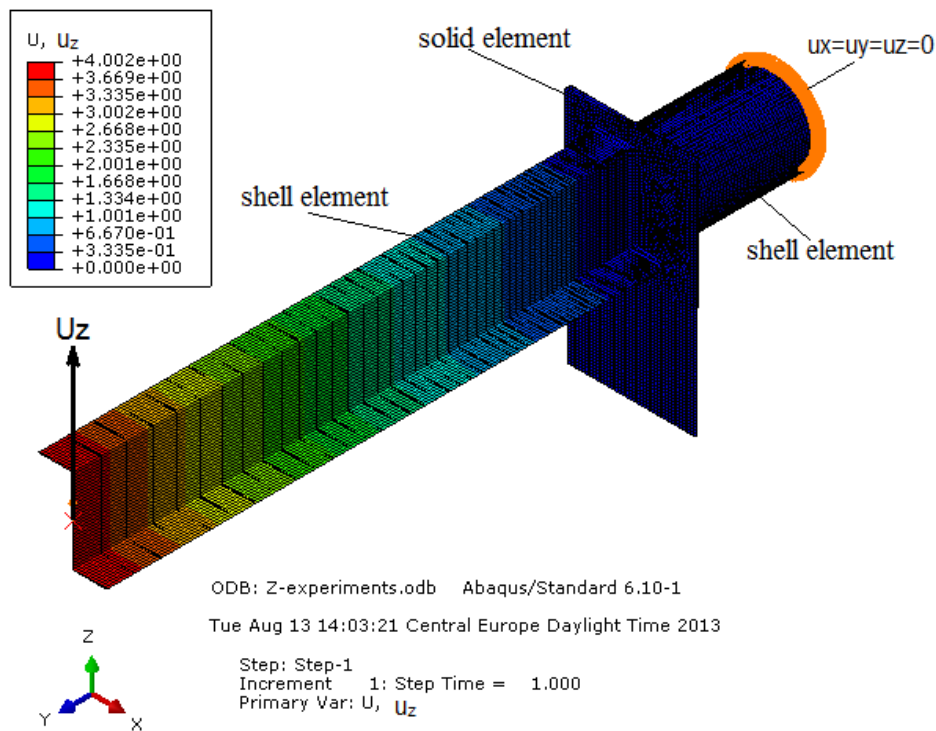


Figure 8.17. General view of the displacement distribution U_z of the Z profile beam using Abaqus.

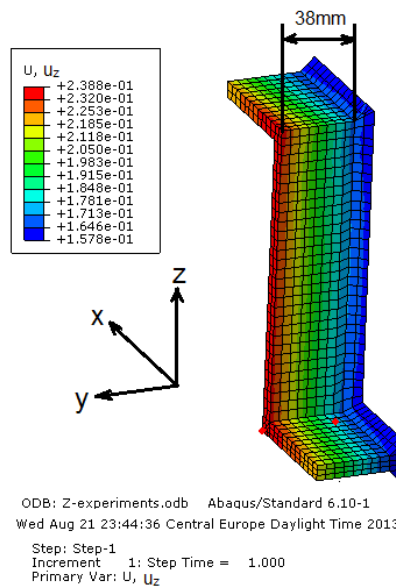


Figure.8.18 Partial view of the FE results of the displacement U_z of 38mm of the Z profile by using Abaqus [59].

Experimental and numerical results of the displacement U_z are shown in Figure 8.15-18. Generally, good agreement of the displacement distribution U_z was obtained

between the FE analyses and experiments. We note that this experiment was done without constraints on the vertical plate.

8.5 X-Section

The corner surface of the X beam profile was prepared by applying a stochastic color spray pattern. The load was applied into 8 stages (see table 8.5). The maximum Uz displacement at the end of the beam is 4mm which corresponds to force 1.9KN.

Table 8.5 The input data for the X profile

Stage number	Displacement Uz (mm)
0	0
1	1
2	2
3	3
4	4
5	3
6	2
7	1
8	0

Figure.8.19 shows the partial view of a X beam profile test: description of 50mm length which is considered to calculate the distribution of the y displacement by using the 3-D DIC .It is clear that the displacement y on the top surface at 50mm from the flange of the X beam profile is 0.4mm .

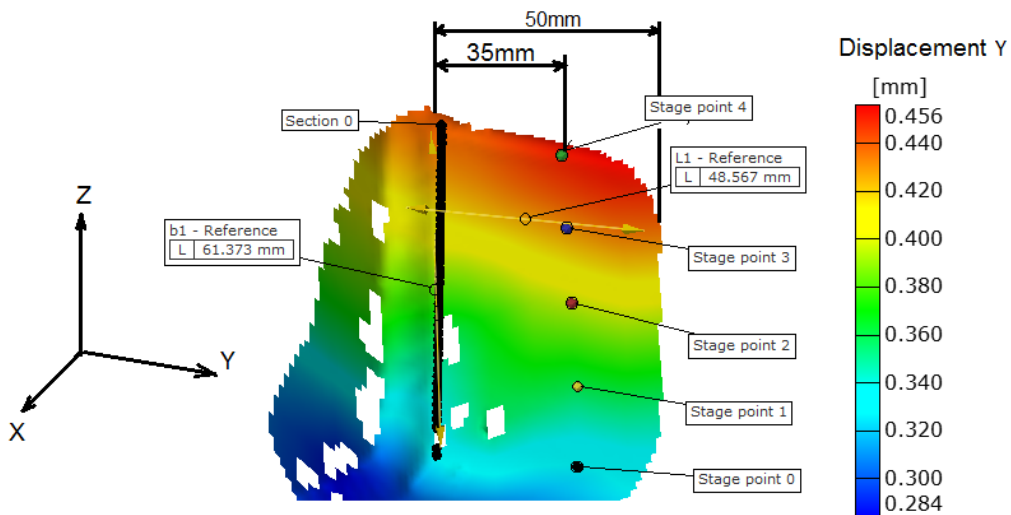


Figure.8.19 Partial view of the experimental results of the displacement z of 50mm length of the X profile.

Figure 8.20-a. shows the section length (see figure.8.19) versus displacement z. It is clear that there is linear distribution of y displacement along the section path. While figure 8.4-b shows five stage points, where the point 4 is located on the top of the beam and 38mm along y direction (see figure 8.19). We can see that each stage has linear distribution of the displacement z. Stage point 0 has displacement (.3mm) because it is near the middle of the beam while point 4 has displacement (0.4mm) because it is located on top of the beam (see figure8.19).

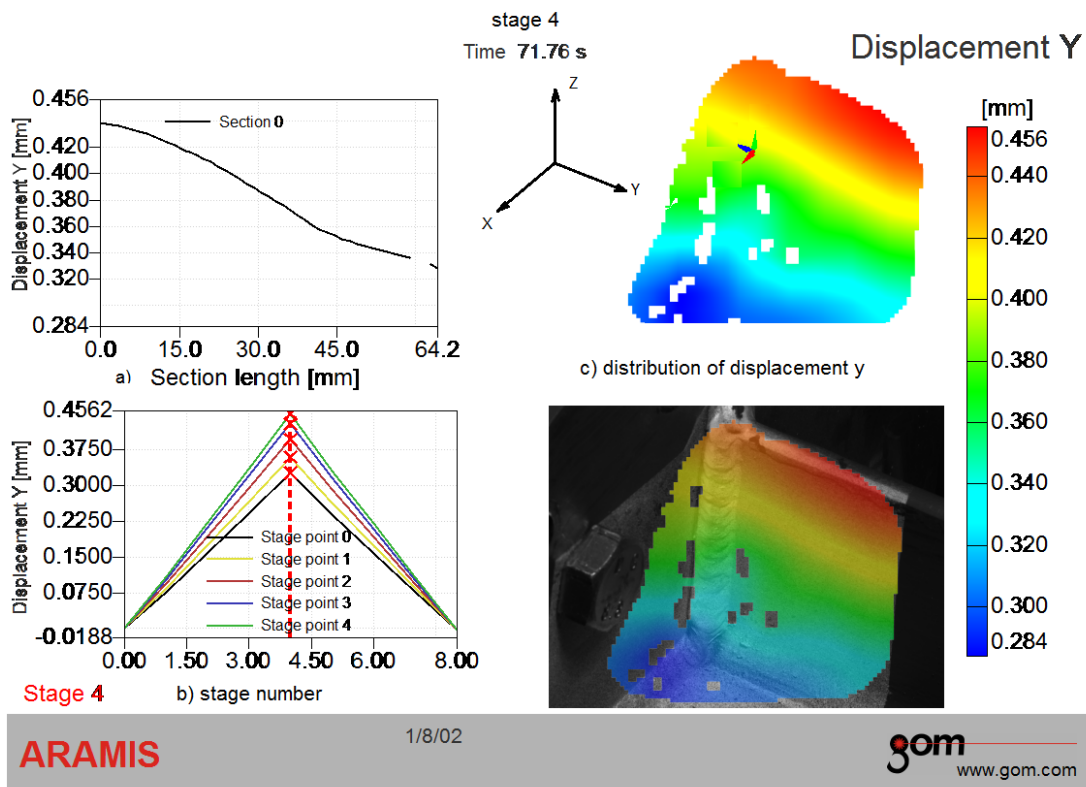


Figure.8.20 The experimental results of the displacement z of the Z profile using aramis. a) Section length versus displacement z b) Strain stage versus displacement z c) Distribution of displacement z.

Figure 8.21 shows the general view of the displacement distribution U_z of the X beam profile. The applied force that makes deflection 4mm at the end of the beam is 1.9KN. Figure.8.22 shows partial view of the FE results of the displacement U_y of 50mm of the X beam profile. The figure shows that the displacement distribution at distance 50mm from the flange is 0.4mm which has displacement distribution close to the displacement that obtained from DIC (Aramis).

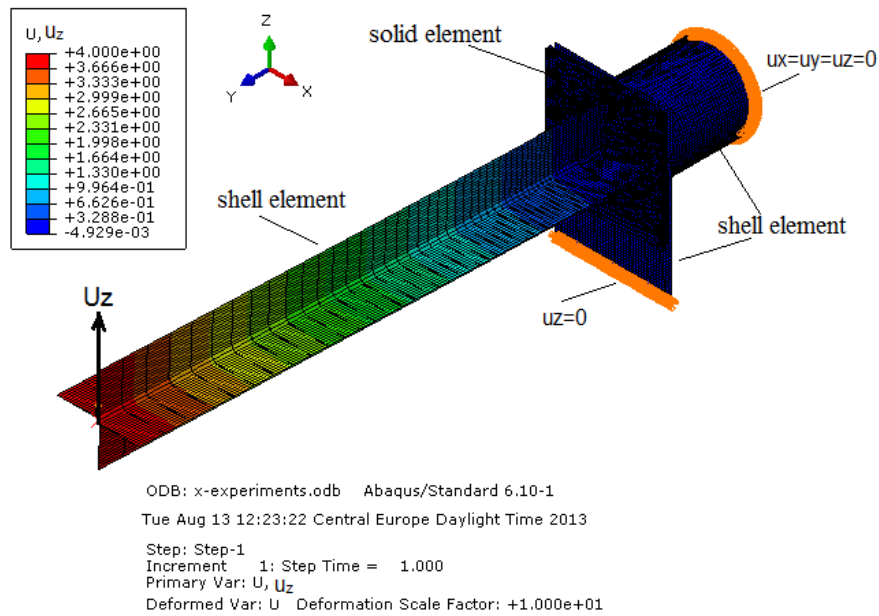


Figure 8.21. General view of the displacement distribution U_z of the Z profile beam using Abaqus [59].

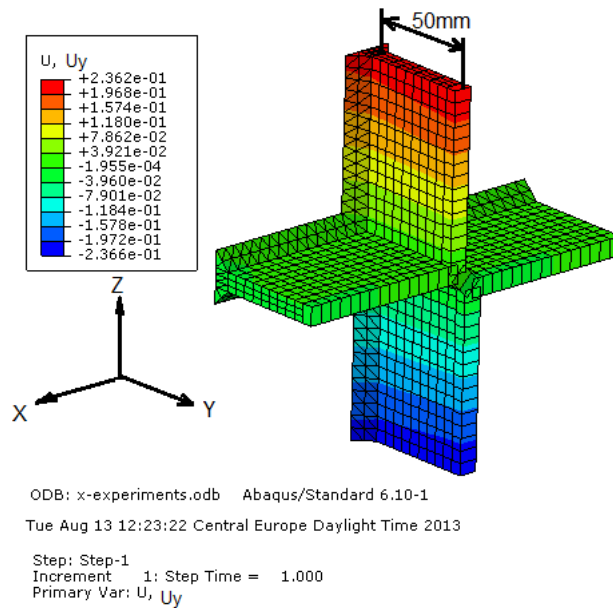


Figure.8.22 Partial view of the FE results of the displacement U_z of 50mm of the X profile by using Abaqus [59].

Experimental and numerical results of the displacement U_y are shown in Figure 8.19,22. Generally, good agreement of the displacement distribution of U_y was obtained between the FE analyses and experiments while no good agreement of the values of the

displacement, U_y was obtained between the FE analyses and experiments. From figure 8.19, it is clear that the boundary conditions were not fixed as we applied in the finite element model. This has effect on the loading and constraints. These constraints involve mechanical contact which depends on the compliances of the structures that impose the load and constraints and the physical properties of the contacting surfaces.

Chapter 9

Conclusion

In this dissertation, the behavior of tubular (box and circle profile) and non tubular (L, Z, C and X profiles) joint connections profiles, subjected to static loads were studied both experimentally and numerically. From a structural analysis point of view, despite of the wide use of corner welded joints as efficient load carrying members, there is no available practical, simple and accurate approach for their design and analysis. For this purpose, engineers must often prepare relatively complicated and time consuming finite element (FE) models made up solid elements. Three-dimensional finite element analysis of complete structural hollow sections can be complex and time-consuming. Due to the complex nature of the finite element analysis codes, this method has limited application. It can be used in research area but cannot be widely used by structural engineers in their real-world projects. Therefore, there is a need to develop a simplified modeling method that can be implemented by using commonly available commercial software and easily employed. This is because unlike solid-section members, when hollow section members are subjected to general loadings, they may experience severe deformations of their cross-sections that results in stress concentrations in the connection's vicinity. One of the objectives/contributions of this research work is the better understanding of the behavior of the corner welded joint connections under out-of- plane bending and torsion loading conditions. Through a detailed Finite Element Analysis (FEA) using shell and solid elements, the stress distribution at the connection of the tubular and non tubular corner welded joints are obtained for different loading conditions. It is observed that at a short distance away from the connection of the corner welded joints, the structure behaves similar to beams when subjected to loadings.

The finite element results of the solid element model show that a generally linear stress distribution across the thickness of the beams is observed. Therefore, the use of shell elements for the analysis of the beam-joint connection is appropriate. Also, at a relatively short distance from the connection, the effects of the local stresses and deformations disappear.

In chapter 5, the finite element simulations were performed using beam element for all the six specimens. The Numerical analyses were carried out to represent the mechanical performance of the fillet weld and V weld beam-sections under bending. The study is summarized and concluded as follows. The predicted stress curves are in good agreement with the analytical results for all six cases of the beam members. The finite element results are in good agreement with the analytical results. Also, the obtained results show that the V weld gives high stress for sections I,C , Circular, Z, and X cross sections while a rectangular cross section gives lower stress when it welded by using V joint. Based on numerical simulation beam element technique for V and fillet welded joints, we can conclude that the analytical approach can be replaced by using a beam element numerical approach. So that for large structures, the beam element can be used to represent the stiffness of the fillet welded joints by increasing the thickness of the beam in the region of welded joints.

In chapter 6 and 7, the numerical modeling of the v-welded and fillet welded joint connections are performed using Abaqus [59], the commercial finite element package. The developed FE model is based on the assumption of linear elasticity and small strains/displacements. Shell and solid elements have been used for modeling both the beams and the welds in this study. Quadratic solid elements (20-noded) with three translational degrees-of-freedom at each node and quadratic shell elements (8-noded) with 6 degrees-of-freedom at each node were used to model the weld and the beam structure in order to accurately capture any non-linear stress gradients on the weld path. The study is summarized and concluded that stress curves of solid elements are in good agreement with stress curves of shell elements. The simulations using shell elements were found generally efficient and accurate compared with solid elements. So that for large structures, the oblique shell element can be used to represent the stiffness of the fillet welded joints.

In chapter 8, the numerical and experimental results were compared to verify the validity of the developed FE models. Static loads were applied in the experiments. The same loads were also applied in the FE models. The experimental and FE displacements for both loading conditions and for all types of beam profiles were compared. The displacements obtained from the simulations and those from the experiments are

depicted in graphs. The results show that in general a good agreement exists between the experimental and numerical displacements.

Finite element models of the welding experiments were carried out to verify the validity of the numerical results. The finite element method was used to obtain results that were not measured in the experiments like stresses and strains, giving insight into the welding that cannot be seen in the laboratory.

From the FEA results of the solid element model, a generally linear stress distribution across the thickness of the beams is observed. Therefore, the use of shell elements for the analysis of the beam-joint connection is appropriate.

The results show that the normal stresses in the 1 or 2-direction are the highest at the weld path (top of the path) on the top surface, and at horizontal weld path of the beam. It can be observed that the 1 or 2-direction component of normal stress causes the most damage. The values of the Von - Mises equivalent stresses are very close to the values of the stresses in the 1 or 2-direction (absolute value). This is expected as the stresses in the 1 or 2-direction are much larger than the other components of stress.

This means that the strains and stresses normal to the weld (i.e., 1 or 2 -direction in this study) are mainly responsible for plasticity/crack initiation and propagation.

The results of the box profile show that the fillet weld has high stress gradient while v-weld has low stress gradient while stress concentrations at the weld ends are high for v-weld. The other section profiles I, C, Z, X and circular profiles, show that v weld has higher stress at edges than the fillet welds. We can conclude that the fillet welds are better than v-welds for these profiles. Also, there is stress concentration near the stiffened region so the designer should take more care near stiffened regions.

References

- [1] J. Wardenier, J.A. Packer, X.-L. Zhao and G.J. van der Vegte, *Hollow Sections in Structural Applications*, CIDECT, Geneva, Switzerland, 2010.
- [2] Butler, L. J., and Kulak, G. L.. “Strength of Fillet Welds as a Function of Direction of Load,” *Welding Journal, Welding Research Supplement* 1971, Vol. 36, No. 5, pp. 231-234.
- [3] Dawe, J. L., and Kulak, G. L. “Welded Connections under Combined Shear and Moment,” *Journal of the Structural Division* 1972, ASCE, Vol. 100, No. ST4, May, pp. 727-741.
- [4] Lesik, D. F., and D. J. L. Kennedy. “Ultimate Strength of Eccentrically Loaded Fillet Welded Connections,” 1988, *Structural Engineering Report 159*, Department of Civil Engineering, University of Alberta, Edmonton, AB.
- [5] Vanam B. C. L., Rajyalakshmi M., Inala R. Static analysis of an isotropic rectangular plate using finite element analysis (FEA) *Journal of Mechanical Engineering Research*, April 2012, Vol. 4(4), pp. 148-162.
- [6] M. F. Ghanameh, D. Thevenet ,A. Zeghloul. “ stress concentration in offshore welded tubular joints subjected to combined loading, *J.Mater. Sci. Technolog.* 2004, Vol.20, pp. 35-37,.
- [7] Pawel Bilous, Tadeusz Lagoda, Structural notch effect in steel welded joints, *Materials and Design*, Vol. 30, pp.4562–4564, 2009.
- [8] . S. Raghavendrantg , M. E. Fourney, Stress Analysis of a Welded Joint, *Engineering Fracture Mechanics* 1994, Vol. 48, No. 5, pp.619-627.
- [9] S. Krscanski, G. Turkalj, FEM stress concentrations Factors For Fillet Welded CHS-Plate T-Joint, *Engineering Review* 2012, Vol. 32, Issue 3, 147-155.
- [10] P.M.Gedkar, D.V. Bhope: Finite Element Analysis of Pipe T-Joint, *International Journal of Engineering Science and Technology (IJEST)*, January 2012, Vol.4 No.01, pp.163-169.
- [11] X.W. Ye, Y.Q. Ni, J.M. Ko, Experimental evaluation of stress concentration factor of welded steel bridge T-joints, *Journal of Constructional Steel Research* 2012, Vol 70, pp. 78–85.

- [12] Shao YB. Geometrical effect on the stress distribution along the weld toe for tubular T- and K-joints under axial loading, *Journal of Constructional Steel Research* 2007, Vol.63 ,pp 1351–1360.
- [13] Hellier AK, Connolly MP, Dover WD. Stress concentration factors for tubular Y and T-joints. *Int J Fatigue* 1990;12(1):13–23.
- [14] Morgan MR, Lee MMK. Parametric equations for distributions of stress concentration factors in tubular K-joints under out-of-plane moment loading. *Int J Fatigue* 1998;20:449–61.
- [15] Chang E, Dover WD. Parametric equations to predict stress distributions along the intersection of tubular X and DT-joints. *Int J Fatigue* 1999;21: 619–35.
- [16] Karamanos SA, Romeijn A, Wardenier J. Stress concentrations in multi-planar welded CHS XX-connections. *J Constr Steel Res* 1999;50:259–82.
- [17] Karamanos SA, Romeijn A, Wardenier J. Stress concentrations in tubular gap K-joints: mechanics and fatigue design, *Eng Struct* 2000;22:4–14.
- [18] Chiew SP, Soh CK, Wu NW. General SCF design equations for steel multiplanar tubular XX-joints. *Int J Fatigue* 2000;22:283–93.
- [19] Karamanos SA, Romeijn A, Wardenier J. SCF equations in multi-planar welded tubular DT-joints including bending effects. *Mar Struct* 2002;15:157–73.
- [20] Gho WM, Gao F. Parametric equations for stress concentration factors in completely overlapped tubular K (N)-joints. *J Constr Steel Res* 2004:1761–82.
- [21] Gao F. Stress and strain concentrations of completely overlapped tubular joints under lap brace OPB load. *Thin-Walled Struct* 2006;44:861–71.
- [22] Gao F, Shao YB, Gho WM. Stress and strain concentration factors of completely overlapped tubular joints under lap brace IPB load. *J Constr Steel Res* 2007;63:305–16.
- [23] Woghiren CO, Brennan FP. Weld toe stress concentrations in multi planar stiffened tubular KK Joints. *Int J Fatigue* 2009;31:164–72.

- [24] Lie ST, Lee CK, Wong SM. Modeling and mesh generation of weld profile in tubular Y-joint. *J Constr Steel Res* 2001;57:547–67.
- [25] N' Diaye A, Hariri S, Pluvinage G, Azari Z. Stress concentration factor analysis for notched welded tubular T-joints. *Int J Fatigue* 2007;29:1554–70.
- [26] N' Diaye A, Hariri S, Pluvinage G, Azari Z. Stress concentration factor analysis for welded, notched tubular T-joints under combined axial, bending and dynamic loading *Int J Fatigue* 2009; 31:367–74.
- [27] T. Wanga, O.S. Hopperstada, O.-G. Lademoa, P.K. Larsena, Finite element modelling of welded aluminium members subjected to four-point bending, *Thin-Walled Structures* 2007, 45: 307–320.
- [28] Seng-Keat Yeoh, Ai-Kah Soh, Chee-Kiong Soh :Behaviour of Tubular T-Joints Subjected to Combined Loadings. *Journal of Constructional Steel Research* Volume 32, Issue 3, 1995, Pages 259-280.
- [29] Shih-Heng tung, Chung-Huan Sui, Application of digital-image-correlation techniques in analysing cracked cylindrical pipes, *Sadhana* 2010; 35, 557–567.
- [30] Grediac M. The use of full-field measurement methods in composite material characterization: interest and limitations *Composites Part A* 2004;35:751–61.
- [31] Rommel Cintron, Victor Saouma, Strain Measurements with the Digital Image Correlation System Vic-2D, University of Colorado,usa, University of Colorado, CU-NEES-08-06 .
- [32] Sun Z, Lyons JS, McNeill SR. Measuring microscopic deformations with digital image correlation. *Opt Lasers Eng* 1997;27(4): 409–28.
- [33] Chevalier L, Calloch S, Hild F, Marco Y. Digital image correlation used to analyze the multiaxial behavior of rubber-like materials. *Eur J Mech /Solids* 2001;20:169–87.
- [34] Wang Y, Cuitin o AM. Full-field measurements of heterogeneous deformation patterns on polymeric foams using digital image correlation. *Int J Solids Struct* 2002;39(13):3777–96.

- [35] Abanto-Bueno J, Lambros J. Investigation of crack growth in functionally graded materials using digital image correlation. *Eng Frac Mech* 2002;69(14):1695–711.
- [36] Knauss WG, Chasiotis I, Huang Y. Mechanical measurements at the micron and nanometer scales. *Mech Mater* 2003;35(3):217–31.
- [37] Li EB, Tieu AK, Yuen WYD. Application of digital image correlation technique to dynamic measurement of the velocity field in the deformation zone in cold rolling. *Opt Lasers Eng* 2003; 39(4):479–88.
- [38] Ait-Amokhtar H, Vacher P, Boudrahem S. Kinematics fields and spatial activity of Portevin-Le Chatelier bands using the digital image correlation method. *Acta Mater* 2006;54(16):4365–71.
- [39] Garcia D, Orteu J-J, Penazzi L. A combined temporal tracking and stereo-correlation technique for accurate measurement of 3D displacements: application to sheet metal forming. *J Mat Process Technology* 2002;125–126:736–42.
- [40] Hartley R, Sturm P. Triangulation. *Compute Vision Image Understanding* 1997;68(2):146–57.
- [41] Jean-Jose Orteu, 3-D computer vision in experimental mechanics, *Optics and Lasers in Engineering* 2009;47: 282–291.
- [42] Michael A. Sutton, Stephen R. McNeill, Jeffrey D. Helm, and Yuh J. Chao, *Advances in Two-Dimensional and Three-Dimensional Computer Vision. Photomechanics* 2000, *Topics Appl. Phys.* 77, 323–372.
- [43] Ivan Gomez et al., Strength and ductility of welded joints subjected to out of plane Bending, American Institute of Steel Construction, July 2008.
- [44] R. S. Khurmi , J.K. Gupta . *A Textbook of Machine Design* ,Ram Nagar,New Delhi,2005.
- [45] Zoran Petkovic, Davor Ostric. *Machine construction 1*,University of belgrade , Belgrade,1996.

- [46] Robert C. Juvinall, Kurt M. Marshek. Fundamentals of Machine Component Design, 5th edition, Wiley, 2012.
- [47] Allen S. Hall, Alfred R. Holowenko, Herman G. Laughlin. Theory and Problems of Machine Design, McGraw-Hill, 1961.
- [48] T. H. G. Megson: Aircraft Structures for engineering students, 4th edition, Elsevier, 2007.
- [49] Shih-Heng Tung, Jui-Chao Kuo, Ming-Hsiang Shih. Strain Distribution Analysis Using Digital-Image-Correlation Techniques, The Eighteenth KKCNN Symposium on Civil Engineering-NTU 29 December 19-21, 2005, Taiwan.
- [50] Aramis user manual, www.gom.com.
- [51] Daryl L. Logan. A First Course in the Finite Element Method, Thomson, 2007.
- [52] Klaus-Jurgen Bathe, Finite Element Procedures, Prentice Hall, 1996.
- [53] Roger T Fenner, Finite Element Methods for Engineers, Imperial College, 1996.
- [54] Ingenieria, Introduction To The Finite Element Method.
- [55] S. Timoshenko, J. N. Goodier. Theory of Elasticity, McGraw-Hill, 1951.
- [56] Robert D. Cook. Finite Element Modeling for Stress Analysis, John Wiley, 1995.
- [57] G. R. Liu, S. S. Quek. The Finite Element Method: A Practical Course, Butterworth-Heinemann, 2003.
- [58] Singiresu S. Rao, The Finite Element Method in Engineering, Elsevier Science, 2004.
- [59] Software Abaqus /standard version 6.10-1.

Biography of the Author

Hasan Mehdi Nagiar was born on 16th of February 1971 in Tripoli Libya, Libyan nationality. He finished his primary school in Asaad Ben Alforat school. He finished his secondary education from Shohada Aldamor school, Tripoli Libya in 1989. In spring 1995, he received his B.Sc. Degree from Tripoli University, department of Aeronautical engineering. In 2001, Nagiar received his M.Sc. Degree from Tripoli University, department of Aeronautical Engineering. His master thesis was entitled “Buckling of Axially Loaded Cylindrical Sandwich Shells”. Since March 2009, he has been Ph.D candidate at the University of Belgrade, Faculty of Mechanical Engineering.

In the period between 1998 and 2003, he worked in research and development center (RDC) in Tripoli Libya. In 2002, he worked as a part time lecturer at Tripoli University, department of Aeronautical engineering and Souk Al-Gumma High Institute. In the period between 2003 and 2007, he worked as a full time lecturer at Tripoli University, department of Mechanical Engineering. He taught some subjects such as: Strength of Material, Mechanics of Machines, Stress Analysis and Finite Elements. He engaged in his Ph.D. research and worked under supervision of Professor Tasko Maneski in the field of Strength of Structures.

Прилог 1.

Изјава о ауторству

Потписани-а Хасан Мехди Нагиар

број индекса D40/09

Изјављујем

да је докторска дисертација под насловом

**НАПОНСКА АНАЛИЗА УГАОНИХ ЗАВАРЕНИХ СПОЈЕВА НОСАЧА
КОНСТРУКЦИЈА САВРЕМЕНИМ НУМЕРИЧКО-ЕКСПЕРИМЕНТАЛНИМ
ПРИСТУПОМ**

- резултат сопственог истраживачког рада,
- да предложена дисертација у целини ни у деловима није била предложена за добијање било које дипломе према студијским програмима других високошколских установа,
- да су резултати коректно наведени и
- да нисам кршио/ла ауторска права и користио интелектуалну својину других лица.

Потпис докторанда

У Београду, 8. 11. 2013.

Прилог 2.

Изјава о истоветности штампане и електронске верзије докторског рада

Име и презиме аутора Хасан Мехди Нагиар

Број индекса D40/09

Студијски програм _____

Наслов НАПОНСКА АНАЛИЗА УГАОНИХ ЗАВАРЕНИХ СПОЈЕВА
НОСАЧА КОНСТРУКЦИЈА САВРЕМЕНИМ НУМЕРИЧКО-
ЕКСПЕРИМЕНТАЛНИМ ПРИСТУПОМ

Ментор проф. Др Ташко Манески

Потписани /а Хасан Мехди Нагиар

Изјављујем да је штампана верзија мог докторског рада истоветна електронској верзији коју сам предао/ла за објављивање на порталу **Дигиталног репозиторијума Универзитета у Београду**.

Дозвољавам да се објаве моји лични подаци везани за добијање академског звања доктора наука, као што су име и презиме, година и место рођења и датум одбране рада.

Ови лични подаци могу се објавити на мрежним страницама дигиталне библиотеке, у електронском каталогу и у публикацијама Универзитета у Београду.

Потпис докторанда

У Београду, 8. 11. 2013.

Прилог 3.

Изјава о коришћењу

Овлашћујем Универзитетску библиотеку „Светозар Марковић“ да у Дигитални репозиторијум Универзитета у Београду унесе моју докторску дисертацију под насловом:

НАПОНСКА АНАЛИЗА УГАОНИХ ЗАВАРЕНИХ СПОЈЕВА НОСАЧА
КОНСТРУКЦИЈА САВРЕМЕНИМ НУМЕРИЧКО-ЕКСПЕРИМЕНТАЛНИМ
ПРИСТУПОМ

која је моје ауторско дело.

Дисертацију са свим прилозима предао/ла сам у електронском формату погодном за трајно архивирање.

Моју докторску дисертацију похрањену у Дигитални репозиторијум Универзитета у Београду могу да користе сви који поштују одредбе садржане у одабраном типу лиценце Креативне заједнице (Creative Commons) за коју сам се одлучио/ла.

1. Ауторство
2. Ауторство - некомерцијално
3. Ауторство – некомерцијално – без прераде
4. Ауторство – некомерцијално – делити под истим условима
5. Ауторство – без прераде
6. Ауторство – делити под истим условима

(Молимо да заокружите само једну од шест понуђених лиценци, кратак опис лиценци дат је на полеђини листа).

Потпис докторанда

У Београду, 8. 11. 2013.

1. Ауторство - Дозвољавате умножавање, дистрибуцију и јавно саопштавање дела, и прераде, ако се наведе име аутора на начин одређен од стране аутора или даваоца лиценце, чак и у комерцијалне сврхе. Ово је најслободнија од свих лиценци.
2. Ауторство – некомерцијално. Дозвољавате умножавање, дистрибуцију и јавно саопштавање дела, и прераде, ако се наведе име аутора на начин одређен од стране аутора или даваоца лиценце. Ова лиценца не дозвољава комерцијалну употребу дела.
3. Ауторство - некомерцијално – без прераде. Дозвољавате умножавање, дистрибуцију и јавно саопштавање дела, без промена, преобликовања или употребе дела у свом делу, ако се наведе име аутора на начин одређен од стране аутора или даваоца лиценце. Ова лиценца не дозвољава комерцијалну употребу дела. У односу на све остале лиценце, овом лиценцом се ограничава највећи обим права коришћења дела.
4. Ауторство - некомерцијално – делити под истим условима. Дозвољавате умножавање, дистрибуцију и јавно саопштавање дела, и прераде, ако се наведе име аутора на начин одређен од стране аутора или даваоца лиценце и ако се прерада дистрибуира под истом или сличном лиценцом. Ова лиценца не дозвољава комерцијалну употребу дела и прерада.
5. Ауторство – без прераде. Дозвољавате умножавање, дистрибуцију и јавно саопштавање дела, без промена, преобликовања или употребе дела у свом делу, ако се наведе име аутора на начин одређен од стране аутора или даваоца лиценце. Ова лиценца дозвољава комерцијалну употребу дела.
6. Ауторство - делити под истим условима. Дозвољавате умножавање, дистрибуцију и јавно саопштавање дела, и прераде, ако се наведе име аутора на начин одређен од стране аутора или даваоца лиценце и ако се прерада дистрибуира под истом или сличном лиценцом. Ова лиценца дозвољава комерцијалну употребу дела и прерада. Слична је софтверским лиценцама, односно лиценцама отвореног кода.